UNIVERSITÉ DU LUXEMBOURG

PhD-FSTC-2015-06
The Faculty of Sciences, Technology and Communication

DISSERTATION

Defence held on 25/02/2015 in Luxembourg

to obtain the degree of

DOCTEUR DE L'UNIVERSITÉ DU LUXEMBOURG

EN SCIENCES DE L'INGÉNIEUR

by

Dmitry SIDOROV
Born on 29 March 1983 in Tver (Russian Federation)

RECEIVER ANTENNA AND EMPIRICAL MULTIPATH CORRECTION MODELS FOR GNSS SOLUTIONS

Dissertation defence committee

Dr Olivier Francis, Chairman
Professor, Université du Luxembourg

Dr Martin Lidberg
Lantmäteriet, Sweden

Dr Tim Springer
PosiTim High Precision GNSS Solutions and Services, Germany

Dr-Ing Felix Norman Teferle, dissertation supervisor
Professor, Université du Luxembourg

Dr Tonie Van Dam, Vice-chairman
Professor, Université du Luxembourg

Abstract

The advent of the Global Navigation Satellite Systems (GNSSs), in particular, the U.S. Global Positioning System (GPS) and the Russia's GLObalnaya NAvigatsionnaya Sputnikovaya Sistema (GLONASS) have revolutionized geodesy by enabling a cheap and robust way of providing precise and continuous position estimates to users. Moreover, GNSSs have been shown to be extremely useful for a wide variety of other applications, in particular, geophysical, atmospheric, oceanographic studies, as well as industrial applications. Although the last two decades of GNSS exploitation were marked by great advances in accuracy and precision of the involved techniques, improvements can still be made. This thesis addresses the topic of receiver antenna and empirical multipath correction models, aiming to further improve GNSS solutions.

GNSS utilizes measurement of ranges between satellites orbiting the Earth and receivers located on the Earth's surface through modulated electromagnetic signals. However, the actual point where the signal is received and which is denoted as a phase centre of an antenna, is not fixed, but varies depending on many parameters. Therefore, high-precision GNSS fundamentally depends on antenna phase centre corrections (PCC) and failing to accurately apply the latter results in biases and elevated uncertainties of estimated GNSS solutions. Additionally, due to repeating satellite-receiver geometry, these phase centre modelling deficiencies may lead to the generation of harmonic signals in the time series of the estimated parameters. In turn, identifying geophysical signals in the time series may be compromised by the presence of these artificial signals, resulting in inaccuracies in derived models.

The geodetic community employs averaged (type-mean) PCC to estimate GNSS orbits, clock biases, tropospheric delays and other parameters, as well as to realize and provide access to the terrestrial reference frame. However, the use of individual PCC is beneficial for GNSS solutions, as it allows for more accurate estimation of satellite orbits and ground station coordinates. The latter is demonstrated using a regional network of 55 GNSS stations and processing the GPS data over a period of 10 years.

Another topic addressed in this thesis concerns development of empirical site models (ESMs) using post-fit phase residuals accumulated over a period of time. These models are aimed to mitigate multipath and other unmodelled site effects that have a negative impact on GNSS solutions. Using a global network of stations the derived ESMs are evaluated for their capability to improve the GPS orbit determination as well as to increase the accuracy of ground station coordinate estimation.

Acknowledgements

This work would have never been possible without the help and support of many people. First of all, I would like to thank my primary adviser, Prof. Dr-Ing. Norman Teferle, for his guidance and persisting help during my time at the University of Luxembourg. Also, I thank the head of Research Unit in Engineering Science, Prof. Dr. Olivier Francis, for his support and inspiration. I express my gratitude to Prof. Dr. Tonie van Dam for believing in me and sharing ideas. I acknowledge the help and support received from my colleagues from the Geophysics Laboratory.

I wish to sincerely thank Dr. Tim Springer and Dr. Ignacio Romero for their help with NAPEOS and for the efforts they spent answering my numerous e-mails.

I thank the stuff of ACT of Luxembourg and BIGF for sharing individual antenna PCC and observation data from their stations. I express my gratitude to Brian Donahue for providing access to the data from the NRCan stations. I acknowledge the efforts of the whole geodetic community for sharing the data and products for the EPN and IGS stations.

I am extremely thankful to the University of Luxembourg HPC department for providing access to the computing resources.

During my work on the PhD I received a lot of support and inspiration from my parents. I am sincerely thankful to them for their belief in me even during the moments of my desperation.

The last, but not least, I wish to thank my wife for her patience during the long evenings I spent at the computer. Truly, a large part of this work was done thanks to her support and encouraging.

Contents

List of Figures

List of Tables

Acronyms and abbreviations

AC	Analysis Center
BIGF	British Isles continuous GNSS Facility
CODE	Center for Orbit Determination in Europe
CTS	coordinate time series
DBD	day boundary differences
DD	double difference
DORIS	Doppler Orbitography and Radiopositioning Integrated by Satellite
EOP	Earth orientation parameters
EPN	EUREF Permanent Network
EUREF	Reference Frame Sub Commission for Europe
ESM	empirical site model
GLONASS	GLObalnaya NAvigatsionnaya Sputnikovaya Systema
GMF	Global Mapping Function
GNSS	Global Navigation Satellite System
GPS	Global Positioning System
GPT	Global Pressure and Temperature model
IERS	International Earth Rotation and Reference Systems Service
IGS	International GNSS Service
ITRF	International Terrestrial Reference Frame
IQR	interquartile range
JPL	Jet Propulsion Laboratory
LC	linear combination
LEO	low Earth orbiter

(continued on next page)

Acronyms and abbreviations *(continued from previous page)*

NAPEOS	NAvigation Package for Earth Observation Satellites
NGS	National Geodetic Survey
NRCan	Natural Resources Canada
PCC	phase centre corrections
PCO	phase centre offset
PCV	phase centre variations
POD	precise orbit determination
PPP	precise point positioning
RINEX	Receiver INdependent Exchange Format
RMS	root mean square
RS	radiosonde
SINEX	Solution INdependent Exchange Format
SLR	Satellite Laser Ranging
SPSLux	Satellite Positioning Service of Luxembourg
SRP	Solar radiation pressure
TRF	Terrestrial Reference Frame
VLBI	Very Long Baseline Interferometry
VMF	Vienna mapping functions
ZHD	zenith hydrostatic delay
ZTD	zenith tropospheric delay
ZWD	zenith wet delay

Chapter 1

Introduction

1.1 Background

Developed in the 1980-s and thought as military tools for global positioning purposes while delivering the accuracy of tens of meters, Global Navigation Satellite Systems (GNSSs) have soon become a valuable scientific instrument, capable of estimating many parameters with an outstanding accuracy and used to broaden our knowledge about the Earth (Moore, 1994). Thus, starting from the earliest days of GNSS, the geodetic community started reaping benefits from processing the observation data of navigation satellites and analysing the results.

Today's fully operational GNSSs are the United States' Global Positioning System (GPS) and Russia's GLObalnaya NAvigatsionnaya Sputnikovaya Sistema (GLONASS). Both systems share the same principle of operation and in general, have much in common. A few distinctive differences make each of them unique and somewhat advantageous for different applications.

The basic idea of GNSS consists in broadcasting coded signals containing information on ranges to the satellites and their almanacs. A user is then capable of estimating his position based on the data received from 4 or more satellites. More information on fundamentals of GNSS operation can be found in, e.g., Hofmann-Wellenhof et al. (2008).

Hand-held GNSS receivers typically represent the simplest solution for providing an estimate of user position that is accurate to several meters. Although GNSSs usually broadcast their signals in two or more frequency bands, due to low cost of such receivers, these operate with signals in only one frequency and utilize unambiguous encrypted signals – pseudorange codes. Alternatively, more advanced geodetic receivers are capable of processing GNSS signals in multiple frequency bands. Moreover, they are able to track carrier-phase data, which are less noisy than the pseudorange codes. Carrier-phase measurements can be exploited when centimetre accuracy is required, due to their millimetre-level precision. However, these measurements are ambiguous and require sophisticated techniques to resolve the integer number of cycles that a satellite signal needs to reach a receiver. More information about ambiguity resolution concepts and methods can be found in, e.g., Teunissen (1996) and Teunissen (2003).

High precision GNSS is required for many geodetic, scientific and industrial applications. Thus, continuous GNSS measurements are used for geodynamic studies, such as crustal movements

and deformations. This involves tracking of tectonic plate motion (e.g., Larson et al., 1997; Prawirodirdjo, 2004; DeMets et al., 2010; Altamimi et al., 2012; Hansen et al., 2012), tidal (Tregoning et al., 2009) and non-tidal (Geng et al., 2012) loading deformations, earthquakes (e.g., Larson et al., 2003; Blewitt et al., 2006; Hoechner et al., 2008), constraining glacial isostatic adjustment models (e.g., Johansson et al., 2002; Dietrich et al., 2005; Geirsson et al., 2006; Lidberg et al., 2007; Khan et al., 2008; Lidberg et al., 2010), mean sea level (e.g., Löfgren and Haas, 2014), etc. Studying geophysical processes using GNSS requires significantly long time series, as these contain combined effects from multiple sources (Blewitt and Lavallee, 2002; Dong et al., 2002; Davis et al., 2012).

In addition to geodynamic studies, GNSSs have demonstrated their importance in atmospheric research and meteorological studies (e.g., Bevis et al., 1992; Ho et al., 1996; Wang et al., 2007), which are possible due to interactions of GNSS signals with charged particles in the Earth's ionosphere and tropospheric refraction, respectively. Furthermore, GNSS reflectometry comprises a large field of research that involves studying GNSS signals that are reflected from the Earth's surface, incorporating such fields as, e.g., altimetry (Rius et al., 2012) and soil moisture studies (e.g., Larson et al., 2008; Tabibi et al., 2015).

Together with Very Long Baseline Interferometry (VLBI), Satellite Laser Ranging (SLR) and Doppler Orbitography and Radiopositioning Integrated by Satellite (DORIS), GNSS is used to define the International Terrestrial Reference Frame (ITRF). Its importance for ITRF combinations stems from the spatial density of the observation network, the ability of providing continuous observations, accurate polar motion tracking and the strengthening of the link between VLBI and SLR networks (Altamimi and Collilieux, 2009). However, GNSS, as a technique for terrestrial reference frame (TRF) definition has some weaknesses, e.g., an imprecise TRF origin and an underdetermined TRF scale, which is a result of imprecisely known satellite and receiver antenna phase centres, see, e.g., Zhu et al. (2003) and Ge et al. (2005).

While some applications require stability in station coordinate time series (CTS) in order to correctly estimate the rate of change in site positions (velocities), other studies are more concerned with the signals that can be extracted. Thus, in addition to (quasi-)linear tectonic plate motion, long CTS may contain harmonic, e.g., seasonal (e.g., Dong et al., 2002; Davis et al., 2012; Chen et al., 2013), tidal (e.g., van Dam et al., 2001) and other non-linear signals (e.g. Nield et al., 2014). These serve as an important data input for studying global climate change and understanding geophysical processes occurring on our planet. Thus, being a "scientific instrument", GNSS plays a key role in many areas, facilitating improvement of models and advancing our knowledge.

The ground segment of this immense "scientific instrument" consists of thousands of stations across the globe, continuously tracking the satellites. Some of these stations contribute to a voluntary federation, namely the International GNSS Service (IGS) (Dow et al., 2009), comprised

of more than 200 agencies worldwide, which make efforts of providing satellite observation data and products of the highest quality, as well as the Earth rotation parameters.

Although the term GNSS refers to navigation systems in general, it should be noted that the dominating contribution to the aforementioned studies belongs to GPS so far. GLONASS was not operational during the late 1990s due to short lifetimes of its satellites and poor constellation maintenance. These were a consequence of financial difficulties after the breakup of the USSR. Although some IGS analysis centers (AC) included GLONASS data in the early 1990s, the lack of operational satellites in the constellation forced them to switch to the GPS-only processing. The routine processing of GLONASS data was restarted only 7-8 years ago. Thus, the accumulated GLONASS data cannot boast of significant continuous time series length. However, GLONASS and the emerging GNSSs (the European Galileo and the Chinese BeiDou) will contribute more to geophysical, geodynamic, meteorological, climatological and other studies in the future.

The space segment of GPS is composed of 32 satellites in 6 nearly circular orbital planes with a semi-major axis of about 26 562 km. This results in the orbital repeat period of about half of a sidereal day, or approx. 11 h 58 m (Agnew and Larson, 2007) and in the fact that the orbital planes appear to be stationary in the Earth-fixed coordinate system. As a consequence, the satellite ground tracks repeat every sidereal day, facilitating prediction and mitigation of errors associated with the repeating satellite-receiver geometry (e.g., multipath). However, systematic errors in the GPS solutions may still persist due to the presence of unmodelled error sources along the signal path, as well as their inter-correlation. These errors result in biases and harmonic signals in the time series of various derived parameters, which may potentially correlate with other geophysical signals and deteriorate estimation and modelling of the associated processes. As an example, both the Moon and Sun interact with the Earth's masses (geophysical fluids), producing tidal displacements at sidereal frequencies, therefore, the presence of systematic unmodelled errors in GPS has an impact on the estimation of these geophysical signals.

Due to the chosen orbital parameters and the resulting precession of the ascending node of the GPS satellites, the constellation performs a full revolution with respect to the Sun after ∼351.2 days (Schmid et al., 2007), a period called a GPS draconitic year. The presence of signatures of the GPS draconitic year and its harmonics has been shown in all GPS-derived products: station CTS, the GPS orbits and Earth orientation parameters (EOP; Ray et al., 2006, 2008; Altamimi et al., 2011; Collilieux et al., 2011; Seitz et al., 2012; Griffiths and Ray, 2013). These spurious signals are artificial, have no geophysical origin and largely result from the application of imprecise models.

Site effects, in particular, multipath and other interactions between an antenna and surrounding environment are among potential contributors to the spurious signals observed in GNSS solutions. Because of the geometry repeating itself every sidereal day and correlations with other

parameters, these modelling errors may propagate into other GNSS solutions. The impact is amplified by deficiencies in the applied ground antenna phase centre corrections (PCC), which together with repeating satellite constellation result in effects similar to multipath.

The problem of accurate determination of these models is of extreme significance in GNSS. The ground antenna PCC are closely related to the respective satellite models due to high correlations between these parameters. Furthermore, these correlate with station heights and tropospheric delays. To highlight the importance of these correlations Zhu et al. (2003) demonstrated that a change in satellite antenna phase centre z-offset for all satellites by, e.g., 10 cm will change the scale of the terrestrial reference frame by -5 mm . Consequently, satellite antenna PCC can only be estimated if the terrestrial scale is fixed and, vice versa, receiver antenna PCC can be estimated if the respective satellite parameters are kept fixed (Schmid and Rothacher, 2003; Schmid et al., 2007). However, despite the direct relationship between ground and satellite antenna PCC, the latter are not addressed in this thesis, as this topic represents a broad field for a substantial investigation.

As mentioned above, antenna and multipath modelling are two very closely related problems. Due to electromagnetic interaction between an antenna and objects in its vicinity, both problems cannot be regarded separately, but have to be treated in junction. In support of this idea, one may refer to, e.g., Dilßner et al. (2008), who reported that monuments may have a significant impact on how signals are received by an antenna and suggested to consider them in junction in studies related to antenna modelling issues.

The existing methods, which address the problem of multipath and other site-specific errors, involve various techniques. There are multipath mitigation algorithms inside receivers that perform data smoothing, e.g., Trimble's EVEREST$^{\text{TM}}$ technology (Trimble Navigation Limited, 1997), however, such methods introduce modifications to collected GNSS data and their application is avoided within the IGS. Therefore, only receiver independent techniques are discussed in the following.

Byun et al. (2002) and Lau and Cross (2007) developed ray-tracing methods to model and correct for multipath errors. Another approach, which is based on the signal-to-noise ratio (SNR) observations, was implemented by Axelrad et al. (1996) and Bilich and Larson (2007). The impact of microwave absorbing material below an antenna was studied by Niell (1997) and Ning et al. (2009, 2011). Additionally, Wübbena et al. (2006a) and King et al. (2012) noted positive effects from calibrating antennas together with the top of the pillar. Finally, in-situ calibration techniques using supplementary, temporary stations were employed by Granström (2006) and Wübbena et al. (2010). Although improvements in GNSS-derived time series could be achieved with the aforementioned techniques, all of them suffer from weaknesses, preventing their widespread usage.

The ray-tracing methods, for example, assume development of a detailed model of the sur-

rounding environment of the antenna. This is often difficult to implement due to diversity and irregularity of object shapes. Additionally, the physical properties of object surfaces need to be known to be modelled correctly. Such methods perform very well when the environment is known and is invariant over time, e.g., for space vehicles. However, its application to ground stations remains difficult and seems not to be feasible for a global network.

The SNR-based technique is very promising for multipath mitigation and has been applied by Rost and Wanninger (2009, 2010) and Bilich et al. (2008). However, the use of the SNR observations is not always applicable to large networks, as receivers of different manufacturers report inconsistent measurements, making the processing of historical data problematic.

The purpose of microwave absorbing material is to reduce signal reflections and scatter from close by objects. Therefore, its usage at GNSS sites brings positive results. However, such materials are often subject to wearing due to environmental exposure and hence need regular replacement. Moreover, placing such materials for the first time may introduce offsets (e.g. Johansson et al., 2002), while the effect of replacing them remains unstudied. Additionally, this method is not applicable to historical data.

Calibration of antennas with the top of the pillar solves problems related to electromagnetic coupling between antennas and monuments. However, this technique cannot be applied to already installed stations. Also, the maximum weight and dimensions of the pillar/antenna connection that calibration robots usually can handle are limited. Due to these constraints some combinations cannot be calibrated using this method.

The in-situ method using supplementary antennas involves the temporary installation of a multipath-free station in the vicinity of the antenna to be calibrated (Park et al., 2003; Granström, 2006). Due to the short baseline between the two antennas, ionospheric, tropospheric and orbit errors can be neglected, allowing to extract the antenna- and site-dependent information and develop respective corrections. This technique is very promising, but may not be applicable to widespread usage due to potential difficulties associated with such temporary installations on a global scale as well as the need of repeating such calibration regularly due to potential changes in the site environment. Furthermore, the technique cannot be applied to historic data.

Another method for multipath mitigation is based on using the post-fit phase residuals. It is adopted in this study. The method was first demonstrated by Hurst and Bar-Sever (1998). The authors used PPP and could achieve a significant reduction in the sensitivity of computed station coordinates to elevation cut-off angle as well as reduction in the number of rejected phase observations. However, the improvement in the daily coordinate repeatability was hardly noticeable.

Using the same method Iwabuchi et al. (2004) compared results from several scientific GNSS processing packages and showed similar results for double-difference and PPP processing. The

authors reconstructed single-difference phase residuals from the double-difference estimates. Such a reconstruction was based on previously performed studies by Alber et al. (2000), which relied on the assumption that one site in the network was free of multipath.

Granström (2006) compared an in-situ calibration method with the post-fit phase residuals approach and found that the latter could provide results as good as the ones obtained using the in-situ calibration. Using either of the two methods, however, did not result in any improvement in the coordinate repeatability. Instead, the quality of tropospheric estimates was increased, which lead to a reduction of biases between GNSS derived estimates and external measurements.

Following the same strategy, Moore et al. (2014) developed and applied empirical site models (ESMs) of post-fit phase residuals in a regional network. Additionally, the authors carried out a detailed study of the derived ESMs, investigating its potential to reconstruct the multipath environment depending on monument height and parameters that are estimated during processing. This assessment was based on the root mean square (RMS) error of recovering the simulated multipath. It was shown that the ESM cannot accurately recover multipath for low monument heights. Also the estimation of clock biases and tropospheric delays reduced the performance of the ESM. The authors noted another limitation of the ESM, which is related to geographical station location. In particular, the use of the ESM may not be effective for stations at high latitudes ($\pm 60°$).

By comparing CTS before and after the application of ESMs Moore et al. (2014) have assessed their potential to reduce draconitic signals. However, the authors witnessed a mixed effect, as the power at draconitic frequencies was amplified at some and reduced at other stations. They could not identify any relationship between the observed effects and other parameters, e.g., monument heights or geographical location of stations.

Thus, different methods exist to address the problem of multipath and other site-specific effects, however, none of the proposed techniques eliminates it completely due to complexity and temporal variability of the real world environment at stations. As a consequence, an antenna PCC obtained by calibration may be significantly altered due to potential site effects once the antenna has been installed. In turn, this may have an impact on parameters that are estimated (e.g., position, tropospheric delays) due to introduction of biases or even periodic signals, which may possibly contribute to the aforementioned draconitic signals.

Although the nuisance problems related to antenna PCC are relevant to every either present or future GNSS, only the US GPS is addressed in this study. Such a limitation is justified by several reasons. Firstly, currently there are only two fully operational GNSS: GPS and GLONASS. The emerging BeiDou and Galileo are not always supported by ground receivers, therefore it is problematic to obtain the observation data from a global network of stations. Even if these can be obtained, the respective time series are fairly short and the results of their analysis are

questionable, whereas individual PCC for these GNSSs are not yet available.

The situation with GLONASS is different, as it has been in operation for a number of years and receiver/antenna manufacturers had enough time to adapt their equipment for it. However, some limitations still persist on the software side. Unlike GPS, GLONASS employs frequency division multiply access, implying that different frequency slots are assigned to the satellites. This creates difficulties for phase integer ambiguity resolution due to the impossibility of elimination of uncalibrated biases on both satellite and receiver sides (see Appendix A for details). Integer ambiguity resolution significantly improves the precision of results and, therefore, is essential for this study (see Section 2.3.4 for details). Unfortunately, the GNSS processing software used in this study (NAPEOS, see Section 5.2) does not yet support phase ambiguity resolution for GLONASS. Hence GLONASS was not included in this research.

1.2 Current research contribution

Although the problem of antenna modelling, in particular, of PCC that are applied to antennas to compensate for the introduced signal biases has been discussed in many studies, there are some gaps that are addressed in this thesis. In particular, the impact of deficiencies in the current IGS type-mean PCC on sub-daily positioning compared to the respective solutions obtained using individual PCC using state-of-the-art models and processing schemes is analysed. Additionally, this study provides an assessment of the impact of deficiencies in antenna PCC on computed satellite orbits and station coordinate solutions obtained through a consistent processing.

Another contribution is related to multipath and interactions between antennas and their surrounding environment that result in a systematic impact on received signals and, consequently, on produced solutions. To address the problem of multipath the current study adopts empirical site modelling (ESM; introduced in Section 3.6). Although a lot has been developed in this field with respect to individual stations and sometimes to regional networks, no studies have been performed on a global scale. A null test discussed in Section 5.8 gives an indication that PCC deficiencies may generate periodicities in GNSS solutions. Thus, this thesis fills the gap by assessing potential contributions to the quality of estimated satellite orbits and station coordinate solutions using a global network of GNSS stations applying ESM corrections.

The following summarizes the pursuits of the current study:

- Evaluation of the impact of using different PCC on sub-daily positioning using recent models and processing schemes.

- Assessment of the impact of deficiencies in the applied PCC on satellite orbits, verification if there are any advantages from consistent processing when both satellite orbits and station

positions are estimated using a set of individual antenna PCC. Evaluation of the impact of PCC on processing in general and assessment of the impact of changes in PCC on draconitic signals in the GPS-derived time series.

- Development of a method for the estimation of ESM for large networks and assessment of its potential to provide additional corrections for stations that suffer from multipath and/or antenna PCC deficiencies.

- By applying the ESM to address the problem of antenna modelling deficiencies and multipath present at sites and to assess its impact on satellite orbits, in particular, on the potential of the ESM to reduce draconitic errors that are observed in the orbits and CTS.

- Assessment of the impact of the ESM-corrected PCC on station positions and evaluation of their potential to reduce draconitic signals through a consistent processing involving orbit estimation.

Additionally, there is a number of features that allow the current study to stand out from the work that has already been performed in this field. However, this will be discussed in detail in the following chapters.

1.3 Thesis outline

The entire thesis is arranged into 8 chapters, which are outlined in the following. This chapter is followed by Chapter 2, which provides details on the artificial signals in time series, i.e., that have no geophysical origin, focusing on draconitic (GPS-specific) signals observed in GNSS solutions.

Chapter 3 introduces the GNSS antenna PCC and discusses deviations between individual (antenna-specific) and the IGS type-mean antenna PCC. Multipath, having similar impact on GNSS solutions is described. The ESM approach to address PCC deficiencies is introduced.

Chapter 4 describes the geodetic networks which were used in this study.

Chapter 5 discusses a software package for processing GNSS data – NAPEOS, used by the European Space Agency (ESA) for routine processing of GNSS data. Basic sequences for performing position and orbit estimation using NAPEOS are provided, including strategies for investigation of PCC deficiencies impact on GNSS solutions. Also, the chapter describes the ESM derivation methodology in relation to NAPEOS. Furthermore, processing results with altered PCC that provide the first indication that PCC deficiencies may generate long period signals in GNSS solutions are shown.

Chapter 6 presents and discusses results of applying individual antenna PCC for orbit determination and station position estimation.

Chapter 7 evaluates the potential of ESM to reduce scatter in the estimated satellite orbits and station coordinates using a global network of GNSS stations.

Chapter 8 summarizes the main points and contribution of the thesis and outlines recommendations for further work.

Chapter 2

Draconitic Signals in GNSS-derived Time Series

This chapter introduces draconitic signals in the GNSS-derived time series, i.e., those having no geophysical nature, but more likely being processing and modelling artefacts. First, an introduction to the nature of these spurious signals is given, followed by description of aliasing effect and details on investigations on the topic.

2.1 Introduction

Unexplained signals in the GPS-derived products were initially discovered by Ray et al. (2006, 2008). The authors analysed residuals of the weekly International GNSS Service (IGS; Dow et al., 2009) solutions, which provided the basis for the ITRF2005 (Altamimi et al., 2007). At that time the ITRF2005 represented the latest International Terrestrial Reference Frame (ITRF) realization. Ray et al. (2008) examined combined power spectra for position residuals of 167 sites and discovered peaks at harmonics of 1 to 6 cycles per year (cpy) in both horizontal and vertical coordinate components (Figure 2.1). Additionally, the frequencies of the discovered harmonic signals did not exactly coincide with the annual signal and its harmonics, but were slightly shifted.

At the same time, other space geodetic techniques, in particular, SLR, VLBI and DORIS, contributing to the ITRF determination, did not show any signs of these signals. Hence, it appeared that those signals had to be attributed to GPS alone. Thus, attention of the geodetic community was attracted by the problem of discovering their source, as, clearly, they did not have a geophysical nature, but appeared to be a processing or modelling artefact.

Additionally, Ray et al. (2008) pointed out that the spurious signals could be related to the GPS draconitic year – the period required for the constellation to repeat its inertial orientation with respect to the sun, which is close to 351.2 days. This, in turn, could very well explain the source of those signals, as the peaks in the power spectra were centred at frequencies matching $1.04 \times n$ cpy, where $n = 1, 2, 3, 4, \ldots$

Later similar signals were discovered by Collilieux et al. (2011) in the reprocessed solutions in preparation for ITRF2008 (Altamimi et al., 2011). Although the new realization of the reference

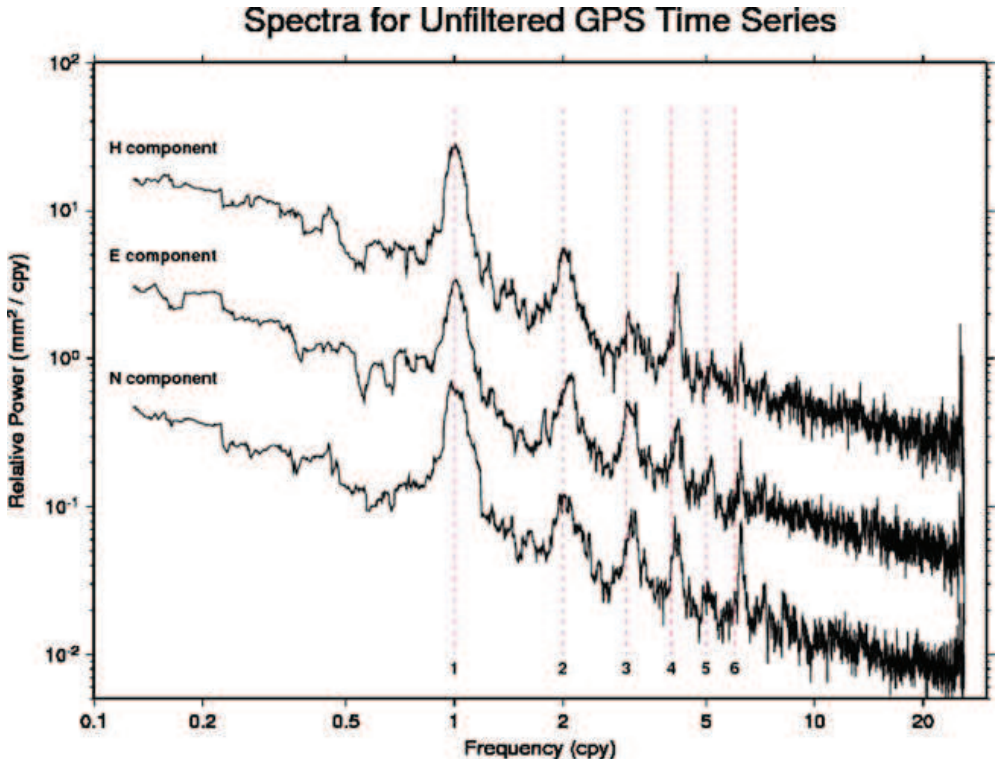

Figure 2.1: Stacked periodograms of non-linear position residuals for the 167 IGS stations having more than 200 weekly measurements between 1996.0 and 2006.0 (Ray et al., 2008).

frame incorporated a number of improvements with respect to ITRF2005, particularly, the use of consistent antenna phase centre models on both the satellite transmitters and ground receivers, little or no improvement was achieved with respect to the spurious signals.

The presence of these anomalous harmonics was also shown in other GPS-derived products. Hugentobler et al. (2006) discovered harmonic signals with periods close to 350 days in geocenter motion estimates, as sensed by GPS satellites. Another more thorough study on the topic was performed later by Meindl (2011), who was investigating the geocenter motion derived using different GNSSs. Griffiths and Ray (2013) analysed the GPS orbit overlaps at day breaks and also discovered draconitic signatures in the respective power spectra. Additionally, signals close to 50 and 70 days, which correspond to the 7^{th} and 5^{th} overtones, respectively, of the fundamental GPS draconitic frequency were discovered by Seitz et al. (2012) in the y-component of the terrestrial pole rate.

2.2 Aliasing as a way of generation long period signals

Harmonic signals are often found in geodetic time series due to various geophysical and non-geophysical reasons. The origins of these signals may be seasonal loadings, sub-daily tidal displacements, multipath, whereas their periodicity may vary from a calendar year to some hours. At the same time, GNSS measurements are typically collected and processed within windows of 24 hours, leading to undersampling of the higher frequency signals and producing their aliases.

The term "aliasing" (Blackman and Tukey, 1958) is a well-known effect in signal processing that may occur when a continuous signal of a certain frequency is sampled at a frequency that is different from that of the original signal, Figure 2.2. The frequency of the aliased signal can be computed as

$$f_a = |f_s \times n - f|, \tag{2.1}$$

where n is the closest integer multiple of the sampling frequency f_s to the original signal f. Thus, in case of presence of a sub-daily signal in a time series with a period close to a nominal orbital period of a GPS satellite (half a sidereal day) and daily processing (i.e., $f = \frac{1}{86164\,s}$ and $f_s = \frac{1}{86400\,s}$) an aliased signal with frequency $f_a = 3.17 \times 10^{-8}\,s^{-1}$ and respective period of 365.1 days is generated. However, if the signal period is reduced by only -5 s with respect to the previous case, the 24 h sampling produces an aliased signal with frequency of $f_a = 3.3 \times 10^{-8}\,s^{-1}$ which is equivalent to a period of 350.2 days.

Thus, aliasing of harmonic signals present in geodetic time series may produce longer period signals that contribute to the spurious signals discovered by Ray et al. (2006). However, more details on the subject is provided in the following sections.

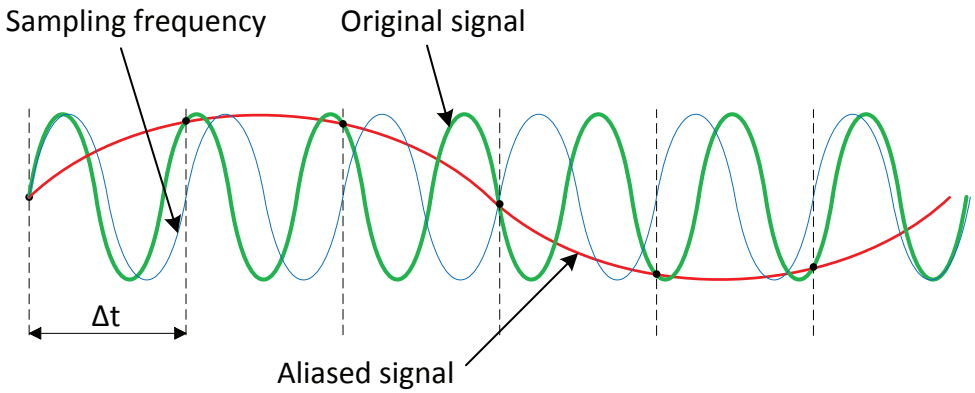

Figure 2.2: Aliasing effect.

2.3 Understanding the sources of draconitic signals

Current advances in resolving the problem of draconitic signals in GNSS-derived time series are presented in the following. These combine both solutions that have already been shown to be effective in reducing the signals and have been implemented by some IGS ACs, as well as other considerations about the error sources, potentially being in relations with the spurious draconitic harmonics observed in GNSS-derived time series.

2.3.1 Solar radiation pressure modelling errors

The discovery of draconitic signals has resulted in many studies aimed to reveal their origins and many ideas were presented. As these spurious harmonics are observed in nearly all GNSS-derived solutions of all IGS ACs, it is suggested that deficiencies in global models appear to contribute to them most (Amiri-Simkooei, 2013). This results in the propagation of errors throughout processing into all obtained solutions.

Solar radiation pressure (SRP) is a non-conservative force acting on GNSS satellites. Therefore, systematic errors in SRP modelling may result in the generation of periodic signals at draconitic frequencies. Rodriguez-Solano et al. (2012c,b) suggested that the radiation pressure caused by the Earth albedo (the fraction of solar radiation that is reflected from the Earth back to space), which was initially not considered, could have an impact both on the orbits (mainly in the radial direction) and consequently on station coordinates. Their studies have shown that some power at the draconitic frequencies in the power spectra of station CTS could be reduced if the albedo radiation modelling is applied.

At the same time, SRP modelling of GPS satellites has been improved. Rodriguez-Solano et al. (2014) showed that part of the draconitic signals in GNSS products could be attributed to orbit modelling deficiencies of GPS satellites. Compared to the established Center for Orbit Determination in Europe (CODE) (5-parameter) radiation pressure model (Beutler et al., 1994), a new box-wing model, introduced by Rodriguez-Solano et al. (2012a) and later improved by Rodriguez-Solano et al. (2013), resulted in a more accurate modelling of the orbits. This modification, as reported by the authors, led to a reduction of the draconitic signals in the orbits (as based on their day boundary overlaps), in the geocenter Z-component, in the X and Y pole rates, and in the station coordinates. These improvements in nearly all GNSS products resulted in its adoption in the second IGS reprocessing campaign (Griffiths et al., 2012).

2.3.2 Sub-daily tides

Penna et al. (2007) have shown how errors in the tidal models propagate into coordinate solutions. This work is linked with the study of Stewart et al. (2005), who suggested that unmodelled

systematic errors could propagate into coordinate solutions due to linearization performed in the least squares estimation and consecutive aliasing. Additionally, Tregoning and Watson (2009, 2011) studied the impact of applying atmospheric loading deformation and concluded that failing to model the S1 and S2 tidal constituents may result in generation of spurious signals that match the main draconitic frequency and its first overtone, or ∼1.04 and ∼2.08 cpy.

Also Griffiths and Ray (2013) demonstrated that errors in the a priori sub-daily Earth orientation parameters (EOP) provided by the International Earth Rotation and Reference Systems Service (IERS) could propagate through processing into solutions. It appears that the produced orbits could very well absorb any artificially introduced tidal error of 20%, resulting in the generation of draconitic signatures in the estimated orbits, and EOPs. As the produced draconitic signals had an appearance similar to those observed previously in the IGS products, the authors suggested that the errors in the IERS EOP tidal models have the potential to largely contribute to the generation of spurious signals.

The aforementioned effect is known as aliasing (Blackman and Tukey, 1958) and usually occurs when frequency of a signal is different from the sampling frequency. In particular, the daily GPS solutions are averaged over one solar day (24 hours) and errors in tidal models with different frequencies may produce longer wavelength aliases.

Additionally, Amiri-Simkooei (2013), while analysing the CTS of GPS stations, came to a conclusion that the observed unexplained signals were most likely related to orbit or tidal modelling issues, while the site-dependent contribution to these errors was presumably small.

2.3.3 Multipath and antenna modelling errors

Sidorov and Teferle (2016) showed that antenna/radome modelling deficiencies may generate harmonic signals in sub-daily coordinate solutions with periods equal to the GPS orbital repeat. Also, by the system design the GPS satellites repeat their ground tracks every sidereal day, whereas the GPS solutions are averaged over 24 hours. Agnew and Larson (2007) showed that the average repeat time of the GPS constellation is 247 seconds less than a day. Therefore, using Equation 2.1 aliases with frequency $f_a = 3.32 \times 10^{-8}\, s^{-1}$ or approx. 1.04 cpy may be generated for daily sampling. Therefore, site-specific errors may also contribute to the draconitic signals. These errors include not only multipath, but also antenna and radome modelling deficiencies, which induce systematic phase shifts to the observed signals. King and Watson (2010) showed through simulations that multipath at stations could propagate into solutions and result in harmonic signals in the CTS with periods matching ∼351.4 days and its multiples. Additionally, the authors pointed at possible errors in vertical site velocities due to multipath. This could be explained through variation of the estimated station heights due to a combination of multipath and the evolving satellite constellation.

The problem of multipath and antenna phase centre modelling errors was addressed in many studies, as its impact on positioning may vary to a large degree. However, as multipath is highly variable at different stations, it is difficult to describe analytically and develop models that would correct for it. The same refers to antenna modelling errors, which may result in substantial biases in solutions (Baire et al. (2014)). However, as these are difficult to quantify due to a rather large amount of effects that contribute to deviations of actual antenna phase centres from their modelled values, this leads to a very limited amount of studies with reference to the aforementioned problem of draconitic signals.

2.3.4 Additional sources of draconitic signals

Another possible source of draconitic signals can be attributed to GNSS processing techniques and is related, in particular, to the phase ambiguity resolution. The studies of Tregoning and Watson (2009) and King and Watson (2010) showed that not fixing phase ambiguities could favour the propagation of spurious signals throughout solutions and, consequently, result in the amplification of harmonic signals in CTS compared to the respective ambiguity-fixed solutions.

However, as ambiguity fixing is routinely performed in today's GNSS processing with a high success rate, presumably this issue should have small influence on the spurious signals observed in the GNSS-derived products. Nevertheless, it is essential to highlight the importance of phase ambiguity resolution in any research related to the generation or propagation of draconitic harmonics throughout processing.

2.4 Summary

Spurious harmonic signals with frequencies close to $1.04 \times n$ cpy, where $n = 1, 2, 3, 4, \ldots$ that were detected in the GNSS-derived time series were introduced. As the frequency of these signals matches the one required for the GPS constellation to repeat its inertial orientation around the Sun, the detected signals likely have no geophysical nature, but are processing artefacts. Among the potential sources of these signals the scientific community highlights systematic deficiencies in the satellite SRP modelling, tidal displacement errors, multipath and station antenna modelling problems as well as unresolved carrier phase ambiguities.

The SRP and tidal modelling deficiencies presumably have the dominating influence on the generation of the aforementioned spurious signals, whereas the impact of multipath and station antenna modelling errors is less studied and may be underestimated. Nevertheless, the initial investigations indicate that these may get aliased in longer period signals with periods matching the length of the GPS draconitic year. Finally, as carrier phase ambiguity resolution success rate is high in today's GNSS processing, its contribution to the generation and propagation of the

artificial signals is small.

Chapter 3

GNSS Antenna- and Site-Specific Errors

This chapter introduces receiver antenna phase centre corrections (PCC) and provides background information on how they are obtained and represented. Through demonstrating the differences between the PCC of particular antennas the importance of using individual antenna models for precise positioning is highlighted. Furthermore, the basics of multipath are explained, focusing on its impact on positioning. Finally, empirical site model (ESM) as an approach for PCC deficiencies and site effects correction is introduced.

Thus, the main points that are addressed in this chapter:

- Provide the background information on the antenna phase centre corrections, in particular on how they are represented and used by the geodetic community.
- Provide details on calibration facilities and the associated methods, summarizing their main characteristics.
- Highlight the importance of performing individual antenna PCC through demonstration of the differences between individual PCC of IGS-standard geodetic antennas within the same model range. Demonstrate the range of deviations of individual PCC from their respective type-mean models.
- Give an overview of multipath and its impact on positioning.
- Introduce an ESM as a method to correct for multipath and other site-specific effects.

3.1 Introduction

In addition to accurate modelling of satellite orbits, clock biases, various loading effects, etc., precise GNSS positioning requires accurate modelling of a large amount of error sources affecting GNSS signals on their path from a satellite to a receiver. Thus, while traversing any medium, the electromagnetic signals are altered due to interactions with it. In a general case, when a receiver is located somewhere on the Earth surface, the signals are affected by the satellite antenna,

ionosphere, troposphere and receiver antenna. On each part of the way the induced errors should be carefully modelled or estimated.

The satellite antenna corrections are not addressed in this thesis and are skipped here. The ionosphere represents the upper part of the Earth atmosphere and extends from about 50 km to 1000 km. Its impact on GNSS signals is characterized by their interactions with free electrons, resulting in delaying GNSS ranging codes and advancing carrier phases. Because of the frequency dependency, the ionospheric effect can be estimated from dual-frequency GNSS observations and to a large percentage removed. The ionosphere-free linear combination (LC) that is commonly used in GNSS processing removes the first order ionospheric effects. These amount to 99.9% of the total interactions between GNSS signals and the ionosphere. An interested reader may obtain more information on this topic in Hofmann-Wellenhof et al. (2008) and Schaer (1999).

The lower part of the atmosphere is composed of the troposphere (from the ground level to approx. 15 km) and the stratosphere, which extends up to the ionosphere. The troposphere is characterized by nondispersive properties for GNSS signals. 90% of tropospheric refraction is caused by the hydrostatic part (dry troposphere), which is a function of temperature and pressure, whereas the rest is attributed to the wet part. The latter depends on the amount of water vapour along the signal path and is highly variable. The hydrostatic part is generally modelled, whereas the wet part is estimated. The two parts are known as a zenith hydrostatic delay (ZHD) and a zenith wet delay (ZWD), respectively, whereas their summation results in a zenith tropospheric delay (ZTD). Mapping functions, e.g., Global Mapping Function (GMF, Boehm et al., 2006) or Vienna mapping functions (VMF, Boehm and Schuh, 2004) are used to convert ZTD into tropospheric delay along the line of sight of a satellite. More information on the impact of neutral atmosphere on space geodetic measurement techniques can be found in, e.g., Saastamoinen (1972); Davis et al. (1985); Elgered et al. (1991).

Satellite antennas also introduce errors due to phase centre offsets (PCO) and phase centre variations (PCV), which require accurate modelling. The geodetic community has invested significant efforts in deriving these models for different GNSS (Schmid and Rothacher, 2003; Schmid et al., 2007; Dach et al., 2011). Accurate application of corrections for satellites is required because the orbits are computed with respect to the centres of mass of the satellites, whereas the ranges to satellites are measured to their antennas. Due to a number of reasons, e.g., early-stage GNSS satellites, confidentiality issues, potential deformation of satellite antenna during the launch phase, etc., the satellite antenna PCC have to be estimated while the satellites are in orbit. As this represents another topic for research, its detailed description is omitted here. Instead, attention of the reader will be drawn to interactions of GNSS signals with receiver antennas, including objects in the vicinity of antennas that may have an impact on the signals due to reflections and electromagnetic interactions and, consequently, introduce errors in the GNSS

parameter estimation.

The importance of performing antenna phase calibrations was shown almost immediately after GNSS started being used for precise positioning (Rothacher et al., 1995). As early as in the middle of the nineties the geodetic community started applying a correction for a mean phase offset to increase accuracy of solutions, because not applying any could result in height errors of up to 10 cm, as was demonstrated by Mader (1999). However, the refinement of the applied models and processing techniques for GNSS has soon revealed the necessity of more sophisticated antenna phase correction approaches. The initially developed relative antenna corrections were replaced by absolute models (Rothacher and Mader, 2003; Schmid et al., 2005), as the latter could solve the problem of biased station heights and reduce scale errors of global GPS solutions (Ge et al., 2005).

Nowadays applying antenna calibrations is vital for achieving millimetre-level precision and accuracy of GNSS solutions. Therefore, the importance of understanding how antenna PCC are obtained and constructed is obvious.

3.2 Basics of antenna phase correction models

Generally speaking, when a pseudorange between a satellite and ground station is measured, it is measured between phase centres of antennas on the satellite and receiver. In the early stages of GNSS geodesy these were not taken into account, which resulted in large positioning errors (Mader, 1999). A lot of efforts were made later to provide the geodetic community with a consistent set of satellite and receiver calibrations (Schmid et al., 2007).

Electromagnetic phase centres of antennas usually do not coincide with the physical ones. It follows that coordinates, which have been obtained using GNSS, are those of the mean phase centre of a receiver antenna that was used for signal reception. Furthermore, the phase centre of an antenna depends on the direction of incoming signals, their intensity and frequency. Strictly speaking, phase centre (a point where the signal is received) is different for each incoming signal. Therefore, respective corrections are always necessary in a strive to achieve high accuracy solutions.

3.2.1 Phase centre offset and variations

From a geometrical perspective the electromagnetic phase centre of an antenna depends on the direction of the incoming signal, in other words, on azimuth and elevation. Thus, for a given frequency the mean phase centre estimated over all azimuth (0°-360°) and elevation (0°-90°) angles is called a phase centre offset (PCO; a constant part). It defines a vector from the antenna reference point (ARP), which often coincides with the mounting point of an antenna. The variable part of phase delays due to changing azimuth and elevation of incoming signals is described by

the phase centre variations (PCV), Figure 3.1.

A combination of PCO and PCV is generally called phase centre correction (PCC). Thus, if the PCO of an antenna is given with respect to the ARP in a Cartesian coordinate system ($PCO(xyz) = \{X, Y, Z\}$), then the total correction to the incoming signal can be expressed as

$$PCC(\phi, \theta) = PCV(\phi, \theta) + X \cdot \cos\phi \sin\theta + Y \cdot \sin\phi \sin\theta + Z \cdot \cos\phi, \tag{3.1}$$

where ϕ and θ are horizontal and vertical angles in the antenna body frame, respectively.

As mentioned before, PCC are different for each GNSS frequency. This implies that the PCC deficiencies may be amplified in LCs of signals. Thus, for the ionosphere-free LC, being the most widely used LC in high-precision applications, errors in antenna PCC modelling may be amplified by a factor of ~3.1 (Rocken et al., 1995). As in today's GNSS processing forming linear combinations of signal observables is vital for, e.g., eliminating the first-order effect of ionosphere or performing phase ambiguity resolution, the importance of accurate PCC modelling is elevated.

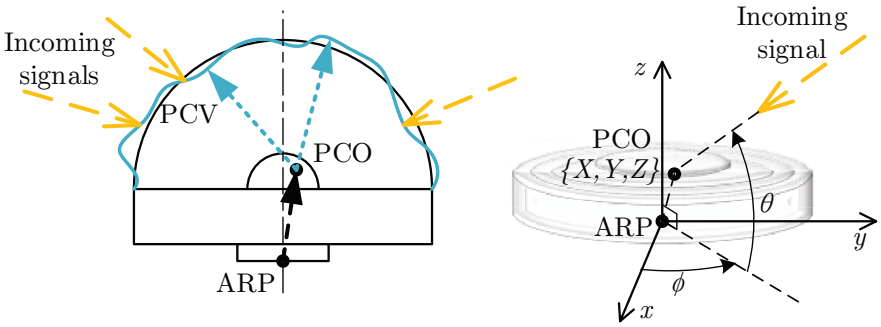

Figure 3.1: Antenna reference point (ARP), phase centre offset (PCO) and phase centre variations (PCV).

3.2.2 Spherical harmonics for PCC representation

While an antenna PCO is constant for a given frequency and can be represented as a vector from the ARP, the PCV are variable. However, the latter can be described using a continuous and harmonic function, which depends on azimuth and elevation. For this purpose Rothacher et al. (1995) suggested to use surface spherical harmonics.

Thus, in order to obtain the azimuth and elevation dependent PCV pattern, a spherical harmonic expansion of degree 8 and order 5 is typically necessary (Wübbena et al., 2006b; Bilich and Mader, 2010), whereas an expansion of degree 8 and order 0 can be used for an elevation-only dependent PCV pattern.

3.2.3 Antenna exchange format (ANTEX)

The IGS has played a key role in defining standards for PCC representation, elaborating the Antenna Exchange Format (ANTEX; Rothacher and Schmid, 2010) and favouring development of antenna PCC for most types of geodetic antennas. The ANTEX format, as follows from its name, has been designed to facilitate the exchange and application of antenna calibration information between different institutions. It clarifies conventions that are specific to GNSS antenna PCC and formulates not only receiver, but also satellite antenna PCC definitions. Thus, for receiver antennas the minimum of required information has to be provided, which includes antenna make, model and its serial number (including radome), calibration type, PCO and PCV blocks for different GNSS frequencies. The most recent format version is ANTEX v. 1.4.

3.3 Individual antenna PCC

Due to small deviations in the manufacturing process, each antenna is unique with respect to its electromagnetic properties, and, consequently, PCC for two antennas are not identical. If a particular antenna is calibrated for PCC, then the notation *individual PCC* is used. This terminology is adopted throughout this thesis, unless stated otherwise.

Antenna calibrations can be split mainly in two categories: relative and absolute. Relative calibrations for antennas are defined with respect to a reference antenna (Mader, 1999). These calibrations were used by the IGS until November 2006 with the reference antenna being the `AOAD/M_T NONE`. Then the IGS switched to a new set of absolute calibration models (Gendt, 2005). Relative calibrations are now obsolete and were not used in this study. Therefore, all further mentioning of antenna calibrations in this thesis will imply absolute PCC.

Absolute calibration defines PCC in an absolute sense, or independent of a reference antenna. Absolute PCC were adopted by the IGS starting from GPS week 1400 (6 November 2006)(Gendt, 2005), bringing GNSS solutions to a new qualitative level and resulting in launching the first IGS reprocessing campaign (Ray, 2009) in an attempt to achieve consistency between the historic and current IGS products.

As GNSS antennas are typically installed with radomes attached that are designed to protect them from the environment (e.g., accumulation of snow, dust, leaves, bird nesting), PCC for antennas must account for radomes used in junction. Although antenna radomes are usually built of dielectric material transparent for electromagnetic waves, their installation is known to deviate antenna PCC and may result in jumps in the time series (Elósegui et al., 1995; Johansson et al., 2002; Williams, 2003). To avoid this, antennas are calibrated with the radomes attached that will be used during future station operation.

3.3.1 Calibration facilities and methods

Several calibration methods have been developed in order to provide accurate antenna/radome PCC. These can be divided into two categories: those that use real GNSS signals (field calibration) and those that use artificial (chamber calibration) with both categories having their own strengths and weaknesses.

Field calibration with a robot

Wübbena et al. (1996) developed a method of absolute antenna calibration and later established a company, Geo++® GmbH (Germany), which specializes on GNSS antenna calibrations. To improve automation of the calibration process the technique was later enhanced by a robot (Wübbena et al., 2006b). The calibration installation consists of a robotic arm with an antenna to be calibrated mounted on it, Figure 3.2a. The robot is able to quickly orientate the antenna by rotation and tilting, achieving between 6000 and 8000 different orientations during the calibration session. The session usually lasts for several hours during which a uniform antenna coverage is achieved. Ionospheric and tropospheric delays are eliminated thanks to a reference antenna installed in the vicinity. Furthermore, multipath is removed or greatly eliminated due to its high correlation between multiple orientations within a short time interval. The developers of the method claim that its repeatability is less than 0.5 mm for L_1 and less than 1 mm for L_2 GPS frequencies.

As the method employs real GNSS signals, PCC for only currently deployed GNSSs can be

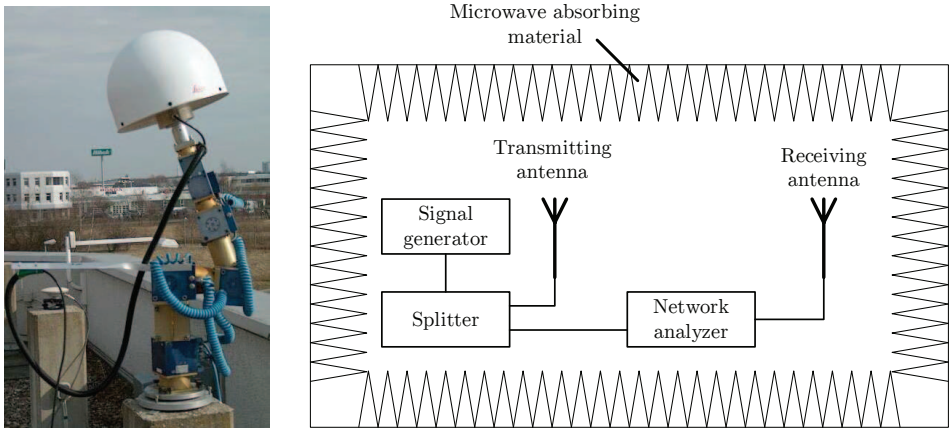

(a) Field calibration with a robot (Wübbena et al., 2006b)

(b) Chamber calibration

Figure 3.2: Antenna/radome calibration methods.

computed. At the same time, the use of real signals with modulated data allows it to be insensitive to group delay variations (Rolf Dach, personal communication, 2014) if they have an impact on PCC estimation.

The technique adopted at the National Geodetic Survey (NGS), USA (Bilich and Mader, 2010), is very similar to that of Geo++. It also uses a fast moving robot to orientate an antenna and, thus, achieve its full coverage. Additionally, a reference antenna at ∼5 m distance is used to account for tropospheric and ionospheric delays.

The main limitation of this method consists in the use of the robotic arm, in particular, in the weight and dimensions of the antenna/radome combination that it can handle. Although the method was used to reduce the impact of near-field effects by calibrating antennas with the top of the monument (Wübbena et al., 2006a), the robotic arm has limited capability in handling large and heavy installations.

Anechoic chamber calibration

A method for absolute antenna calibration in an anechoic chamber (see, e.g., Görres et al., 2006) has been adopted by the University of Bonn. Its principle consists in placing two antennas: one that radiates a test signal and another that receives it (an antenna under test) in an anechoic chamber, where the walls of the chamber are designed to absorb high-frequency electromagnetic signals to avoid their reflection and generation of multipath, Figure 3.2b. The transmitter antenna is kept fixed and its phase centre is known, whereas the antenna under test can be rotated and tilted. The test signal from a signal generator via a splitter comes to the transmitter antenna and to a network analyser. The latter is also connected to the receiver antenna and through comparing the phase shifts between the transmitted and received signals for various antenna orientations, antenna PCC can be obtained.

The strength of this method is in its potential to estimate antenna PCC for any frequency of current or future GNSS. Therefore, the method is not limited to only those that are operational and have sufficient number of satellites in view, which is a requirement for field calibrations with a robot. For example, by the end of the first decade of the GLONASS operation (2000-2001), the constellation had only 6 operational satellites. This resulted in impossibility of performing antenna/radome calibrations using the field method. In this sense the chamber method provides full flexibility with respect to the choice of frequencies that can be used for calibration.

A limitation that a chamber method has is related to a test signal, which represents a simple sine wave without any modulation and distortion by the atmosphere. This may potentially result in biased estimates of PCC compared to the field calibration, however this area is not well studied. Nevertheless, as suggested by Görres et al. (2006) and Zeimetz and Kuhlmann (2008), the chamber calibrations provide results that agree to less than 1 mm for elevations above 10° with those

obtained by field calibrations. Recently Baire et al. (2014) investigated several antennas calibrated using both methods and found that deviations between the PCC for the same antennas were below 2 mm. However, the authors reported large biases in computed positions, in particular, in the vertical direction using differently obtained PCC.

3.3.2 PCC differences between antennas

As mentioned previously, each antenna is unique with respect to its electromagnetic properties, therefore, PCC that are estimated for two different antennas may vary. Although the design and built quality of modern geodetic antennas is high, their PCC may exhibit significant variations even for antennas of the same manufacturer and model. These variations can be partly attributed to the limited accuracies of the calibration methods, as these are accurate to 1 mm for the GPS frequencies. However, the differences in PCC between individual antennas may reach much larger values than the aforementioned threshold, suggesting that there could be a positive effect in calibrating each individual antenna.

In order to give an idea to what extent PCC for different antennas may vary, four geodetic antennas were compared for the L_1 and L_2 GPS frequencies. The chosen antennas are all `LEICA AR25.R3 LEIT`, which are a commonly used within the IGS community. These antennas are installed in Luxembourg at stations BASC, ECHT, ERPE and TROI, which are part of the regional network SPSLux. The antennas together with their radomes were calibrated using the robot calibration method by Geo++. PCC differences BASC-ECHT, BASC-ERPE and BASC-TROI are shown in Figure 3.3.

According to Wübbena et al. (2006b), PCC that are obtained using the field calibration method are accurate to ∼0.5 mm and ∼1 mm for the GPS L_1 and L_2 frequencies, respectively. However, as seen from Figure 3.3, the differences BASC-ECHT and BASC-ERPE for L_1 reach up to 4 mm, whereas differences BASC-TROI for L_2 reach 2.8 mm. Therefore, the observed deviations in PCC between different antennas of the same type are not only due to the calibration method accuracy, but also due to real deviations in PCC between different antennas. Although the demonstrated discrepancies are based on the analysis of only six `LEICA AR25.R3 LEIT` antennas of the SPSLux network, similar discrepancies may be observed for other geodetic antennas (see Appendix B).

Taking into account that antenna PCC modelling errors may be amplified in LCs of observables, the shown differences may lead to significant bias in the estimated parameters. In turn, this highlights the importance of performing calibration of each antenna before its usage.

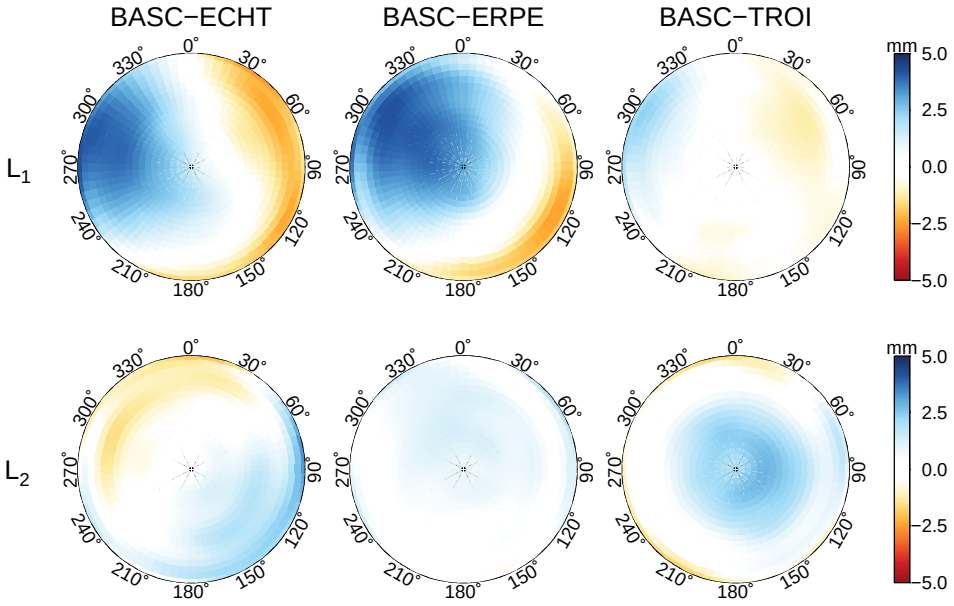

Figure 3.3: Skyplots of PCC differences between the LEIAR25.R3/LEIT antenna/radome combination installed at BASC and at ECHT, ERPE and TROI for the L_1 and L_2 GPS frequencies, respectively. Perimeter represents 0° elevation, while at the zenith (centre) an elevation of 90° is reached.

3.4 The IGS type-mean antenna PCC

Although the importance of antenna calibration is obvious, due to several reasons not all antenna/radome combinations installed at GNSS stations have individual PCC. Firstly, antenna/radome calibration is associated with additional delays and expenses due to logistics and the calibration procedure itself. Additionally, some stations have been operational for many years and their antenna/radome combinations were installed when calibration procedures were not developed and the application of individual PCC was not convincing. On the other hand, PCC of antenna/radome combinations within the same model type are believed to be fairly consistent and a set of type-mean PCC for a variety of antenna/radome combinations was developed and is constantly refined by the IGS.

3.4.1 Status of the IGS08 type-mean PCC

With each realization of the GPS-specific reference frame within the IGS, i.e., IGS00, IGS05, IGS08, etc., the IGS also releases an update to the antenna PCC set that is used for production of the respective frame. Such updates usually contain major changes both in receiver and satellite antenna PCC. The last major update of the IGS type-mean PCC (igs08.atx) took place on 17

April 2011 (GPS week 1632) together with the switch to the IGS08 reference frame in the IGS routine processing (Rebischung, 2011). Although soon after the announcement of the IGS08 reference frame its modification IGb08 was released, the type-mean PCC contained in igs08.atx are consistent with the updated frame and, therefore, can be used for processing.

In addition to major updates that occur together with switches of the reference frame, the IGS releases minor updates to the type-mean PCC. While the major updates usually concern all PCC and are associated with, e.g., switching from relative to absolute PCC, the minor updates are mainly due to modifications of PCC of particular antenna/radome combinations or the addition of a new satellite. The IGS type-mean PCC contained in igs08_1793.atx (Schmid, 2014) were used throughout this study. This PCC set corresponds to the modification announced in May 2014 (GPS week 1793).

Type-mean PCC represent averaged models for various antenna/radome combinations obtained from individual PCC produced by the field or chamber calibration methods, which have been introduced in Section 3.3.1. For different antenna/radome combinations the number of individual PCC used to produce a type-mean model may vary significantly. Thus, the type-mean PCC for GPS for the antenna/radome combination `AOAD/M_T NONE` are based on calibrations of only 2 antennas of this kind, whereas the type-mean PCC for the antenna/radome combinations `LEIAR25.R3 LEIT` and `TRM59800.00 NONE` are based on 5 and 25 antennas, respectively. Therefore, it is reasonable to assume that the associated quality of PCC for different antenna/radome combinations may vary significantly.

Unfortunately, type-mean PCC do not exist for all antenna/radome combinations, as some of them have never been calibrated using the field or chamber calibration methods. At the same time, thanks to the two absolute calibrations of the antenna/radome combination `AOAD/M_T NONE`, relative PCC previously provided by the NGS for a number of antenna/radome combinations were converted to absolute calibrations. This has allowed to fill a gap caused by the missing absolute PCC for some antennas, resulting in a number of them being known as "converted from relative NGS".

Additionally, due to similarities in construction between particular antennas, suggesting closeness between their electromagnetic properties, type-mean PCC for some antenna/radome combinations are copied from their respective counterparts.

Statistical data on the availability of type-mean PCC for 454 stations within the IGS network as of 14 December 2014 are given in Table 3.1. Although for the majority of stations (362) field/robot-based PCC (or copied from them) are available, PCC for 35 stations are those converted from relative NGS PCC. At the same time, for the antenna/radome combinations employed at 57 stations no respective matches for type-mean PCC were found.

It should be noted that the PCC converted from relative NGS models contain only elevation

Table 3.1: Statistical data on type-mean PCC available for the IGS stations as of 14 December 2014.

Calibration method	N of stations	Percentage
Field/robot	346	76.2%
Converted from relative NGS	35	7.7%
Copied from field/robot	16	3.5%
No calibration	57	12.6%
Total	454	100.0%

Information about antenna/radome calibrations for stations is taken from the IGS website (`http://www.igs.org/network` accessed on 14 December 2014).

dependent information, not considering azimuth dependency. At the same time, as shown in Figure 3.3, the PCC may exhibit large variations for the same elevation angles.

As for those stations that have no matches for their respective antenna/radome combinations it is likely that they employ uncalibrated radomes, which may introduce additional biases in the PCC, potentially resulting in degradation of solutions (Romero et al., 2013; Dach and Jean, 2014).

3.4.2 Type-mean and individual antenna PCC differences

As was shown in Section 3.3.2, individual PCC for antenna/radome combinations within the same model type may exhibit fairly large deviations, which are above the accuracies of calibration methods, pointing at deviations in the physical properties of the antennas (and radomes). As a consequence, type-mean PCC which represent averaged corrections for antennas are able to describe properties of each antenna within its model range only with limited accuracy. This depends on many parameters, including the number of antennas used to develop type-mean models, calibration methods and physical properties of each individual antenna. Therefore, it is not always possible to say blindly how well a type-mean PCC fits a particular antenna. However, one can assume that those type-mean PCC, which are based on the field/robot or chamber calibrations, have the best accuracy, which is still limited due to averaging.

Some examples of differences between the type-mean and individual PCC are demonstrated in Figure 3.4. The shown antenna/radome combinations `LEAR25.R3 LEIT` and `LEIAT504 LEIS` have type-mean PCC based on the field/robot calibration method. Nevertheless, differences for these antennas reach more than 3 mm and 2 mm in L_1 and L_2, respectively. The IGS type-mean PCC for the antenna/radome combination `LEIAT504GG SCIT` are based on the relative NGS model that has only elevation dependent PCC. As a consequence, the lack of azimuth modelling results in larger deviations compared to the respective individual model. The differences between the IGS type-mean and individual PCC for the full list of the examined antenna/radome combinations are

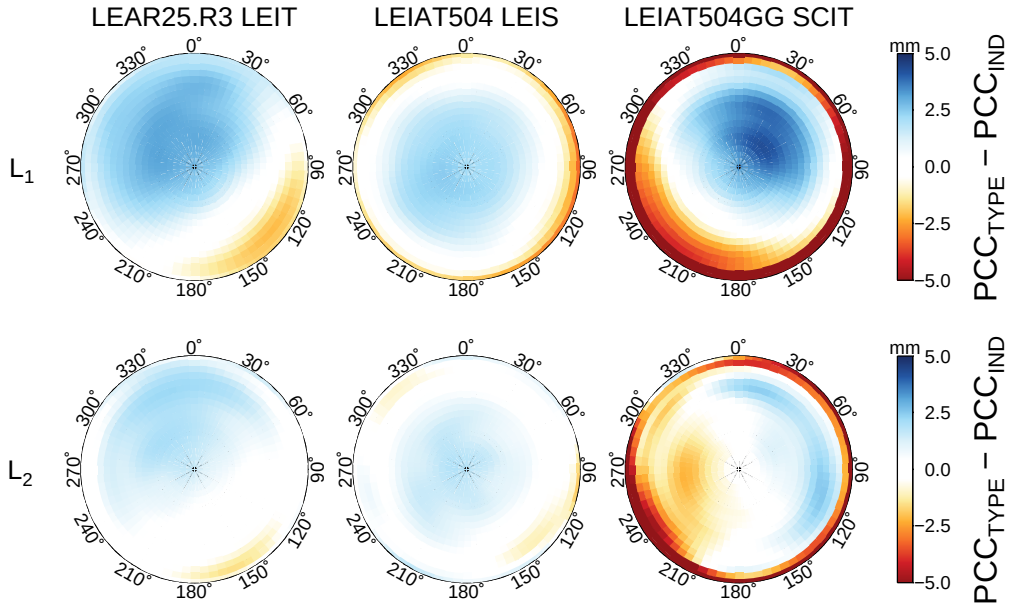

Figure 3.4: Skyplots of PCC differences between type-mean and individual PCC.

provided in Appendix B.

The PCC differences shown in Figure 3.4 are large and may have a significant impact on station positions. However, the behaviour of those antenna/radome combinations that have no IGS type-mean PCC and which comprise 12.6% of the total number of IGS stations, as shown in Table 3.1, is even more unpredictable. Considering that errors in PCC models may be amplified in LCs of observables in processing GNSS data, their impact on parameter estimation may be, to a large degree, underestimated.

Table 3.2 summarizes type-mean and individual PCC differences for 22 antenna/radome combinations used within the IGS. For the majority of antenna/radome combinations these differences on average stay below ±1 mm for both *L1* and *L2*. However, some PCC significantly exceed this threshold, in particular, `JAV_RINGANT_G3T NONE`, `LEIAR10 NONE`, `LEIAR25.R3 NONE`, `LEIAT504 LEIS` and `TRM55971.00 TZGD` showing mean differences up to 5.53 mm and 3.54 mm for L_1 and L_2, respectively. Also noteworthy are such antenna/radome combinations as `JAV_RINGANT_G3T NONE` and `TRM55971.00 TZGD`, which show high standard deviation of the differences. The PCC differences for these antenna/radome combinations reach up to 9.49 mm.

The actual individual PCC for all examined stations as well as the aforementioned differences can be also found on the supplied CD-ROM.

Table 3.2: Statistical data on the differences between the IGS type-mean and individual antenna/radome PCC.

Antenna/radome combination		N of samples	PCC difference for *L1* [mm] Mean	Min	Max	PCC difference for *L2* [mm] Mean	Min	Max
AOAD/M_T	NONE	2	-0.34 ± 1.02	-4.89	1.99	-0.20 ± 1.35	-6.11	4.12
JAV_RINGANT_G3T	NONE	1	5.53 ± 2.42	-0.87	8.20	3.48 ± 1.70	-1.59	6.14
LEIAR10	NONE	1	1.08 ± 0.78	-1.95	2.57	3.54 ± 1.27	-3.02	4.67
LEIAR25	LEIT	13	0.76 ± 0.69	-1.97	2.66	-0.68 ± 0.96	-3.69	3.57
LEIAR25.R3	LEIT	14	-0.31 ± 1.21	-3.14	3.41	-0.63 ± 0.84	-3.30	2.36
LEIAR25.R3	NONE	1	-2.10 ± 0.62	-2.69	0.26	-0.51 ± 0.29	-1.04	0.30
LEIAR25.R4	LEIT	3	0.63 ± 0.54	-1.44	1.71	-0.24 ± 0.46	-1.39	1.26
LEIAT504GG	LEIS	7	-0.10 ± 0.87	-2.12	2.09	0.04 ± 0.91	-1.56	2.20
LEIAT504	LEIS	1	-1.69 ± 0.76	-2.48	2.12	-1.08 ± 0.58	-1.88	1.04
LEIAT504	NONE	6	-0.44 ± 0.90	-2.45	1.60	-0.12 ± 0.75	-1.30	1.79
NOV750.R4	NONE	2	0.33 ± 0.34	-0.83	1.60	0.05 ± 0.81	-1.21	1.73
TPSCR3_GGD	CONE	7	-0.76 ± 0.65	-1.98	1.19	-0.76 ± 0.70	-2.09	1.55
TPSCR.G3	TPSH	1	-0.50 ± 0.35	-0.96	0.87	0.06 ± 0.31	-1.56	2.94
TRM29659.00	NONE	2	0.93 ± 0.71	-1.11	2.01	0.00 ± 0.45	-2.53	1.77
TRM29659.00	SNOW	2	-0.28 ± 0.44	-1.09	0.67	0.41 ± 0.42	-1.33	1.18
TRM33429.20+GP	NONE	1	0.56 ± 0.31	-0.47	1.07	-0.06 ± 0.22	-0.71	0.68
TRM41249.00	NONE	1	-0.45 ± 0.24	-0.92	0.56	-0.11 ± 0.31	-1.49	0.84
TRM41249.00	TZGD	1	0.97 ± 0.44	-0.51	1.53	0.39 ± 0.41	-1.44	1.12
TRM55971.00	NONE	2	0.44 ± 0.39	-0.83	1.30	-0.11 ± 0.32	-0.79	0.84
TRM55971.00	TZGD	3	2.28 ± 1.63	-0.73	5.66	2.91 ± 3.29	-1.50	9.49
TRM57971.00	TZGD	1	-0.17 ± 0.26	-0.73	0.92	-0.29 ± 0.31	-0.95	1.08
TRM59800.00	NONE	1	0.35 ± 0.20	-0.49	0.68	-0.08 ± 0.18	-1.07	0.57

Only PCC differences for elevations $> 10^\circ$ are considered.

3.5 Multipath and site-specific effects

While antenna calibration procedures discussed in Section 3.3.1 are aimed to provide corrections for antenna- and radome-specific errors, those that may originate on-site are not accounted for. These errors are produced due to the presence of signal obstructions, objects that may reflect satellite signals and electromagnetic interactions between the antenna and objects in the near-field (e.g., monument). Satellite signals may also be reflected from the ground, as has been shown by Bilich and Larson (2007) and Bilich et al. (2008).

Generally, multipath means that a signal reaches an antenna through multiple ways: directly (line-of-sight) and indirectly (reflected from other objects), Figure 3.5. The signal that is received by the antenna represents, therefore, a direct signal superimposed by its reflections.

With respect to the distance to an antenna, the surrounding space can be split into near-field

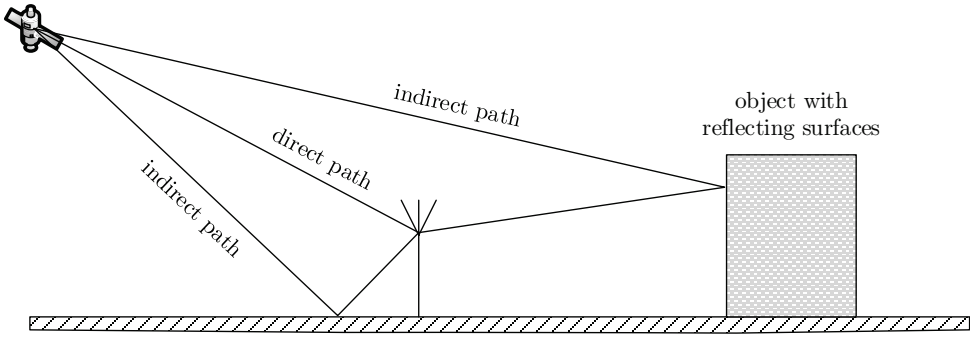

Figure 3.5: Multipath effect.

(reactive and radiating) and far-field (Balanis, 2005). King and Watson (2010) define these regions for GPS frequencies and a standard choke ring antenna to below ∼0.03 m, between ∼0.03 m and ∼1.5 m, and above ∼1.5 m from the antenna for reactive and radiating near-field, and far-field, respectively.

The impact of the reactive near-field on positioning was studied by Dilßner et al. (2008). Objects in this region may induce electric currents inside the antenna and, therefore, have a direct impact on its PCC pattern. The radiating near-field can be modelled as demonstrated by King and Watson (2010) and results in introduction of biases in solutions due to phase shifts of incoming signals. The effect of the far-field environment of an antenna is difficult to predict, however, as it has a systematic effect, it can be estimated and reduced.

Due to the complexity of the real-world environment, applying an accurate model to correct for it is not yet possible. A simplified model accounting for only horizontal reflectors below an antenna was adopted by (Elósegui et al., 1995) and was modified by (King and Watson, 2010) to account for antenna gain reads:

$$\delta\phi_L = \frac{\lambda}{2\pi}\left(\tan^{-1} \frac{\alpha \sin[4\pi \frac{H}{\lambda} \sin\varepsilon]}{g_d + \alpha \cos[4\pi \frac{H}{\lambda} \sin\varepsilon]} \right) \tag{3.2}$$

where

$\delta\phi_L$	...	phase bias due to multipath,
λ	...	carrier phase wavelength of the incoming signal (e.g., L_1 or L_2),
α	...	attenuation of the signal voltage amplitude,
H	...	vertical distance between the reflecting surface and antenna phase centre,
ε	...	elevation angle of the incoming signal,
g_d	...	antenna gain.

The problem of mitigating multipath, and therefore, better modelling of the actual phase centre

of an antenna has been addressed in many studies (see Section 1.1). Although the majority of proposed solutions could be applied to individual sites, no common solution has yet been developed for a large-scale (global) geodetic network.

3.6 Empirical Site Models

As was shown in Section 3.4.2, individual antenna PCC may significantly vary from the type-mean models. Moreover, once an antenna is installed, the actual phase centre may be biased with respect to the initial PCC due to electromagnetic coupling between the antenna and the monument (e.g., Dilßner et al., 2008; King et al., 2012). The influence of other objects in the vicinity of the antenna, possibly reflecting the incoming signals, may produce multipath, which may further degrade solutions (e.g., Hatanaka et al., 2001a,b). To ease studying of geophysical processes, noise and other signals, which have no geophysical origins, e.g., draconitic, should be reduced. At the station level this generally implies either elimination, or modelling the error sources. While elimination of the error sources is often impossible or not applicable (e.g., for historical data), modelling is more feasible, especially if one considers that the aforementioned effects are often systematic or invariant over time. Therefore, site-specific correction models can be developed based on already accumulated data.

This section introduces a method to model deficiencies in the applied antenna PCC, as well as surrounding site environment. It takes advantage of accumulated data, in particular, of postprocessed phase residuals to reconstruct the vicinity of the antenna. The obtained phase residual maps are later re-applied for processing. Such residual-based phase maps in literature are referred as empirical site models (ESM; Moore et al., 2014). The method is attractive, because it depends only on historical station data and, therefore, may be applicable to any site after the minimum amount of observation data has been accumulated and post-fit phase residuals to solutions have been generated. The last aggregate information on both deficiencies in antenna PCC models and antenna environment, being very inviting for further processing, reshaping and reusing.

3.6.1 Realization of ESM

The least-squares parameter estimation is the most common technique in GNSS. It is employed to find the best estimate for a solution in presence of errors (or noise) in the observations. The persisting presence of these is always the case in GNSS processing due to a large number of error sources that affect satellite observations, which are difficult to describe analytically. In presence of these unaccounted effects the method of least-squares provides a good estimate of a solution by reaching a compromise among the input parameters (observables).

Following Hofmann-Wellenhof et al. (2008), and given satellite and receiver coordinates denoted as $X^s(t), Y^s(t), Z^s(t)$ and X_r, Y_r, Z_r, respectively, the distance ϱ_r^s between the satellite and receiver can be written as

$$\varrho_r^s = \sqrt{(X^s(t) - X_r)^2 + (Y^s(t) - Y_r)^2 + (Z^s(t) - Z_r)^2} \tag{3.3}$$

and can be generally formulated as

$$\varrho_r^s = f(X_r, Y_r, Z_r), \tag{3.4}$$

which after linearization can be written in a simplified form

$$\boldsymbol{\ell} = \mathbf{A}\mathbf{x}, \tag{3.5}$$

where

$\boldsymbol{\ell}$	$[n \times 1]$	...	vector of observables,
$\mathbf{A}$	$[n \times u]$	...	design matrix,
$\mathbf{x}$	$[u \times l]$	...	vector of unknowns (parameter vector).

In presence of noise the equation (3.5) reads

$$\boldsymbol{\ell} = \mathbf{A}\mathbf{x} + \mathbf{v}, \tag{3.6}$$

where $\mathbf{v}$ is a vector of residuals, i.e., information on unmodelled biases. In case of GNSS parameter estimation, it can be interpreted as far- and near-field effects, as well as other unmodelled errors affecting the signal along its path. Based on this residual information a correction to the incoming signals can be derived and applied.

3.6.2 Limitations of ESM

Moore et al. (2014) have shown that the choice of estimated parameters during GNSS processing affected the performance of the ESM method. They concluded that the estimation of clock biases and ZTDs degraded the efficiency of ESM. Additionally, they recommended to use higher elevation cutoff angles for the ESM estimation, as for low values the RMS of recovered multipath was larger, especially for low monument heights. Also, they have demonstrated that observation elevation dependent weighting could also affect performance of the ESM. In particular, uniform weighting resulted in degradation of their simulation results compared to the case when elevation dependent weighting was employed.

At the same time, according to the results presented by Moore et al. (2014), observation weighting was the main factor contributing to the ESM performance degradation. Clock estimation was the second in the list of the contributors, while ZTD estimation and elevation cutoff had a

small impact. It needs to be mentioned that clock estimation resulted in elevated RMS of recovered multipath for all monument heights. At the same time, when clock estimation was performed, particularly increased RMS of recovered multipath was observed for $\sim$ 0.4 m, $\sim$ 0.75 m and $\sim$ 1.1 m monument heights. Similar monument height dependency was demonstrated for the ZTD estimation impact. In general, however, the ESM method showed poor performance for low monument heights ($\leq$ 0.25 m) irrespectively of the processing options, i.e., parameters that were estimated.

3.7 Summary

As the phase centre of a GNSS antenna depends on the frequency and direction of incoming signals, its accurate modelling is required for precise GNSS applications. Therefore, several calibration methods for antenna/radome combinations have been developed in order to produce PCC. These methods include robotic field and chamber calibrations. Employing essentially different techniques, these methods show high repeatability between each other for high elevation angles ($> 10°$), which reaches $\sim$1 mm and $\sim$0.5 mm for the GPS L_1 and L_2 frequencies, respectively. At the same time, individual PCC for IGS-standard choke ring antennas within the same model type show deviations for high elevation angles of incoming signals, which may reach up to $\sim$4 mm and $\sim$2.8 mm for the GPS L_1 and L_2 frequencies, respectively. This suggests that these differences can be associated not only with the accuracies of the calibration techniques, but can also be attributed to differences in the physical properties of antennas.

In its routine processing the IGS uses type-mean PCC, which are averaged models mostly composed of individual PCC of calibrated antenna/radome combinations. Differences between individual antennas, however, suggest that the type-mean PCC may potentially exhibit large deviations between the modelled phase patterns and their respective real values. Considering that more than 10% of the IGS stations employ only elevation-dependent PCC, which are converted from relative NGS calibrations, and additional $\sim$12.8% may potentially employ antennas with uncalibrated radomes, the impact on station positions due to errors in PCC modelling may be significant.

Furthermore, once antennas are installed, deviations from the modelled PCC may be further increased due to interactions between the antenna and objects in its vicinity. This can be described as multipath impact which is difficult to model and correct due to complexity of the real world environment. In turn, underestimated errors in PCC modelling may introduce biases and harmonic signals in GNSS-derived parameter time series. They may potentially contribute to spurious signals at draconitic frequencies that are observed in the IGS products.

Finally, a method to correct for site-specific effects based on post-fit phase residuals, namely,

the empirical site model (ESM) was introduced and its limitations were outlined. Unlike other methods, ESM offers a flexibility that would allow to apply it on a global scale without having a priori information about near- and far-field environments on sites.

Chapter 4

Observation Networks

This chapter provides an overview of geodetic networks with individually calibrated antenna/radome combinations that were used for this study. In particular, the Reference Frame Sub Commission for Europe (EUREF) Permanent Network, the United Kingdom GNSS network and the Satellite Positioning Service of Luxembourg (SPSLux) network are introduced. Information on antenna/radome combinations that were employed by stations in these networks is provided. Additionally, other stations that are not part of the aforementioned networks, but also have freely available calibrations for their antenna/radome combinations are introduced.

Finally, the chapter introduces a network that is used by the IGS for its routine processing and definition of the TRF – the IGb08 core network. Although it does not include any stations with individually calibrated antennas/radome combinations, it is used to perform orbit determination and produce other global solutions in this study.

4.1 Introduction

The necessity of the use of individual calibrations faces a lot of discussion due to a number of reasons. Firstly, deviations of individual PCC from the corresponding type-mean models are small and in most cases the latter are believed to demonstrate fairly good performance. Additionally, the presence of site effects (multipath), which may potentially cause larger impact on computed solutions than the deviations of individual PCC from the type-mean ones has discouraged the geodetic community to invest additional time and efforts to perform more individual calibrations of antenna/radome combinations. Moreover, on-site calibration is not yet possible, whereas the existing calibration methods require mounting the antennas on a robot or placing them into an anechoic chamber. This leads to an obligation to perform antenna calibration before it is permanently installed. The above results in a very small number of individually calibrated antenna/radome combinations and difficulty in finding stations with individual PCC that are freely available.

4.2 GNSS networks with individual PCC available

The total number of stations with individual PCC that were used in this study is 55, of which 52 stations are located in Europe, two stations are in North America and one on South Georgia Island in the South Atlantic Ocean (Figure 4.1). The differences between the IGS type-mean and individual antenna/radome PCC for all antenna/radome combinations are provided in Appendix B, whereas the actual individual PCC can be found on the supplied CD-ROM. More information on the employed stations is given in the following sections.

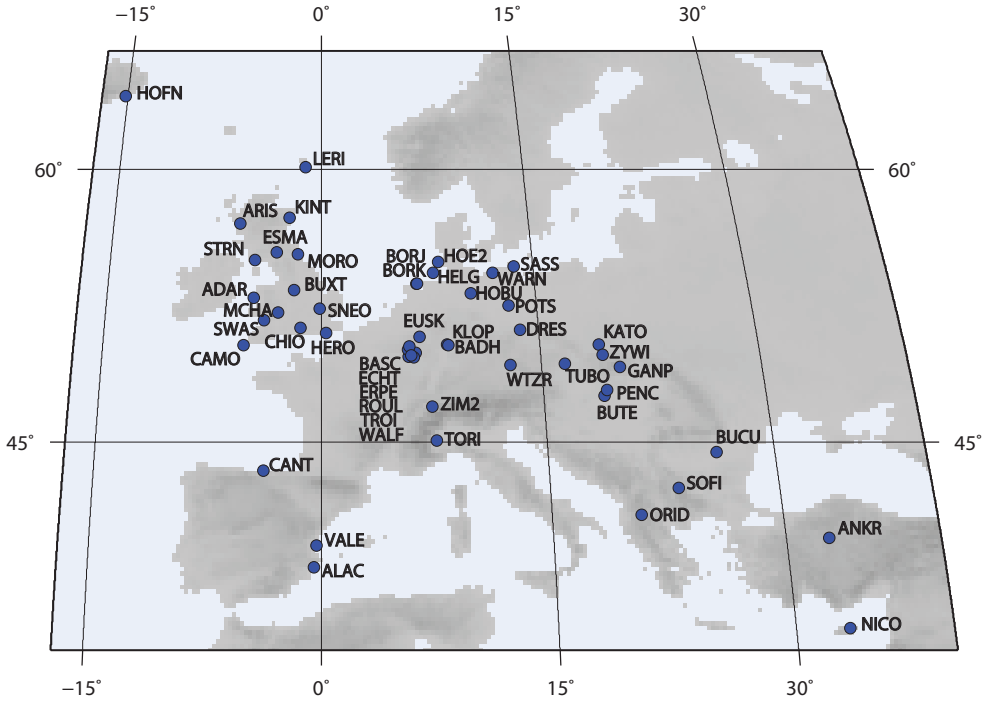

Figure 4.1: Stations with individually calibrated antenna/radome combinations that were used in this study. Two stations in North America and one station on South Georgia Island (South Atlantic Ocean) are not shown.

4.2.1 The EUREF Permanent Network

The IAG Regional Reference Frame Sub-commission for Europe, (EUREF; Bruyninx et al., 2012) is responsible for defining and maintaining the European Terrestrial Reference System (ETRS89). In order to provide access to the reference frame, EUREF uses a network of stations, namely, the EUREF Permanent Network (EPN), which currently consists of 264[1] permanently operating GNSS tracking stations located in different European countries. Based on EPN data, the EU-

[1] as of 31 Jan 2015, `http://www.epncb.oma.be/_networkdata/stationlist.php`

REF community estimates station coordinates and velocities, provides satellite orbit and clock correction streams and produces network solutions, which are available to users.

Stations within the EPN belong to different institutions from various countries, therefore their installations and instrumentation compositions, although sometimes very similar within national networks, overall are very different from each other. As some stations within the EPN have individually calibrated antenna/radome combinations, EUREF provides access to the individual PCC and recommends their usage (Bruyninx, 2006). Although the number of stations employing antenna/radome combinations with individual PCC constantly increases and currently has reached 73, during selection of stations to be included in this study preference was given to those having longer operation time without antenna changes. Finally, only 32 stations were selected, employing various types of antenna/radome combinations, Table 4.1. As some stations were switching antennas, the number of actual antenna/radome combinations that were examined within the EPN reached 47.

Table 4.1: EPN stations with individually calibrated antenna/radome combinations used in this study.

Station	DOMES	Lat/Lon		Start date	End date	Antenna/Radome		Cal. method
ALAC	13433M001	38.2°N	0.7°W	15/09/2010	31/12/2013	LEIAR25.R3	LEIT	ROBOT
ANKR	20805M002	39.9°N	32.8°E	06/05/2008	31/12/2013	TPSCR3_GGD	CONE	ROBOT
BADH	14288M001	50.1°N	8.4°E	28/02/2005	18/09/2012	TRM41249.00	NONE	ROBOT
BADH	14288M001	50.1°N	8.4°E	18/09/2012	31/12/2013	LEIAR10	NONE	CHAMBER
BORJ	14268M002	53.3°N	6.5°E	10/06/2005	01/09/2010	TPSCR3_GGD	CONE	ROBOT
BORJ	14268M002	53.3°N	6.5°E	02/09/2010	31/12/2013	LEIAR25.R3	LEIT	ROBOT
BORK	14268M001	53.3°N	6.5°E	01/07/2003	31/12/2013	TRM29659.00	SNOW	ROBOT
BUCU	11401M001	44.5°N	26.1°E	31/10/2008	31/12/2013	LEIAT504GG	LEIS	ROBOT
BUTE	11209M001	47.5°N	19.1°E	31/07/2007	31/12/2013	TRM55971.00	TZGD	ROBOT
CANT	13438M001	43.3°N	3.9°W	20/10/2011	31/12/2013	LEIAR25.R4	LEIT	ROBOT
DRES	14108M001	51.0°N	13.5°E	26/01/2003	23/05/2007	TRM29659.00	NONE	ROBOT
DRES	14108M001	51.0°N	13.5°E	24/05/2007	22/09/2010	TPSCR3_GGD	CONE	ROBOT
DRES	14108M001	51.0°N	13.5°E	23/09/2010	31/12/2013	LEIAR25.R3	LEIT	ROBOT
EUSK	14258M003	50.4°N	6.5°E	17/11/2009	31/12/2013	LEIAT504GG	LEIS	ROBOT
GANP	11515M001	49.0°N	20.2°E	25/08/2006	19/04/2012	TRM55971.00	NONE	ROBOT
HELG	14264M001	54.1°N	7.5°E	03/09/2008	31/12/2013	LEIAT504GG	LEIS	ROBOT
HOBU	14202M003	53.0°N	10.3°E	07/06/2002	21/06/2002	TRM33429.20+GP	NONE	ROBOT
HOBU	14202M003	53.0°N	10.3°E	21/06/2002	28/02/2007	TRM29659.00	SNOW	ROBOT
HOBU	14202M003	53.0°N	10.3°E	28/02/2007	22/11/2010	LEIAT504GG	LEIS	ROBOT

(continued on next page)

Table 4.1: EPN stations with individually calibrated antenna/radome combinations used in this study *(continued from previous page)*.

Station	DOMES	Lat/Lon		Start date	End date	Antenna/Radome		Cal. method
HOBU	14202M003	53.0°N	10.3°E	22/11/2010	31/12/2013	LEIAR25.R4	LEIT	ROBOT
HOE2	14284M002	54.5°N	8.2°E	01/07/2005	20/10/2010	TPSCR3_GGD	CONE	ROBOT
HOE2	14284M002	54.5°N	8.2°E	20/10/2010	31/12/2013	LEIAR25.R3	LEIT	ROBOT
HOFN	10204M002	64.3°N	15.2°W	23/09/2007	05/05/2013	TPSCR3_GGD	CONE	ROBOT
KATO	12219S001	50.5°N	18.6°E	08/04/2008	17/12/2010	TRM41249.00	TZGD	ROBOT
KATO	12219S001	50.5°N	18.6°E	17/12/2010	31/12/2013	TRM57971.00	TZGD	ROBOT
KLOP	14214M002	50.1°N	8.4°E	02/07/2002	27/06/2007	TRM29659.00	NONE	ROBOT
KLOP	14214M002	50.1°N	8.4°E	27/06/2007	31/12/2013	TRM55971.00	TZGD	ROBOT
METS	10503S011	60.2°N	24.4°E	19/08/2010	28/06/2013	AOAD/M_T	NONE	ROBOT
NICO	14302M001	35.1°N	33.4°E	10/06/2008	16/07/2013	LEIAT504GG	LEIS	ROBOT
ORID	15601M001	41.1°N	20.5°E	07/11/2008	31/12/2013	LEIAT504GG	LEIS	ROBOT
PENC	11206M006	47.5°N	19.2°E	13/07/2007	31/12/2013	LEIAT504GG	LEIS	ROBOT
POTS	14106M003	52.2°N	13.0°E	15/02/2011	31/12/2013	JAV_RINGANT_G3T	NONE	ROBOT
REYK	10202M001	64.1°N	21.9°W	14/03/2008	31/12/2013	TPSCR.G3	TPSH	ROBOT
SASS	14281M001	54.3°N	13.4°E	24/10/2003	31/12/2013	TPSCR3_GGD	CONE	ROBOT
SOFI	11101M002	42.6°N	23.4°E	29/04/2010	31/12/2013	LEIAR25.R3	LEIT	ROBOT
TORI	12724M002	45.0°N	7.4°E	08/03/2011	31/12/2013	LEIAR25.R3	NONE	ROBOT
TUBO	11503M001	49.1°N	16.4°E	15/12/2005	12/12/2011	LEIAT504	LEIS	ROBOT
TUBO	11503M001	49.1°N	16.4°E	12/12/2011	31/12/2013	LEIAR25.R4	LEIT	ROBOT
VALE	13439M001	39.3°N	0.6°W	17/09/2010	31/12/2013	LEIAR25.R3	LEIT	ROBOT
WARN	14277M002	54.1°N	12.1°E	23/10/2003	15/09/2010	TPSCR3_GGD	CONE	ROBOT
WARN	14277M002	54.1°N	12.1°E	16/09/2010	31/12/2013	LEIAR25.R3	LEIT	ROBOT
WTZR	14201M010	49.1°N	12.5°E	17/06/1999	19/01/2009	AOAD/M_T	NONE	ROBOT
WTZR	14201M010	49.1°N	12.5°E	19/01/2009	30/06/2010	LEIAR25	LEIT	ROBOT
WTZR	14201M010	49.1°N	12.5°E	30/06/2010	31/12/2013	LEIAR25.R3	LEIT	ROBOT
ZIM2	14001M008	46.5°N	7.3°E	09/11/2007	12/05/2009	TRM55971.00	NONE	ROBOT
ZIM2	14001M008	46.5°N	7.3°E	13/05/2009	31/12/2013	TRM59800.00	NONE	ROBOT
ZYWI	12220S001	49.4°N	19.1°E	27/11/2007	31/12/2013	TRM55971.00	TZGD	ROBOT

4.2.2 The United Kingdom GNSS network

The British Isles continuous GNSS Facility (BIGF[2]; Greaves et al., 2014), hosted at the Nottingham Geospatial Institute, which, in turn, is located at The University of Nottingham (UNOTT), was created to collect, archive, process and disseminate data from GNSS stations installed in the United Kingdom (UK) and the Republic of Ireland to scientific users. The total number of active stations that are processed by the BIGF reaches 158. These are operated by various institutions and belong to different networks, among which GeoNet, being the fundamental network for the TRF definition, is operated by the Ordnance Survey of Great Britain (OSGB). GeoNet includes 12 "zero order" stations that are installed on high-standard monuments connected to bedrock. All stations were installed in 2008-2009 and are equipped with antenna/radome combination `LEIAR25.R3 LEIT`. To ensure the highest quality, all antennas and radomes within GeoNet were calibrated using the field/robot method by Geo++.

Two other stations that contribute to the BIGF data archive and used within this study are operated by UNOTT. Unlike the GeoNet stations, these employ antenna/radome combination `LEIAT504GG SCIT`. These stations are also located in the UK and have individually calibrated antennas. The complete list of the GeoNet and UNOTT stations is provided in Table 4.2.

Table 4.2: GeoNet and UNOTT stations with individually calibrated antenna/radome combinations used in this study.

Station	DOMES	Lat/Lon		Start date	End date	Antenna/Radome		Cal. method
ADAR	19161M001	52.8°N	4.7°W	04/03/2009	31/12/2013	LEIAR25	LEIT	ROBOT
ARIS	19190M001	57.0°N	5.8°W	02/06/2009	31/12/2013	LEIAR25	LEIT	ROBOT
BUXT	19191M001	53.2°N	1.9°W	13/08/2009	31/12/2013	LEIAR25	LEIT	ROBOT
CAMO	19187M002	50.2°N	5.3°W	04/08/2009	31/12/2013	LEIAR25	LEIT	ROBOT
CHIO	19194M001	51.1°N	1.4°W	30/06/2009	31/12/2013	LEIAR25	LEIT	ROBOT
HERO	19168M001	50.9°N	0.3°E	20/03/2009	31/12/2013	LEIAR25	LEIT	ROBOT
KINT	19192M001	57.2°N	2.3°W	06/08/2009	31/12/2013	LEIAR25	LEIT	ROBOT
LERI	19159M003	60.1°N	1.2°W	16/06/2009	31/12/2013	LEIAR25	LEIT	ROBOT
MORO	13299M002	55.2°N	1.7°W	25/11/2008	31/12/2013	LEIAR25	LEIT	ROBOT
SNEO	19135M002	52.2°N	0.1°W	13/05/2009	31/12/2013	LEIAR25	LEIT	ROBOT
STRN	19176M001	54.9°N	4.7°W	11/03/2009	31/12/2013	LEIAR25	LEIT	ROBOT
SWAS	19193M001	51.6°N	4.0°W	14/08/2009	31/12/2013	LEIAR25	LEIT	ROBOT
ESMA	19102M001	55.3°N	3.2°W	24/06/2008	31/12/2013	LEIAT504GG	SCIT	ROBOT
MCHA	19101M001	52.0°N	3.0°W	25/06/2008	31/12/2013	LEIAT504GG	SCIT	ROBOT

[2]available through `http://www.bigf.ac.uk/`

4.2.3 The SPSLux network

The Administration of cadastre and topography (French name: "Administration du cadastre et de la topographie"; ACT) of Luxembourg operates and maintains a real-time kinematic (RTK) network entitled Satellite Positioning Service of Luxembourg (SPSLux). The network consists of 6 permanently operating stations installed in Luxembourg, all collecting GPS and GLONASS data. These are processed in real-time by ACT to generate corrections and deliver them to users. Thus, the service provides access to the national reference frame of Luxembourg (LUREF). More information on the ACT and SPSLux can be found on the institution website[3].

Data from the SPSLux stations are available from the second half of 2006 until present, however, all stations experienced equipment changes in September/October 2010. Thus, the previously installed antenna/radome combinations `LEIAT504 LEIS` were replaced by `LEIAR25.R3 LEIT`, Table 4.3. All antennas and radomes were calibrated by Geo++ prior to their installation.

Table 4.3: SPSLux stations with individually calibrated antenna/radome combinations used in this study.

Station	DOMES	Lat/Lon		Start date	End date	Antenna/Radome		Cal. method
BASC	n/a	49.6°N	5.9°E	01/08/2006	14/09/2010	LEIAT504	LEIS	ROBOT
BASC	n/a	49.6°N	5.9°E	15/09/2010	31/12/2013	LEIAR25.R3	LEIT	ROBOT
ECHT	n/a	49.8°N	6.4°E	01/08/2006	30/09/2010	LEIAT504	LEIS	ROBOT
ECHT	n/a	49.8°N	6.4°E	01/10/2010	31/12/2013	LEIAR25.R3	LEIT	ROBOT
ERPE	n/a	49.5°N	6.3°E	01/08/2006	21/09/2010	LEIAT504	LEIS	ROBOT
ERPE	n/a	49.5°N	6.3°E	22/09/2010	31/12/2013	LEIAR25.R3	LEIT	ROBOT
ROUL	n/a	50.0°N	5.9°E	01/08/2006	05/10/2010	LEIAT504	LEIS	ROBOT
ROUL	n/a	50.0°N	5.9°E	06/10/2010	31/12/2013	LEIAR25.R3	LEIT	ROBOT
TROI	n/a	50.1°N	6.0°E	01/08/2006	11/10/2010	LEIAT504	LEIS	ROBOT
TROI	n/a	50.1°N	6.0°E	12/10/2010	31/12/2013	LEIAR25.R3	LEIT	ROBOT
WALF	n/a	49.7°N	6.1°E	01/08/2006	17/10/2010	LEIAT504	LEIS	ROBOT
WALF	n/a	49.7°N	6.1°E	18/10/2010	31/12/2013	LEIAR25.R3	LEIT	ROBOT

4.2.4 Additional stations

In addition to the GNSS stations discussed in previous sections other stations that do not take part in any of the aforementioned networks were included in the processing (Table 4.4). Among these are two stations, namely ALG2 and FLIN, that are located in North America and operated by Natural Resources Canada (NRCan). Both stations employ antennas/radome combination `NOV750.R4 NONE`, which are by construction and properties similar to `LEIAR25.R4 NONE`. FLIN,

[3] Administration of cadastre and topography – `http://www.act.public.lu`

Table 4.4: Additional stations with individually calibrated antennas and radomes used in this study.

Station	DOMES	Lat/Lon	Start date	End date	Antenna/Radome		Cal. method
ALG2	40104M005	46.0°N 78.1°W	15/10/2010	23/08/2012	NOV750.R4	NONE	ROBOT
FLIN	40135M001	54.7°N 102.0°W	21/12/2010	31/12/2013	NOV750.R4	NONE	ROBOT
KEPA	42701M001	54.3°S 36.5°W	14/02/2013	31/12/2013	TRM59800.00	SCIS	ROBOT

being an IGS site, is still in operation, whereas ALG2 was damaged in August 2012 by lightning. Antennas at both stations were calibrated using the field/robot method by Geo++.

Another station, namely KEPA, that has also been included in the processing is located on South Georgia Island in the South Atlantic Ocean. It was set up in February 2013 together with the King Edward Point (KEP) Geodetic Observatory to support studying seismic, geomagnetic and oceanic processes in that region (Teferle et al., 2014).

4.3 The IGb08 core network

The International GNSS Service (IGS; Dow et al., 2009) unites worldwide activities to produce high quality GNSS-based products and solutions aimed to facilitate a variety of scientific applications. These include monitoring Earth rotation, deformations of the solid Earth, variations in mean sea level, etc. However, the primary mission of the IGS is its contribution to stability improvement and densification of the International Terrestrial Reference Frame (ITRF) maintained by the International Earth Rotation and Reference System Service (IERS). The IGS mission is fulfilled through voluntary contributions of over 200 agencies and institutions in more than 100 countries. These institutions ensure operation of globally distributed GNSS stations, which provide the IGS ACs with the observation data. Thus, the IGS network consists of more than 400 globally distributed stations.

Due to a number of reasons (land-ocean distribution, installation costs, maintenance capability, accessibility, provision of security, access to the data, etc.) the number of the IGS stations is denser in some regions compared to others. Thus, the IGS network is very irregular and has more stations in the Northern, than in the Southern Hemisphere. This results in reduced robustness of solutions for some regions and potentially biases modelling of geophysical processes (Collilieux et al., 2012).

In order to partly overcome the irregularity problem, a homogeneous global network of stations has been extracted from the complete network. This reduced network is known as the IGb08 core network (Rebischung et al., 2012; Rebischung, 2012). This network has become the basis for the IGb08 reference frame, which is the IGS realization of the ITRF. The list of the IGb08 core stations

is provided in Appendix C.

Global coverage implies uninterrupted tracking of satellites, therefore, using a global network is essential for orbit determination, which needs to be performed in the current study. Thus, the IGb08 core network became a good candidate as a base network, taking into account its uniformity and global coverage. Additionally, a relatively small number of stations (91) results in a fairly low computational burden, which becomes important if multiple years of GNSS data need to be processed and reprocessed. For a number of stations within the IGb08 core network supplementary (substitutional) stations are defined, which have to be used in case of missing data for stations from the main list. This ensures that the network geometry remains similar from session to session

Similar to the complete IGS network, the IGb08 core includes antenna/radome combinations from various manufacturers and types. This implies that although the majority of stations employ antenna/radome combinations with absolute type-mean PCC obtained by field/robot methods (70.3% calibrated and 4.4% copied from them), some stations employ antennas with PCC that are converted from relative NGS models (6.6%). At the same time, the number of stations that employ antennas without calibrations or with uncalibrated radomes reaches 18.7%, Table 4.5. If substitutional sites are taken into account, then these numbers change slightly to 68.8%, 5.2%, 8.3% for stations with absolute field/robot calibrations, copied from them, and converted from relative NGS calibrations, respectively. Furthermore, the number of stations employing uncalibrated antennas, radomes or their combinations remains the same as for the primary sites –17.7%.

Taking the above statistical data into account, the IGb08 core network creates a good basis for studying the impact of PCC and ESM on GNSS solutions. The methodology of this investigation will be discussed in details in Chapter 5.

Table 4.5: Statistical data on type-mean antenna/radome PCC available for the IGS core stations as of 14 December 2014.

	IGS core only		IGS core with subst.	
Calibration method	N of stations	Percentage	N of stations	Percentage
Field/robot	64	70.3%	132	68.8%
Converted from relative	6	6.6%	16	8.3%
Copied from field/robot	4	4.4%	10	5.2%
No calibration	17	18.7%	34	17.7%
Total	91	100.0%	192	100.0%

Information about antenna/radome calibrations for stations is taken from the IGS website (`http://www.igs.org/network` accessed on 14 December 2014).

4.4 Summary

In order to support investigations on the influence of antenna PCC on the GPS satellite orbits and station coordinates 55 stations employing individually calibrated antennas and radomes were selected. These are mainly located in Europe (52 stations) and belong to different networks, in particular, the EPN, GeoNet, SPSLux and NRCan. Additionally, two UNOTT and one station located on South Georgia Island containing a station installed and operated by the University of Luxembourg were included.

Since many stations within the selection experienced antenna/radome changes, the actual number of antenna/radome combinations that were investigated reached 76 with average time series length of 3-4 years. The included antennas were produced by several manufacturers, e.g., Leica, Trimble, Topcon, etc. and are typical examples of equipment used within national or international GNSS networks.

Additionally, the IGb08 core network that includes the reference frame sites was discussed providing details on composition of type-mean antenna PCC for its stations. Due to a relatively low number of stations and its global coverage, this network is used as a basis for orbit determination in this study. Additionally, it will be used to support performance evaluation of empirical site models, which will be discussed in Chapter 5.

Chapter 5

Methodology for the Assessment of PCC/ESM Models

This chapter introduces the NAvigation Package for Earth Observation Satellites (NAPEOS) used to process GNSS data in this study, and provides examples of processing sequences for satellite orbit determination as well as station position estimation. Additionally, the methodology of the results assessment based on the daily orbital discontinuities is outlined. Furthermore, the derivation of ESMs in connection to NAPEOS is discussed and the methodology of ESM application on a global scale is provided. Methods for PCC and ESM impact assessment, taking into account peculiarities related to correlation of parameters to be investigated, are developed. These include both regional and global scenarios. The topic of solution consistency is also addressed and the respective strategies for achieving it are proposed. Finally, a null test showing the generation of periodicities in GNSS solutions due to deficiencies in PCC is performed.

5.1 Introduction

The meaningfulness of making investigations with respect to the impact of different PCC on orbits and station coordinates often faces a lot of debates. It is particularly questionable in case of type-mean and individual PCC, considering the generally small deviations between the two PCC types. Therefore, the potential impact that deficiencies in PCC may have on solutions is small compared to that of other parameters. Additionally, in case of a large (global) network involving hundreds of stations, the PCC contribution may be indiscernible. On the other hand, correlation between satellite and receiver antenna PCC, ZTDs and station heights (Springer, 2000) highlights the importance of the topic, as the accuracy of employed PCC is an essential step towards improving consistency and robustness of the entire processing chain.

As was shown in Chapter 3, deviations between different PCC for antennas of the same type and model may reach values that are far above the current PCC accuracies. Additionally, due to a number of reasons, the GNSS networks generally have non-uniform spatial distribution. Therefore, it may happen that a station in a remote area (e.g., in the South Pacific, South Atlantic and Indian Oceans, as well as Arctic and Antarctic regions) that suffers from significant PCC modelling issues,

would result in a pronounced effect on the estimated orbits. For this reason it is important to develop techniques that would allow to perform an investigation with respect to the matter.

Draconitic signals are seen in nearly all IGS products (see Section 2.1), however, the contribution of errors in PCC to these signals is hard to estimate. At the same time, modifications to PCC potentially have an impact on all estimated parameters. In case of GNSS processing when satellite products are known from external providers (e.g., the IGS ACs) and fixed, whereas only station positions are estimated, the applied PCC will have a direct impact on station position and estimated ZTDs due to correlation of the last with the employed corrections.

In case of satellite orbit determination station positions are usually tightly constrained to the a priori values. Obviously, errors in PCC have an impact on satellite orbits, however, this effect may be less pronounced compared to station positions due to averaging. At the same time, any observed change in satellite orbits would also indicate changes in geocenter motion. In the last case, a more profound analysis is required.

Special care should be taken with respect to consistency of solutions and mutual influence of antennas on each other. Thus, to achieve consistency satellite clocks and orbits need to be estimated using PCC that will be further applied by users in position estimation. In particular, draconitic signals that contaminate satellite products may propagate into station solutions, hiding the effect from modifications in the PCC.

As for the inter-station influence, since modifications to antenna PCC may result in biases and variations of station positions, links between stations, i.e. baselines, should be eliminated or minimized. For this reason double-difference processing is not preferred, as in this case PCC deficiencies at each station will propagate between stations that are linked together. Hence, preference should be given to precise point positioning (PPP; Zumberge et al., 1997), as only by the use of PPP each station can be evaluated independently. However, this leads to a slight reduction in accuracy of solutions, as double-difference processing usually provides more robust results due to cancellation of common errors of stations and satellites through the differencing process.

5.2 NAPEOS overview

This section gives an overview of the NAvigation Package for Earth Observation Satellites (NAPEOS; Springer, 2009). In contrast to the software packages that employ a double-difference processing strategy, NAPEOS adopts PPP. This is advantageous for the current study, as it allows to minimize inter-station effects and assess each PCC and ESM (see Section 3.6) independently. At the same time, NAPEOS provides the ambiguity resolution functionality, which allows to considerably improve solution accuracy and robustness of PPP solutions. Below a general

description of the key NAPEOS routines, which are involved in typical GNSS processing, is given.

NAPEOS is a state of the art software for GNSS processing and is currently maintained by PosiTim (UG[1])[2] with a focus on high processing efficiency, robustness and simplicity of operation. NAPEOS is a cross-platform package, which is fully coded in FORTRAN 90/95 and which consists of a number of routines accessible through a common graphical user interface (GUI). Being a multifunctional package, it supports not only multi-GNSS processing using ground stations, but also precise orbit determination (POD) for low Earth orbiters (LEO).

NAPEOS is capable of performing single frequency as well as dual frequency processing. The single frequency processing may be accommodated for LEO, as some of them are equipped with single frequency GNSS receivers. Dual-frequency processing is the most common way for processing GNSS observations, as it allows for the mitigation of the first-order effect of the ionosphere through performing LCs between signals and facilitates integer ambiguity resolution. For dual-frequency processing NAPEOS employs the ionosphere-free linear combination, which allows to nearly eliminate the effect of ionosphere on signal propagation. This implies that the first-order ionospheric effects, which amounts to 99.9% of total ionospheric impact is removed, however, the higher order effects are left unaccounted for (Kedar, 2003; Fritsche et al., 2005; Petrie et al., 2010).

NAPEOS adopts PPP, which is essential for this study. PPP processing allows to minimize inter-station influence and analyse the behaviour of each station independently. Thus, modifying, e.g., PCC at one station does not have an impact on the parameter estimates at other stations.

Although the integer phase ambiguity resolution is not yet implemented for PPP due to the presence of uncalibrated phase biases at stations and satellites, NAPEOS overcomes this problem by forming and resolving phase ambiguities on baselines, which then serve as additional constraints for solutions (see Appendix A for details). Thus, integer phase ambiguity resolution becomes another valuable functionality of NAPEOS, as it allows to significantly improve solution accuracy and robustness. However, forming these constraints using baselines may introduce some inter-station effect, which cannot be quantified here. Nevertheless, the benefits of the ambiguity resolution in terms of solution accuracy overcome the aforementioned issue.

Finally, one of the strong points of NAPEOS is that it is routinely used by the European Space Operations Center (ESOC) – an IGS analysis center at the European Space Agency (ESA). Although the NAPEOS ver. 3.3.1, which is used in this study is different from ver. 3.8 used by the ESA, the main functional elements are effectively very similar. Differences in the NAPEOS versions are related to enhanced multi-GNSS processing capabilities and adaptations to other

[1] Unternehmergesellschaft (haftungsbeschränkt) – entrepreneurial company (with limited liability), *translation by author from German*

[2] `http://www.positim.com`

missions performed by ESA. Taking into account that the ESA products are among the main contributors to the IGS combined products, the highest levels of performance can be expected in all solutions that are produced using NAPEOS.

5.2.1 Basic functional elements

Similar to other GNSS processing packages, processing in NAPEOS is divided into several steps, namely, data preprocessing, e.g., cleaning, forming required linear combinations, format conversion, etc., and parameter estimation, during which parameters that have been requested, e.g., satellite orbits, station coordinates, etc., are computed. This is a very simplified view of the required steps, which are employed by all GNSS processing packages. This does not account for data input and output, which needs to be performed to support automation and further use of the estimated parameters.

For a typical GNSS processing using a network of ground stations, when station coordinates and/or orbits are estimated, the flowchart of a basic processing sequence is shown in Figure 5.1. Thus, data preparation mainly consists of downloading the necessary data, e.g., satellite products (orbit and clocks), observation data, orbit and clock file sampling, observation data sampling, conversion between different formats. Data preprocessing involves initial data quality checks, data screening, cleaning and clock initialization. During the parameter estimation step the normal equations are formed and the parameters are estimated. The latter may include, e.g., station coordinates, satellite and receiver clocks, orbits, zenith wet delays, etc. After the parameters are estimated, they can be compared to the a priori or external values, which effectively performs a quality control of the produced solutions. Additionally, multiple solutions may be combined, e.g., daily solutions may be combined to produce weekly ones, etc. The last step involves data conversion from binary to human-readable formats, e.g., Solution INdependent Exchange Format (SINEX; Rothacher and Thaller, 2006), and data archiving.

A brief description of main NAPEOS routines is provided below (see also Springer, 2009):

CMDLine: Performs file copying, runs scripts.

BuildCat: Creates catalogues of files to be processed (e.g., Receiver INdependent Exchange Format (RINEX) files, broadcast ephemeris files, etc.).

ClockUpd: Converts clock files from RINEX to NAPEOS format, allows for clock sampling.

OrbUpd: Provides initial orbit initialization, also performs orbit sampling if needed.

Nav2Sp3: Performs conversion of orbit data given in Keplerian elements to RINEX SP3 format.

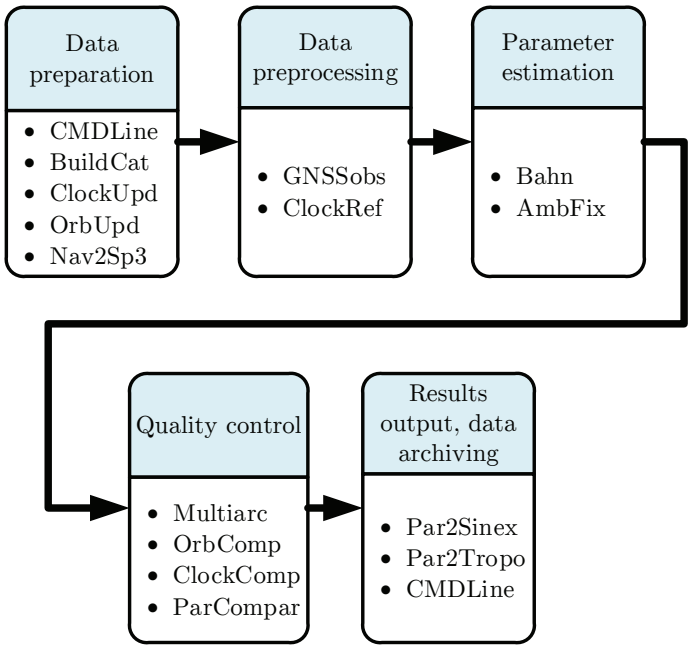

Figure 5.1: Basic functional elements of NAPEOS.

GNSSObs: Provides initial data cleaning using a number of tests and converts observation data to the NAPEOS tracking data format (NTDF). The tests involve outlier detection using, e.g., observed minus simulated test using a priori station and satellite positions, forming ionosphere free and Melbourne-Wübbena LCs, performing cycle slip corrections.

ClockRef: Initializes clocks for stations and satellites by selecting a reference clock and aligning other clocks to the reference one.

Bahn: Generates normal equations and performs parameter estimation using least-squares, e.g., station coordinates, clock biases, satellite orbits, troposphere, carrier phase ambiguities, etc.

AmbFix: Creates all possible double-difference ambiguities and fixes them to integer values.

Multiarc: Performs solution combination, e.g., to obtain a weekly solution out of daily ones, aligns solutions to a reference frame.

OrbComp: Compares two different sets of orbital arcs, e.g., in two SP3 files.

ClockComp: Compares two sets of clock biases, e.g., RINEX clock files.

ParCompar: Compares two sets of solutions, e.g., a solution from `Bahn` to a solution that is aligned to a reference frame by `Multiarc`.

Par2Sinex: Data conversion from NAPEOS binary to human readable format.

Par2Tropo: Data conversion from NAPEOS binary to human readable format.

5.2.2 PPP and orbit determination in NAPEOS

Both station coordinate estimation and orbit determination involve essentially equivalent processing steps in NAPEOS. In particular, a basic PPP processing sequence assumes that the satellite orbits and clocks are provided and kept fixed, whereas parameters related to ground stations, e.g., coordinates, clock biases, ZTDs are estimated. In case of satellite orbit determination station coordinates are tightly constrained to a priori values, e.g., coordinates that are defined in a reference frame (e.g., IGb08), while satellite positions, clock biases, etc., are estimated. In both cases modelling of additional parameters, such as satellite and receiver PCC, a priori ZTDs, tides, solar radiation pressure (in case of orbit determination), including albedo radiation, etc., provides additional constraints to the estimated parameters. As both PPP and orbit determinations are performed in this study, these are discussed in details in the following sections.

Daily PPP

The PPP processing relies on orbits and clocks that are introduced from an external source, which can be represented by the IGS or any of its ACs (e.g., CODE, ESA, etc.) or from a previous orbit estimation run.

The general PPP processing sequence in NAPEOS adopted for this study is shown in Figure 5.2. Raw observation data are initially checked and prepared for consecutive preprocessing. The initial step involves execution of a number of command line tools using `CmdLine`. Together with data fetching and uncompressing the data it performs RINEX files checks for integrity (this is done using the UNAVCO toolkit for GNSS data – `Teqc` (Estey and Meertens, 1999). Additionally, biases between C1 and P1 code are corrected using `cc2noncc` (Ray, 1999, 2000; Romero, 2008a,b) and the differential code bias information provided by CODE (Schaer, 2001). Precise ephemeris in the SP3 format are fed to `OrbUpd`, which provides data sampling and insures that the orbit files have no bad data. At the same time `ClockUpd` performs clock sampling and format conversion from RINEX to NAPEOS format, namely, transmitter (for satellites) and receiver (for stations) clock bias (tcb and rcb), respectively. As no rcb is available at this point, only tcb files are created. A list of observation files is created by `BuildCat`.

Preprocessing of the observation data is performed in `GnssObs`. In particular, the routine performs data sampling and provides initial check for the data quality – it uses code observations to estimate pseudoranges to satellites, the ionosphere free and Melbourne-Wübbena LC to reject outliers. Additionally, it checks for cycle slips and defines satellite passes which have no cycle slips and for which phase ambiguities will be estimated afterwards. Also `GnssObs` performs initial clock

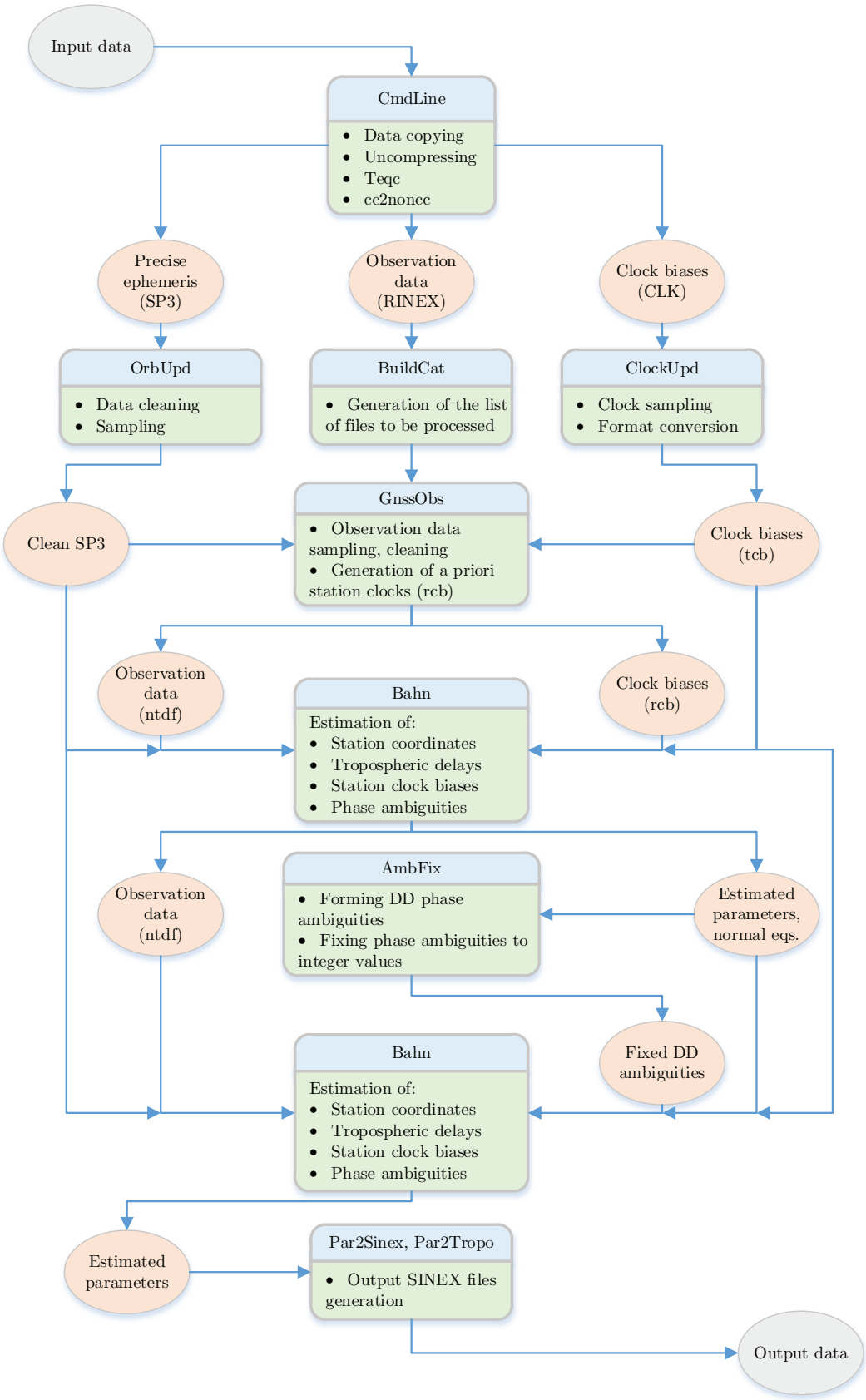

Figure 5.2: Flowchart of the PPP processing sequence in NAPEOS used in this study.

initialization and estimation for ground stations (rcb). Finally, the routine writes the cleaned observation data in the NAPEOS format (ntdf), which is processed by `Bahn` afterwards.

`Bahn` receives the observation data and preliminary receiver clocks from `GnssObs`, precise ephemeris from `OrbUpd`, and satellite clocks from `ClockUpd` to generate normal equations and perform parameter estimation. At this stage ground station parameters (station coordinates, clock biases, ZTDs and phase ambiguities) are estimated, whereas the satellite parameters (orbits and clocks) are kept fixed. However, satellite clocks at this stage are not entirely fixed, but estimated with very tight constraints ($\sigma = 10^{-3}$ ps), which effectively keeps the clocks fixed. This is done to perform ambiguity fixing on the next stage.

Due to the presence of uncalibrated phase biases at receivers and satellites, which are not accounted for in processing, phase ambiguity resolution cannot be done at the undifferenced level. Performing differences between observations allows for elimination of common biases. Thus, a single difference between observations from two satellites and one receiver eliminates a common bias at the receiver level. Alternatively, differences in observations from two receivers that observe the same satellite eliminates biases at the satellite. Hence, performing double differences between two satellites and two receivers would eliminate both receiver and satellite biases (see Appendix A for details).

In order to overcome the problem of the uncalibrated phase biases, `AmbFix` forms all possible double difference phase ambiguities that are linearly independent from each other. After the ambiguities are fixed to integer values, they are introduced to `Bahn` to re-estimate the remaining parameters, while the phase ambiguities are kept fixed. Satellite orbits and clocks are also kept fixed as they are produced by `OrbUpd` and `ClockUpd`, respectively.

After the second `Bahn` run station coordinates, clock biases and ZTDs are estimated. `Bahn` produces clock files directly in the RINEX format, however, other estimated parameters, e.g., station coordinates and ZTDs, etc., are stored in a binary format that requires the use of additional routines to perform conversion from the `Bahn` binary output to the commonly used SINEX format. This is done using the `Par2Sinex` and `Par2Tropo` routines, which output station coordinates and tropospheric estimates in the SINEX format, respectively.

Typically, the options listed below were used for PPP processing throughout this study. In order to reduce processing time, the observation data were sampled every 300 s, additionally, the observation elevation mask was set to 5°. For the a priori ZTDs the Saastamoinen a priori tropospheric zenith path delay model (Saastamoinen, 1972) along with the GMF and Global Pressure and Temperature model (GPT, Boehm et al., 2007) were used. Corrections to the a priori ZTDs were estimated at each station every 3600 s. The estimation of the troposphere was enhanced by the estimation of tropospheric gradients once per day in the East and North directions (Chen and Herring, 1997). Ocean tide loading parameters for all stations were generated

using the FES2004 model by the free ocean tide loading provider at Onsala Space Observatory (Chalmers University of Technology; `http://holt.oso.chalmers.se/loading/`) and introduced to the processing. The ITRF2008 a priori station coordinates were computed for all stations, in particular, the IGb08 realization of ITRF was used for this purpose. Additionally the Earth orientation parameters were taken from the IERS.

Sub-daily PPP

Sub-daily PPP processing sequence is almost identical to the daily one. The only difference is in the observation data, clock and orbit sampling. Thus, in order to increase the number of observations to be processed, instead of 300 s sampling employed for daily PPP, 30 s sampling was used. This resulted in the finer resolution of sub-daily estimates compared to that of the daily ones.

Sub-daily position estimation can be achieved in NAPEOS through two techniques: by limiting the session length in `Bahn` and thus reaching the required position sampling, and by switching to time-dependent coordinate estimation.

The first option assumes completely independent solutions for each session, however, it suffers from low precision of the computed estimates due to long convergence times required for PPP. Due to high correlation between the estimated parameters and little change in the satellite/receiver geometry during short time periods, session lengths should not be too short, as this results in elevated noise in solutions. In practice, when observations are processed with 30 s sampling rate, the session length needs to be long enough, otherwise the uncertainties in solutions expressed as their standard errors, become too large. Thus, the average standard errors for the hourly solutions are 1.5 cm, 5 cm and 5 cm for the north, east and up components, respectively. However, when session length is extended to 3 hours, these are reduced to 0.4 cm, 0.7 cm and 1.2 cm for the north, east and up components, respectively. Since RMS of the horizontal coordinate components computed with GNSS is usually smaller than that of the vertical component, the hourly solutions are underconstrained. Such a significant reduction of the east component uncertainty suggests that the associated noise of the hourly sessions may result in underestimation of potential improvements brought by changes in the PCC.

Alternatively, time-dependent station coordinate estimation can be enabled in `Bahn`, while keeping session length equal to 24 h. This implies that the solution is based on a long session (e.g., 1 day), eliminating the problems associated with poor convergence. In this case solution sampling may be reduced to 1 hour or even finer values.

As the time-dependent coordinate estimation yields more accurate solution estimates with finer sampling compared to the other approach, it was used to produce sub-daily position estimates in this study. As mentioned previously, processing options for sub-daily estimation were identical to

those in the daily sequences, except for the observation data sampling, which was set to 30 s.

Orbit determination

Generally, the orbit determination sequence in NAPEOS reminds that of PPP, however, the input and estimated parameters are different. The sequence adopted for this study is shown in Figure 5.3.

Unlike in the PPP sequence, where satellite orbits and clocks are known, only the approximate a priori data are used in the orbit determination scenario. Thus, processing starts from the observation data and some a priori estimate of the satellite orbits, e.g., the broadcast satellite ephemeris. Prior to processing, RINEX data undergo the same set of actions performed in the PPP processing sequence (uncompressing, `Teqc`, `cc2noncc`, etc.). `Nav2Sp3` allows to convert satellite broadcast ephemeris, which are given as Keplerian elements to satellite positions in an Earth-fixed and centred Cartesian reference frame. After a priori satellite orbits in the SP3 format are obtained, the observation data are processed with `GnssObs`, however, both station and satellite clock biases (rcb and tcb, respectively) are now estimated. These clock biases will be used later as a priori estimates in `Bahn`. Observation data are generated in NAPEOS format.

For further processing, NAPEOS requires a reference clock that is available for all epochs. The selection of the reference clock is performed in `ClockRef`, which checks for the clock availability and selects the most stable one. Based on the selected clock a linear fit for the entire processing window is computed and necessary adjustments to all clocks are performed.

On the next step the observation data which have been preprocessed by `GnssObs` are provided to `Bahn`, which also uses the station and satellite clock biases generated by `ClockRef` as a priori. `Bahn` forms normal equations and tries to solve them, however, unlike in the PPP case, satellite orbits and clocks are estimated, whereas station coordinates are tightly constrained to the a priori values.

GNSS orbit determination requires accurate modelling of forces that have an impact on the satellites. These are affected by the gravitational forces of the Earth, Moon, Sun and other planets. Additionally, due to the large solar panel arrays, the solar radiation pressure and the Earth albedo have a significant effect on the orbit. Furthermore, satellite attitude variations, while passing through the Earth's shadow, need to be taken into account.

As the orbit height of the GPS satellites is approximately 20 200 km, the Earth gravitational field causes smaller perturbations compared to, e.g., LEO satellites. However, they still sense irregularities of the Earth gravitational potential, as well as perturbations caused by various tides. Thus, the GNSS satellites orbital arcs are split into 120 steps for numerical integration. Additionally, the `GPS Attitude mode` is chosen for the satellite attitude behaviour to account for eclipse phases and other manoeuvres. Because of the orbit height, degree and order of the Earth gravitational field can be set to 12, which is sufficient for this case. It should be noted that the

same values are used by ESA during generation of their orbit products that are submitted for the IGS combination. In addition to the earth gravity modelling, the solar, lunar, planetary gravity, as well as the J2/Moon interactions are considered. Solid and ocean tides are also taken into account with the number of tidal constituents set to 12, whereas their modelling order and degree is set to 12 (Tim Springer, personal communication, 2014). Furthermore, relativistic effects are taken into account.

In order to assess the solar radiation pressure affecting the satellites, the CODE five parameter a priori model is used (Springer et al., 1999). To improve further the solar radiation estimation the box-wing models are used for satellites. Additionally, the same models are used for assessing the impact of the Earth albedo and infra-red radiation from the Earth surface. Parameters of the box-wing models that were used in this study are similar to those used by the ESA in its routine processing. These were shown to be very efficient for orbit determination (Springer et al., 2014). Furthermore, perturbations due to unmodelled forces that affect the satellites are accounted for.

Station positions need to be constrained to the coordinates defined in a reference frame. If this is done, the orbit frame is consistent with the frame of the ground network. Thus, if ground station coordinates are given in IGb08, the determined orbits also appear to be consistent with the IGb08. Tight constraints (σ = 0.5 cm) for ground station coordinates are applied in `Bahn` during its' first run.

Thus, `Bahn` forms normal equations and estimates satellite clock biases, orbits, station clock biases, coordinates, ZTDs and phase ambiguities. The tropospheric modelling is performed in the same way as this is done for the PPP processing, i.e., GMF, GPT and the estimated parameters, which are corrections to the a priori values computed every 3600 s and two gradients (East and North).

After the first `Bahn` run the station clock biases may undergo significant changes compared to those estimated by `GnssObs`. This is due to the fact that in `GnssObs` the clocks are estimated based on the code observations only. Therefore, in case of code smoothing employed at a receiver, clock estimates by `GnssObs` from this station may show very high stability. At the same time, `Bahn` estimates of clocks are based on both code and carrier phase observations, which may significantly change the a priori values. Thus, a second `ClockRef` run needs to be performed to select another reference clock.

Similar to the PPP scenario, the normal equations are handed over to `AmbFix`, which forms all possible DD ambiguities and tries to fix them to integer values. This significantly increases the solution accuracy.

After the phase ambiguities are resolved, they are imported into the second `Bahn` run. Additionally, the second `Bahn` run uses cleaned observation data that were produced by `Bahn` on the previous step. As a priori estimates for orbits, clocks, station coordinates and ZTDs, the `Bahn`

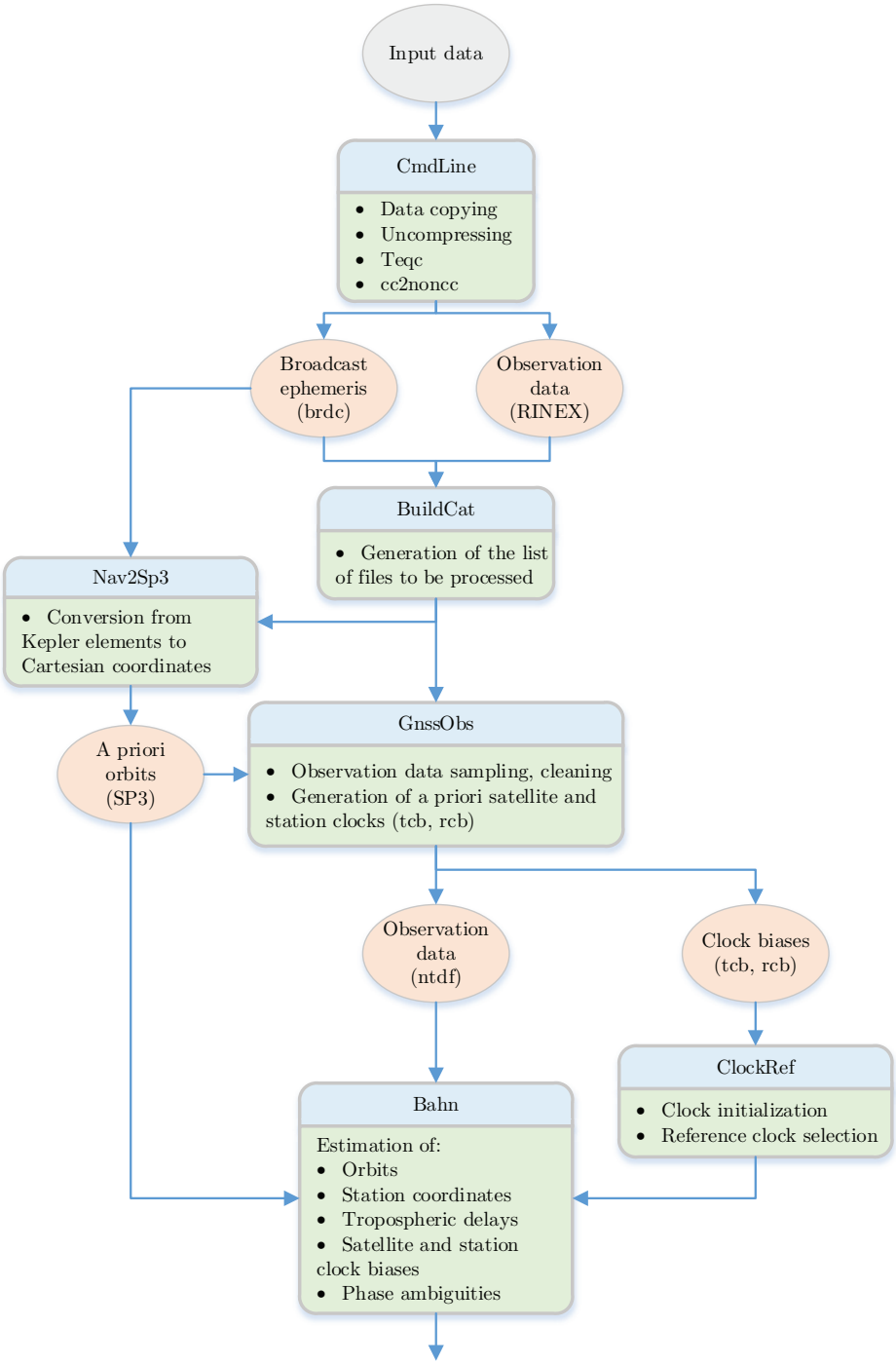

Figure 5.3: Flowchart of the orbit determination sequence in NAPEOS used in this study *(cont. on next page).*

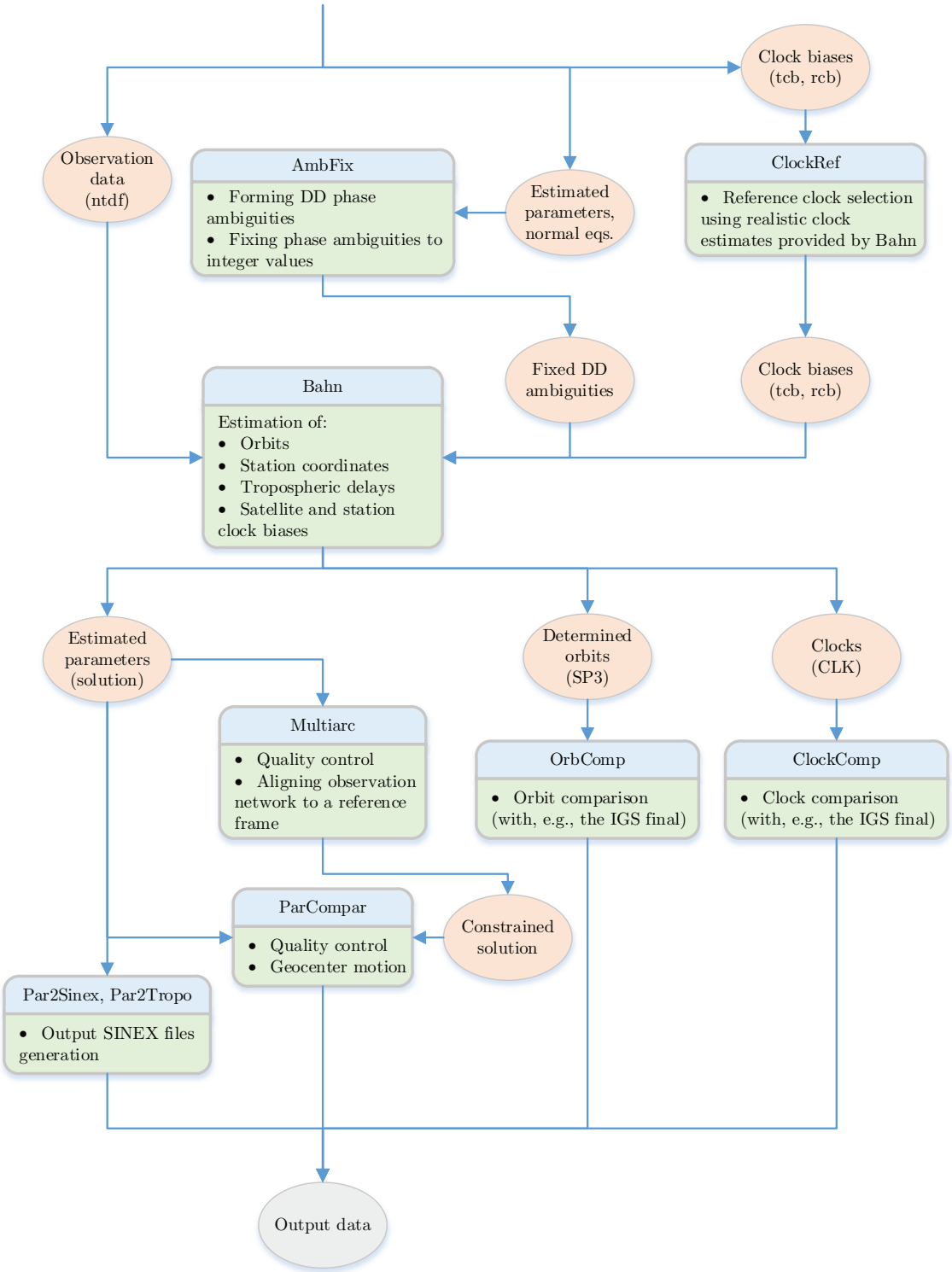

Figure 5.3: Flowchart of the orbit determination sequence in NAPEOS used in this study *(continued from prev. page).*

output from the previous step is used. Using the resolved ambiguities, `Bahn` solves the system of normal equations to produce a solution. Parameter options that are used for this run are very similar to those used in `Bahn` on the previous step. The only difference is in the constraints of the station coordinates, which are set to $\sigma = 1$ cm instead of $\sigma = 0.5$ cm. This is done to allow for more freedom to the solution, considering that new constraints in the form of resolved ambiguities are now available.

After the second `Bahn` run a refined solution is computed and quality control can be performed. This is done through several routines, namely, `Multiarc`, `ParCompar`, `OrbComp` and `ClockComp`. Using the `Bahn` solution, `Multiarc` produces a minimum constraints solution, in which station coordinates are aligned to the a priori values (the reference frame). Comparison of the `Multiarc` and `Bahn` solutions using `ParCompar` allows to assess the geocenter motion. Additionally, two sets of orbits, e.g., the computed and those from an external source (IGS) can be compared using `OrbComp`, whereas `ClockComp` compares two sets of clock biases. Thus, both orbits and clocks that have been computed may be compared to those of an external provider, e.g., the IGS.

Typically, the options listed below were used for orbit determination throughout this study. In order to reduce processing time, the observation data were sampled every 300 s, additionally, observation elevation mask was set to 5°. The troposphere estimation was identical to the PPP processing sequence, in particular, the ZTDs were computed every 3600 s, whereas two gradients (North and East) were computed once per day. Ocean tide loading parameters for all stations were generated using the FES2004 model by a free ocean tide loading provider at Onsala Space Observatory and introduced to the processing. The IGb08 a priori station coordinates were used for all stations. Additionally the Earth orientation parameters were taken from IERS.

5.3 Assessment of orbit overlaps

GNSS satellites are subject to external influences, e.g., gravitation of the Earth, moon, Sun and other planets, solar radiation pressure, etc. The complexity of these is not fully accounted in currently applied models, leading to the existence of errors, which, in turn, result in errors in the estimated satellite orbits. Without an alternative technique for orbit determination, e.g., SLR, assessment of the produced solutions is challenging. However, orbit estimation techniques, including models that are involved in processing can be assessed based on the orbit overlaps. In the most ideal scenario where all error sources are perfectly modelled, positions of satellites in the end of preceding and beginning of consecutive orbital arcs should match. The tests of this kind serve as another way of investigating how well the modelled orbit fits reality. In addition to the general overview of the quality of computed orbits, the time series of the day boundary differences (DBD) may be a valuable source of information about errors in the models that were

used during the orbit estimation. Thus, the power spectra of the DBD time series for the IGS final orbits discussed by Griffiths and Ray (2009), showed presence of draconitic signals. In turn, this has pointed to possible sources for these errors, e.g., solar radiation pressure, errors in the EOPs, antenna phase centres and multipath.

As the IGS orbits are daily, and cover periods from 00:00:00 until 23:45:00, Griffiths and Ray (2009) decided to propagate the orbits to compare them. For each daily orbital arc backward and forward propagation by 7 minutes 30 seconds was performed, allowing for the comparison of two successive orbits, having the common epoch at 23:52:30. Finally, the time series of the overlaps were obtained and analysed.

Similar to the IGS, the orbits produced in NAPEOS for this study are daily, therefore, the methodology based on the DBD analysis can be applied. However, NAPEOS allows for flexibility in the choice of the produced orbital arc length. Thus, the daily orbits produced for this study covered intervals from 00:00:00 until 23:55:00 with 5 minute sampling. Additionally, on the interval from 23:55:00 until 00:00:00 of a consecutive day orbit propagation was performed, so that two consecutive orbital arcs could be directly compared (Figure 5.4).

It should be noted that orbit propagation, as it depends on the applied models, results in solutions that are not constrained by observations, therefore, it is often associated with loss of accuracy. However, in the study of Griffiths and Ray (2009) two orbit propagations were performed each one being 7.5 minutes long, whereas only one 5-minute propagation needs to performed for the orbits produced in this study. This suggests that the associated errors should be smaller compared to the case of 2×7.5-minute propagations.

According to the SP3 standard (Spofford and Remondi, 1994), satellite positions are defined in the Earth fixed reference frame, therefore, computing the distance between two satellite positions of two consecutive orbital arcs in their common point is straightforward. However, decomposing this distance in three components, namely, the radial, cross- and along-track components may be useful for further analysis.

Thus, if at common epoch t X_1, Y_1, Z_1 and X_2, Y_2, Z_2 are coordinates, whereas v_{x1}, v_{y1}, v_{z1} and v_{x2}, v_{y2}, v_{z2} are the associated velocities of a satellite in orbital arc 1 and 2, respectively, then one

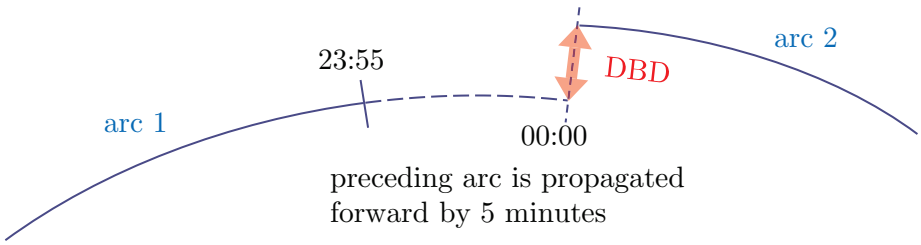

Figure 5.4: Orbit propagation model for two consecutive orbital arcs.

may define a vector between the two satellite positions

$$\mathbf{dX} = \{X_1 - X_2; Y_1 - Y_2; Z_1 - Z_2\}\,, \tag{5.1}$$

the mean velocity vector

$$\mathbf{v_{mean}} = \left\{ \frac{v_{x1} + v_{x2}}{2}; \frac{v_{y1} + v_{y2}}{2}; \frac{v_{z1} + v_{z2}}{2} \right\}, \tag{5.2}$$

and a vector from the origin to the satellite

$$\mathbf{x_{mean}} = \left\{ \frac{X_1 + X_2}{2}; \frac{Y_1 + Y_2}{2}; \frac{Z_1 + Z_2}{2} \right\}. \tag{5.3}$$

Thus, radial, along- and cross-track components of $\mathbf{dX}$ can be computed using

$$\mathit{Radial} = \frac{\mathbf{dX} \times \mathbf{x_{mean}}}{|\mathbf{x_{mean}}|} \tag{5.4}$$

$$\mathit{Along\text{-}track} = \frac{\mathbf{dX} \times \mathbf{v_{mean}}}{|\mathbf{v_{mean}}|} \tag{5.5}$$

$$\mathit{Cross\text{-}track} = \frac{\mathbf{dX} \times (\mathbf{x_{mean}} \times \mathbf{v_{mean}})}{|\mathbf{x_{mean}} \times \mathbf{v_{mean}}|} \tag{5.6}$$

with "×" denoting the cross-product. This method has been implemented by the author in a Python routine.

5.4 Estimation of ESMs

In dual-frequency processing mode NAPEOS uses the ionosphere-free LC

$$\varrho + c\ \Delta\delta = R_1 \frac{f_1^2}{f_1^2 - f_2^2} - R_2 \frac{f_2^2}{f_1^2 - f_2^2}, \tag{5.7}$$

where

ϱ	...	pseudorange,
c	...	speed of light,
$\Delta\delta = \delta_r - \delta^S$	...	total clock bias between receiver and satellite,
$R_{1,2}$	...	observed ranges on two GNSS frequencies,
$f_{1,2}$	...	GNSS frequencies.

As $R_{1,2}$ in equation (5.7) is pseudorange in general, the LC for code or phase is obtained depending on the type of observables employed. For clarity and consistency the ionosphere-free LC will follow the same notation as in Dach et al. (2007), namely L_3. The aforementioned notation will be used hereinafter unless stated otherwise.

The observed ranges $R_{1,2}$ in equation (5.7) are affected by the multipath error $\delta\phi_L$ from equation (3.2) as well as other unmodelled errors due to, e.g., signal propagation, poor orbit

modelling, etc. While this can be interpreted as stochastic errors, multipath effects depend on the direction of the incoming signals and on physical properties of objects located in the antenna vicinity. As for, e.g., permanent GNSS stations, access to these areas is usually restricted, resulting in limited changes in the antenna environment. GNSS stations, however, may undergo seasonal changes in their multipath environment due to vegetation growth, precipitations, etc. In a simplified scenario the introduced multipath effect for given directions of incoming signals should remain constant. In other words, at each instance $\mathbf{v}$ in equation (3.6) contains a constant and a variable part, or, multipath and other possible errors, respectively.

In the PPP processing in NAPEOS, as described in Section 5.2.2, the observation data are sampled at 300-s intervals and residuals are produced accordingly. Due to repeating ground tracks of the GPS satellites and the aforementioned observation sampling rate, residuals extracted for a station for only 1 day and plotted against azimuth and elevation, forming a skyplot, result in a rather sparse image. Additionally, noise observed in residuals due to modelling errors discussed above, introduces further limitations and should be removed or reduced. In order to overcome this problem, persistence of multipath across multiple days can be used to filter out the undesirable noise. Figure 5.5 provides examples of the L_3 phase residuals at the IGS station SPT0. As seen from Figure 5.5a, noise in phase residuals has minimum at zenith and increases in low elevations, which is directly related to the noise in the input data – L_1 and L_2 phase residuals in this case. Figure 5.5b demonstrates the skyplot coverage by showing the L_3 phase residuals accumulated over 1 day (01 Jan 2004), 1 month (01-31 Jan 2004) and 4 years (Jan 2004 - Dec 2007) after computing PPP solutions using the IGS final products. The blank space in the north direction is due to the absence of satellites in that area, as latitude of SPT0 is 57.7° North whereas the inclination of the GPS orbital planes is 55°. The example of SPT0 shows that accumulation of phase residuals over multiple days reduces the problem of uncovered areas on skyplots except for the area over the pole. Large uncertainties in the observed residuals especially in low elevations suggest that their better estimates can be obtained by, e.g., averaging the residuals across a given sector of the sphere.

In NAPEOS the L_3 residuals are produced separately for code and phase and can be easily extracted. While residuals in the binary format contain full information on residuals, those that are produced in the ASCII[3] format provide only minimum information. In particular, a code for a satellite-station pair, the epoch and the value of the residual. Therefore, in order to map each residual on a skyplot the satellite position relative to a given station at given epoch is required. While station coordinates are known, satellite positions can be obtained from, e.g., broadcast ephemeris. Considering, e.g, Warren and Raquet (2003), these are as close as $\sim$ 1 m to precise ephemeris. For reference, when converted to azimuth and elevation at station level, an error of

[3]American Standard Code for Information Interchange

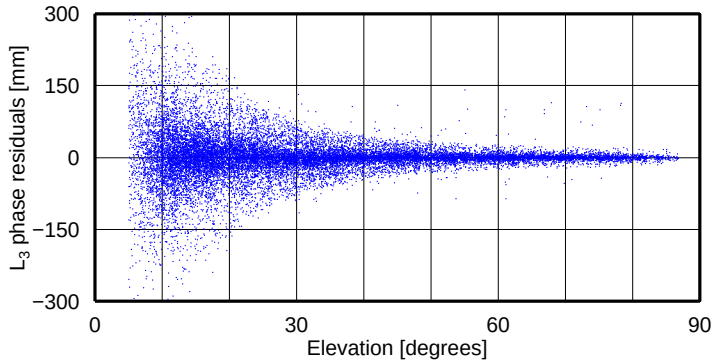

(a) L_3 phase residuals accumulated over 30 days.

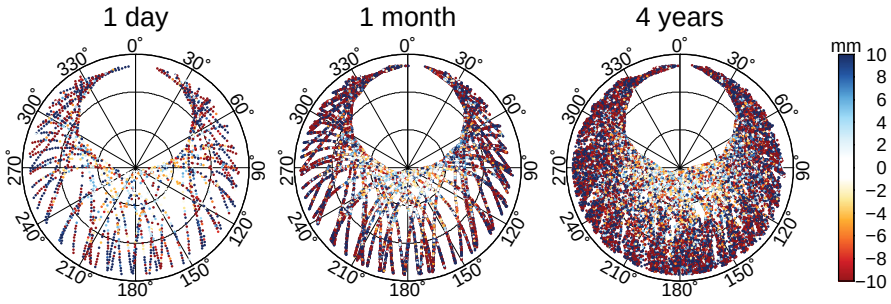

(b) Skyplots of L_3 phase residuals accumulated over periods with different length

Figure 5.5: L_3 phase residuals at station SPT0.

1 m in the orbit cross-plane direction would produce a $\sim 3 \times 10^{-6}$ ° error in azimuth/elevation of a computed satellite position, which is negligible for this application. Thus, in order to obtain satellite positions relative to processed stations, RINEX observation data together with broadcast ephemeris are processed using `Teqc`. The output of `Teqc`, containing station-specific satellite positions is used to map residual measurements on a sphere.

As multipath results in phase biases of the incoming signals, it is possible to suppress those by introducing additional corrections to already applied PCC. These corrections are obtained from the phase residuals, however, assimilation of phase residual maps into existing PCC models in case of NAPEOS requires converting the collected L_3 phase residuals into the GPS L_1 and L_2 frequency bands.

The following step is splitting the hemisphere representing a skyplot shown in Figure 5.5b into sectors of $1° \times 1°$ degrees. Due to accumulation of phase residuals over multiple days numerous L_3 residuals may fall into each sector. Therefore, considering equation (5.7), the L_1 and L_2 phase residuals for each sector can be obtained using least-squares solution of equation

$$\mathbf{A}\mathbf{x} = \boldsymbol{b}, \tag{5.8}$$

where

$\mathbf{A}$	$[n \times 2]$	...	matrix containing coefficients ($\frac{f_1^2}{f_1^2-f_2^2}$, $\frac{f_2^2}{f_1^2-f_2^2}$) from equation (5.7),
$\mathbf{x}$	$[n \times 2]$	...	vector of unknowns (L_1 and L_2 residuals),
$\boldsymbol{b}$	$[n \times 1]$	...	vector of L_3 residuals.

To accomplish this, the author used DGELSY routine of the Linear Algebra PACKage (LAPACK). More details on LAPACK and DGELSY are provided Appendix D.

Certainly, due to insufficient satellite passes, data rejection during processing or other reasons, no L_3 phase residuals may be assigned to individual sectors. The current method assumes that default residual value for each sector is 0 for L_1, L_2 and their LC. Also, to reduce sensitivity of results to noise, only those sectors are used, where 10 or more residuals have been accumulated.

After solutions for L_1 and L_2 for each sector that has observations of L_3 are obtained, they can be used to create spherical harmonic fits separately for both frequencies. In this study spherical harmonic functions of degree and order 9 were used. Spherical harmonic representation was performed using the freely available software archive SHTOOLS (Wieczorek, 2014). The discussed algorithm was implemented by the author in the software tool `antennaSH` (see Appendix D for details). With this step the ESM derivation is completed.

Finally, to be compatible with the IGS ANTEX format, in particular, for the possibility of merging with the applied PCC models, correction values for both L_1 and L_2 are extracted for each $5^\circ \times 5^\circ$ bin.

Reconstructed L_1 and L_2 phase residual maps represent phase corrections that can be directly applied to the PCC values used for obtaining these residuals. As residuals effectively represent phase biases of the incoming signals, they can be interpreted as updates to the PCC and merged with the latter. Considering the ANTEX v1.4 format specifications (Rothacher and Schmid, 2010), summation of respective PCC values and the obtained residual corrections should be performed.

Thus, taking SPT0 as an example, according to the information provided in the site log file available at the IGS FTP server[4], `AOAD/M_T OSOD` antenna/radome combination was used from 1995 until present. Therefore, the respective type-mean PCC from the igs08.atx[5] should be merged with the derived ESM to produce the ESM-corrected PCC.

According to NAPEOS algorithm, if no PCC for antenna/radome combination `ANTENNA RADOME` is found in the ANTEX file, antenna/radome combination `ANTENNA NONE` is searched and applied. Therefore, since no type-mean PCC exist for antenna/radome combination `AOAD/M_T OSOD`, `AOAD/M_T NONE` should be used for merging with the derived ESM. Figure 5.6 shows the result of such ESM correction. The ESM was computed for the period from 2004 until 2007.

[4] `http://igscb.jpl.nasa.gov/igscb/station/log/spt0_20140121.log`

[5] available online at `http://igscb.jpl.nasa.gov/igscb/station/general/igs08.atx`

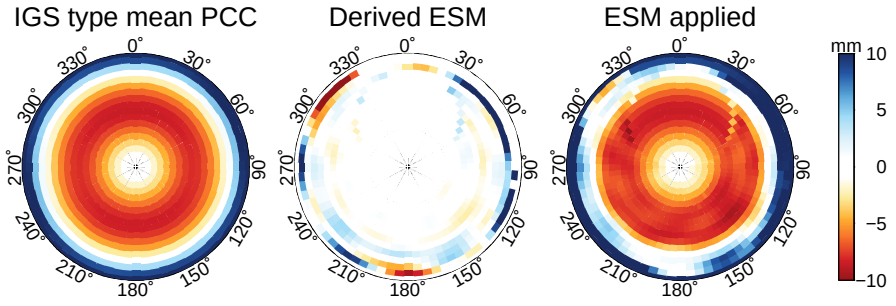

Figure 5.6: Initial IGS type-mean PCC for SPT0 (only PCC for L_1 is shown), derived ESM and the type-mean PCC merged with the ESM.

5.4.1 ESM temporal validity

To give an idea of how residuals change over time, those collected for SPT0 during the PPP processing using the IGS final products were processed separately for three consecutive years using the aforementioned methodology. Figure 5.7 shows the reconstructed residuals separately for each GPS frequency (L_1 and L_2) and for each year (2004, 2005, 2006). Thus, residuals mapped against azimuth and elevation for SPT0 show concentric patterns, which persist from 2004 until 2006. Similar patterns for SPT0 were also observed by Granström (2006) for the period from 1999 until 2004. Similarities between the results from other studies and the patterns shown for 2004-2006 suggest that the site environment did not undergo many changes from 1999 until 2006. Thus, the ESM derived from phase residuals after processing historical data should be similar to that derived from processing recent data. However, this is valid only if no changes happened at a site during the period considered. This has also been confirmed by Moore et al. (2014).

The ESM technique is based on the analysis of already acquired data, therefore it does not require any physical interaction with stations. Due to preserving the required continuity in the CTS together with providing site calibrations to mitigate multipath, it also enables fixing the problem of uncalibrated antenna/radome combination. Therefore, it may be easily extended to global GNSS networks.

5.4.2 Estimation methodology and considerations

Estimation of an ESM for each site converges to a choice of an optimal time frame, during which the post-fit phase residuals are collected and analysed. A short time period would result in a good agreement between instantaneous site states and the derived ESM, whereas the model itself may suffer from elevated uncertainties due to the low amount of observations. At the same time, this also depends on the observation data sampling used for processing. Some of the local effects, e.g., precipitations are extremely difficult to predict and, therefore, to model. Snow cover thickness

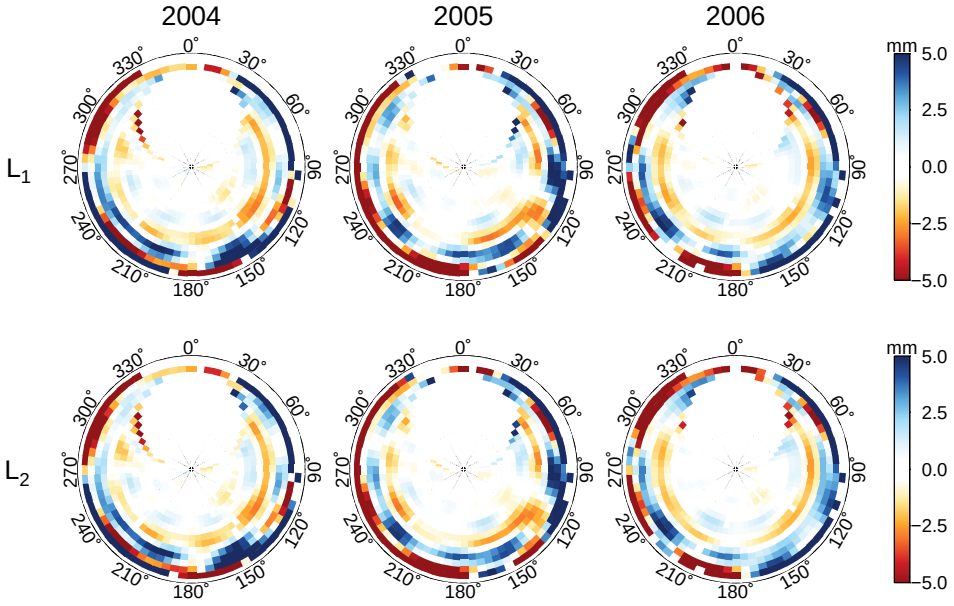

Figure 5.7: Reconstructed L_1 and L_2 phase residuals for station SPT0 accumulated over 3 consecutive years.

may change rapidly within hours, leading to significant variations in site states, therefore, an ESM obtained over a certain period may not be valid for other periods. Alternatively, estimation of ESMs during only short time periods increases its uncertainty due to high noise in the observations. This is a trade-off that one has to solve if correction using the ESM method is performed.

On the other hand, most of the time the GNSS stations are installed at locations with restricted access, e.g., on roofs of buildings, areas surrounded by a fence, or just at remote locations. This significantly reduces the chance of unforeseen changes on site during station operation. Thus, daily and seasonal meteorological fluctuations are the most significant error source, from which ESM estimation should suffer.

Referring to the work of Moore et al. (2014), who estimated their ESMs yearly, and considering small variation of the derived ESM over several consecutive years (Figure 5.7), the following strategy for ESM estimation was used in this study:

- For each antenna employed within the time interval from 2004 until 2014 on a site the ESM is estimated using post-fit phase residuals from the PPP processing as discussed in Sections 3.6.1 and 5.2.2 with the IGS final products.
- In case of any change in the antenna or radome a new ESM is estimated.
- To minimize uncertainties in the derived ESMs, only those are considered, which are based on residuals accumulated over a period of 10 days and more.

- To take advantage of ambiguity resolution in NAPEOS, stations, for which ESMs need to be estimated, may be combined into a network and processed at once.

The computed ESMs for stations discussed in Section 4.2 of Chapter 4 are shown in Appendix E, whereas those for all stations employed in the frame of this research are provided on the supplied CD-ROM.

5.5 Assessment of the PCC/ESM impacts

The assessment of the PCC impact on station coordinates is relatively simple and straightforward. Generally, it requires two PPP runs with identical settings, during which station coordinates are estimated. For instance, if the impact from using individual instead of type-mean PCC needs to be investigated, a PPP run using type-mean PCC needs to be performed to produce a reference solution. Another PPP run with individual PCC would show the impact, Figure 5.8. PPP is essential for this case, as forming baselines between different stations may introduce inter-station effects, making an independent analysis of each station impossible.

Processing a network of stations in NAPEOS allows for phase ambiguity resolution, which, in turn, improves the accuracy of solutions and, consequently, the reliability of the entire assessment. At the same time, the scheme shown in Figure 5.8 may not be perfect, considering an independent estimation of station clocks and tropospheric delays in both PPP runs. In particular, correlation between the employed PCC, ZTDs and station heights may produce biased results. However, the basic idea remains the same.

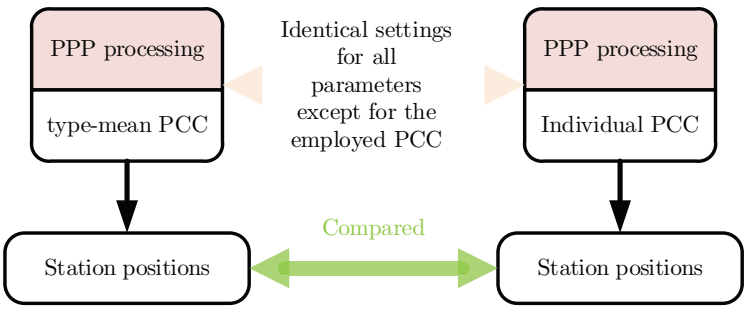

Figure 5.8: Basic technique for the PCC impact assessment.

5.6 Prevention of PCC error propagation into other parameters

As discussed in Section 5.5, the impact of deficiencies in the applied PCC on the example of type-mean and individual models may be investigated by producing solutions using different antenna corrections and comparing the results. However, during such an examination other parameters that are estimated, e.g., station clock biases and ZTD data may be altered. While the impact on station clocks may be small, changes in the PCC may provoke biased estimation of station positions and ZTDs, due to high correlation between these parameters.

In order to overcome the problem caused by correlation between different parameters, estimation of ZTDs should be limited. If possible, the tropospheric parameters should be used from an external source, or they can be estimated only in one of the PPP runs and imported into the other, as shown in Figure 5.9.

The PPP processing discussed above addresses only the problem of PCC impacts on station coordinates. A similar technique can be applied to assess the PCC impacts on the orbits. However, one should take into account that satellite orbit determination is based on observations from multiple stations. Thus, the impact of differences in the applied PCC on the orbits may be less pronounced compared to the PPP case. The same refers to the tropospheric estimates, implying that even though they may exhibit significant changes due to PCC modifications, as sensed by the satellites, their effect may be averaged out, because each satellite is observed by multiple stations. The ways of dealing with tropospheric delays and other parameters in orbit determination while making modifications to station PCC will be discussed in the following sections.

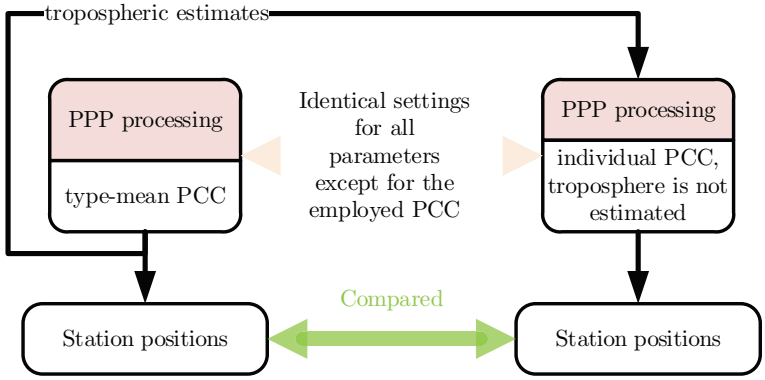

Figure 5.9: Elimination of the tropospheric effect in the PCC impact assessment.

5.7 Strategies for solution consistency

When investigating the contribution of PCC to the draconitic signals seen in the orbits, special care should be given to the consistency of the applied products. The actual impact of PCC cannot be assessed by applying a simplified scheme shown in Figures 5.8 or 5.9, as deficiencies in the PCC may contribute to the constellation-specific signals in the satellite products that are generated using these PCC. This is especially important for any studies involving frequency analyses.

Figure 5.10 shows the basic approach for achieving the solution consistency. Purely independent sets of solutions, each one obtained using a set of PCC (e.g., type-mean or individual) for all stations, need to be estimated. Thus, it will allow for the orbit and station coordinate comparison. The orbit comparison can be performed based on the orbit overlaps, as discussed in Section 5.3, whereas the impact on site coordinates can be assessed through comparison of two sets of station positions obtained using different PCC. Finally, frequency analysis of the obtained time series can be performed.

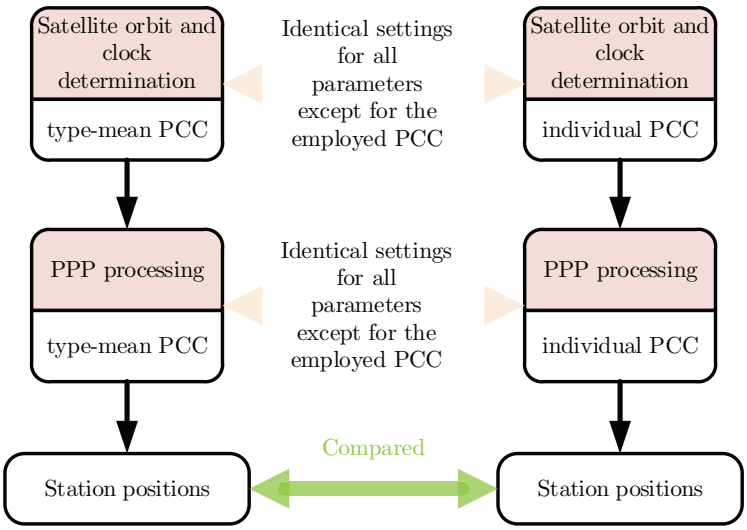

Figure 5.10: Solution consistency while investigating the contribution of PCC deficiencies to generation of draconitic signals.

5.7.1 Regional scenarios

It should be noted that the number of stations that have antennas with individual PCC is very limited. As was discussed in Chapter 4, these are mainly located in Europe. Therefore, orbit determination with only these stations is challenging, especially taking into account that the orbit quality is assessed through the orbit overlaps at consecutive days (DBD).

The problem consists in very loose constraints of the parameters, in particular, the orbital

arcs are constrained only over the region where the satellites are observed, whereas the rest, to a large degree, depends on the models that are employed. As will be shown in Section 6.4.1, the underconstrained solutions may result in inaccurate ZTD and clock biases estimation, leading to very poor quality of orbits over the areas where no observations are available.

There are two ways for solving this problem. The most straightforward way is to complement the regional network with stations that are globally distributed. This will impose additional constraints on the orbits through the improved network geometry, however, it should be noted that these additional stations will have only type-mean PCC. Therefore, it is questionable whether the effect from using individual PCC within the regional network will be noticeable by looking at the DBD.

Alternatively, estimation of troposphere and clock biases may be limited. In order to separate PCC from the other parameters, the latter should be fixed, implying that they have to be accurately estimated beforehand in another, separate run and then introduced as input values in the following orbit determination runs. The separate orbit determination run is required to obtain a homogeneous and consistent set of parameters for all stations, including those not taking part in the IGS network or EPN, for which these parameters are routinely estimated by ACs and, consequently, may be used. To support the described idea, Figure 5.11 provides a block diagram of the test, in which the first part of it, *Step 1*, represents estimation of the set of parameters, in particular, station positions, satellite and station clock biases and ZTDs, which will be used in consecutive steps. In *Step 2* the aforementioned estimates are imported during processing and are kept fixed, while satellite positions are estimated using type-mean and individual PCC. At this step differences in satellite positions from the "type-mean" and "individual" run, will show the effect induced by the applied PCC. It needs to be mentioned, however, that as the evaluation of orbit DBDs is performed on a global scale, the effect from the applied PCC within the regional network may be small and hardly discernible. To overcome this and to reduce the scope to the regional scale, the test can be extended even further – to *Step 3*. Here satellite positions obtained in *Step 2*, satellite and receiver clock biases and tropospheric estimates obtained in *Step 1* are introduced in the "type-mean" and "individual" PPP runs using corresponding PCC, while station positions are estimated. Resulting differences between station coordinates from the two runs in *Step 3* will reveal to what extent deficiencies in applied PCC propagate into GNSS solutions once their effect on satellite orbits has been considered.

The results for both approaches will be presented and discussed in detail in Chapter 6.

5.7.2 Global network

As discussed in the previous section, the number of stations employing antennas with publicly available individual PCC is very limited. This suggests that a network ensuring global coverage will

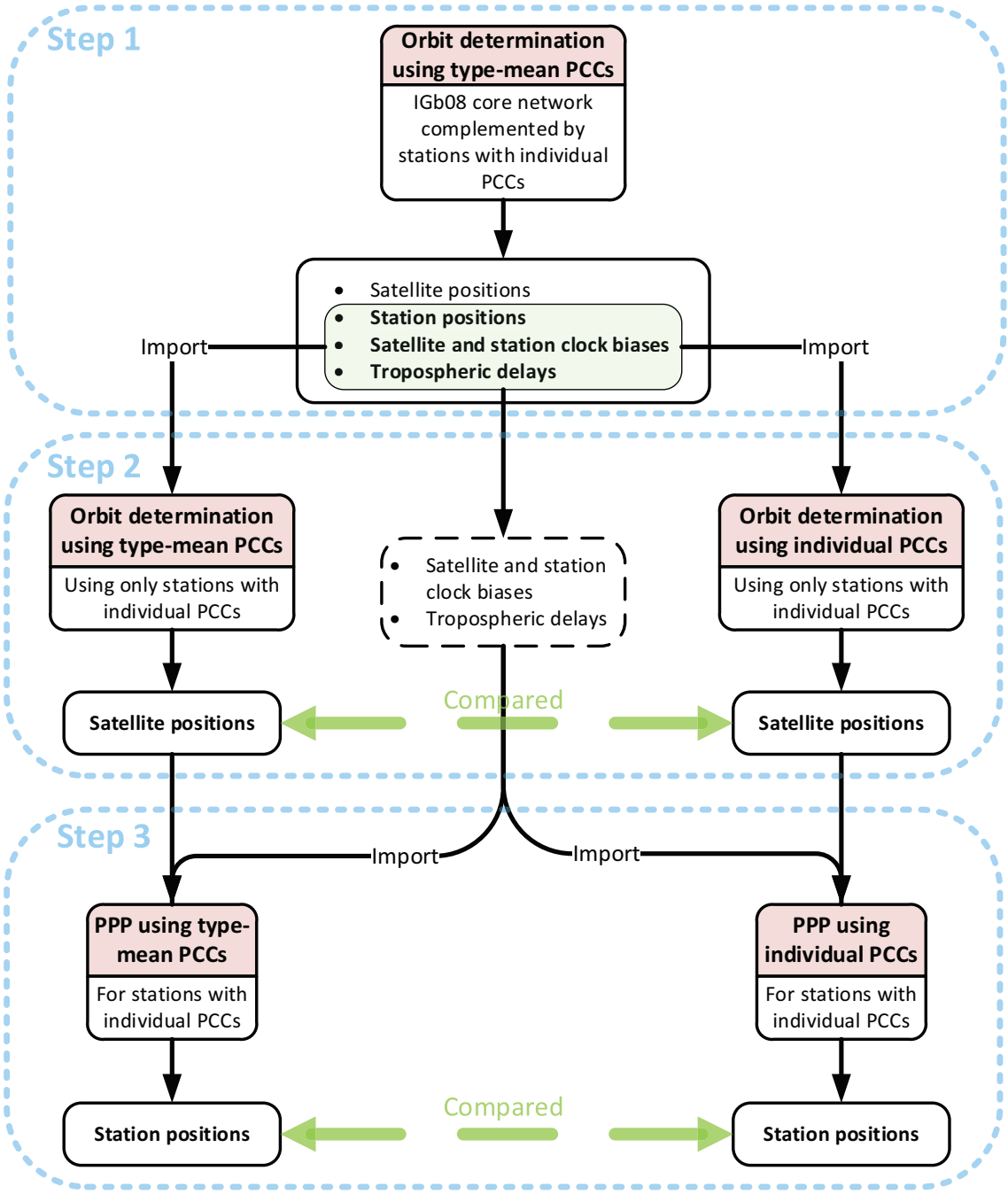

Figure 5.11: Experiment description. Three steps show the way to assess the effect of PCC on the satellite orbits and station coordinates.

inevitably contain stations with type-mean PCC. Considering that mixing stations with type-mean and individual PCC in the network may be harmful for studying the impact of PCC deficiencies on solutions, preference should be given to a homogeneous set of PCC for all stations. This can be easily achieved through applying the ESM technique that was described in Section 3.6. Thus, the scheme shown in Figure 5.10 can be applied and full consistency of solutions can be achieved. The two sets of solutions, "type-mean" and "ESM-corrected", which include both satellite and station parameters, can be compared.

Additionally, one may be interested in reducing the impact of PCC modifications on the tropospheric estimates and clock biases, and, thus, in removing the estimation of these parameters from processing. As the accurate estimates of these parameters are essential in precise GNSS processing, they may be obtained in a separate processing and later imported. This may be useful for the current study, as it shows the impact of PCC modifications on GNSS solutions, in particular, satellite orbits and station positions without spreading into other parameters.

Thus, for this more sophisticated case the entire processing sequence can be split into several steps according to the tasks that are performed, Figure 5.12. In *Step 1*, a preparative orbit determination run is performed, in which a priori satellite and station clock biases, as well as station coordinates are estimated. Simultaneously, ESMs for all stations included in processing are estimated using the methodology described in Section 3.6.1. It is important to mention that the IGS final products were used for the ESM estimation in the current study. Alternatively, to reduce the computational burden and avoid another PPP run, the ESMs for stations can be estimated from the preparative orbit determination run in *Step 1* directly. In this case, however, possible reduction in the accuracy of the ESMs may occur due to additional estimation of satellite products, in particular, the clock biases, as reported by Moore et al. (2014).

In *Step 2* the impact of the ESM-corrected PCC on satellite orbits is assessed. This is done through two parallel orbit determination runs, in which the parameters estimated during *Step 1*, in particular, clock biases, ZTDs and station coordinates are imported. Thus, two orbit sets: one estimated using type-mean and another one using ESM-corrected antenna PCC, can be compared and the impact of the applied PCC on orbit determination using a global network of stations can be assessed.

Finally, to estimate the PCC impact on site positions, the orbits estimated from *Step 2* are used. In turn, this allows to achieve consistency in processing, as type-mean and ESM-corrected PCC are used with respective orbit sets. Again, parameters estimated during *Step 1*, in particular, clock biases and ZTDs are imported to eliminate the potential absorption of PCC modelling errors by these estimates. This part of the entire processing sequence corresponds to *Step 3* in Figure 5.12. Thus, the obtained station coordinates in both runs can be compared. To conclude, the processing sequence in Figure 5.12 allows to completely eliminate potential absorption of PCC-induced effects

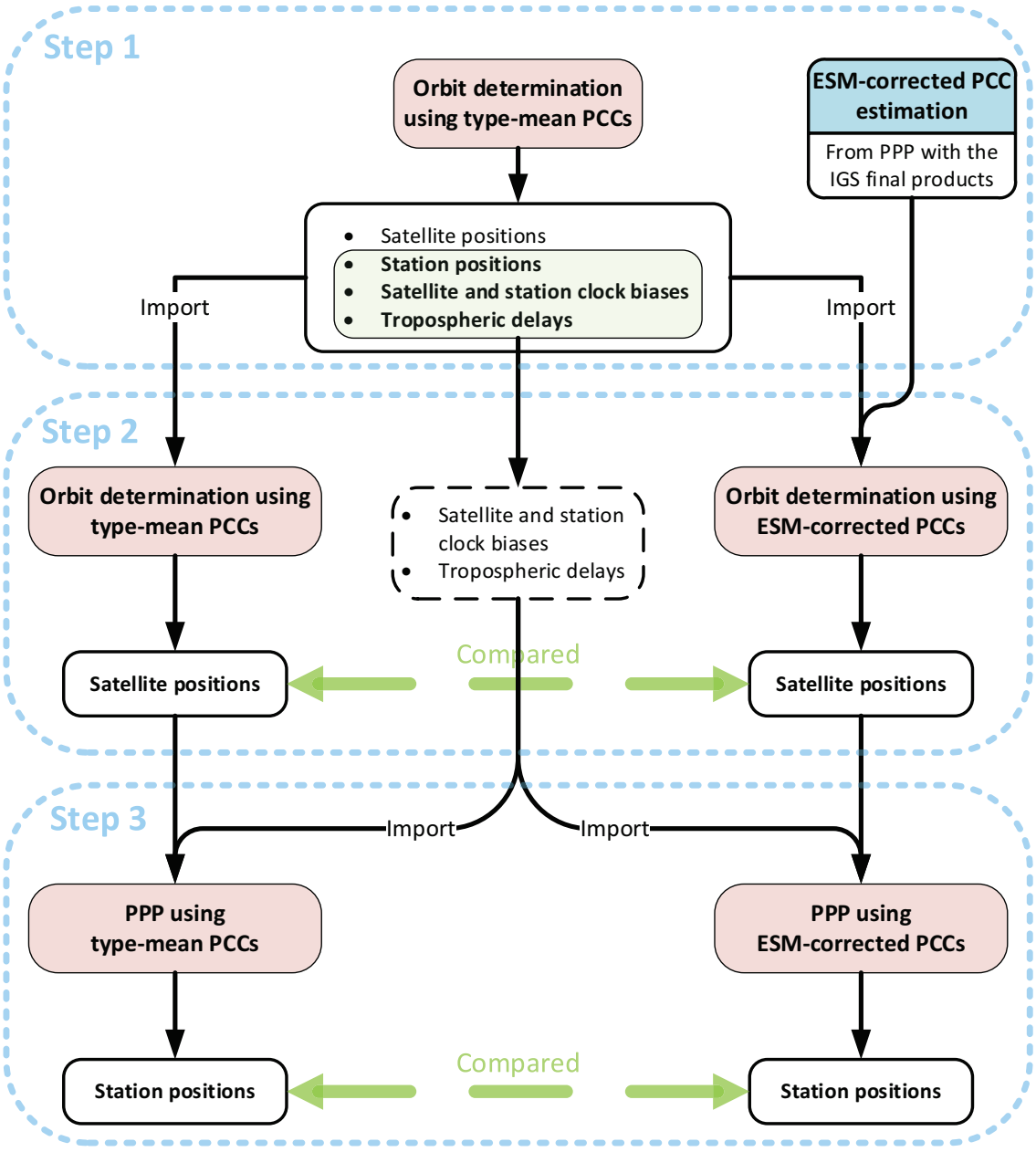

Figure 5.12: Processing sequence that minimizes absorption of the effect from PCC modifications by ZTD, clock and station position estimates. Three steps show the way to assess the effect of PCC on satellite orbits and station PPP coordinates.

by troposphere and clock biases.

The results of the ESM application will be discussed in details in Chapter 7.

5.8 Null test

Before weighing the performance of PCC models, a test involving orbit determination was performed to assess to what extend GNSS products are affected by modifications in the PCC models. The test was comprised in producing GPS orbits using a global network of stations once with type-mean PCC and second time after having those altered. In particular, for each antenna/radome combination only the constant part of the PCC, the PCO, was applied, whereas the variable part, PCV, was neglected. The aim of this test was to provide an indication of how the application of fine-tuned individual PCC and ESMs would impact the solutions. As the individual PCC in this study are available mostly for stations in Europe, the proposed test should refer to the application of ESMs on a global scale.

For this processing a global network of stations consisting of the IGb08 core network and additional stations in Europe was used. The coordinates for the IGS stations were tightly constrained to the official IGb08 coordinates, propagated to the processing epochs using official IGb08 velocities. A priori coordinates for the EPN stations were extracted from official EPN solutions. Coordinates and velocities for stations not taking part in IGS or EPN were estimated using PPP with the IGS final products. All observation data were sampled every 300 s, ZTDs were estimated every 3600 s and tropospheric gradients were estimated once a day. The GPS orbits were computed from 2004 to 2014 only applying PCOs for all stations.

Finally, the orbit DBD were estimated according to the methodology described in Section 5.3. The DBD for each satellite were computed and Lomb-Scargle periodograms (Lomb, 1976; Scargle, 1982) were obtained for each time series and orbital component separately. In order to allow more contribution to less noisy time series the periodograms of respective components were weighted according to the inverse of the time series variances and then combined. This was done separately for each solution. Then the results were compared to those obtained with type-mean PCC and introduced in Section 6.3.1.

Figure 5.13 demonstrates the results of the spectral analysis. Thus, the power spectra of both solutions show sharp peaks at frequencies matching $1.04 \times n$ cpy, where $n = 1, 2, 3, 4, \ldots$ (Figure 5.13a). However, the power spectra of the solution with the altered PCC appears to be noisier, which is expected. In order to highlight the differences between the power spectra of the two solutions, their ratios for respective components were computed (Figure 5.13b). While the higher frequencies (> 10 cpy) show elevated noise in the altered solution in all orbital components, their behaviour at lower frequencies is different. Interestingly, the radial component appears to

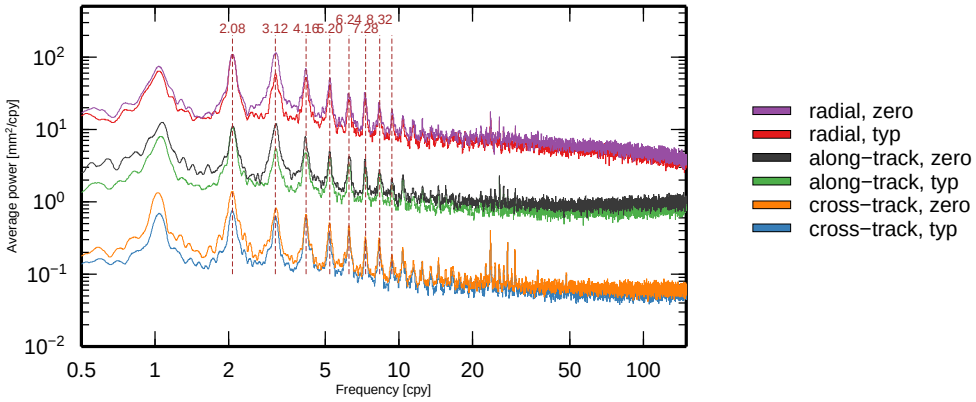

(a) Power spectra of the orbit DBD time series for radial, along- and cross-track components for 2004-2014 computed using type-mean and altered PCC. For clarity radial and cross-track components have been shifted by +20dB and −20dB, respectively.

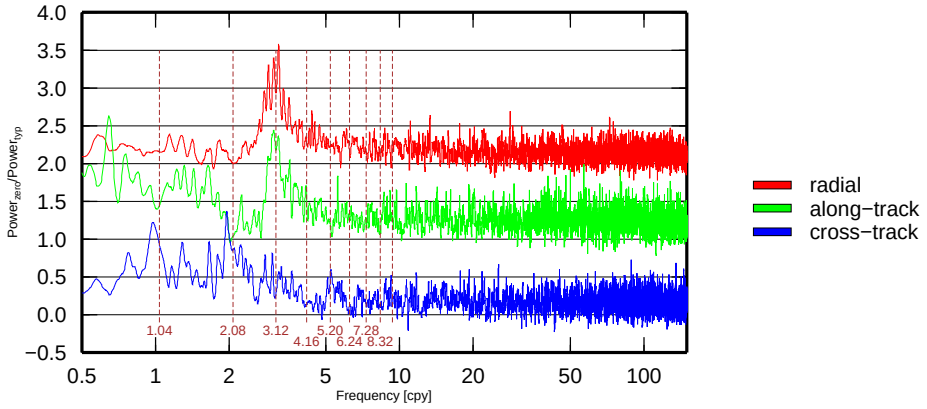

(b) Ratios of the power at respective frequencies the orbit determination runs using altered and type-mean PCC. Radial and cross-track components are shifted by +1 and −1, respectively.

Figure 5.13: Orbit DBD power spectra with altered and type-mean PCC and their ratios.

be very little affected at low frequencies (< 2 cpy). At the same time, the along- and cross-track components in the same frequency range are affected much stronger. In particular, both components show elevated power close to 1.04 cpy. Additionally, the cross-track component is affected at ∼2.08 cpy. Noteworthy is the power amplification at ∼3.12 cpy for both the radial and along-track components.

Thus, as both individual PCC and the ESMs are refinements of the type-mean PCC, their application may affect the entire frequency range. At the same time, as demonstrated by the results of the null test, the largest improvement is expected at the lower frequency range (< 5 cpy). In turn, the improvements in satellite orbits should have a positive impact on station coordinates.

5.9 Summary

A software package for GNSS data processing (NAPEOS) was introduced. In this study NAPEOS is used to produce solutions with different sets of antenna/radome PCC for further assessment. The basic functional elements of NAPEOS were introduced and the processing sequences for PPP and orbit determination were discussed.

In order to evaluate the quality of produced orbits, a method based on successive orbit overlaps at day boundaries (day boundary differences; DBD) was introduced. The DBD time series of GPS orbits computed with different sets of PCC will be a basis for further assessment.

To address the problem of multipath and site-specific effects, a method to correct for these effects through development of ESMs was discussed in details. In order to adapt the method for NAPEOS, the reconstruction of the GPS L_1 and L_2 phase residuals from the ionosphere-free linear combination (L_3) is required. To provide smoothing and simplify further usage, spherical harmonics representation of the obtained post-fit phase residuals is employed. Finally, the methodology for the ESM estimation on a global scale was suggested.

Additionally, strategies for PCC and ESM impact assessment for orbit determination and PPP were discussed. While the ESM can be produced and evaluated on a global scale, no issues are expected in the respective orbit determination scenarios. However, the number of stations with individual PCC is limited, making the orbit determination challenging. To overcome this difficulty, several scenarios for orbit determination using a regional network were suggested. All proposed strategies target achieving consistency in solutions.

In order to highlight performance of the assessment, a test with altered PCC was performed. In particular, PCOs were used for all stations, whereas PCV were neglected. The analysis of the orbit DBD time series obtained with the altered PCC showed that deficiencies in the PCC models may contribute to harmonic signals observed in GNSS solutions. However, the main contribution from applying individual PCC and ESMs is expected at lower frequency range (< 5 cpy).

Chapter 6

Evaluation of Antenna PCC Models

This chapter assesses the performance of antenna-specific (individual) antenna/radome PCC compared to that of the IGS type-mean models. In particular, the impact on computed satellite orbits and station coordinates is analysed.

Firstly, the impact of applied PCC on station coordinates is evaluated through assessing sub-daily position estimates. Then analysis of the impact on precise orbit determination is performed. As the correctness of the orbit determination sequence discussed in Section 5.2.2 is crucial, it is rigorously validated. Due to the geometry of the employed network of stations different strategies for orbit determination are evaluated and the obtained results are discussed. Finally, daily PPP results obtained using type-mean and individual antenna/radome PCC are assessed.

6.1 Introduction

As was shown in Chapter 3, individual PCC may significantly deviate from the corresponding type-mean models. As a consequence, these modelling errors should propagate into both sub-daily and daily solutions, leading to biases and harmonic signals.

Due to non-uniformity of the satellite sky distribution with respect to a user, the estimated parameters at the receiver side (e.g., coordinates, ZTDs, etc.) may be expressed as a function of the constellation change with time. In case of GPS, which was designed in such a way that the satellite ground tracks repeat every sidereal day (SD), this function is periodic with frequency $\frac{1}{1SD}$. As errors in PCC modelling as well as multipath are direction-dependent, together with the repeating satellite sky distribution this leads to generation of harmonic signals in the time series of parameters that are estimated. These harmonic signals may be observed in, e.g., station CTS (Sidorov and Teferle, 2016). Furthermore, aliasing of these high frequency signals may result in longer period artefacts that contribute to draconitic signals in solutions discussed in Chapter 2.

6.2 Sub-daily PPP results

In order to verify how deficiencies in station PCC propagate in sub-daily solutions, the GPS data of the SPSLux stations were processed and hourly PPP solutions were obtained for 01/01/2011 –

31/06/2011. While station parameters were estimated, the IGS final products, in particular, satellite orbits and clock biases were used and kept fixed. The tropospheric delays were estimated every hour. To account for the azimuthal variation of tropospheric delays, gradients in the east and north directions were estimated once a day. The observation data were sampled every 30 s, however, the elevation cutoff angle for observations was set to 10° during routine operations at the receiver level, thus, limiting the amount of collected observations.

The data for the aforementioned period were processed using the IGS type-mean and individual PCC. The obtained coordinate solutions were converted from Cartesian to topocentric and analysed. In each time series the outliers defined by a tolerance of ±4 times the interquartile range (IQR) were removed. Statistical data on solutions computed over 181 days are summarized in Tables 6.1 and 6.2.

As can be seen, the changes in the employed antenna calibrations result in shifts in the solutions, which are below 1 mm for the horizontal components, but may reach much larger values for the vertical component. While BASC and TROI demonstrate small (below 1 mm) shifts in the vertical component, ERPE and ROUL show shifts ∼1.5 mm. At the same time, the change of PCC resulted in −4.14 mm and 7.20 mm shifts in the vertical component for ECHT and WALF, respectively. There appears to be no correlation between the shift magnitude in the horizontal and vertical components. The magnitudes of observed shifts, in particular, in the vertical direction

Table 6.1: Mean shifts [*mm*] in sub-daily 1-h solutions of the SPSLux stations after switching from type-mean to individual PCC over 01/01/2011 – 30/06/2011.

	BASC	ECHT	ERPE	ROUL	TROI	WALF
north	0.51 ± 0.65	-0.48 ± 0.63	-0.28 ± 0.53	0.23 ± 0.48	0.03 ± 0.60	0.19 ± 0.60
east	-0.18 ± 0.61	-0.57 ± 0.71	0.06 ± 0.66	-0.76 ± 0.72	0.06 ± 0.68	-0.38 ± 0.81
up	-0.72 ± 1.96	-4.14 ± 2.40	1.54 ± 1.39	1.65 ± 2.02	-0.78 ± 1.76	7.20 ± 2.43

Table 6.2: RMS [*cm*] of sub-daily 1-h solutions for the SPSLux stations computed using type-mean and individual PCC for 01/01/2011 – 30/06/2011.

	BASC	ECHT	ERPE	ROUL	TROI	WALF
$\text{north}_{\text{typ}}$	0.594	0.695	0.601	0.592	0.625	0.603
$\text{north}_{\text{ind}}$	0.597	0.705	0.608	0.601	0.635	0.606
east_{typ}	0.549	0.640	0.582	0.618	0.553	0.604
east_{ind}	0.566	0.656	0.600	0.632	0.569	0.613
up_{typ}	1.619	1.480	1.657	1.437	1.528	1.562
up_{ind}	1.593	1.503	1.703	1.440	1.562	1.578

are unexpected considering that all stations employ antenna/radome combinations of the same model. Such large deviations in the vertical are partly due to the estimated tropospheric delays, which are highly correlated with station heights. Fixing the tropospheric parameters, as shown in Figure 5.9 reduces shifts in the vertical component by a factor of ∼2.5, suggesting differences in the estimated ZTDs in both solutions.

Table 6.2, in turn, discovers another peculiar observation: applying type-mean antenna calibrations resulted in slightly better repeatability of solutions, as expressed by the RMS, compared to solutions obtained with individual PCC. The degradation caused by the use of individual calibrations is very small (not more than ∼ 1-2%), however, it is observed for all 6 SPSLux stations. Only the vertical component of BASC shows some improvement in repeatability with individual PCC employed.

In order to assess if the use of different PCC contributes to generating harmonic signals in position time series, frequency analysis of each time series was performed using the Lomb-Scargle method. The power spectra of respective components were weighted according to the inverse of the time series variances and combined. This was done separately for solutions obtained using type-mean and individual PCC.

Figure 6.1 demonstrates the obtained combined power spectra, as well as the differences between them. The results are focused on the high frequency range, in particular, around diurnal and semi-diurnal frequencies. As one can notice, the "type-mean" and "individual" solutions, Figure 6.1a, are very similar. The largest power peaks in both solutions can be seen close to diurnal (365.25 cpy) and semi-diurnal (730.5 cpy) frequencies. Large contribution to these signals may be brought by deficiencies in the tidal models. Thus, the principal solar diurnal (P_1), lunisolar diurnal (K_1), principal solar semi-diurnal (S_2) and lunisolar (K_2) tidal constituents, having periods of 24.07 h, 23.93 h, 12.00 h and 11.97 h, respectively, may contribute to the signals observed in the time series. Other peaks that can be distinguished in Figure 6.1a, in particular, in the horizontal components, match the principal lunar diurnal (O_1) and semi-diurnal (M_2) tidal constituents, having periods close to 25.82 h and 12.42 h, respectively. The lunar elliptic (N_2) tidal constituents with a period close to 12.66 h, is not observed, however, it is still marked, as it belongs to a group of tidal constituents with the largest amplitude.

As ground track repeat periods of the GPS satellites are close to 23.93 h (Agnew and Larson, 2007), any improvement due to the antenna phase centre modelling is most likely to be discovered around 23.93 h or 11.97 h, thus, matching K_1 and K_2, respectively. Figure 6.1b, however, showing the ratio of the power values of the "individual" and "type-mean" results at respective frequencies demonstrates almost no changes around diurnal frequencies. On the other hand, large power spectra variations due to the PCC changes are observed around M_2, S_2 and K_2.

Table 6.3 provides the exact power values at the GPS orbital frequencies, as well as at

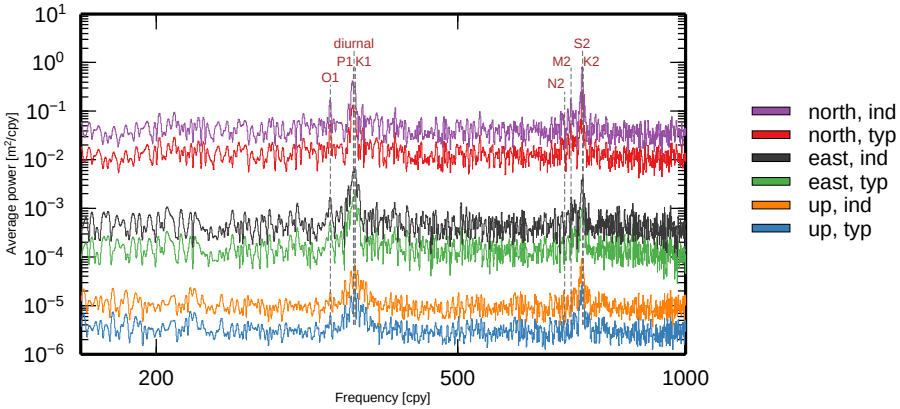

(a) Combined power spectra of 1-h solutions obtained for the SPSLux stations using type-mean and individual PCC for 01/01/2011 – 30/06/2011. For clarity north and up components have been shifted by +40dB and −40dB, respectively. Additionally, the "individual" power spectra are shifted by +10dB with respect to the corresponding type-mean results.

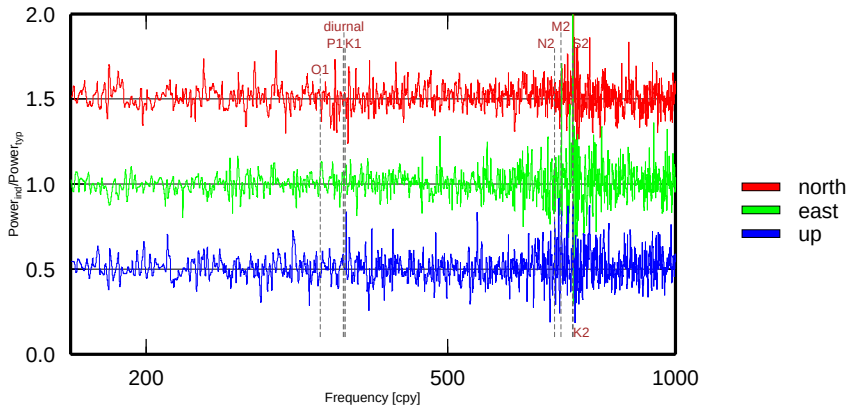

(b) Ratios of the power at respective frequencies in the "individual" and "type-mean" PPP runs. North and up components are shifted by +0.5 and −0.5, respectively.

Figure 6.1: "Type-mean" and "individual" sub-daily PPP power spectra and their ratios.

Table 6.3: Power values [$\times 10^{-2}$ m^2/cpy] at dominating frequencies for 1-h solutions computed using type-mean and individual PCC for 01/01/2011 – 30/06/2011.

	O_1 24.82 h	P_1 24.07 h	diurnal 24 h	K_1 23.93 h	N_2 12.66 h	M_2 12.42 h	S_2 12 h	K_2 11.97 h
$\text{north}_{\text{typ}}$	0.530	0.969	0.995	0.945	0.088	0.523	2.375	0.565
$\text{north}_{\text{ind}}$	0.536	0.937	1.011	0.964	0.082	0.537	2.264	0.881
east_{typ}	0.506	1.727	1.781	1.941	0.162	0.497	0.940	0.415
east_{ind}	0.538	1.766	1.793	2.100	0.176	0.512	1.077	0.834
up_{typ}	0.631	0.946	1.983	1.993	0.163	0.246	2.358	1.847
up_{ind}	0.603	1.023	2.003	1.994	0.198	0.272	2.344	2.491

frequencies of the aforementioned tidal constituents. While for the majority of the discussed tidal constituents a very little change (usually amplification) in their power is observed, large variations are seen for K_2, or the half-sidereal frequency. Thus, changes in the PCC result in large amplification (up to a factor of 2) of the power at this frequency in both horizontal and vertical components. No explanation of this phenomena could be provided.

Although deviations of individual PCC from the type-mean models for the antennas analysed are substantial, they seem to have a minor impact on harmonic signals that are seen in station PPP CTS in this particular example. The only exception was observed at signals with 11.97 h periods, as their power has increased after the PCC switching by up to a factor of 2.

As was shown on sub-daily solutions, applying the individual instead of type-mean PCC did not result in improvements of the coordinate solution repeatability. Conversely, the RMS of the sub-daily station CTS has increased after the PCC switching. Although the increase is in the order of only 1-2%, it is unforeseen as a fact. A possible explanation of the observed effect may be in large deviations of the actual antenna phase centres from their modelled values due to site-specific effects and multipath. Application of site models that account for this effect will be addressed in Chapter 7.

On the other hand, the shifts that are observed in all coordinate components after switching the PCC are more spectacular, as both horizontal and vertical components are affected. Although in horizontal these were below 1 mm for all stations, the observed vertical shifts reached 7.2 mm. Certainly, changes in the PCC have an impact on the tropospheric estimates and the observed shifts in station positions are partly attributed to uncertainties in the estimated ZTDs. Thus, special care needs to be taken due to the correlation between the PCC and tropospheric estimates.

6.3 Validation of the orbit determination sequence

In order to show the performance of NAPEOS and to justify the processing sequence and settings of individual routines discussed in Section 5.2.2, orbit determination for GPS satellites was performed for a period of 10 years, in particular, between 2004 and 2014. The employed network consisted of the IGb08 core network to ensure global coverage and uninterrupted, simultaneous satellite tracking by multiple stations complemented by additional stations from the EPN, GeoNet, SPSLux and NRCan networks. In particular, these additional stations represented those discussed in Chapter 4. The orbit determination sequence accurately followed the one discussed in section 5.2.2, including settings for individual routines.

A priori station coordinates and velocities for the IGS stations were extracted from the official IGb08 solution[1]. For the EPN class A stations coordinates and velocities were obtained from the official IGb08 realization, which is available at the EPN central bureau FTP[2]. However, for the other stations, e.g., remaining EPN, GeoNet and SPSLux stations, coordinates in the IGb08 reference frame were not defined. To overcome this problem PPP processing with the IGS final products was performed for these stations. Then for each station the computed coordinates were averaged to obtain accurate positions at midpoints of respective processing intervals, whereas their velocities were estimated using the GNSS Coordinate Time Series Analysis (CTSAna) Tools (Teferle, 2013; Williams, 2008). Thus, an accurate and consistent set of coordinates and velocities was obtained for all stations within the processing network. These data were used as tightly constrained a priori coordinates in the consecutive orbit determination runs.

6.3.1 Orbits

In order to assess the quality of the produced orbits, these have been compared to the IGS final orbits, as this is done by `OrbComp`. Results of this assessment are demonstrated in Figure 6.2, which shows excellent agreement (RMS is generally below 2 cm) between the computed and the reference orbits. Outliers in Figure 6.2 are associated with manoeuvres of particular satellites, which were not taken into account during processing, and consequently, which resulted in elevated RMS of the differences for the days when these manoeuvres took place. Since the combined RMS of the differences shown in Figure 6.2 is computed as the average of all differences between respective satellites, sudden increase in the RMS for one satellite leads to the increase of the average RMS of that day. Overall for the period from 2004 until 2014 there were 29 days with RMS $>$ 50 mm. After excluding these days the average combined RMS between the computed and the IGS final orbits for the aforementioned period was 18.6 mm. These results reach the level of orbit agreement

[1] available online at `ftp://igs-rf.ign.fr/pub/IGb08/IGb08.snx`

[2] `ftp://epncb.oma.be/epncb/station/coord/EPN/EPN_A_IGb08.SNX.Z`

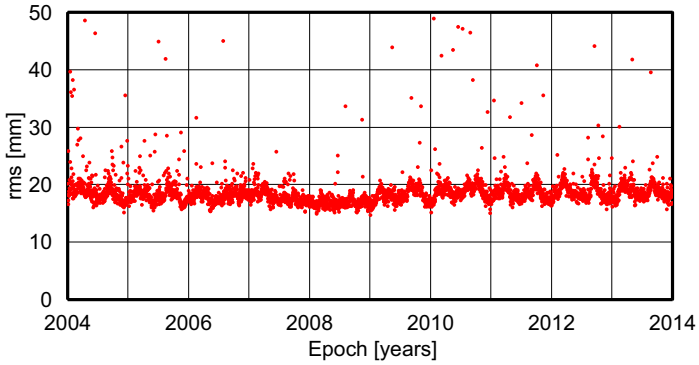

Figure 6.2: Combined RMS of the differences between the computed and the IGS final orbits.

between different ACs in the IGS solution combination (Kouba, 2009).

The computed RMS of the differences shows annual periodic variations, which disappear between 2007.5 and 2009. This suggests that the observed variations are potentially associated with solar radiation pressure modelling, as the last minimum of solar activity was observed in 2008-2009.

The IGS final products represent a combination of solutions of different ACs. After the IGS final orbits are computed, transformations of each AC orbital solution to the combined product are estimated using 7-parameter Helmert transformations. This information is then published on the IGS Central Bureau (CB) FTP server in summary files. On the other hand, `OrbComp` also provides transformations of the computed orbits to a reference solution. As the reference is the IGS final orbit in this example, direct comparison of the Helmert transformation parameters produced by `OrbComp` and those published in the IGS summary files can be performed.

Time series of Helmert transformation parameters for CODE, ESA and the computed orbits to the IGS final solutions are presented in Figure 6.3. Daily transformation parameters for CODE and ESA are presented only after GPS week 1400, whereas for the computed orbits these were estimated for the entire period from 2004 until 2014. As can be seen, the time series of Helmert transformation parameters of the computed orbits show stability and behaviour similar to the other two ACs. The z-translations of the computed orbits experience periodic variations with a fairly large amplitude. The same can be observed for the CODE and ESA solutions for 2011-2014 and 2007-2008, respectively. It should be noted that the two ACs introduced modifications to their processing over time, leading to the observed changes in the Helmert transformation parameters. Alternatively, the orbits in this study were computed with the same settings for the entire processing interval. Furthermore, although the computed orbits demonstrate good quality compared to the IGS final ones, it should be noted that rotations and scale are noisier than those for the other ACs. This can also be explained through variable settings of other ACs or through

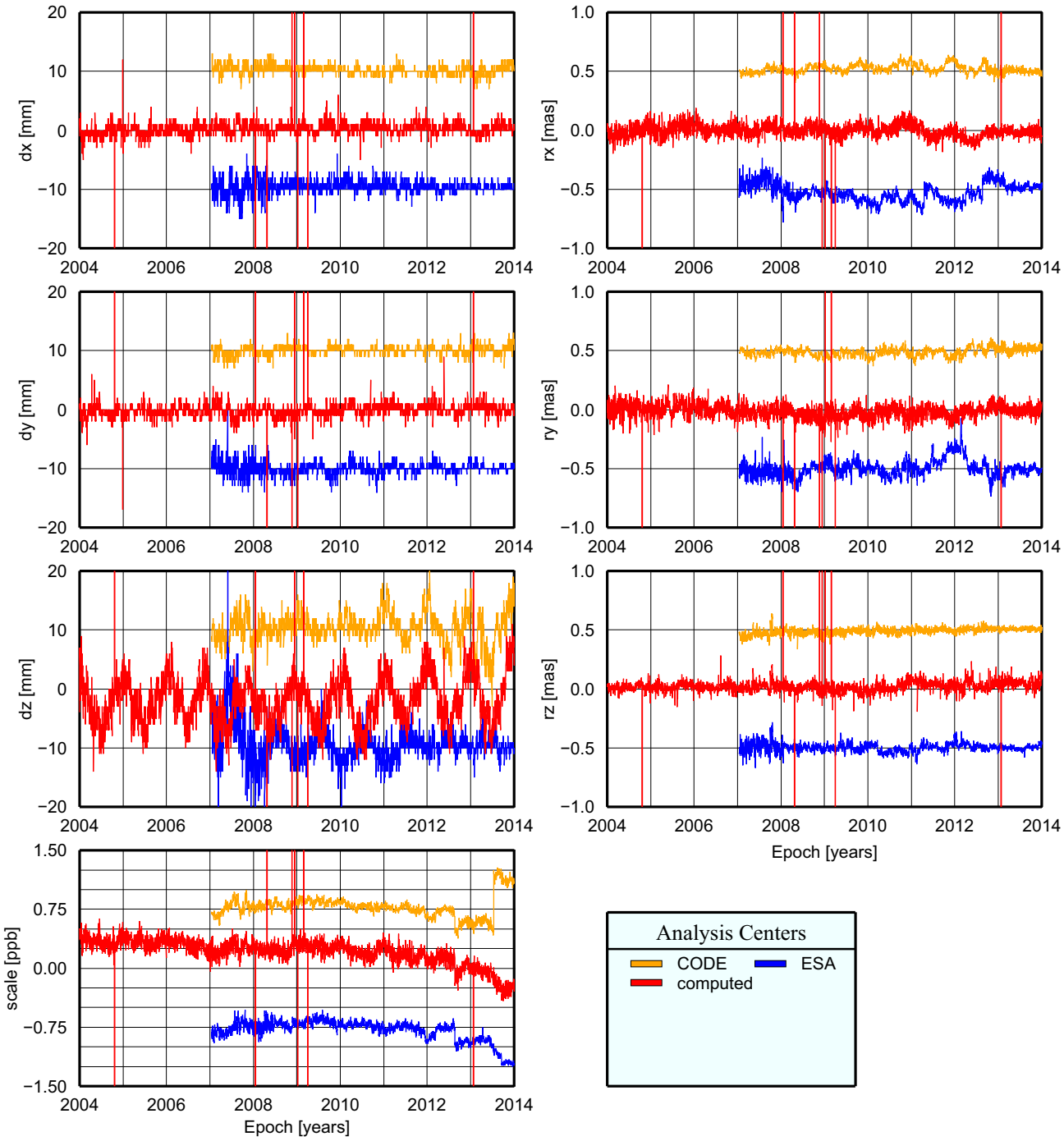

Figure 6.3: Helmert transformation parameters of CODE, ESA and the computed orbits to the IGS final solutions. For clarity, translations, rotations and scale for CODE and ESA were shifted by +10 mm and −10 mm, +0.5 mas and −0.5 mas, and +1 ppb and −1 ppb, respectively.

the fact that both CODE and ESA solutions have large weights during the combination performed by the IGS.

Thus, despite some days with outliers that result in large RMS of the differences between the computed and the IGS final orbits and that are noticeable in the time series of the discussed Helmert transformation parameters, it can be concluded that the quality of the obtained orbits is comparable to that of the IGS ACs. In turn, this suggests that the orbits computed with NAPEOS in this study using the procedure discussed in Section 5.2.2 can be used for further analyses.

6.3.2 Clock products

Only orbit differences between the IGS final and computed orbits have been discussed so far. The quality of satellite and receiver clock biases, as well as tropospheric estimates is important and, therefore, has to be considered. `ClockComp` provides a functionality to compare two sets of clock biases. These are compared between respective stations and satellites common in both files. Analogous to the orbits, the IGS final clocks were taken as a reference and the difference between the computed and reference satellite clocks was assessed.

Figure 6.4 demonstrates daily mean differences for the GPS satellite clocks for the period from 2004 until 2014. At this point it should be noted that in this processing the igs08_1793 type-mean PCC models (igs08_1793.atx) were used throughout the complete period, whereas for the IGS products different, constantly evolving PCC models were employed. These changes in the used PCC models between the two product sets have resulted in evolution of the differences in the estimated satellite (as well as receiver) clock biases. One of the most noticeable changes occurred in the first half of 2011, in particular, on 17^{th} April – the date when the IGS switched from the use of the IGS05 to IGS08 PCC models in its routine processing (Rebischung, 2011), leading to a sudden jump in the estimated satellite (and receiver) clock differences. This correlates with approx. -1 ppb[3] scale difference between the IGS08 and IGS05 reference frames. Overall, the estimated satellite clock biases remained very stable with respect to the IGS final products for the entire period from 2004 until 2014.

performed The Saastamoinen a priori tropospheric zenith path delay model along with the GMF and GPT were used. Additionally, corrections due to the wet path delay to these a priori values as well as the gradients in East and North directions were estimated.

[3]part per billion; 1 ppb on the Earth surface corresponds to ∼6.4 mm

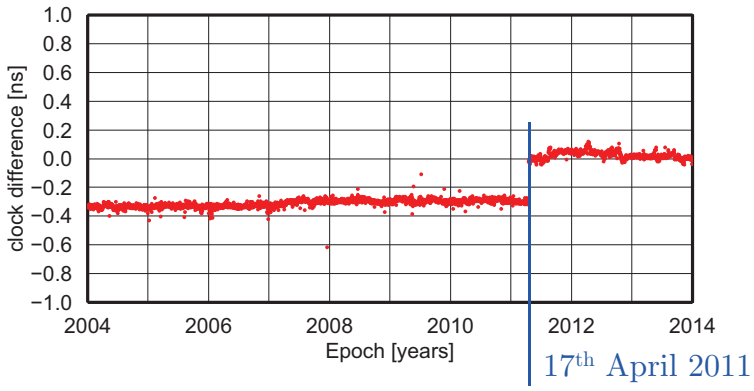

Figure 6.4: Daily mean differences between the GPS satellite clocks in the IGS final and computed products. Jump on 17^{th} April 2011 corresponds to a switch from the IGS05 to IGS08 PCC.

6.4 Orbit determination using a regional network

An experiment was set up to answer a question if modifications in the applied PCC, in particular, when switching from type-mean to individual antenna models, are noticeable in satellite orbits. Despite the seemed obviousness of the answer, it is not clear to what extent the orbits are affected, as the ground antenna influence may be averaged or even vanished when the number of employed antennas is big and their distribution is global and uniform. At the same time, the used network of stations with individual PCC, which covers only a limited part of the globe, in particular, Europe, may not give a trusted answer.

In order to investigate the impact of GNSS antenna phase centre corrections on satellite orbits, a set of sites that have individual calibrations was composed. In particular, stations discussed in Chapter 4 and shown in Figure 4.1 were used. These are mostly located in Europe with two sites in the North America and one on South Georgia island, belonging to the EPN, GeoNet, SPSLux and NRCan networks. GNSS processing was performed using NAPEOS as discussed in Section 5.2.2. As the phase ambiguity fixing improves the quality of the results and due to the ambiguity resolution mechanism employed in NAPEOS, which is performed on the network basis, it is beneficial to use a network of relatively closely located stations. Experience showed that the ambiguity fixing success rate reached 90% and above when the number of stations across an area similar to, e. g., Europe, is at least 4-5. This, in turn, has defined the lower border of the time frame to be January 2004. Before 2004 the number of stations having individually calibrated antennas is very low. However, during 2004 the number of stations having individual calibrations within the aforementioned networks has grown from 2-3 to 6 in the beginning and end of 2004,

respectively.

One satellite (SVN-49) was not processed due to signal anomalies, with which GNSS users were facing during its complete in-service period. More details about the satellite issues can be found in, e.g., Hauschild et al. (2012) and Thoelert et al. (2012). Due to the observed anomalies in the received signals from the satellite, SVN-49 was excluded from processing for the entire period.

The GPS broadcast ephemeris, which are known to be accurate to ∼1 m, were used as a priori satellite orbits. The observation data were sampled at 300 seconds intervals. Accordingly, such sampling rate has allowed to produce solutions every 300 seconds. Thus, a set of three parameters, in particular, position, velocity and clock was computed for each satellite and for each epoch with 300 seconds sampling on a daily basis from 00:00:00 until 23:55:00. The station clock biases were estimated at the same sampling rate. For each station used in the processing, accurate a priori coordinates in the IGb08 reference frame were computed. These coordinates were tightly constrained by applying $\sigma = 10$ mm. Additionally, ZTDs and two tropospheric gradients (in the north and east directions) were estimated every 1 and 24 hours, respectively. Taking into account the geometry of the network, it is fair to assume that the computed orbits had higher accuracy over those areas where the satellites could be observed, whereas orbit propagation was performed for the rest of the orbital arcs.

Initially, orbit determination was performed only using the network of stations discussed above, however, analysis of results suggested to implement two modifications to the processing: add complementary stations and introduce additional constraints through limiting parameter estimation. Thus, orbit determination was performed for three *cases*: only using stations that have individual calibrations, adding a sparse and uniform network of globally distributed stations and limiting the number of estimated parameters. In each *case* satellite orbits were estimated twice: applying the IGS08 type-mean (igs08_1793.atx) and the antenna-specific (individual) PCC. In each processing run all other parameters within the NAPEOS software were kept identical. Finally, satellite positions at the day boundaries were extracted, their differences were computed as discussed in Section 5.3 and corresponding time series were created. These time series from the "individual" and "type-mean" runs were compared.

6.4.1 Case 1: Regional network

This section discusses results of the GPS orbit determination for the period from 2004 until 2014 using only the set of stations with individual calibrations, discussed in Section 4.2.

Figure 6.5 shows the evolution of the number of stations that had individual antenna calibrations and, consequently, that were used for orbit determination, as well as the number of satellites observed by these stations. Due to the increasing amount of stations and broadening network geometry the amount of simultaneously observed satellites has grown from 27-28 to 31 in 2004

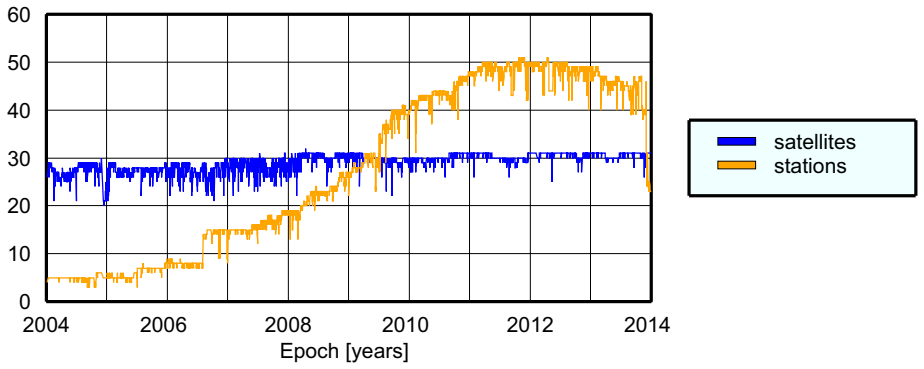

Figure 6.5: Number of observed satellites and number of stations that have individual PCC and that were used for orbit determination.

and 2013, respectively.

As mentioned previously, due to the NAPEOS mechanism of ambiguity resolution, the number of stations within the observation network affects the ambiguity resolution success rate. Percentage of successfully resolved ambiguities is demonstrated in Figure 6.6. During the period from 2004 until 2014 the ambiguity fixing percentage has grown from ∼75% to ∼95%. In turn, this agrees with the amount of stations used for the period.

It needs to be pointed out that orbit improvement in this case was performed only within the area of visibility of the ground stations. This implies that the determined satellite orbital arcs should be fairy well estimated over Europe, whereas they are propagated over the rest of the globe, having no constraints through observations. Since at each epoch the GPS constellation ensures global coverage, at midnight of each day some of the satellites may pass over the regions where (in case of a regional network) no stations are present. As the orbit estimation in this case relies only on the accuracy of models used for orbit determination, this leads to the fact that the DBDs in the orbits may become very large and, thus, the effect from the use of different PCC is hidden.

Figure 6.7 provides more explanations of the problem by demonstrating the time series of the DBDs for PRN10 for three components: radial, along-track and cross-track. PRN10 was chosen because it has one of the largest amount of observations, and, consequently, does not have gaps in the shown time series. A similar picture is observed for other GPS satellites. Although Figure 6.7 demonstrates results using type-mean PCC, similar figure is observed for the scenario that employs individual PCC and, therefore it is not shown here.

One can notice that from 2004 until the second half of 2008 DBDs for this satellite may reach several kilometres. The reason for such large uncertainties in the estimated orbits is in the very low number of observations of the satellite during certain periods, resulting in extremely poor orbit quality. The picture improves when the network grows by including more stations, in

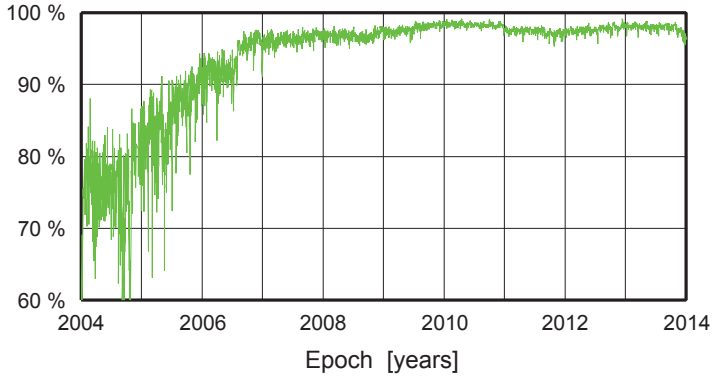

Figure 6.6: Percentage of successfully resolved ambiguities for the orbit determination scenario when only stations with individual PCC were used.

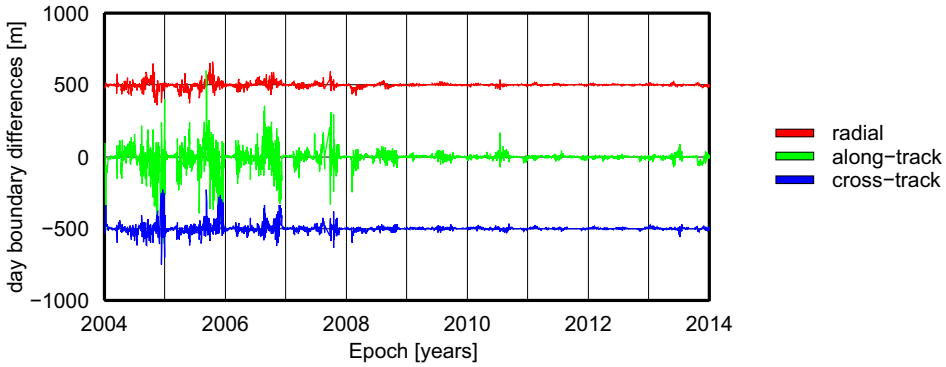

Figure 6.7: Orbit DBD for PRN10 for radial, along-track and cross-track components. The time series of the radial and cross-track components are shifted by +1000 and -1000 m, respectively. The *case* when only a regional network is used for the period from 2004 until 2014 with type-mean PCC applied.

particular, between July and August 2008 12 GeoNet and 2 UNOTT stations located in the UK were included. Additionally, in October and December 2010 two more sites located in the North America were added. This has resulted in a big improvement of the network geometry, allowing to reduce the DBDs from kilometres to meters in the beginning and the end of the processing period, respectively.

Despite the very large discrepancies in the orbit DBDs, as shown in Figure 6.7, the power spectra of the latter were analysed. For each satellite and each orbital component individual power spectra using the Lomb-Scargle method (Lomb, 1976; Scargle, 1982) were computed. Later the power spectra of respective orbital components were combined. In order to allow more contribution to less noisy time series, each time series was weighted according to the inverse of the variance. This was done separately for the "type-mean" and "individual" cases.

Due to noise in the time series of individual satellites (Figure 6.7) the obtained periodograms demonstrate high noise in all three components, Figure 6.8. Despite this, the periodograms reveal presence of power peaks at 1.04, 2.08, 3.12 cpy, or $1.04 \times n$ cpy, where $n = 1, 2, 3, 4, \ldots$, which points at the draconitic origin of these signals. The results for the "type-mean" and "individual" runs are very similar. The elevated noise in both solutions does not allow for reliable statement whether using the individual PCC brings any advantage over the type-mean PCC or vice versa. However, checking exact power values at the aforementioned frequencies gives an indication that the individual calibrations do have the potential to reduce draconitic errors in the orbits.

As seen from Table 6.4, applying individual PCC reduces power at frequencies corresponding to $n = 1, 2$ and 9 for all three components, whereas for other harmonics the improvement is not always noticeable. It is important to point out that the along-track component, being the noisiest, is improved for all shown n. The other two components do not follow the same tendency, showing improvement in some and degradation in the other frequencies. Coming back to the along-track component, its average improvement is the largest and reaches 4% for $n \leq 4$.

In order to assess the change across the entire frequency range, ratios of the estimated power values from the "individual" and "type-mean" runs were computed for respective frequencies. Figure 6.9 demonstrates the obtained ratios ($\frac{P_{ind}}{P_{typ}}$) plotted against frequency, showing a much more ambiguous picture. However, one can see that ratios for the along- and cross-track components for $n \leq 4$ and $n \leq 6$, respectively, most of the time are below 1, implying attenuation of corresponding frequencies when switching from type-mean to individual PCC. Alternatively, no apparent improvement is achieved in the radial component. With respect to the noise floor, no improvement is noticeable in any of the orbital components.

It is important to note that ratios for all orbital components show peaks around $n = 4.85$ cpy, which corresponds to 75.3 days. It it unclear, however, what are the reasons for amplification of the power at this frequency.

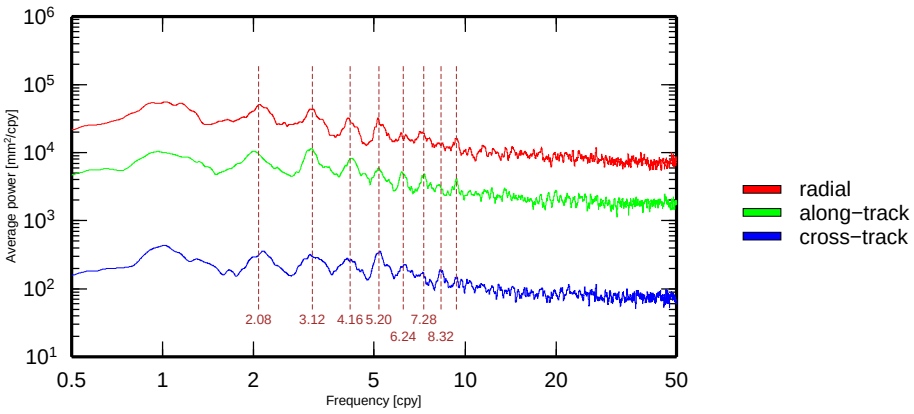

Figure 6.8: Power spectra of the orbit DBD from 2004 until 2014 for radial, along-track and cross-track components computed using the set of stations described in Section 6.4.1 applying type-mean PCC. For clarity radial and cross-track components have been shifted by +20dB and −20dB, respectively.

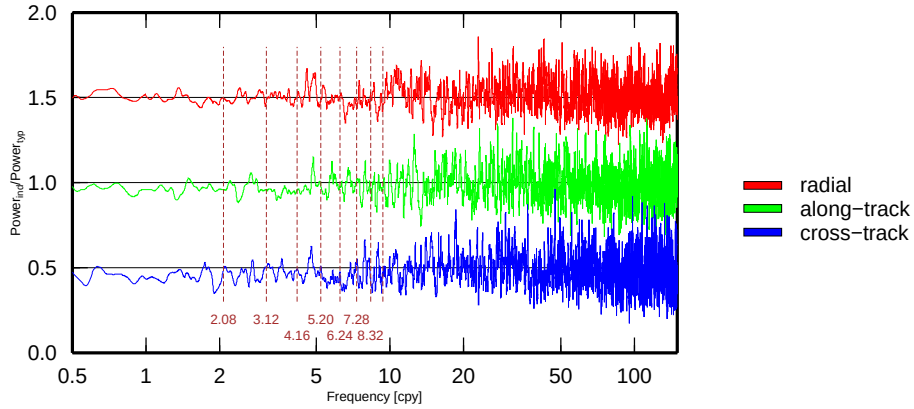

Figure 6.9: Ratios of the power at respective frequencies in the "individual" and "type-mean" runs in *case 1*. Radial and cross-track components are shifted by +0.5 and −0.5, respectively.

Table 6.4: The GPS orbit DBD power values $[mm^2/cpy]$ at harmonics of 1.04 cpy.

Component	Sol.	1.04	2.08	3.12	4.16	5.20	6.24	7.28	8.32	9.36
Radial	typ	5508	5097	4291	2990	2823	1560	1931	1261	1585
Radial	ind	**5452**	**5078**	**4244**	3009	**2789**	1570	**1838**	1302	**1513**
Along-track	typ	9860	9481	11 427	8072	5858	4835	4377	3034	4107
Along-track	ind	**9466**	**9090**	**10 936**	**7715**	**5777**	**4736**	**4365**	**2883**	**3989**
Cross-track	typ	4191	3160	3003	2570	3442	2170	1694	1812	1414
Cross-track	ind	**3952**	**3127**	3005	**2550**	3481	**2113**	1727	**1688**	**1349**

Bold indicates improvement in the "individual" solution with respect to the "type-mean".

Broad peaks in Figure 6.8 and the elevated noise floor in all components, suggest that higher harmonics ($n > 9$) of the GPS draconitic year may remain indiscernible, indicating that the full potential of the applied technique has not been reached.

To summarize, due to large discrepancies in the observed day boundaries, a different strategy should be developed, which would reduce the uncertainties in the estimated parameters and, therefore, contribute to the reduction of noise in the time series. At this point immense errors in orbit modelling hide the effect of differences in the applied PCC, suggesting that more constraints should be imposed on the estimated parameters. Although in low frequencies of the along- and cross-track components some improvement from using individual PCC can be seen, their benefits with respect to the type-mean ones are not convincing. The achieved improvements are minor, if any, moreover, sometimes even degradations are observed, e.g., for $n = 4.85$ cpy.

6.4.2 Case 2: Regional network supplemented with a sparse global network

In the previous section a problem resulting from underconstrained orbital solution was shown, implying that minimization of the day boundary differences had to be performed in order to see the effect of the different PCC. One way of imposing tighter constraints on the satellite orbits is to include more stations in the network, providing global tracking of the GPS satellites. At this point it should be noted that nearly all globally distributed GNSS networks, which provide data to the scientific community, have only type-mean PCC. This adjoins with the dilemma in ensuring global satellite tracking and not hiding the effect of the individual PCC on the orbits at the same time.

To balance between the need of global coverage and the possibility of tracing the effect of the differences in the PCC, a sparse network of globally distributed stations was defined. In addition to the list of stations having individual PCC, 11 stations belonging to the IGb08 core network were added, Figure 6.10. These stations were selected based on the availability of observation data and existence of well-defined coordinates in the IGb08 reference frame. A low number of supplementary stations in the network is important, as according to Figure 6.5 already starting from the middle of 2006 the number of stations with individual PCC becomes greater than 50% of the total number of stations in the network. This suggests that starting from the middle of 2006 stations with individual PCC may reach a significant weight in the network, allowing the assessment of their impact on solutions.

As expected, adding stations that are distributed sparsely and globally has a positive effect on the DBDs. Figure 6.11 demonstrates results for the same satellite, PRN10, “type-mean” run. Compared to the time series shown in Figure 6.7 the orbital DBDs have been reduced largely. Although more noise is observed in the beginning of the processing interval compared to its end, the orbit DBDs have decreased by more than 3 orders of magnitude: from several kilometres to

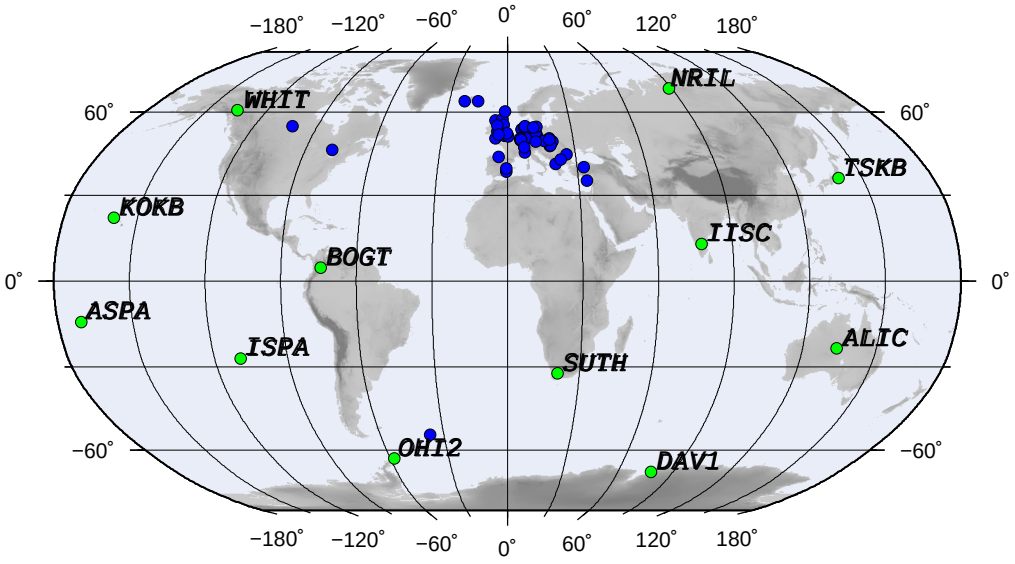

Figure 6.10: Processed network of stations with individual PCC complemented by 11 globally distributed stations, shown in blue and green, respectively.

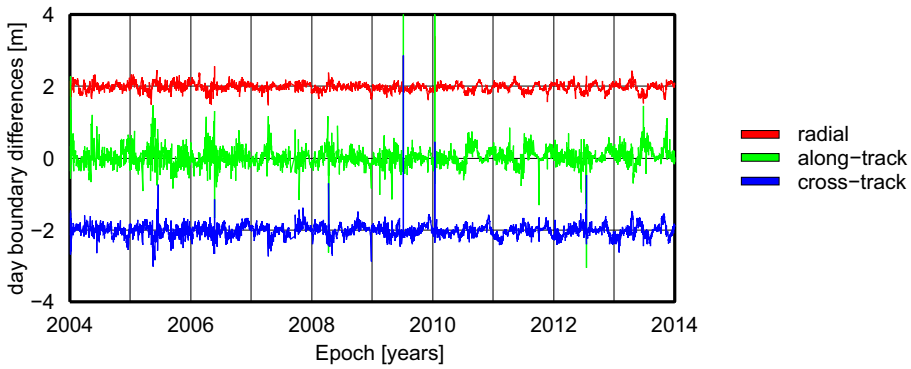

Figure 6.11: Orbit DBD for PRN10 for radial, along-track and cross-track components in *case 2*. The time series of the radial and cross-track components are shifted by +2 and -2 m, respectively.

meters.

In Figure 6.11 one can notice the presence of periodic variations in all components. Similar to *case 1* (Section 6.4.1), such pattern of the computed DBDs is common for all analysed satellites. In order to assess the frequencies of periodic signals seen in the time series, power spectra for each satellite were computed using the Lomb-Scargle periodogram, weighted according to the inverse of the variance and then combined. The employed technique was identical to *case 1*.

Similar to the "type-mean" run, the "individual" run was performed, in which individual PCC were used for the list of stations discussed in Section 4.2 and shown in Figure 4.1. Satellite orbits were again estimated, DBDs for each satellite were computed and the corresponding time series were analysed. The DBD time series of satellites obtained using individual PCC are similar to the "type-mean" case shown in Figure 6.11 and, therefore, not shown here. The same applies to the combined power spectra for each orbital component of the "individual" solution, which was computed in the same manner as in the "type-mean" case.

As followed from the improvements in orbit DBDs of individual satellites the obtained power spectra demonstrate power reduction across the entire frequency range, Figure 6.12. The peaks at frequencies corresponding to $1.04 \times n$ cpy, where $n = 1, 2, 3, 4, \ldots$, are much sharper compared to Figure 6.8 and can be identified up until $n = 14$ in the radial and cross-track components. Harmonics with $n > 10$ in the along-track component are less pronounced than in the other components and disappear with growing n.

Overall, supplementing the regional network with globally distributed stations resulted in a large improvement in the orbit DBDs, exposing the draconitic frequencies more clearly than

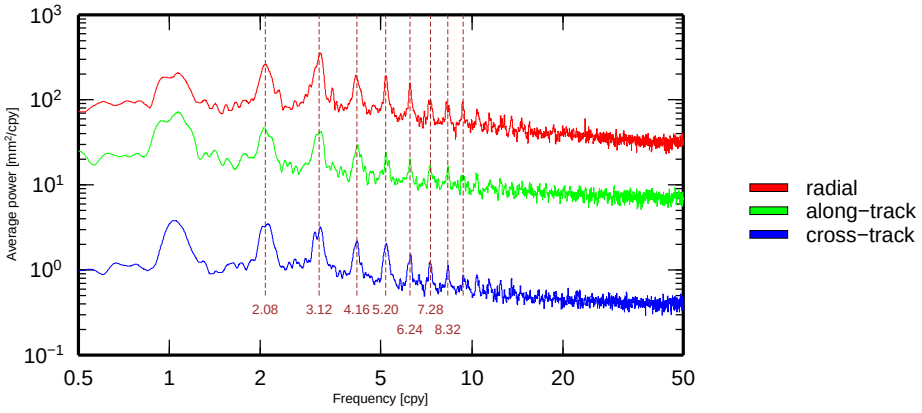

Figure 6.12: Power spectra of the orbit DBD from 2004 until 2014 of the radial, along-track and cross-track components computed using a set of stations described in Section 6.4.2 applying type-mean PCC. For clarity radial and cross-track components have been shifted by +20dB and −20dB, respectively.

before. However, the power spectra of both solutions, namely, the "type-mean" and "individual", are very similar to each other, not showing any positive effect from using the individual PCC. As seen from Table 6.5, the improvement in the along-track component observed in *case 1* has almost disappeared after adding globally distributed stations. The spectra demonstrate only very little decrease in power at individual harmonics of the GPS draconitic year, almost vanishing any benefits from using the individual calibrations.

Analogous to *case 1*, in order to quantify the effect of the ground PCC on the estimated satellite orbits for each frequency, the ratio of the power of the "individual" spectra to the power of the "type-mean" spectra at corresponding frequencies was computed. This was performed for each orbital component individually and the results are shown in Figure 6.13. In each orbital component the "individual" solution demonstrates both improvements and degradations at individual frequencies with respect to the "type-mean" one, however, neither positive, nor negative trend can be identified.

Table 6.5: Numerical values [mm^2/cpy] of the GPS orbit DBD power spectra at harmonics of 1.04 cpy.

Component	Sol.	1.04	2.08	3.12	4.16	5.20	6.24	7.28	8.32	9.36
Radial	typ	19.5	26.1	33.0	18.8	19.1	15.9	9.0	7.1	8.1
Radial	ind	21.2	27.1	**31.4**	**18.2**	**18.3**	**15.7**	9.2	7.7	8.1
Along-track	typ	67.6	45.4	40.9	28.4	24.1	20.2	16.8	16.1	12.3
Along-track	ind	**66.7**	46.1	**40.2**	29.2	**23.6**	20.5	17.5	16.7	12.7
Cross-track	typ	38.3	32.6	27.7	21.7	19.9	14.0	12.2	10.6	8.7
Cross-track	ind	38.4	**32.1**	28.0	**21.7**	20.0	**13.3**	**12.2**	10.8	**8.5**

Bold indicates improvement in the "individual" solution with respect to the "type-mean".

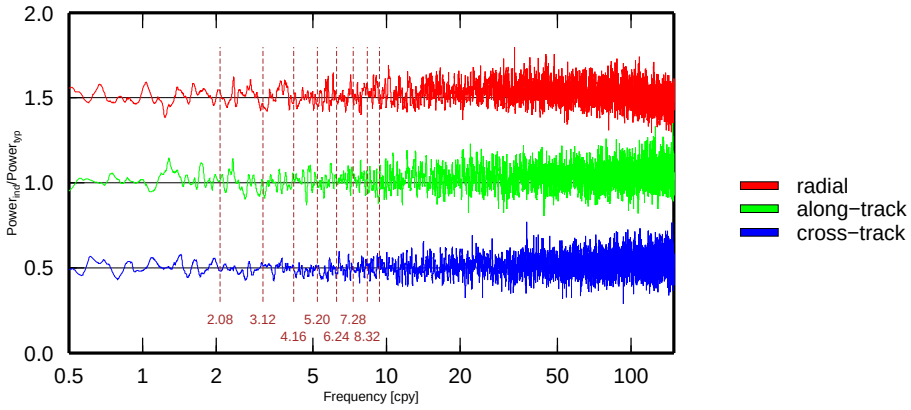

Figure 6.13: Ratios of the power at respective frequencies in the "individual" and "type-mean" runs. Radial and cross-track components are shifted by +0.5 and −0.5, respectively

Thus, the improvements due to switching from the type-mean to individual PCC observed in *case 1*, in particular, positive trends in attenuation of power at the draconitic frequencies have disappeared after adding globally distributed stations into the network. This indicates that the global stations with type-mean PCC start to dominate over the regional stations with individual PCC, even though the latter are in the majority. This may be explained through the network geometry shown in Figure 6.10, where stations with individual PCC are regionally clustered, and the orbit DBDs are analysed on a global scale. Thus, the effect from stations with individual PCC vanishes after the satellites leave the area of visibility of these stations. Even when a satellite is still visible, but is at low elevation, the effect of the applied PCC becomes imperceptible, due to the elevation-dependent weighting of the observations applied ($1/cos$). Thus, changes in PCC due to switching from type-mean to individual models at some stations have noticeable effect for only those satellites, which are located within a limited viewing angle. At the same time, multipath and other site effects that exist at stations may prevail over the differences in the applied PCC, resulting in large draconitic errors seen in both "type-mean" and "individual" solutions. As a consequence, this may explain why only small differences are observed between the two solutions. This suggests that a setup in which only part of the ground network equipped with antennas having individual PCC is not optimal to reveal advantages from using the improved PCC. On one hand, as was observed in *case 1*, the solution is too uncertain to make any judgement, alternatively, additional constraints imposed by supplementary stations start dominating over differences in the applied PCC.

Clearly, the approach that could provide an unambiguous answer would require a global network of stations with individual PCC. In addition to a good geometry, the network should provide data availability for a sufficient time span. Unfortunately, due to the lack of publicly available individual PCC for stations, this seems to be difficult to implement. At the same time it is important to consider multipath and other site effects that may dominate over the imperfections in the applied PCC and, therefore, the effect of the latter may remain difficult to reveal.

The results of this assessment show that, indeed, there exist differences in the estimated orbits, which are caused by the applied PCC. However, there is no clear evidence that applying individual antenna calibrations leads to attenuation of draconitic signals observed in these orbits. Furthermore, in the processing described above, tropospheric delays and clock biases, also being estimated, may absorb those changes in satellite positions that originate from the introduced PCC differences. Also, estimation of these parameters introduced additional uncertainty in the performed computations, resulting in elevated noise and, consequently, large DBD errors. In order to resolve the questions that arise from these findings, a thoroughly independent analysis of each estimated parameter should be performed. This is not a trivial task considering the complexity of the computations.

Another approach has been worked out aimed to bring more light on the problem. The new strategy involves constraining solutions through reduction of the number of parameters that are estimated. Thus, during processing some parameters can be kept fixed to a priori computed values. This will be discussed thoroughly in Section 6.4.3.

6.4.3 Case 3: Constraining solutions

In Sections 6.4.1 (*case 1*) and 6.4.2 (*case 2*) two sets of orbits were compared. These were produced using different PCC, in particular, type-mean and individual. However, while in *case 1* some benefits from switching the PCC were observed, no apparent advantage was observed from using individual antenna corrections in *case 2*. At the same time, it should be noted that during the aforementioned orbit determination runs in addition to satellite positions such parameters as, e.g., satellite and station clocks, tropospheric delays were estimated. Moreover, although tight constraints (σ = 10 mm) with respect to a priori coordinates were applied to station positions, these were still estimated. These parameters may mask the effect of PCC on the orbits due to absorption. Clearly, changes in PCC and the estimated tropospheric delays and clocks are correlated. Therefore, all these parameters are needed to be considered in order to assess the effect on satellite positions, making the task very complicated.

The estimation of troposphere and clock biases was limited through computation of these parameters in another orbit determination run using a global network of stations, as described in Section 5.7.1, Figure 5.11. Then the estimated tropospheric delays and clock biases for both stations and satellites were reused in the orbit determination runs with only a regional network.

To obtain accurate clock and tropospheric estimates for the network of stations, the GPS orbit determination was performed for the period from 2004 until 2014. As a base network for this preparative run the IGb08 core network was used, complemented by stations discussed in Section 4.2. The total amount of stations used in processing, therefore, ranged between 56 and 131 stations. The minimum amount of stations, 56, corresponds to 21 May 2012. For this day observation data for many stations were missing in the internal GNSS data repository of the University of Luxembourg. Such days when few observation data were processed, were rare, resulting in only 3 days out of 10 years processed when < 70 stations were used for orbit determination. This statistic considers also those stations, which were rejected due to, e.g., noisy data, little number of observations, etc. Consequently, occasions with few stations processed had very little impact on the estimated parameters. On average, for the discussed period, 103 stations were used for orbit determination on a daily basis. In this processing satellite positions, satellite and receiver clock biases, ZTDs (including north and east gradients) and station coordinates were estimated. The IGS08 type-mean PCC were used for all stations.

In fact, the exact orbit determination, during which the required parameters were estimated,

was discussed in Section 6.3. As was shown the estimated satellite orbits and clocks demonstrated high quality, whereas that of the other parameters was expected to be comparable.

Impact of PCC on satellite orbits

In order to assess the effect of the applied PCC on satellite orbits, the estimated parameters were introduced in two orbit determination runs that employed only stations with individual PCC that were discussed in Section 4.2. This part of the experiment corresponds to the *step 2*, shown in Figure 5.11. As mentioned previously, station positions, ZTDs (including north and east gradients) and satellite and receiver clock biases were kept fixed to the values obtained during the preparative run. Similar to the experiment discussed in Section 6.4.1 two different orbit determination runs were performed: one applying the type-mean and the other – individual PCC and results were compared.

Fixing satellite and station clock biases and ZTDs to accurately estimated a priori values considerably reduces the uncertainties in the computed orbits. This can be judged based on the orbit DBDs shown in Figure 6.14. In contrast to the *case 1*, Figure 6.7, where the clock biases and ZTDs were estimated, the RMS of the orbit DBDs shown in Figure 6.14 is largely reduced. Although Figure 6.14 demonstrates only results computed using type-mean PCC, those obtained using individual PCC are very similar and are not shown here.

To assess presence and power of harmonic signals in the obtained satellite positions, orbit DBDs for each satellite were analysed for the complete processed period. Again, the orbit differences

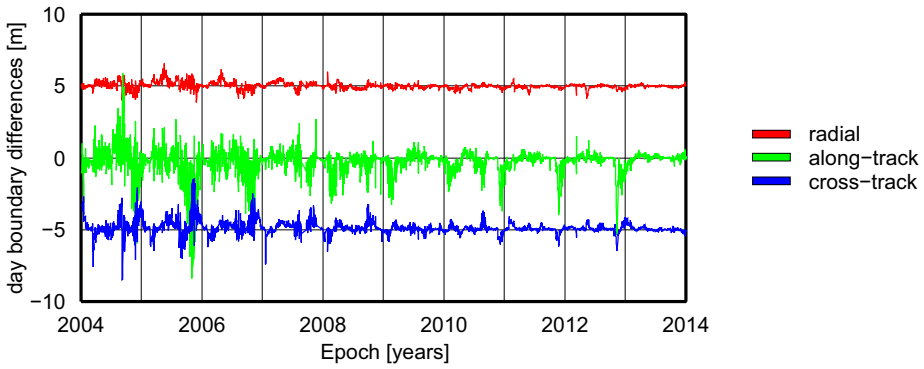

Figure 6.14: Orbit DBD for PRN10 for radial, along-track and cross-track components. The time series of the radial and cross-track components are shifted by +5 and -5 meters, respectively. Only a regional network is used for orbit determination for the period from 2004 until 2014 with type-mean PCC applied. Clock biases and tropospheric estimates are fixed to preliminary computed a priori values.

were split into three components, namely, radial, along-track and cross-track. Lomb-Scargle periodograms for each satellite and component were computed and the respective components were combined. In order to allow more contribution from less noisy time series, each one was weighted according to the inverse of the variance. The above was performed for the "type-mean" and "individual" scenarios.

Interestingly, while other satellite and station parameters are fixed to preliminary well defined values, the use of individual PCC for stations results in significant improvement in the orbit DBDs with respect to the "type-mean" solution. Similar to previous solutions (Figures 6.8 and 6.12), "individual" and "type-mean" power spectra discover peaks at frequencies matching the GPS draconitic year and its harmonics, or $1.04 \times n$ cpy, where $n = 1, 2, 3, 4, \ldots$, Figure 6.15. However, compared to *case 1*, where identical network of stations was used, the observed peaks are much sharper and visible up to $n = 16$. Nonetheless, the most important change compared to *cases 1* and *2* concerns the power values of "individual" solutions, which are smaller compared to the respective values of the "type-mean" solution, indicating improvement. In addition to the reduced power of the draconitic harmonics, the noise floor of respective "individual" solutions has also been reduced. This, in turn, resulted in revealing additional high-frequency draconitic harmonics (up to $n = 20$).

To track the power change across the entire frequency range, the ratios of power at respective frequencies in the "individual" and "type-mean" runs were computed. As seen from Figure 6.16, not only was the power at the draconitic harmonics reduced, but the entire frequency ranges of all orbital components were attenuated. Thus, power of the higher frequencies ($f > 100$ cpy) was

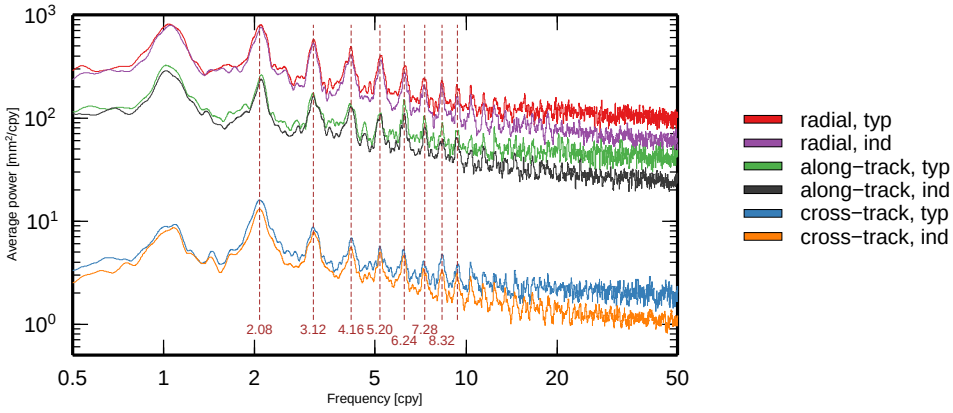

Figure 6.15: Power spectra of the orbit DBD from 2004 until 2014 of the radial, along- and cross-track components computed only using stations with individual PCC, while station and satellite clock biases, tropospheric parameters and station coordinates were kept fixed. For clarity radial and cross-track components have been shifted by +20dB and −20dB, respectively.

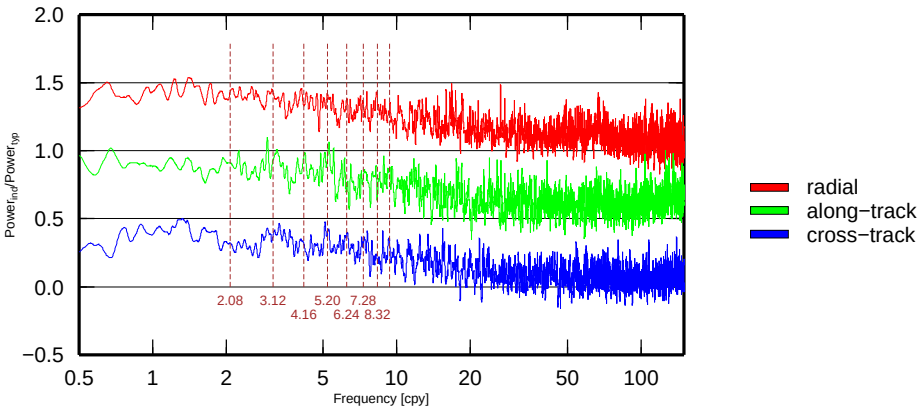

Figure 6.16: Ratios of the power at respective frequencies in the "individual" and "type-mean" orbit determination runs. Radial and cross-track components are shifted by +0.5 and −0.5, respectively.

reduced by 44%, 36% and 43%[4] for the radial, along- and cross-track component, respectively.

The observed improvements in the orbit DBDs are presumably associated with changes in data screening, as the employed individual antenna/radome PCC are expected to fit better compared to the type-mean models. As a consequence of the improved data screening, the satellite orbits are constrained heavier, which may have a tremendous effect on the results in case of a network composed only of the stations discussed in Section 4.2. The impact of individual PCC on data screening will be more thoroughly addressed in Section 6.4.4.

Although improvement was achieved in a broad frequency range, this research is more focused on draconitic frequencies. Table 6.6 summarizes changes at frequencies that satisfy the condition $1.04 \times n$ cpy, where $n = 1, 2, 3, 4, \ldots$ Thus, across the frequencies presented the average improvement is ∼11%, ∼15% and ∼16% for radial, along- and cross-track component, respectively.

The fact that the applied PCC propagate into the orbits is an important discovery. Although the presented results were obtained using only a rather small network with a distribution of stations far from being optimal for orbit determination, the effects from more accurate PCC are not averaged away, but clearly seen in the orbits. In addition to overall noise reduction in the computed orbit DBDs time series, the draconitic harmonics observed in the orbits have been reduced. This effect, however, almost disappeared when additional globally distributed stations were added into the network. Although in the last case stations with individual calibrations were in majority, most of the time, the network spatial distribution dominated over the amount of stations with individual calibrations. Thus, in *case 2* supplementary stations (which employed only type-mean

[4] Average reduction for $100 < f < 158$ cpy

Table 6.6: Numerical values [mm^2] of the GPS orbit DBD power spectra at harmonics of 1.04 cpy.

Component	Sol.	1.04	2.08	3.12	4.16	5.20	6.24	7.28	8.32	9.36
Radial	typ	81.0	79.2	57.1	49.1	39.6	30.9	23.6	23.0	19.6
Radial	ind	78.5 (3%)	74.3 (6%)	52.8 (8%)	40.9 (17%)	36.4 (8%)	27.2 (12%)	20.1 (15%)	20.6 (10%)	16.1 (13%)
Along-track	typ	317.7	251.2	172.8	133.6	111.7	151.0	103.3	86.9	73.4
Along-track	ind	279.2 (12%)	228.9 (9%)	162.1 (6%)	126.9 (5%)	104.7 (6%)	109.0 (28%)	81.7 (21%)	55.3 (36%)	64.0 (13%)
Cross-track	typ	87.6	158.7	87.4	68.0	56.4	51.3	37.3	48.0	35.4
Cross-track	ind	81.4 (7%)	130.5 (18%)	76.9 (12%)	55.5 (18%)	49.7 (12%)	45.3 (12%)	29.5 (21%)	33.7 (30%)	29.7 (16%)

Values in brackets indicate improvement in percent with respect to the "type-mean" solution.

PCC) observed satellites most of the time, while the effect from stations with individual PCC was limited due to observation elevation weighting applied. As overwhelming part of orbital arc was estimated using the set of stations with only type-mean PCC, almost no difference was observed between the "type-mean" and "individual" solutions in *case 2*.

Impact of PCC on station coordinates

In previous section satellite orbits based on the day boundary differences (DBD) were evaluated. Using a regionally clustered network of stations it was shown that small imperfections in the applied antenna PCC do not average out, but propagate into the orbits. In order to show this, two orbit determination runs were performed: with type-mean and individual PCC. The results have shown that the use of individual PCC reduced noise in the DBD time series compared to the type-mean case. This could be achieved only after limiting the number of estimated parameters by fixing satellite and station clock biases, as well as tropospheric estimates to predefined values.

This section is focused on the impact of the applied PCC on station coordinates. The experiment described here refers to *Step 3* in Figure 5.11. By evaluating the PPP coordinate time series (CTS), obtained using different sets of PCC while station and satellite clock biases, as well as tropospheric estimates, are kept fixed to predefined values, the PCC impact on station positions is assessed. In order to preserve processing consistency, in each PPP run the respective orbit set obtained in Section 6.4.3 was used. The time interval for the PPP processing was identical to that of the orbit determination.

During the period from 2004 until 2014, antenna changes were performed at some stations due to various reasons. In order to avoid possible abrupt changes in the CTS caused by these changes, breakpoints were introduced in respective CTS if an antenna change occurred. Thus, the resulting CTS referred to particular antennas, rather than to stations. As a consequence of the introduction of breakpoints in the original CTS, the number of evaluated CTS has increased. Thus, the total number of the CTS that were actually considered has grown from 55 to 75.

Due to barely visible differences in the CTS obtained using type-mean and individual PCC, these are not shown here. However, all CTS as well as their differences can be found on the supplied CD-ROM.

Before performing frequency analysis of the CTS, coordinate conversion from Cartesian to geodetic system was done. In this way for each considered antenna, time series for the north, east and up components were obtained. Finally, Lomb-Scargle periodograms were computed for each CTS and each coordinate component separately. Similarly to the previous orbit analysis, each periodogram was weighted according to the inverse of the time series variance, allowing more contribution from less noisy data. Then the power spectra were combined separately for each coordinate component. The above was performed using type-mean and individual PCC.

A priori coordinates for the stations that were used for orbit determination in *steps 1* and *2* were extracted from accurate linear models. Additionally, tight constraints $\sigma = 10$ mm were applied to these coordinates during processing. Since requirements for *step 3* included importing of accurately estimated station clock biases and ZTDs, the same stations were used in the PPP processing. In turn, this has resulted in very little noise in the obtained PPP CTS, and consequently, led to low values in the computed power spectra. Nevertheless, these were still affected by the applied PCC.

Similar to the picture observed for the satellite orbits, the combined power spectra of station PPP CTS, Figure 6.17, demonstrates advantage from using individual PCC with respect to the type-mean models. Both solutions show peaks at $1.04 \times n$ cpy, where $n = 1, 2, 3, 4, \ldots$, but in contrast to the orbit DBD power spectra, Figure 6.15, only those until $n = 3$ stand out clearly in all coordinate components. While in the north components peaks up until $n = 9$ can still be observed, in the east and up components peaks tend to disappear for $n \geq 4$. Generally, benefits from using the individual calibrations are seen, as power values in the "individual" solution are smaller than those of the "type-mean" solution.

In order to obtain a better idea of how the power spectra were affected across the entire frequency range, ratios of power values at respective frequencies for the "individual" and "type-mean" solution were computed. As demonstrated in Figure 6.18, all coordinate components show considerable reduction in power in almost the entire frequency range from 0.5 to 150 cpy when the individual PCC are employed. At the same time no power reduction is observed for $n = 1$ and 4 in the north component, very little change in power is observed for $n = 2, 3, 5$ with no reduction at all (increase) for $n = 8$ (exactly at 8.3635 cpy) in the east component, with respective frequencies defined as $1.04 \times n$ cpy. No rule, however, could be applied to these exceptions to explain their origins. In contrast to the north and east, the up component is the one affected most, demonstrating reduction in power across the entire frequency range.

To summarize at this point, all coordinate components were greatly affected, showing large power reduction across the entire frequency range from 0.5 to 150 cpy except at a number of individual frequencies, however, no logic has been found behind these exceptions. Similar to the case with the satellite orbits, applying individual PCC resulted in substantial reduction of power at higher frequencies. Thus, for frequencies with $f > 100$ cpy power was reduced by 40%, 52% and 54%[5] for the north, east and up coordinate component, respectively.

Table 6.7 outlines power reduction of the discussed PPP CTS at the frequencies that match harmonics of the GPS draconitic year, or $1.04 \times n$ cpy, where $n = 1, 2, 3, \ldots$ While the horizontal components are affected in an unpredictable manner, showing large improvements at some and almost no improvement (or even slight degradation) at other frequencies, the effect in the vertical

[5]Average reduction for $100 < f < 158$ cpy

Table 6.7: Numerical values [$\times 10^{-4}$ mm^2] of station PPP CTS power spectra at harmonics of 1.04 cpy.

Component	Sol.	1.04	2.08	3.12	4.16	5.20	6.24	7.28	8.32	9.36
North	typ	6.26	2.73	2.23	2.24	1.81	1.90	1.48	1.35	1.55
North	ind	6.23 (1%)	2.50 (8%)	2.05 (8%)	2.25 (-0%)	1.55 (14%)	1.40 (26%)	1.34 (9%)	1.14 (15%)	1.15 (26%)
East	typ	5.62	2.52	2.37	1.70	1.43	1.48	1.41	1.08	1.12
East	ind	4.80 (15%)	2.40 (5%)	2.28 (4%)	1.35 (21%)	1.39 (3%)	1.20 (19%)	1.08 (23%)	1.06 (2%)	0.88 (22%)
Up	typ	11.21	6.66	5.25	4.63	4.33	5.03	3.33	3.44	2.67
Up	ind	9.49 (15%)	5.72 (14%)	3.97 (24%)	3.39 (27%)	3.11 (28%)	2.83 (44%)	2.32 (30%)	2.47 (28%)	2.16 (19%)

Values in brackets indicate improvement in percent with respect to the “type-mean” solution.

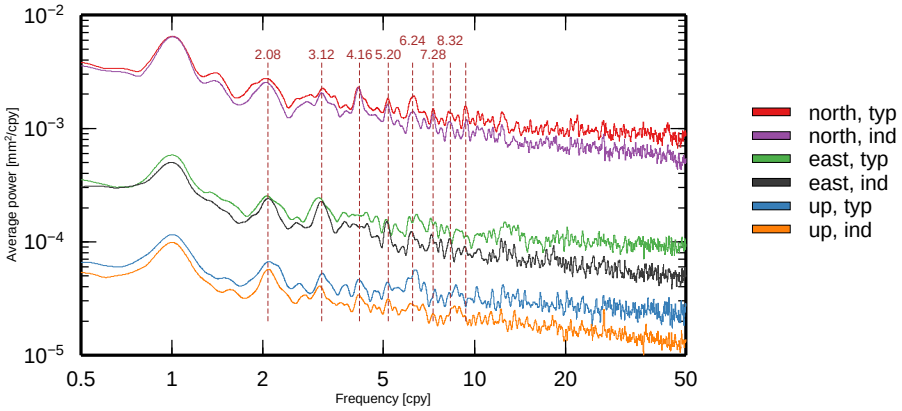

Figure 6.17: Power spectra of station PPP solutions applying type-mean and individual PCC and using respective orbits.

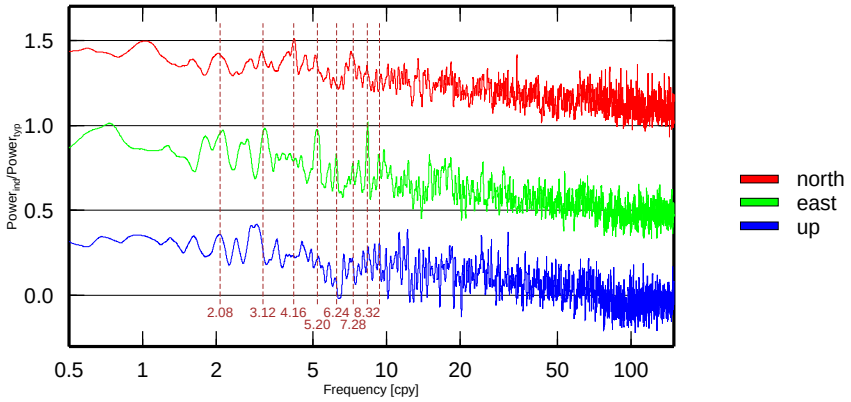

Figure 6.18: Ratios of the power values at respective frequencies in the "individual" and "type-mean" PPP runs. North and up components are shifted by +0.5 and −0.5, respectively

component is consistent for all shown frequencies. Average reduction in the power values for frequencies shown in Table 6.7 is 12%, 13% and 25% for the north, east and up component, respectively. Thus, the use of individual PCC for station antennas resulted in similar improvements of the horizontal components, whereas the improvement in the vertical component was almost twice as large as that in horizontal components.

6.4.4 Impact of PCC on data screening

As mentioned previously, in addition to corrections performed at station level, e.g., station clock bias, tropospheric delays, tide loadings, etc., each observation is subject to individual correction based on the applied antenna PCC. During the least squares process used in `Bahn` noisier observations are rejected until the user defined criteria for the RMS of observation residuals is fulfilled. This implies that the applied PCC directly affect the number of observations that are accepted in processing. Thus, by keeping all parameters as well as the criteria for the RMS of residuals identical, while changing only the PCC, judgement on their quality can be made. The greater number of accepted observations will indicate the better "fit" of the applied PCC for a given antenna for current conditions. Thus, the number of accepted observations is another measure of the processing quality.

For the orbit determination runs, performed in *step 2*, Figure 5.11, identical observation data were used. Nevertheless, the number of rejected observations using the type-mean PCC is greater than that using the individual ones. The plot showing the differences in the numbers of accepted observations and corresponding histogram are shown in Figure 6.19. As one can see, using identical settings in `Bahn`, the observations, to which the individual PCC were applied, appeared to be less noisy, resulting in the smaller numbers of rejected observations. Generally, the individual PCC performed better during the entire period. The end of 2013, however, stands out from the rest of the time, as the number of rejected observations using the individual PCC is greater than that using the type-mean for a number of days. This period coincides with the problems occurred with the internal repository of the University of Luxembourg, from where the observation data were obtained. This includes days 331:365 of 2013, when a lot of observation data were missing, affecting the total number of observations (not shown). This shortage of data could also affect the number of accepted observations in both solutions, however, as the change was not dramatic, no further investigation was performed.

As the number of stations used in processing was changing during the processing period, so did the number of observations. No statistical analysis was performed for the "raw" number of accepted/rejected observations. Instead the ratio of the difference in the number of accepted observations in the "type-mean" and "individual" runs to the number of accepted observations in the "type-mean" run was computed. The median value of this ratio considering the period from 2004 until 2014 was -7.1×10^{-5}, indicating that on average an improvement, although very little, was achieved when the individual PCC were employed. This stands in line with the histogram shown in Figure 6.19, also indicating a greater number of accepted observations during the "individual" orbit determination run.

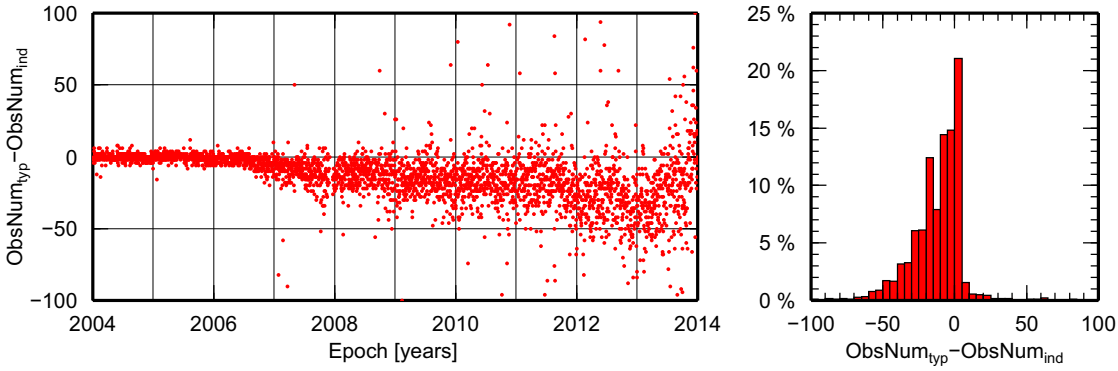

Figure 6.19: Difference between the total numbers of accepted observations in the "type-mean" and "individual" orbit determination runs and the corresponding histogram.

6.4.5 Impact of individual PCC on estimated ZTDs

In order to assess the impact of applied PCC on the estimated tropospheric delays, the latter computed using type-mean and individual PCC were analysed. Two sets of hourly ZTDs were obtained during orbit determination for a period 01-30 May 2013 using the global IGb08 core network of stations complemented with stations discussed in Section 4.2. The orbit determination was performed twice: once applying type-mean PCC for all stations and second time applying individual PCC where possible. Differences between respective ZTDs for each station and each epoch were computed.

While the hydrostatic part of tropospheric delays is modelled in GNSS, the wet part is estimated, and thus, it compensates for deficiencies of the applied ZHD models. As a result, ZTD, being a summation of ZHD and ZWD is a more direct product of GNSS processing. Thus, comparison of only ZTD data obtained from GNSS analyses is sufficient for this assessment.

Table 6.8 provides results of the ZTD comparison for all investigated stations. The results show that for the investigated stations the impact of applying individual PCC is small. Thus, mean biases in ZTD estimates for all stations over the period of one month are generally below 1 mm with an average value of 0.2 mm and standard deviation 0.8 mm. The largest bias of 2.7 mm is observed at station BADH correlating with large differences in the applied antenna/radome PCC for this station (see Appendix B). The extreme differences in ZTDs over the entire period reach 10.3 mm. In turn, station ALAC demonstrates the maximum difference in ZTDs of 11.5 mm over 30 days, however, the mean bias in ZTDs for this station for the entire period is only −0.1.

The small differences in computed ZTDs demonstrated in Table 6.8 can be explained through the way these have been obtained. In particular, during satellite orbit determination station coordinates are tightly constrained to their a priori values and the PCC-induced errors do not

Table 6.8: Differences between ZTDs computed using type-mean and individual antenna/radome PCC. All values are in $[mm]$.

GNSS station	Bias	Std. dev.	Difference		GNSS station	Bias	Std. dev.	Difference	
			Min.	Max.				Min.	Max.
ALAC	−0.1	1.1	−7.0	11.5	KEPA	−0.1	0.6	−3.9	2.3
ANKR	0.2	0.6	−3.9	4.1	KLOP	1.3	0.7	−2.7	6.6
BADH	2.7	0.9	−1.9	10.3	METS	0.8	1.0	−2.2	5.8
BASC	1.2	0.7	−3.6	6.2	NICO	−0.2	0.6	−2.8	3.9
BORJ	−0.1	0.8	−4.8	4.6	ORID	−0.1	0.7	−9.1	5.6
BUCU	0.2	0.6	−2.8	4.9	PENC	−0.2	0.9	−6.1	7.5
BUTE	−1.0	0.6	−3.9	4.6	POTS	−0.1	0.8	−3.8	3.6
CANT	−0.8	0.8	−5.1	3.5	REYK	0.5	1.2	−7.1	6.5
DRES	0.0	0.7	−3.0	5.3	ROUL	0.2	0.6	−4.6	3.6
ECHT	1.7	0.6	−1.8	5.4	SASS	0.4	0.7	−2.7	6.0
ERPE	0.4	0.7	−4.9	8.5	TORI	1.5	0.8	−6.7	5.6
EUSK	0.3	0.6	−3.4	5.4	TROI	0.3	0.6	−2.9	4.3
FLIN	0.0	0.8	−7.6	4.6	TUBO	−0.7	0.6	−5.6	3.4
GANP	0.1	0.6	−3.0	4.7	VALE	−0.6	0.9	−4.5	5.2
HELG	0.1	0.8	−4.6	6.5	WALF	−1.7	0.5	−3.8	3.0
HOBU	−0.2	0.7	−3.8	4.5	WARN	−0.3	0.7	−4.5	4.3
HOE2	0.7	0.8	−0.8	2.7	WTZR	0.3	1.2	−5.9	8.1
HOFN	0.1	1.0	−4.1	4.8	ZIM2	0.1	0.5	−3.6	3.4
KATO	0.4	0.5	−1.8	3.6	ZYWI	0.1	0.6	−2.7	4.7
All	0.2	0.8	−9.1	11.5					

primarily propagate in ZTD, but get spread to other estimated parameters. This impact, however, may be amplified if station coordinate constraints are loose.

To provide an independent assessment of the computed ZTDs, meteorological data, in particular, radiosonde (RS) measurements were used. RSs are an excellent source of upper-air humidity observations. During their ascending time, which typically lasts about 90 minutes, RSs collect pressure, temperature and humidity measurements, providing vertical profiles of atmosphere up to the height of 25-35 km. The RS data have been used in many studies for validation of GNSS-derived ZTD data. A very short list of these studies includes, Vedel et al. (2001), Pacione et al. (2002), Haase et al. (2003), Wang and Zhang (2008), Dousa and Bennitt (2013), Ahmed et al. (2016), etc.

There are, however, certain limitations associated with RSs, in particular, sparse temporal and spacial resolution of measurements. For instance, due to high costs RSs are typically launched only twice a day delivering atmospheric profiles at noon and at midnight. Additionally the launching

sites often do not collocate with GNSS stations and, thus, not only horizontal distances, but also the corresponding altitude differences need to be considered for ZTD comparison. Nevertheless, having a dense network of GNSS stations, as the one used in this study, it is often possible to obtain a number of RS profiles to allow for comparisons.

Keeping in mind horizontal variations in atmospheric properties and aiming for a good level of agreement between RS and GNSS-derived results, the separation between pairs of GNSS stations and launching sites of RSs for this study did not exceed 50 km. As ZTDs are a strong function of atmospheric pressure which varies with altitude, altitude differences between lowermost border of RS profiles and respective GNSS stations were taken into consideration. The methodology of these adjustments and of integration of RS profiles rigorously followed the one discussed in Haase et al. (2003) and is not discussed here.

RS profiles for this study were obtained from National Oceanic and Atmospheric Administration (NOAA) Earth System Research Laboratory (ESRL) Radiosonde Database[6]. Overall 10 RS launching sites were identified closer than 50 km from the investigated GNSS stations, Table 6.9. The distances between GNSS stations and RS launching sites ranged from 2 to 49 km. At the same time, the differences between the lowermost border of RS profiles and the altitudes of corresponding GNSS stations extended from −109 to 418 m. One RS launching site with ID 12843 was in the vicinity of two stations: BUTE and PENC.

It may be of interest to see the evolution of ZTD estimates computed at one of GNSS stations, in particular, CANT. This station was selected because of its' small separation from the closest RS launching site (RS ID 08023): the distance is only 2 km and the height difference is 49 m. This results in extremely good agreement between GNSS- and RS-derived ZTD, Figure 6.20. Interestingly, the switch from the type-mean to individual PCC at CANT did not result in reduction of the small bias between GNSS- and RS-derived ZTDs. Alternatively, the bias has increased from 1.6 mm to 2.4 mm, whereas the standard deviation of the differences grew from 10.0 mm to 10.2 mm, respectively. ZTD plots for other stations listed in Table 6.9 are provided on the supplied CD-ROM.

Agreements between GNSS- and RS-derived ZTDs for all examined stations are summarized in Table 6.10. Regardless of the employed PCC the ZTD values from both techniques agree very well. These results are also consistent with evaluations of GNSS-derived ZTDs discussed in other studies (Haase et al., 2003; Ahmed et al., 2016). Although for several stations, in particular, REYK and ZIM2, GNSS-RS ZTD biases up to 15.1 mm are observed, these can be explained through distances up to 40 km between the GNSS stations and the respective RS launching sites. In general, the extreme ZTD differences for all GNSS-RS pairs at individual epochs reached 63 mm, while the mean GNSS-RS ZTD bias was −0.7 mm and −0.6 mm for type-mean and individual

[6]NOAA/ESRL Radiosonde Database `http://www.esrl.noaa.gov/raobs/`

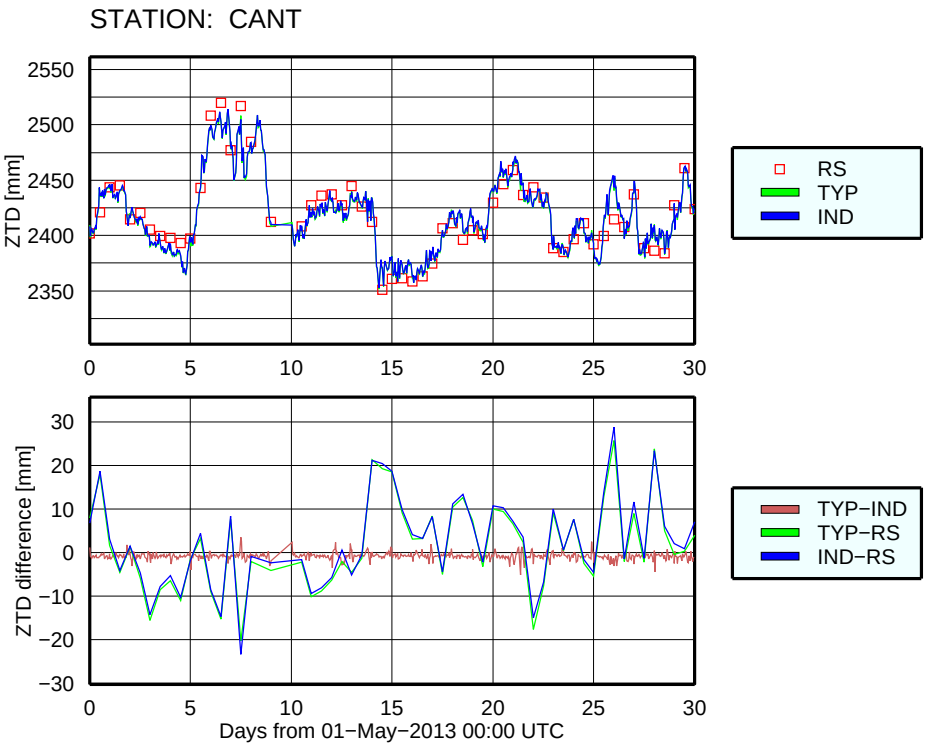

Figure 6.20: ZTD estimates at station CANT from GNSS analysis using type-mean and individual PCC and from RS data as well as their differences.

PCC. The mean standard deviation of the GNSS-RS ZTD differences across all stations was 10.3 mm for both GNSS solutions.

Table 6.9: GNSS ZTD-radiosonde comparison table.

GNSS station	Radiosonde ID	Dist. [km]	GNSS alt. [m]	Height diff. [m]	Number of RS profiles
ANKR	17130	13	939	45	60
BUCU	15420	4	109	−18	60
BUTE	12843	11	137	2	28
CANT	08023	2	49	16	59
GANP	11952	12	704	−3	60
HOBU	10238	10	111	−42	122
NICO	17607	18	162	−1	17
PENC	12843	41	248	−109	28
REYK	04018	37	27	27	57
SASS	10184	49	33	−27	60
ZIM2	06610	40	908	418	59

Heights are provided relative to mean sea level, using the geoid 1996 Earth Gravitational Model (EGM96).

Table 6.10: Differences between GNSS ZTDs computed using type-mean and individual PCC and the respective radiosonde data for 01-30 May 2013. All values are in $[mm]$.

GNSS station	$ZTD_{GNSS\ TYP}$ - ZTD_{RS}				$ZTD_{GNSS\ IND}$ - ZTD_{RS}			
	Bias	Std. dev.	Min. diff.	Max. diff.	Bias	Std. dev.	Min. diff.	Max. diff.
ANKR	−0.7	9.4	−18.9	20.6	−0.9	9.4	−19.2	20.1
BUCU	−6.6	10.5	−38.6	17.9	−6.9	10.6	−39.3	17.3
BUTE	−1.6	7.6	−15.1	13.5	−0.6	7.9	−15.1	15.6
CANT	1.6	10.0	−20.2	25.7	2.4	10.2	−23.4	28.8
GANP	3.4	12.1	−27.1	24.4	3.2	12.1	−28.4	25.1
HOBU	3.1	11.8	−26.2	43.6	3.4	11.8	−25.3	43.8
NICO	1.1	7.7	−13.0	13.7	1.4	7.8	−12.7	13.9
PENC	0.2	12.4	−24.9	21.2	0.8	12.5	−25.5	21.7
REYK	−14.5	11.2	−63.0	11.2	−15.1	11.0	−62.5	11.5
SASS	−4.5	11.5	−34.0	27.9	−5.0	11.6	−36.1	26.4
ZIM2	10.7	6.8	−13.7	23.8	10.4	6.6	−12.6	23.9
All	−0.7	10.3	−63.0	43.6	−0.6	10.3	−62.5	43.8

6.5 Summary

In order to answer the question, to what extent the individual PCC can be beneficial for geodetic applications, the impact of these was evaluated in sub-daily and daily GNSS processing. While the sub-daily processing involved computation of PPP solutions of only 6 stations located in Luxembourg, all stations for which individual PCC were available (see Chapter 4) were used in daily processing. The daily processing was aimed to assess importance of individual PCC for global GNSS solutions including datum definition, e.g., definition of the terrestrial reference frame involving orbit determination and consecutive PPP processing. The methodology of the analysis consisted in processing the GPS data using identical settings, but modifying the applied PCC and comparing the results. Two sets of solutions were analysed and compared by checking the impact on satellite orbits and on computed station coordinates.

The use of individual PCC in sub-daily PPP resulted in shifts of solutions compared to those obtained using type-mean PCC. Averaged over one month these shifts for all six investigated stations of the SPSLux network remained below 1 mm for horizontal coordinate components, whereas the vertical components was more severely affected. Thus, the maximum shift of 7.2 mm was observed for station WALF. These shifts in the vertical direction are partly associated with the estimated tropospheric delays, which are highly correlated with station heights. Interestingly, all six stations employ antenna/radome combinations of the same make and model (LEIAR25.R3/LEIT).

The analysis of the sub-daily PPP CTS revealed small degradations (∼1-2%) in coordinate repeatabilities due to the switch to the individual PCC for nearly all stations and coordinate components. RMS of only the vertical component of station BASC was improved. Also, the power spectra of the produced PPP solutions, revealed no improvements at dominating frequencies after the switch of the PCC.

As the correctness of the employed orbit determination sequence is crucial in this study, it was rigorously validated. In particular, the quality of the computed orbits and clocks was evaluated. To provide the assessment, these were compared to the IGS final products, resulting in an excellent agreement. The combined 3D RMS of the differences between the computed and the IGS final orbits reached 18.6 mm, whereas high stability was observed between the computed and IGS final satellite clock biases. Additionally, the orbits produced from 2004 to 2014 were compared to those of other IGS ACs, in particular, CODE and ESA. The assessment was based on the time series of Helmert transformation parameters between the computed and the IGS final orbits. The time series of the transformation parameters demonstrated good agreement with other IGS ACs with an RMS of < 2 cm.

Due to the network geometry, in particular, its inhomogeneity and actual station clustering in mainly one region - Europe, processing the data of the network required special approaches,

particularly, for orbit determination. Several strategies suggested in Section 5.7.1 were evaluated with respect to their appropriateness for the PCC assessment. The orbit determination using only these stations was challenging. When this was performed using the aforementioned network, the orbit determination was implemented only in the area of satellite visibility, while the rest of the orbital arc was propagated. This resulted in large uncertainties of the estimated orbits, particularly, of the orbit day boundary differences (DBDs). At the same time, the DBD time series constructed a basis for the assessment. As a consequence, large errors in orbit DBDs prevented from unambiguous interpretation of results. Nevertheless, the power spectra analysis at the GPS draconitic frequencies has demonstrated that some improvement could be achieved at individual frequencies in the radial and cross-track components, while the along-track component showed improvement in all considered harmonics.

In order to overcome the problem of large uncertainties in orbit estimation, globally but sparsely distributed stations with only type-mean PCC were added to the processed network. Unfortunately, the initially achieved positive result, when some improvement had been spotted, has vanished suggesting that the network station distribution prevailed over its composition. Therefore, almost no effect was marked in the estimated orbits (as well as the orbit DBDs) from using individual PCC, where available, instead of the type-mean models.

Constraining the solutions by reducing the number of estimated parameters, i.e. by fixing satellite and station clock biases and ZTDs to accurately predefined values, brought improvements to orbit determination and allowed to see benefits from using individual PCC. The analysis of the orbit DBD time series power spectra has shown that using individual PCC reduced power across the entire frequency range considered. The biggest improvement was observed in the higher frequencies ($f > 100$ cpy), where power reduction up to 44% was observed.

Finally, using individual PCC was beneficial also for station coordinates. Between the two PPP runs applying individual and type-mean PCC with respective orbit solutions obtained previously, the "individual" run showed considerable improvement in terms of noise in the time series compared to the "type-mean" run. Thus, the respective frequency analysis has indicated large power reduction across almost the entire frequency range considered in all coordinate components. However, no power reduction when switching from type-mean to individual PCC was observed at some frequencies in horizontal components. The vertical component was the one mostly affected by changes in the PCC with average power reduction in the higher frequencies ($f > 100$ cpy) reaching 54%.

Additionally, the orbit determination runs using different PCC were evaluated based on the number of rejected observations. Thus, applying individual PCC compared to the type-mean resulted in small ($\sim 7.1 \times 10^{-3}\%$) increase in the number of accepted observations. This suggests a better correction of the raw observations and smaller residuals in the least squares performed in

`Bahn`.

Evaluation of PCC models was also extended onto the computed tropospheric estimates. The ZTDs computed using type-mean and individual PCC were compared based on 30 days of analysis, however, the impact from switching the PCC was small. The GNSS-derived ZTDs were compared with those from the RS atmosphere profiles showing very good agreement between each other. Although the GNSS-RS ZTD biases up to 15.1 mm were observed at some stations, these are likely associated with distances up to 40 km between GNSS stations and respective RS launching sites. For a set of 11 stations with RS launching sites closer than 50 km mean biases computed across all GNSS-RS pairs were nearly identical with -0.7 mm and -0.6 mm for the type-mean and individual PCC, respectively. Thus, from this perspective the use of individual instead of type-mean PCC did not show any benefits. This can be attributed to tight constraints imposed on station coordinates during the analysis and loosening those will likely show different results.

In conclusion, based on the orbit determination and PPP runs applying individual and type-mean PCC, the following has been revealed:

- No reduction in power specifically at draconitic frequencies, following the convention $f = 1.04 \times n$ cpy, where $n = 1, 2, 3, 4, \ldots$, was observed in computed orbits when individual PCC were used. Instead, frequencies in the entire range considered ($0.5 < f < 158$ cpy) were attenuated. The attenuation was the largest of the higher frequencies ($f > 100$ cpy), reaching ∼44%, 36% and 43% for the radial, along- and cross-track component, respectively. Average attenuation of the lower draconitic frequencies observed ($1 \leq n \leq 9$, $n \in \mathbb{Z}$) was ∼11%, ∼15% and ∼16% for radial, along- and cross-track component, respectively.

- Following the overall decrease in noise in the orbits when using individual PCC, noise reduction was also observed in the PPP CTS when individual PCC with respective orbits were used. Unlike in the orbits, some low draconitic frequencies in horizontal components were hardly attenuated (e.g., $n = 1, 4$ and $n = 2, 3, 5$ in the north and east components, respectively) or even amplified ($n = 8$ in the east component), whereas the entire frequency range considered ($0.5 < f < 158$ cpy) was attenuated. The largest improvement was observed in the vertical component. The attenuation of the higher frequencies ($f > 100$ cpy) reached 40%, 52% and 54% for the north, east and up coordinate component, respectively. Average attenuation of the lower draconitic frequencies observed ($1 \leq n \leq 9$, $n \in \mathbb{Z}$) was ∼12%, ∼13% and ∼25% for the north, east and up component, respectively.

- When orbit determination is performed using a global network of stations, introduction of individual PCC only for the stations clustered regionally does not have a large impact on the orbits, because spatial distribution of stations in the network prevails over its composition. Consequently, as individual PCC for the IGS sites are available mostly for Europe only, their

introduction in processing will unlikely attenuate draconitic frequencies, observed by, e.g., Griffiths and Ray (2013). The effect may be seen only in the fractions of orbital arcs located above the areas where PCC changes are performed. The same refers to the estimated site coordinates: only the sites located in the areas, where individual PCC are used for orbit determination are affected.

- Individual PCC do not solve the problem of multipath and potential antenna phase centre shift due to electromagnetic coupling between, e.g., monument and antenna. These effects may possibly dominate over the applied PCC, resulting in modelling errors both in satellite orbits and site coordinates.

Chapter 7

Evaluation of Empirical Site Models

7.1 Introduction

As was shown in Chapter 6, the use of individual PCC during the processing of GPS observations positively affected the results. In particular, applying individual PCC improved solutions by reducing noise in the estimated parameter time series. In contrast, adding a limited number of stations with the type-mean PCC to constrain solutions globally, resulted in vanishing the positive effect that was seen in the orbits previously. Nevertheless, for global processing having a uniform and dense network of globally distributed stations is essential. The uniformity of the network ensures equal number of observations (and constraints) across the entire area, therefore, producing unbiased solutions. The density of stations guarantees robustness of solutions due to reduced sensibility to possible external disturbances, e.g., environmental hazards, hardware failures, etc.

It is clear that only using stations with individually calibrated antenna/radome combinations, the aforementioned uniformity and density in the network cannot be achieved. Additionally, analysing historical datasets is essential for understanding geodynamic and geophysical processes, such as tectonic plate motion and global sea level changes. To conclude, definition of geodetic datum without including historical data is nearly impossible, therefore, adding stations with type-mean PCC into the network, although being undesirable, cannot be avoided.

To overcome this limitation, the ESM technique introduced in Section 3.6 can be applied to all sites on a global scale. This allows to correct deficiencies in the applied PCC, as well as to smooth unaccounted errors originating from multipath and other site-specific effects. However, the technique has some limitations discussed in Section 3.6.2, which need to be evaluated.

This chapter provides results on the ESM validation in challenging scenarios. It addresses the topic of the differences between PCC and ESM. Finally, the ESM performance is assessed on the sub-daily and daily basis. However, the sub-daily results are limited to PPP processing of only 6 stations in Luxembourg. The daily solutions include both orbit determination and PPP using a global network of stations.

7.2 ESM validation in challenging scenarios

Despite the limitations of ESMs outlined in Section 3.6.2 and reported by Moore et al. (2014), the estimation of clock biases and tropospheric delays has to be performed. This is necessary, as it provides with a consistent set of solutions for all involved stations. At the same time, if troposphere estimation is not performed, but a model is used instead, the quality of solutions reduces significantly. This suggests that the estimation of clock biases and ZTDs cannot be avoided.

According to Moore et al. (2014), low monument height also poses limitations for the ESM estimation. Luckily, the majority of geodetic stations is set up using monuments with heights greater than 0.5 m. Still, it is interesting to investigate how good is the repeatability of ESMs for low monument heights and when both clock and ZTD estimation is performed.

The IGS station BOGT, which is included in the IGS core station list, consists of an antenna installed on a low concrete monument of only 0.1 m high[1] surrounded by a barrier, Figure 7.1. The flat concrete surface surrounding the antenna should reflect a large portion of incoming signals. At the same time, the barrier across the site perimeter blocks signals from low elevations.

To estimate an ESM for BOGT, the PPP solutions from the beginning of 2010 until the end of 2012 were obtained. For this the IGS final products were used, therefore, the satellite clock biases were not solved for, however, the ZTDs and station clock parameters were estimated.

BOGT is an example of a station, for which the ESM method should not perform well, considering very low monument height. However, as seen from Figure 7.2a, even though clock and tropospheric parameters were estimated, leading to degradation of the method performance,

[1]Taken from the station log file available online at `ftp://igs.org/pub/station/log/bogt_20130131.log` (last accessed on 24 Oct 2014)

Figure 7.1: The IGS station BOGT (source: `http://igscb.jpl.nasa.gov/network/site/bogt.html`).

the derived ESM demonstrate good stability over time. Thus, for three consecutive years (2010-2012) the produced ESMs show very high repeatability even for signals at low elevations. This suggests that despite the aforementioned weaknesses of the method with respect to the estimated parameter set and physical site properties, it is capable to produce stable result given sufficient amount of observations available to reduce the uncertainty of results.

To monitor the effect from applying the derived ESM, observation data for BOGT were reprocessed again but the antenna type-mean PCC were modified according to the ESM obtained earlier applying the methodology described in Section 3.6.1. The CTS for the discussed period for both cases are shown in Figure 7.3. And although the impact from applying the ESMs at BOGT shown in Figure 7.2a is barely noticeable on the CTS, it is well seen in the resulting residuals, Figure 7.2b. The same "site" patterns are seen in both sets of images, however, after the initial ESM was applied, the reprocessed ESM demonstrates a much weaker appearance as compared to the initial one, suggesting that a substantial amount of multipath has been mitigated.

Another important finding is that both sets of ESMs in Figure 7.2 demonstrate very good repeatability for consecutive years. This proves that the developed ESM method performs well for low monument heights, when large amounts (1 year in this case) of data are available.

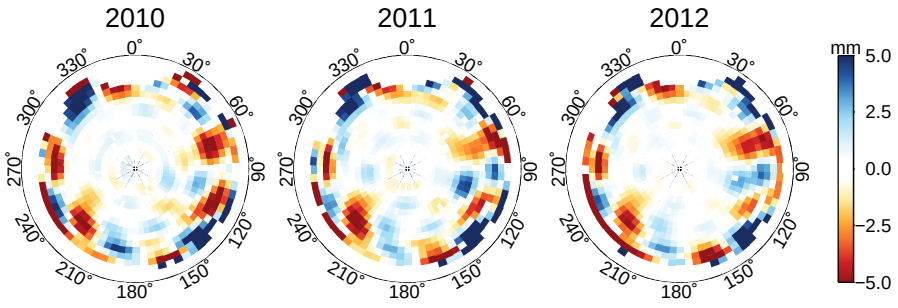

(a) initial ESM

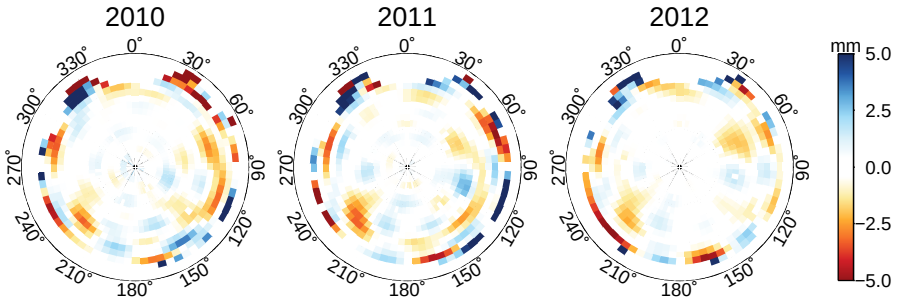

(b) reprocessed ESM after the station PCC was corrected for the initial ESM

Figure 7.2: Repeatability of the derived ESM for the IGS station BOGT with 0.1 m monument height for 3 consecutive years (only L_1 is shown).

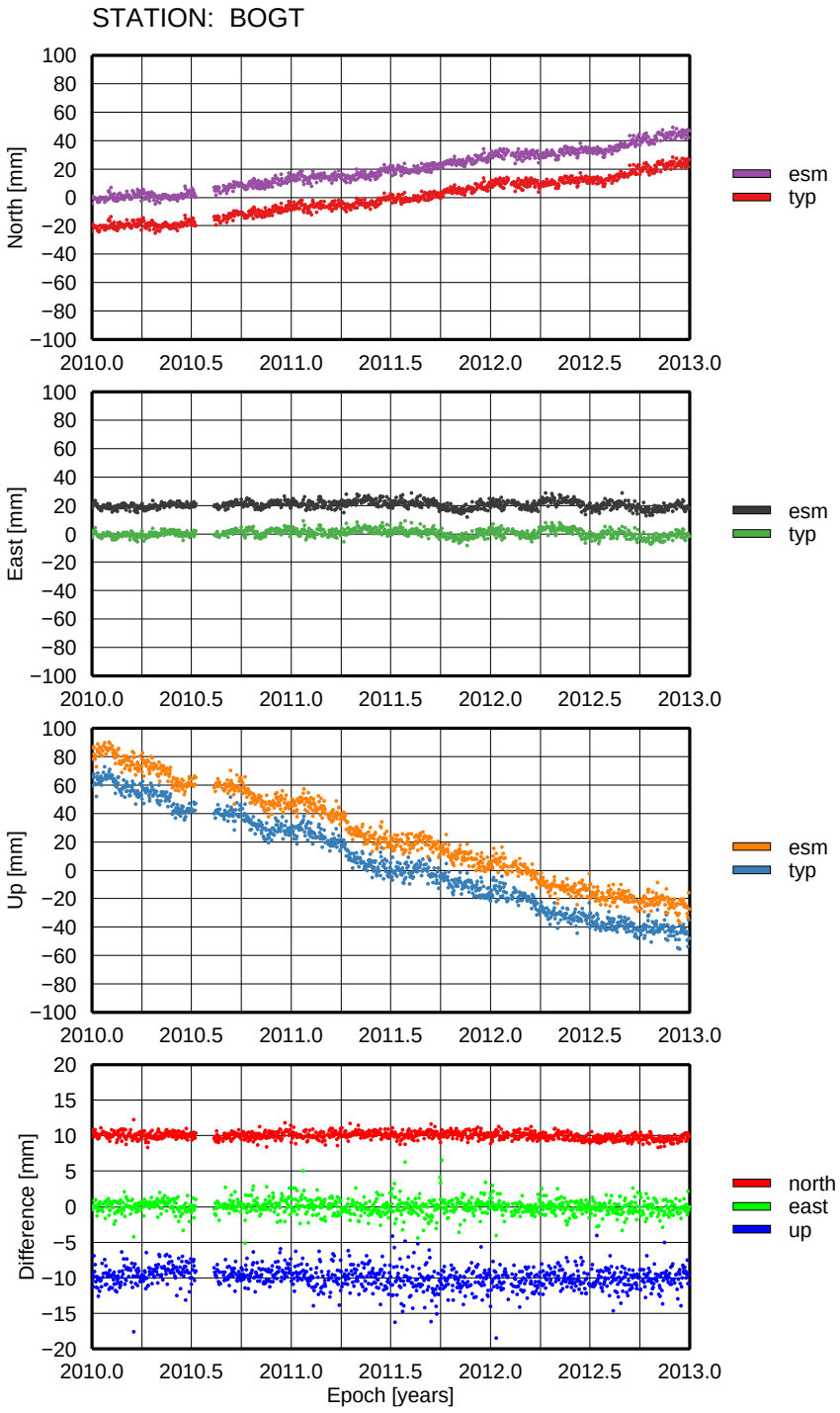

Figure 7.3: CTS for BOGT obtained using type-mean and ESM-corrected PCC decomposed into North, East and Up, and the respective differences.

7.3 On the differences between individual and ESM-corrected PCC

As was shown previously, the ESM method is capable of producing corrections to the applied PCC based on phase residuals that are accumulated during processing. However, it is erroneous to assume that ESMs should provide results that are identical or similar to antenna/radome calibrations performed by corresponding facilities (see Section 3.3.1). Although some similarities are possible, actual PCC of GNSS antennas may be altered after their installation due to, e.g., EM coupling between antenna and monument. Additionally, incoming signals may be affected by multipath. Thus, an ESM represents a complex product, which is composed of the deficiencies in PCC, while being altered by the environment surrounding the antennas.

Nevertheless, to show how close the derived ESMs are to individual antenna PCC, daily PPP solutions for the SPSLux stations BASC, ECHT and ERPE were obtained and respective post-fit phase residuals were analysed. The aforementioned PPP solutions were computed using the IGS final products and type-mean PCC. It is noted that all stations of the SPSLux network were equipped with antennas of the same manufacturer and model (LEICA AR25.R3/LEIT). The post-fit phase residuals for each station were accumulated starting from the moment when the antennas were installed (approx. October 2010) and until December 2013. Then ESMs for each site were computed according to the methodology outlined in Section 5.4.2.

Differences between type-mean and individual PCC, as well as ESMs for BASC, ECHT and ERPE are shown in Figure 7.4. As can be seen, the ESMs for BASC and ERPE show similarities, suggesting some closeness in surroundings between the two sites. However, as the environment at each site is different from one another, the ESMs demonstrate large variations. At the same time the obtained ESMs do not agree well with the differences between the respective type-mean and individual PCC. This demonstrates that the actual site effects dominate over the antenna-specific phase modelling errors at each of the three sites. In turn, this proves the importance of site calibration, as clearly, the multipath dominates over PCC modelling errors in its impact on processing.

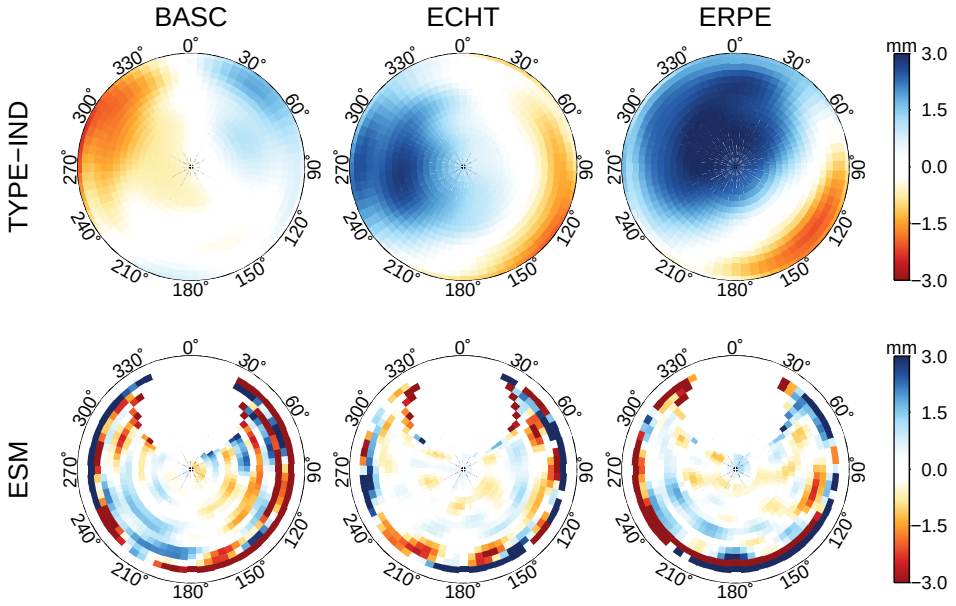

Figure 7.4: Difference between type-mean and individual PCC (top) and ESM (bottom) for stations BASC, ECHT and ERPE, equipped with antennas of the same model (LEICA AR25.R3/LEIT, only L_1 is shown).

7.4 Sub-daily PPP results

As the ESM technique is designed to reduce multipath, which depends on the direction of incoming signals, and, consequently, is a function of the satellite orbit, the sub-daily position estimates should also be affected. Thus, in order to assess this impact, ESMs were computed for the SPSLux stations according to the methodology described in Section 5.4.2. In particular, for each station the computed ESM was based on post-fit phase residuals from PPP processing over a period of approximately 3 years (from November 2010 until December 2013).

Hourly PPP solutions were obtained for the period from 01/01/2011 until 30/06/2011 using the settings identical to those used for the sub-daily processing described in Section 6.2, but applying the ESM-corrected PCC. Then the produced pseudo-kinematic solutions were compared to those produced with the type-mean PCC. In each time series the outliers defined by a tolerance of $\pm 4\times$IQR were removed.

The actual time series obtained using different PCC are visually indistinguishable from each other. However, compared to the results obtained with the type-mean PCC, the application of the ESMs resulted in small shifts in solutions, Table 7.1. In general, shifts in horizontal direction are smaller compared to those in the vertical. Thus, in the north direction these do not exceed ± 0.6 mm, however, the spread is twice as large in the east direction, reaching -1.16 for ERPE. The

spread of the shifts due to the PCC modification is the largest in the vertical direction, reaching up to ±2 mm. A larger spread of shifts in the vertical direction is associated with estimation of tropospheric delays, which are correlated with station heights. However, considering the standard deviations of the differences in solutions, only 5 of 18 shifts are statistically significant (at the 1-σ level).

Additionally, the PPP solutions were checked for changes in their repeatabilities. The results, expressed as RMS values for each station are shown in Table 7.2. It can be seen that the RMS values of the "ESM-corrected" solution are very similar to those of the "type-mean". However, it should be noted that while repeatabilities are neither improved, nor degraded in the north direction, the east component shows little systematic degradation (below 1-2%). Alternatively, applying the ESM-corrected PCC resulted in improvement (approx. 1-2%) of the RMS in the vertical direction for four of the six stations.

Analogous to the analysis performed in Section 6.2, the combined Lomb-Scargle periodograms for each coordinate component were computed, Figure 7.5. As seen from Figure 7.5a, the obtained power spectra are very similar and discover dominating presence of diurnal (365.25 cpy) and semi-diurnal (730.5 cpy) harmonic signals. One needs to remember that a large contribution to these signals may stem deficiencies in the tidal models, in particular, of the P_1, K_1, S_2 and K_2 tidal constituents, which have periods of 24.07 h, 23.93 h, 12.00 h and 11.97 h, respectively. In addition to the aforementioned harmonic signals, the O_1 and M_2 tidal constituents, which have periods close to 25.82 h and 12.42 h, respectively, can be identified.

The ESM-corrected PCC should reduce the power of signals at the GPS orbital frequencies, in particular, at those that correspond to 23.93 h and 11.97 h. Although changes in the observed power cannot be clearly identified from the ratios of the power spectra, Figure 7.5b, the exact power values at the aforementioned frequencies, as well as at frequencies of the main tidal constituents reveal a more detailed picture, Table 7.3.

Indeed, the ESM-corrected solutions show reduced signals at the GPS orbital frequencies and close to them, in particular, in the vertical direction. Thus, the power of harmonic signals with periods matching 24 h (diurnal) and 23.93 h (sidereal) has reduced from 1.983×10^{-2} m^2/cpy to 1.607×10^{-2} m^2/cpy and from 1.993×10^{-2} m^2/cpy to 1.522×10^{-2} m^2/cpy, respectively. At the same time, those in the east directions have experienced an amplification by ∼10%, whereas the north component did not change.

Interestingly, signals with periods close to 11.97 h were also attenuated, but only for horizontal components. This attenuation reached 25% and 30% for the north and east component, respectively. The vertical component, however, remained unchanged.

As the ESM-corrected PCC are derived from the type-mean models, in general, they perform very similar to the latter. However, some important differences can be observed and respective

Table 7.1: Mean shifts [mm] between hourly pseudo-kinematic solutions for the SPSLux stations computed using type-mean and ESM-corrected PCC for 01/01/2011 – 30/06/2011.

	BASC	ECHT	ERPE	ROUL	TROI	WALF
north	-0.57 ± 0.60	-0.10 ± 0.44	0.38 ± 0.60	0.04 ± 0.41	0.08 ± 0.53	-0.36 ± 0.38
east	0.10 ± 0.44	-0.72 ± 0.47	-1.16 ± 0.35	0.03 ± 0.47	-0.64 ± 0.41	-0.79 ± 0.45
up	-1.14 ± 2.10	1.92 ± 2.48	0.11 ± 2.49	0.49 ± 2.05	1.68 ± 1.61	0.25 ± 1.83

Table 7.2: RMS [cm] of hourly pseudo-kinematic solutions for the SPSLux stations computed using type-mean and ESM-corrected PCC for 01/01/2011 – 30/06/2011.

	BASC	ECHT	ERPE	ROUL	TROI	WALF
$\text{north}_{\text{typ}}$	0.594	0.695	0.601	0.592	0.625	0.603
$\text{north}_{\text{esm}}$	0.603	0.691	0.585	0.588	0.619	0.605
east_{typ}	0.549	0.640	0.582	0.618	0.553	0.604
east_{esm}	0.561	0.652	0.589	0.628	0.563	0.610
up_{typ}	1.619	1.480	1.657	1.437	1.528	1.562
up_{esm}	1.652	1.456	1.601	1.426	1.532	1.543

Table 7.3: Power values [$\times 10^{-2}$ m^2/cpy] at dominating frequencies for 1-h solutions computed using type-mean and ESM-corrected PCC for 01/01/2011 – 30/06/2011.

	O_1 24.82 h	P_1 24.07 h	diurnal 24 h	K_1 23.93 h	N_2 12.66 h	M_2 12.42 h	S_2 12 h	K_2 11.97 h
$\text{north}_{\text{typ}}$	0.530	0.969	0.995	0.945	0.088	0.523	2.375	0.565
$\text{north}_{\text{esm}}$	0.520	0.987	0.988	0.916	0.088	0.534	2.321	0.429
east_{typ}	0.506	1.727	1.781	1.941	0.162	0.497	0.940	0.415
east_{esm}	0.507	1.813	1.965	2.142	0.156	0.474	0.915	0.292
up_{typ}	0.631	0.946	1.983	1.993	0.163	0.246	2.358	1.847
up_{esm}	0.655	0.954	1.607	1.522	0.179	0.264	2.448	1.897

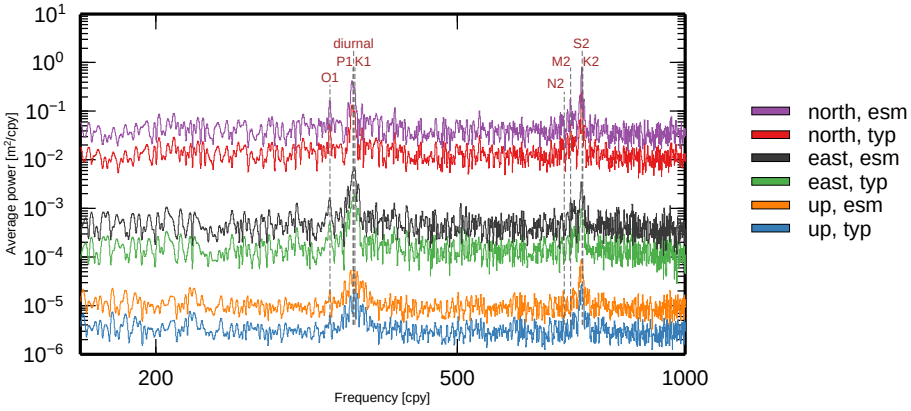

(a) Combined power spectra of hourly solutions obtained for the SPSLux stations using type-mean and ESM-corrected PCC for 01/01/2011 – 30/06/2011. For clarity north and up components have been shifted by +40dB and −40dB, respectively. Additionally, the "ESM-corrected" power spectra are shifted by +10dB with respect to the corresponding type-mean results.

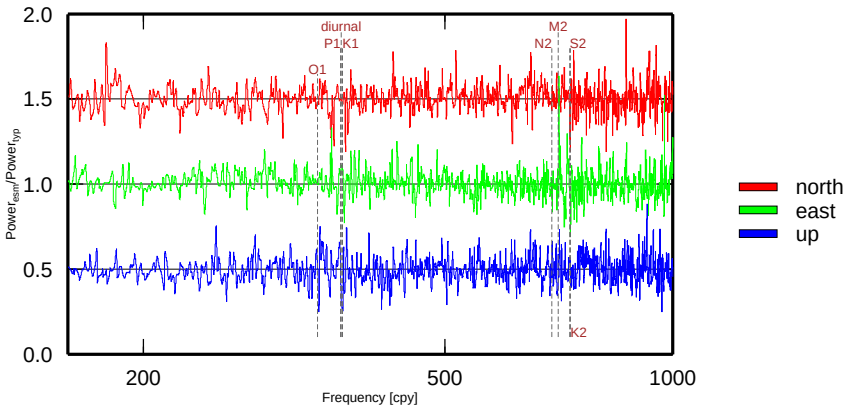

(b) Ratios of the power at respective frequencies in the "ESM-corrected" and "type-mean" PPP runs. North and up components are shifted by +0.5 and −0.5, respectively.

Figure 7.5: "Type-mean" and "ESM-corrected" sub-daily PPP power spectra and their ratios.

conclusions can be outlined. Firstly, the PCC modifications lead to systematic shifts in PPP solutions, which are small for horizontal coordinate components, but may reach several mm in the vertical direction. It should be noted that this is associated with estimation of ZTDs, which are highly correlated with PCC and station heights. Secondly, the repeatability of PPP solutions in the vertical direction is improved for 4 out of 6 stations analysed. This is an indication that the tropospheric estimation may be more accurate when the ESM-corrected PCC are employed. Furthermore, the use of these PCC has resulted in attenuation of harmonic signals with periods close to 24 h and 23.93 h by 19% and 24%, respectively. Additionally, harmonic signals with periods close to 11.97 h in the horizontal components were attenuated. This suggests that overall the ESM-corrected PCC resulted in a reduction of multipath effects and demonstrated good performance, especially in the vertical direction.

7.5 Daily results

It has been shown that the ESM method allows to assess multipath together with other site-specific effects and to reduce their influence on solutions. Additionally, the methodology of the ESM estimation for any site regardless of its location and network affiliation was demonstrated in Section 5.4.2. Also, the details on how this was implemented for the IGb08 core network complemented by stations discussed in Section 4.2 were provided (see Appendix E for the accuracy of the ESMs). Thus, it becomes possible to investigate to what extend site-specific effects propagate into the orbits by analysing those obtained with the type-mean and ESM-corrected PCC.

The basic concept for the PCC impact analysis on both satellite orbits and station coordinates, respecting solution consistency, was discussed in Section 5.7. It involves orbit determination and consecutive PPP processing using different sets of PCC and analysis of the produced results. Such a processing chain is useful as it resembles the one employed within the IGS or commonly used by the geodetic community – typically all parameters are estimated during GNSS processing.

However, one may be interested in avoiding estimation of ZTDs and clock biases and, therefore, directly look at the impact of modifications in the applied PCC on satellite orbits or station PPP solutions. To implement this, clock and tropospheric estimation should not be performed, but accurate estimates of these need to be imported and kept fixed. The description of this approach is given in Section 5.7.2

It should be noted that although the orbit determination runs using type-mean PCC in *Step 1* and *Step 2* in Figure 5.12 are effectively equivalent, the produced orbital solutions in both cases were slightly different. This is caused by differences in the sets of estimated parameters for both cases and the way the parameters are estimated in `Bahn`. Thus, to avoid introducing potential

processing artefacts into the results, all solutions were split into two groups: with estimated and with imported troposphere and clock biases. Then the solutions within each group were compared.

In order to facilitate distinction among different solution sets, the following notations are used hereinafter:

- "$IGSTM_e$" for a solution with the type-mean PCC and estimated troposphere and clock biases;
- "ESM_e" for a solution with the ESM-corrected PCC and estimated troposphere and clock biases;
- "$IGSTM_i$" for a solution with the type-mean PCC and imported troposphere and clock biases that were estimated during the $IGSTM_e$ run;
- "ESM_i" for a solution with the ESM-corrected PCC and imported troposphere and clock biases that were estimated during the $IGSTM_e$ run.

7.5.1 Impact on the orbits

In order to assess the quality of each solution set, in particular, $IGSTM_e$, ESM_e, $IGSTM_i$ and ESM_i, four sets of GPS orbits covering 10 years (2004-2013) were computed. ZTD, clock and station position estimates from solution $IGSTM_e$ were imported into $IGSTM_i$ and ESM_i. Configuration options for each orbit determination run were identical to those discussed in Section 5.2.2, however, it might be useful to list them briefly:

- The network of stations was composed of the IGb08 core network complemented by additional stations mainly located in Europe, taking part in the EPN, GeoNet, SPSLux and NRCan networks.
- The type-mean PCC were used for all stations in $IGSTM_e$ and $IGSTM_i$, whereas the ESM-corrected PCC were used in ESM_e and ESM_i.
- In $IGSTM_e$ and ESM_e, the station coordinates were tightly constrained to the official IGb08 coordinates, propagated to the processing epoch using official IGb08 velocities. Coordinates and velocities in the IGb08 reference frame for the EPN sites were extracted from official EPN solutions. Coordinates and velocities for sites that do not take part in the IGS network or the EPN were estimated using PPP with the IGS final products. In $IGSTM_i$ and ESM_i station coordinates were imported and not estimated.
- Prior to processing the observation data were sampled every 300 s.

- In $\mathrm{IGSTM_e}$ and $\mathrm{ESM_e}$ ZTDs were estimated every 3600 s and tropospheric gradients were estimated once a day. Imported tropospheric estimates were used in solutions $\mathrm{IGSTM_i}$ and $\mathrm{ESM_i}$.

The use of a global network of stations benefited the production of high quality orbits, which in all cases were comparable to those of the IGS. The agreement between the computed and the IGS final orbits was assessed using `OrbComp`, as detailed in Section 6.3.1.

It should be noted that the number of days processed in each particular case slightly varied, possibly due to computational issues. Additionally, due to manoeuvres of particular satellites, which were not taken into account during processing, the combined RMS of the differences in satellite positions (as provided by `OrbComp`) was elevated during some days. In order to exclude possible outliers, a tolerance of 4×IQR was applied, resulting in 96, 89, 79 and 79 days with RMS $\geq (4 \times \mathrm{IQR})$ in solutions $\mathrm{IGSTM_e}$, $\mathrm{ESM_e}$, $\mathrm{IGSTM_i}$ and $\mathrm{ESM_i}$, respectively. As inclusion of these days could bias statistical data, they were removed from further computations.

Table 7.4 summarizes statistical data for the comparison between the IGS final and estimated orbits. As can be seen, the total number of processed days equals 3598, 3598, 3588 and 3587 in solutions $\mathrm{IGSTM_e}$, $\mathrm{ESM_e}$, $\mathrm{IGSTM_i}$ and $\mathrm{ESM_i}$, respectively. However, after excluding outlying days these numbers were reduced to 3502, 3509, 3509 and 3508 in solutions $\mathrm{IGSTM_e}$, $\mathrm{ESM_e}$, $\mathrm{IGSTM_i}$ and $\mathrm{ESM_i}$, respectively. Interestingly, the average RMS (computed across samples with RMS $\leq (4 \times \mathrm{IQR})$) between solutions $\mathrm{IGSTM_i}$ and $\mathrm{ESM_i}$ are nearly identical with 18.42 mm and 18.42 mm, respectively, while those of solutions $\mathrm{IGSTM_e}$ and $\mathrm{ESM_e}$ differ slightly more with 18.33 mm and 18.28 mm, respectively. In turn, this already points at similarities between solutions $\mathrm{IGSTM_i}$ and $\mathrm{ESM_i}$. However, it is worth analysing the DBDs for the orbits before making further conclusions.

Each set of orbits was analysed for overlaps at day boundaries using the model discussed in Section 5.3. Thus, the DBD for each satellite were computed and spectral analysis of the obtained time series was performed using the Lomb-Scargle method. In order to allow more contribution to less noisy time series the periodograms of respective components were weighted according to the inverse of the time series variances and then combined. This was done separately for each solution.

Figure 7.6 shows the results of the spectral analysis of the orbit DBD time series from solutions $\mathrm{IGSTM_e}$ and $\mathrm{ESM_e}$. The power spectra for all orbital components, Figure 7.6a, are very similar in both solution sets, showing sharp peaks at frequencies matching $1.04 \times n$ cpy, where $n = 1, 2, 3, 4, \ldots$ More details on the differences between the two solutions are seen in Figure 7.6b, depicting the power ratios at respective frequencies between solutions $\mathrm{IGSTM_e}$ and $\mathrm{ESM_e}$. Thus, at low frequencies ($\leq$ 10 cpy) all orbital components of solution $\mathrm{ESM_e}$ mainly show reduced power (on average by 2%) compared to solution $\mathrm{IGSTM_e}$, suggesting improvements brought by

Table 7.4: Statistical data for the comparison between the IGS final and estimated orbits.

	$IGSTM_e$	ESM_e	$IGSTM_i$	ESM_i
N_{total}	3598	3598	3588	3587
RMS_{median} [mm]	18.2 $\pm$ 1.8	18.1 $\pm$ 1.9	18.3 $\pm$ 1.8	18.3 $\pm$ 1.8
$N_{RMS\geq (4 \times IQR)}$	96	89	79	79
$N_{RMS< (4 \times IQR)}$	3502	3509	3509	3508
RMS_{mean} [mm]	18.33 $\pm$ 1.39	18.28 $\pm$ 1.41	18.42 $\pm$ 1.42	18.42 $\pm$ 1.41

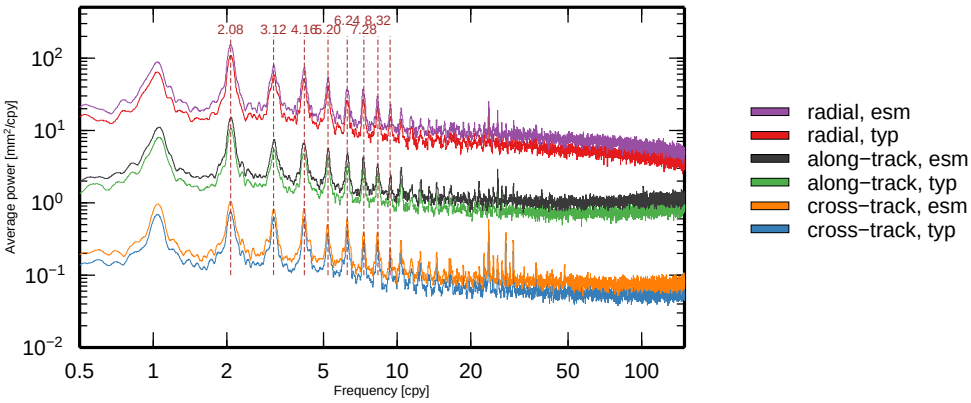

(a) Power spectra of the orbit DBD time series for radial, along- and cross-track components in solutions $IGSTM_e$ and ESM_e for 2004-2014. For clarity radial and cross-track components have been shifted by +20dB and −20dB, respectively. Additionally, the ESM_e power spectra are shifted by +3dB with respect to the corresponding $IGSTM_e$ results.

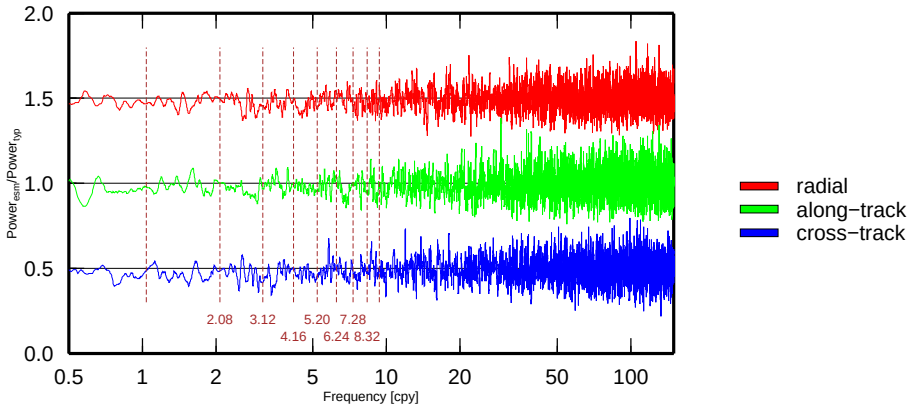

(b) Ratios of the power at respective frequencies in the ESM_e and $IGSTM_e$ orbit determination runs. Radial and cross-track components are shifted by +0.5 and −0.5, respectively.

Figure 7.6: $IGSTM_e$ and ESM_e orbit DBD power spectra and their ratios.

ESM-corrected PCC.

Alternatively, frequency analysis of the orbit DBD time series performed for solutions $IGSTM_i$ and ESM_i shows very little difference (Figure 7.7). Similarly to solutions $IGSTM_e$ and ESM_e, the computed periodograms (Figure 7.7a) show peaks at frequencies matching $1.04 \times n$ cpy, where $n = 1, 2, 3, 4, \ldots$ in both solutions. However, the respective power ratios, Figure 7.7b, reveal no significant changes in the orbit DBD time series due to the performed PCC modifications.

To support the produced results, the exact power values for draconitic frequencies in the computed orbits are provided in Table 7.5. Generally, power at draconitic frequencies for the along-track component is larger than that for the radial and cross-track components. This agrees

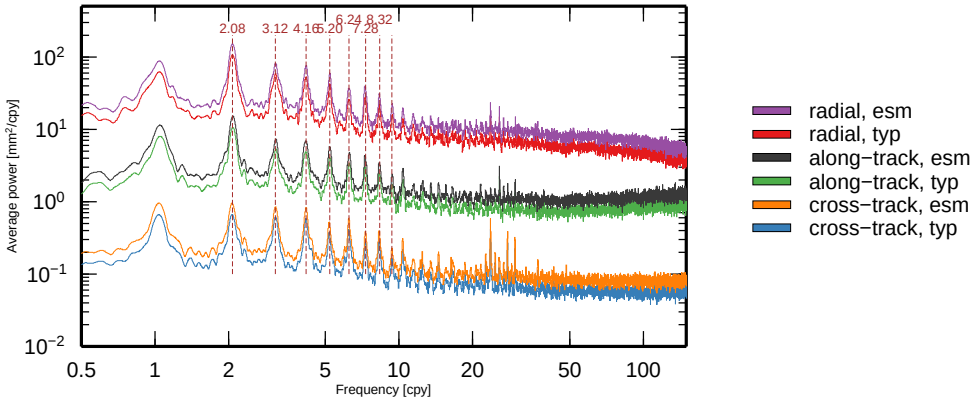

(a) Power spectra of the orbit DBD time series for radial, along- and cross-track components in solutions $IGSTM_i$ and ESM_i for 2004-2014. For clarity radial and cross-track components have been shifted by +20dB and −20dB, respectively. Additionally, the ESM_i power spectra are shifted by +3dB with respect to the corresponding $IGSTM_i$ results.

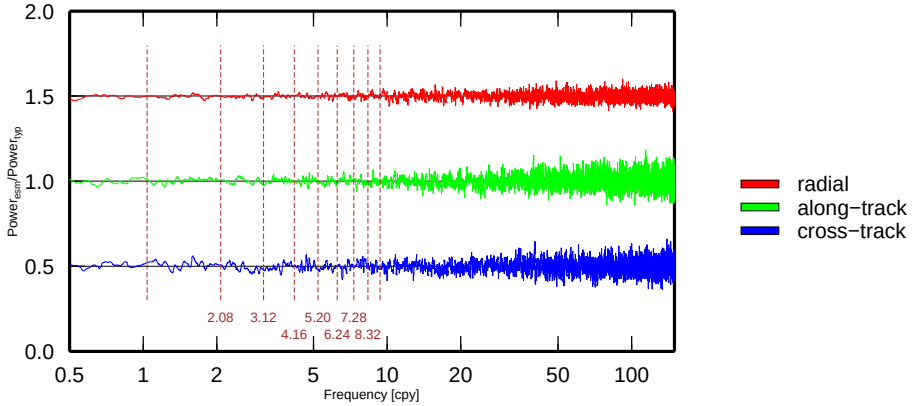

(b) Ratios of the power at respective frequencies in the ESM_i and $IGSTM_i$ orbit determination runs. Radial and cross-track components are shifted by +0.5 and −0.5, respectively.

Figure 7.7: $IGSTM_i$ and ESM_i orbit DBD power spectra and their ratios.

Table 7.5: Numerical values $[mm^2/cpy]$ of the GPS orbit DBD power spectra at harmonics of 1.04 cpy.

Component	Sol.	1.04	2.08	3.12	4.16	5.20	6.24	7.28	8.32	9.36
Radial	$IGSTM_e$	6.40	10.75	5.83	5.17	4.13	2.46	2.58	2.02	1.44
Radial	ESM_e	6.20 (3.2%)	10.71 (0.3%)	5.59 (4.1%)	5.17 (0.0%)	3.86 (6.4%)	2.43 (1.6%)	2.43 (5.8%)	1.99 (1.5%)	1.53 (-6.6%)
Along-track	$IGSTM_e$	7.76	10.58	5.37	4.66	4.12	3.30	2.92	2.48	1.60
Along-track	ESM_e	7.60 (2.1%)	10.58 (-0.0%)	5.21 (3.0%)	4.63 (0.6%)	3.95 (4.3%)	3.41 (-3.6%)	2.93 (-0.3%)	2.35 (5.2%)	1.57 (2.2%)
Cross-track	$IGSTM_e$	6.85	7.43	6.20	5.94	3.45	4.12	2.84	2.59	1.62
Cross-track	ESM_e	6.76 (1.3%)	7.33 (1.4%)	5.70 (8.1%)	5.95 (-0.2%)	3.29 (4.6%)	4.14 (-0.4%)	2.78 (2.2%)	2.52 (2.8%)	1.63 (-0.8%)
Radial	$IGSTM_i$	6.17	10.65	5.82	5.29	4.19	2.51	2.65	2.13	1.52
Radial	ESM_i	6.17 (0.0%)	10.65 (-0.0%)	5.77 (0.8%)	5.31 (-0.3%)	4.21 (-0.5%)	2.50 (0.4%)	2.66 (-0.2%)	2.12 (0.3%)	1.53 (-0.6%)
Along-track	$IGSTM_i$	7.89	10.60	5.26	4.85	4.09	3.30	2.83	2.43	1.64
Along-track	ESM_i	7.98 (-1.2%)	10.66 (-0.6%)	5.14 (2.3%)	4.83 (0.2%)	4.09 (-0.0%)	3.27 (1.0%)	2.87 (-1.5%)	2.44 (-0.3%)	1.64 (0.0%)
Cross-track	$IGSTM_i$	6.60	6.60	6.16	5.83	3.46	4.12	2.76	2.57	1.63
Cross-track	ESM_i	6.73 (-2.1%)	6.66 (-0.9%)	6.03 (2.1%)	5.85 (-0.3%)	3.39 (2.1%)	4.13 (-0.1%)	2.75 (0.5%)	2.62 (-1.9%)	1.60 (1.6%)

Values in brackets indicate improvement in percent with respect to the"type-mean" solution.

with a general rule, according to which the along-track orbital component has larger uncertainties compared to the other two. Overall, solution ESM_e shows better results compared to $IGSTM_e$. Thus, for $n = 1, 3, 5$ and 8, power is attenuated in all three components with maximum reduction of 8.1% ($n = 3$, cross-track). For other n the effect induced by the PCC modifications is less pronounced.

Differences between solutions $IGSTM_i$ and ESM_i are barely visible in the power spectra and power ratios derived from the orbit DBD time series. Presumably, due to multiple stations tracking each satellite, their impact on the orbits is averaged out, leading to almost zero effect. At the same time, the ZTD and clock estimates are sensitive to the changes in PCC. Thus improvements in the GNSS orbit solutions are presumably achieved through a more accurate estimation of these parameters.

Interestingly, while in general the observed power reduces with growing n, for the radial and along-track components, it is ∼50% larger for $n = 2$ compared to that for $n = 1$ in all solutions. The cross-track component behaves differently, as the power for $n = 1$ and $n = 2$ in solutions $IGSTM_i$ and ESM_i are nearly equal, whereas in solutions $IGSTM_e$ and ESM_e only little (∼8%) difference is observed between $n = 1$ and $n = 2$.

At this point it appears that when a global network of stations is employed, PCC have little impact on the estimated orbits. Thus, when the ZTDs and clock biases are imported, the modifications introduced to the PCC are nearly not sensed by the satellites at all, as the latter are observed by multiple stations and the effect is averaged out. However, when the ZTDs together with the satellite and station clock biases are estimated, little improvement in the DBD time-series is observed. As suggested by other studies (e.g., Iwabuchi et al., 2004; Granström, 2006), etc., application of ESMs leads to a more accurate estimation of ZTDs, therefore the benefits from using the ESMs to a large degree are associated with a more accurate estimation of troposphere.

It should be noted that as the obtained periodograms demonstrate the dominating presence of signals at the GPS draconitic frequencies, which have equal power in all solutions, the contribution of the performed modifications in PCC to reducing these signals is indistinct. This suggests that the main contribution to the draconitic signals does not stem from site-specific effects, but rather from errors in EOP tidal models, as suggested by Griffiths and Ray (2013), as well as deficiencies in the solar radiation pressure modelling (Rodriguez-Solano et al., 2013).

7.5.2 Impact on station coordinates

Finally, the performance of the ESM-corrected PCC was assessed based on the computed PPP solutions. Using the orbits discussed in Section 7.5.1, solutions with type-mean and ESM-corrected PCC were obtained and analysed. The results were subdivided into two groups: with estimation of ZTDs and clock biases ($IGSTM_e$ and ESM_e), and with these parameters being imported ($IGSTM_i$

and ESM_i). While solutions $IGSTM_e$ and ESM_e represent a more commonly used scenario, solutions $IGSTM_i$ and ESM_i correspond to *Step 3* in Figure 5.12 and are meant to show more details on the mechanism of the PCC deficiency propagation into the computed station coordinates. Although the changes in PCC have resulted in no significant impact on the orbit overlaps, station coordinates may potentially be more affected, as the latter should be more sensitive to the changes in PCC.

Similar to the orbit determination runs, a priori station coordinates were accurately estimated in the IGb08 reference frame. In particular, for the IGS stations the official station coordinates were used, whereas for the rest of the network the a priori coordinates were estimated following the procedure discussed in Section 6.3. However, unlike in the orbit determination case, very loose constraints ($\sigma = 1\,\mathrm{m}$) were applied to all coordinates during processing.

Observation data for the aforementioned global network were processed from 2004 to 2014. For all obtained CTS, breakpoints were introduced at epochs where changes to antennas or radomes were made. Thus, in total 244 time series were produced, out of which only those covering at least 3 years were considered for consecutive frequency analysis, resulting in 167 time series available for further examination. Due to barely visible differences in the CTS obtained using type-mean and ESM-corrected PCC, these are not shown here. However, all CTS as well as their differences can be found on the supplied CD-ROM.

To prepare the CTS for comparison, the computed coordinates for all stations were converted from Cartesian to topocentric representation. Furthermore, in order to remove potential outliers, a tolerance of 4×IQR was applied to all CTS. Finally, the Lomb-Scargle periodograms were computed for each station and each coordinate component. In order to allow for more contribution from the less noisy time series, the respective periodograms were weighted according to the inverse of the time series variance and combined. This was done separately for all solutions.

The results of the frequency analysis of the PPP time series for solutions $IGSTM_e$ and ESM_e are presented in Figure 7.8. As the same network of stations was used for the preceding orbit determination, during which the station coordinates were tightly constrained to their a priori linearly approximated estimates, the resulting PPP positions, and the derived power spectra, show extremely low noise. However, the presence of harmonic signals at the GPS draconitic frequencies is noticeable in all components, Figure 7.8a. While looking at the differences in the combined periodograms of both solutions, Figure 7.8b, no clear benefits are observed in the scatter of the horizontal components after switching from type-mean to the ESM-corrected PCC. However, the attenuated power spectrum for the vertical component in Figure 7.8b suggests that the repeatability of the respective component of station PPP time series in solution ESM_e is improved compared to that of $IGSTM_e$. Although the reduction is small, it is stable across the entire frequency range, showing on average a ∼1% improvement.

Results of the frequency analysis of PPP CTS in solutions $IGSTM_i$ and ESM_i, where ZTDs and clock biases were imported, are shown in Figure 7.9. The periodograms of both solutions, Figure 7.9a, are very similar, also discovering the harmonic signals at the GPS draconitic frequencies. Differences between the results of both solutions are hardly noticeable, Figure 7.9b.

To support the produced results, the exact power values for the GPS draconitic frequencies in the computed PPP time series are provided in Table 7.6. The actual numerical values for solutions with estimated and imported ZTDs and clock biases are nearly identical. Noteworthy, the estimation of these parameters results in larger variations in the final PPP solutions. However, no clear pattern can be identified at this point to support the idea that the modifications to the

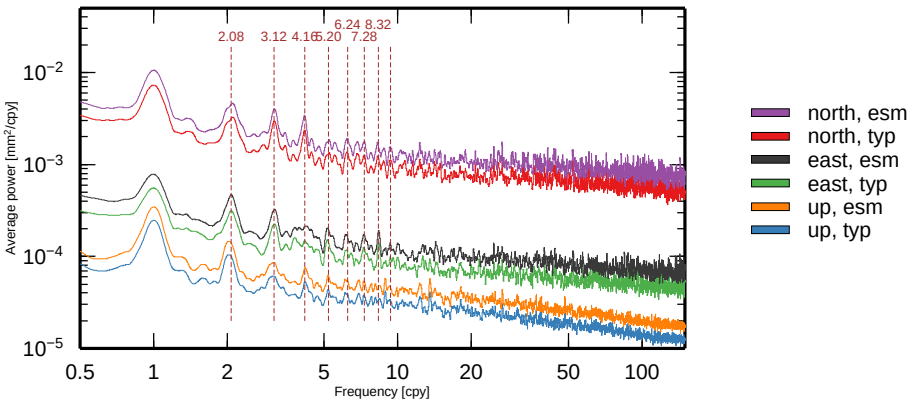

(a) Power spectra of the PPP time series in solutions $IGSTM_e$ and ESM_e for 2004-2014. For clarity north and up components have been shifted by +20dB and −20dB, respectively. Additionally, the ESM_e power spectra are shifted by +3dB with respect to the corresponding $IGSTM_e$ results.

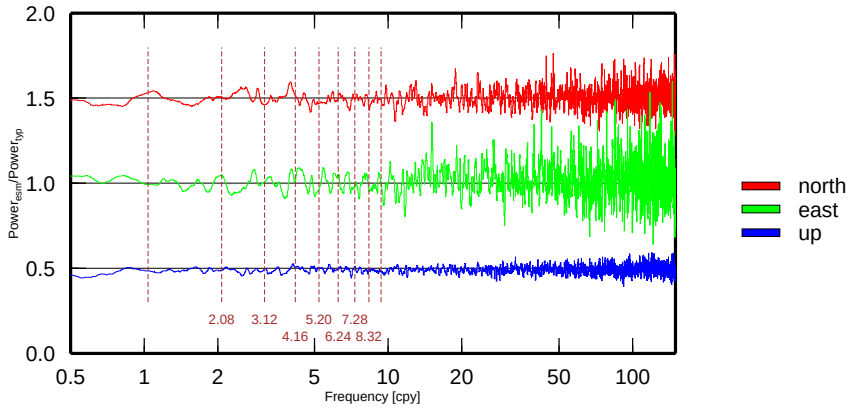

(b) Ratios of the power at respective frequencies in PPP runs of solutions ESM_e and $IGSTM_e$. North and up components are shifted by +0.5 and −0.5, respectively.

Figure 7.8: $IGSTM_e$ and ESM_e PPP power spectra and their ratios.

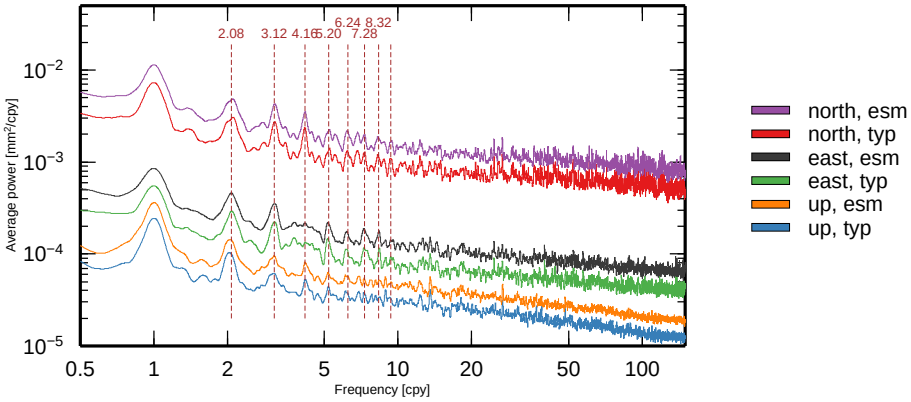

(a) Power spectra of the PPP time series in solutions IGSTM$_i$ and ESM$_i$ for 2004-2014. For clarity north and up components have been shifted by +20dB and −20dB, respectively. Additionally, the ESM$_i$ power spectra are shifted by +3dB with respect to the corresponding IGSTM$_i$ results.

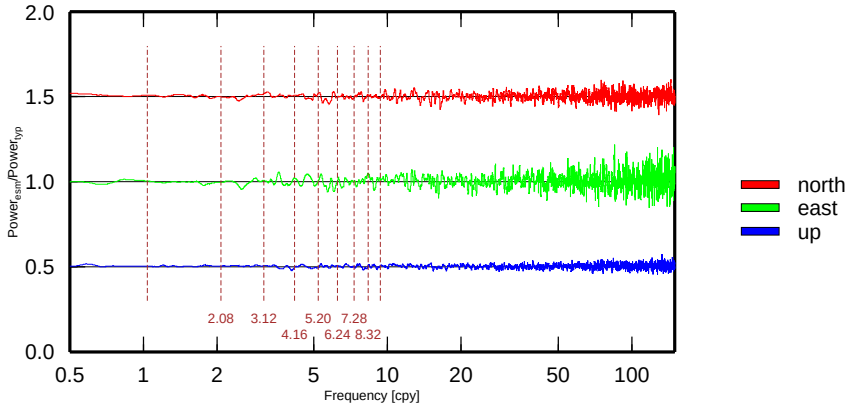

(b) Ratios of the power at respective frequencies in PPP runs of solutions ESM$_i$ and IGSTM$_i$. North and up components are shifted by +0.5 and −0.5, respectively.

Figure 7.9: IGSTM$_i$ and ESM$_i$ PPP power spectra and their ratios.

Table 7.6: Numerical values [$\times 10^{-3}$mm^2/cpy] of the PPP solution power spectra at harmonics of 1.04 cpy.

Component	Sol.	1.04	2.08	3.12	4.16	5.20	6.24	7.28	8.32	9.36
North	$IGSTM_e$	0.68	0.32	0.29	0.24	0.13	0.13	0.13	0.12	0.11
North	ESM_e	0.70 (-3.3%)	0.32 (-0.7%)	0.28 (3.8%)	0.24 (-1.5%)	0.13 (2.9%)	0.14 (-1.1%)	0.12 (0.5%)	0.11 (5.0%)	0.11 (1.4%)
East	$IGSTM_e$	0.52	0.32	0.23	0.15	0.14	0.11	0.13	0.14	0.10
East	ESM_e	0.52 (0.7%)	0.33 (-4.6%)	0.23 (-0.7%)	0.15 (-0.9%)	0.14 (3.5%)	0.11 (-5.1%)	0.12 (1.8%)	0.13 (3.5%)	0.10 (0.5%)
Up	$IGSTM_e$	2.27	1.00	0.61	0.53	0.44	0.38	0.38	0.33	0.33
Up	ESM_e	2.24 (1.5%)	0.99 (0.9%)	0.61 (0.4%)	0.53 (-0.6%)	0.44 (-0.4%)	0.38 (0.6%)	0.38 (-1.2%)	0.33 (1.0%)	0.32 (1.8%)
North	$IGSTM_i$	0.68	0.30	0.27	0.24	0.14	0.13	0.13	0.12	0.11
North	ESM_i	0.68 (-0.9%)	0.30 (0.0%)	0.28 (-1.8%)	0.24 (-0.9%)	0.14 (-1.8%)	0.13 (0.4%)	0.13 (1.0%)	0.12 (-1.4%)	0.11 (0.4%)
East	$IGSTM_i$	0.52	0.29	0.22	0.13	0.14	0.11	0.12	0.11	0.09
East	ESM_i	0.52 (-0.5%)	0.29 (0.3%)	0.23 (-0.8%)	0.14 (-2.3%)	0.14 (-0.4%)	0.11 (-0.6%)	0.12 (-0.1%)	0.11 (-4.9%)	0.10 (-1.4%)
Up	$IGSTM_i$	2.25	1.00	0.61	0.53	0.44	0.37	0.38	0.33	0.32
Up	ESM_i	2.26 (-0.4%)	1.00 (-0.4%)	0.62 (-0.8%)	0.53 (0.4%)	0.44 (0.4%)	0.38 (-0.8%)	0.38 (-0.2%)	0.33 (-0.7%)	0.32 (-0.7%)

Values in brackets indicate improvement in percent with respect to the "type-mean" solution.

PCC help to reduce the GNSS-specific signals in solutions.

7.5.3 Impact on the number of accepted observations

As the ESMs are based on phase residuals, their application should correct (delay or advance) the GNSS signals, thus, reducing the magnitude of these residuals. The impact of the application of the ESM-corrected PCC was discussed in Section 5.4.2 and the respective reduction in the magnitude of the phase residuals was demonstrated (Figure 7.2). As a consequence, this should be reflected in the number of observations that are finally accepted after the least-squares adjustment in `Bahn`. Because of identical convergence criteria in `Bahn` in all orbit determination or PPP runs, the number of accepted observations due to application of the type-mean and ESM-corrected PCC should be affected. The higher number of accepted observations would indicate a better "fit" of the applied PCC and, thus, give another appraisal of the processing quality.

As the number of stations in the processed network was changing, only the differences between the daily numbers of accepted observations were analysed. Plots showing differences in the numbers of accepted observations and corresponding histograms are shown in Figure 7.10. The results from the comparison of the number of observations in orbit determination runs of solutions $\mathrm{IGSTM_e}$ and $\mathrm{ESM_e}$, Figure 7.10a, suggest that the use of the ESM-corrected PCC leads to an increase in the number of accepted observations. Thus, the daily ratio of the difference in the number of accepted observations in solutions $\mathrm{IGSTM_e}$ and $\mathrm{ESM_e}$ to the number of accepted observations in solution $\mathrm{IGSTM_e}$ was computed. The median value of this ratio for 2004 to 2014 was -2.8×10^{-5}, suggesting that on average the use of the ESM-corrected PCC was more advantageous.

Although the number of accepted observations of solution $\mathrm{ESM_e}$ is in general larger compared to that of $\mathrm{IGSTM_e}$, an anomaly is observed from mid-2009 to mid-2010. As seen in Figure 7.10a, during this period the ESM-corrected PCC demonstrate poor performance, as the number of accepted observations is decreased compared to solution $\mathrm{IGSTM_e}$. The reason for this anomalous behaviour, however, was not identified, as this neither coincides with any large modifications of the observation network, nor with any other events, e.g., earthquakes that could have resulted in significant crustal displacements, and, consequently, affect the employed stations, etc.

Interestingly, in solutions with imported ZTDs and clock biases the use of the ESM-corrected PCC does not bring benefits in terms of the number of accepted observations (Figure 7.10b). Similar to the previous analysis, the daily ratio of the difference in the number of accepted observations in solutions $\mathrm{IGSTM_i}$ and $\mathrm{ESM_i}$ to the number of accepted observations in solution $\mathrm{IGSTM_i}$ was computed. The median value of this ratio for 2004 to 2014 was 6.3×10^{-6}, suggesting a little degradation of solution $\mathrm{ESM_i}$ with respect to $\mathrm{IGSTM_i}$. This is most likely the result of merging inconsistent data, as the imported ZTDs and clock biases were estimated using the type-mean PCC, and therefore, fixing these estimates does not allow for their fitting to the ESM-

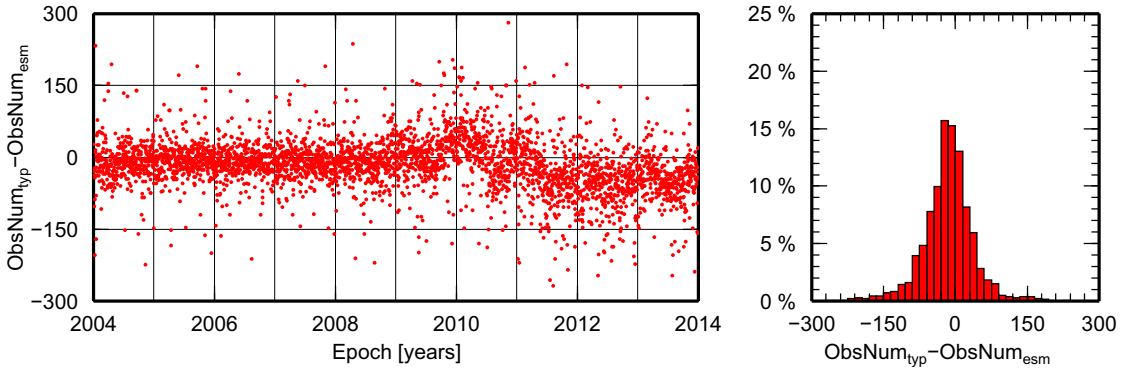

(a) Differences in the number of accepted observations in solutions $IGSTM_e$ and ESM_e.

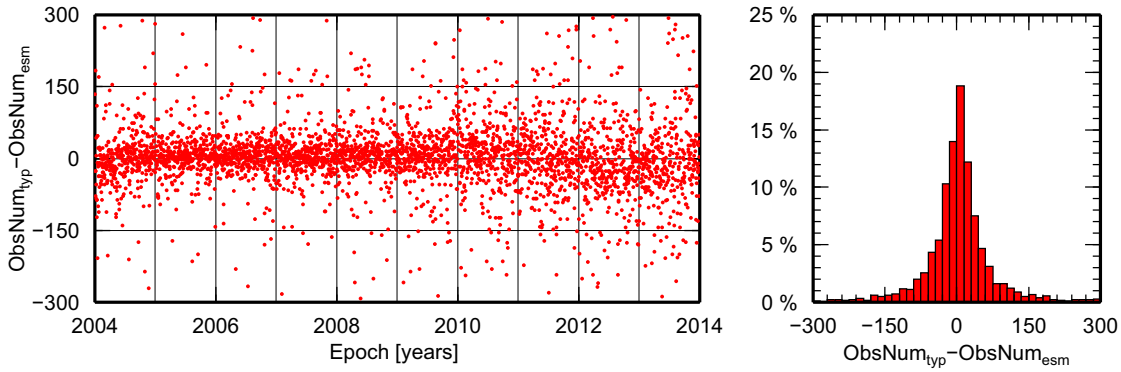

(b) Differences in the number of accepted observations in solutions $IGSTM_i$ and ESM_i.

Figure 7.10: Impact on the number of accepted observations after application of the ESMs in the orbit determination runs.

corrected PCC employed in solution ESM_i.

While analysing both Figures 7.10a and 7.10b, the scatter of the differences increases after 2010. Potentially, this is related to the aforementioned anomaly in solutions $IGSTM_e$-$IGSTM_e$ around 2010.0, however, the exact reason for such behaviour could not be identified.

7.5.4 Impact of ESMs on estimated ZTDs

Similar to the evaluation discussed in Section 6.4.5, ZTD estimates computed using ESM-corrected PCC were compared to those obtained with the type-mean ones. For consistency with the already described ZTD analysis the same procedure was used to obtain tropospheric estimates this time using the ESM-corrected PCC. In particular, orbit determination using a global network of GNSS stations was performed with tight constraints applied to station coordinates. Hourly ZTDs for the stations discussed in Section 4.2 were extracted for further assessment. As for the analysis discussed in Section 6.4.5, the dataset from 01 to 30 May 2013 was considered.

The ZTD results obtained using ESM-corrected PCC ("ESM-corrected" ZTDs) are similar to those computed using the type-mean antenna/radome models ("type-mean" ZTDs). The comparison results is summarized in Table 7.7. On average for all examined stations the introduced PCC modifications result in a negligible shift in the ZTDs of only 0.1 mm. The mean standard deviation of the ZTD differences across all stations reached only 0.9 mm with absolute minimum and maximum differences of −16.5 mm and 15.7 mm, respectively. However, some stations, in particular, BADH, CANT and METS are much more affected by the modifications in the PCC. The absolute average difference in the estimated ZTDs for these stations over 30 days ranges from 3.0 mm to 8.8 mm.

The increase of the mean standard deviation of the ZTD differences compared to that demonstrated in Section 6.4.5 (Table 6.8), shows a higher variability of the "ESM-corrected" ZTDs with respect to the "type-mean" estimates than the ZTDs obtained using individual PCC. In turn, this gives an indication that ESM-corrected PCC may provide more accurate ZTD estimates at individual epochs, resulting, in particular, in a more accurate estimation of station heights, as was shown for sub-daily PPP results discussed in Section 7.4.

The GNSS-derived ZTDs computed using ESM-corrected PCC for several stations were also compared to the respective RS estimates. The selected pairs of GNSS stations and RSs were discussed in Section 6.4.5. For these 11 pairs (see Table 6.9) separations between GNSS stations and RS launching sites were less than 50 km.

Figure 7.11 demonstrates the evolution of ZTDs at station CANT computed using type-mean and ESM-corrected PCC and their differences. RS-derived ZTD values are also shown for comparison. Interestingly, the use of the ESM-corrected PCC for this station results in an increase of the estimated ZTDs by 3.8 mm on average over 30 days. It should be noted that the shift in the ZTDs increased the bias between the GNSS- and RS-derived tropospheric estimates from 1.6 mm to 5.1 mm. The observed biases, however, are rather small and may be attributed to assumptions and simplifications in ZTD computations from RS data discussed in Haase et al. (2003) and also used in this study. ZTD plots for other stations listed in Table 6.9 are provided on the supplied CD-ROM.

Differences between ZTDs from 11 pairs of GNSS stations and located nearby RSs are summarized in Table 7.8. The results suggest that overall the switch from type-mean to ESM-corrected PCC did not have a big impact on the estimated ZTDs. Due to changes in the PCC the mean bias in ZTDs across 11 GNSS-RS pairs reduced from −0.7 mm to −0.6 mm, whereas the standard deviation over all assessed GNSS-RS ZTD differences did not change remaining at the level of 10.3 mm. No significant changes were also observed in the minimum and maximum ZTD differences across all GNSS-RS pairs over the period of 30 days.

Table 7.7: Differences between ZTDs computed using type-mean and ESM-corrected antenna/radome PCC. All values are in $[mm]$.

GNSS station	Bias	Std. dev.	Difference		GNSS station	Bias	Std. dev.	Difference	
			Min.	Max.				Min.	Max.
ALAC	−1.4	1.1	−10.7	7.0	KEPA	0.8	0.8	−3.5	4.0
ANKR	0.2	0.7	−3.8	2.6	KLOP	1.8	0.7	−3.2	4.7
BADH	3.0	1.0	−1.4	12.1	METS	−8.8	1.4	−16.5	−4.5
BASC	0.6	0.8	−6.2	4.0	NICO	−0.3	0.9	−4.9	3.8
BORJ	1.2	0.7	−2.1	5.0	ORID	0.6	0.7	−5.8	2.8
BUCU	−1.1	0.8	−5.8	4.7	PENC	0.8	0.9	−4.2	8.2
BUTE	0.2	0.8	−4.2	4.1	POTS	2.3	0.8	−2.7	4.9
CANT	−3.8	1.0	−8.8	−0.1	REYK	2.6	1.4	−6.9	9.3
DRES	1.2	0.8	−2.9	4.8	ROUL	0.2	0.6	−4.3	3.6
ECHT	−0.6	0.7	−5.9	5.6	SASS	1.2	0.8	−2.8	6.2
ERPE	0.2	0.9	−4.3	6.8	TORI	1.2	1.3	−5.1	13.4
EUSK	−0.6	0.6	−3.4	3.3	TROI	−0.2	0.6	−4.6	6.1
FLIN	−0.2	1.0	−5.7	15.7	TUBO	0.2	0.8	−4.1	7.3
GANP	−0.7	0.7	−4.5	3.4	VALE	−0.8	1.0	−4.3	6.0
HELG	−0.5	1.1	−5.3	5.9	WALF	0.1	0.5	−4.3	4.9
HOBU	1.8	0.8	−2.9	6.3	WARN	0.5	0.7	−3.3	3.8
HOE2	0.0	0.7	−1.6	1.8	WTZR	1.1	1.2	−3.6	7.5
HOFN	1.0	1.0	−4.4	5.5	ZIM2	−1.9	0.7	−5.7	2.3
KATO	−0.7	0.7	−4.5	4.2	ZYWI	1.0	0.8	−4.5	6.6
All	0.1	0.9	−16.5	15.7					

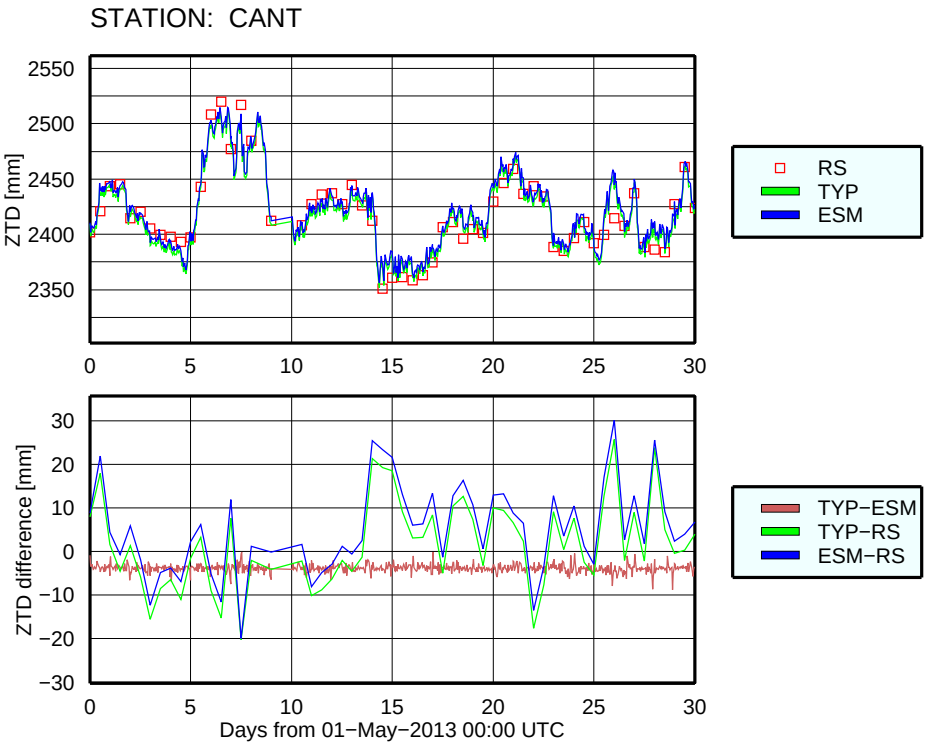

Figure 7.11: ZTD estimates at station CANT from GNSS analysis using type-mean and ESM-corrected PCC and from RS data as well as their differences.

Table 7.8: Differences between GNSS ZTDs computed using type-mean and ESM-corrected PCC and the respective radiosonde data for 01-30 May 2013. All values are in $[mm]$.

GNSS station	$ZTD_{GNSS\ TYP}$ - ZTD_{RS}				$ZTD_{GNSS\ ESM}$ - ZTD_{RS}			
	Bias	Std. dev.	Min. diff.	Max. diff.	Bias	Std. dev.	Min. diff.	Max. diff.
ANKR	−0.7	9.4	−18.9	20.6	−1.0	9.5	−19.1	20.6
BUCU	−6.6	10.5	−38.6	17.9	−5.6	10.2	−37.9	18.6
BUTE	−1.6	7.6	−15.1	13.5	−2.0	7.8	−17.1	11.3
CANT	1.6	10.0	−20.2	25.7	5.1	10.2	−19.9	30.1
GANP	3.4	12.1	−27.1	24.4	3.9	12.2	−26.9	25.1
HOBU	3.1	11.8	−26.2	43.6	1.5	11.7	−28.2	41.4
NICO	1.1	7.7	−13.0	13.7	1.7	7.8	−12.5	14.2
PENC	0.2	12.4	−24.9	21.2	−0.5	12.5	−25.6	20.2
REYK	−14.5	11.2	−63.0	11.2	−17.2	11.2	−65.0	8.2
SASS	−4.5	11.5	−34.0	27.9	−5.8	11.4	−36.1	27.1
ZIM2	10.7	6.8	−13.7	23.8	12.8	6.7	−10.5	25.7
All	−0.7	10.3	−63.0	43.6	−0.6	10.3	−65.0	41.4

7.6 Summary

The ESM performance was evaluated from different perspectives. As the ESM method suffers from weaknesses related to its performance at sites with low monument heights (Moore et al., 2014), the ESM for the IGS station BOGT with 0.1 m monument height was analysed for 3 consecutive years. The observed repeatability of the computed ESM and the reprocessed results with the ESM applied validated the method for further usage. Additionally, the topic of the differences between PCC and ESM was addressed.

Performance of the ESM-corrected PCC in sub-daily and daily positioning was analysed. For the sub-daily analysis a small network of 6 SPSLux stations (Luxembourg) was used, whereas for the daily positioning data from a large network of globally distributed stations were employed. The use of the global network allowed to estimate orbits of a high quality and favoured investigation of the PCC error propagation into them. Also, the time series of the daily positions were inspected for repeatabilities.

Sub-daily results. The details of the investigation results are summarized in the following:

- Analysis of the sub-daily pseudo-kinematic PPP solutions of the SPSLux stations obtained using the type-mean and ESM-corrected PCC has shown that the latter favour attenuation of harmonic signals with frequencies close to the GPS orbital repeat. This attenuation was primarily observed in the vertical component. The vertical component was also marked by improved repeatabilities of solutions. At the same time, the horizontal components, in particular, the north direction, remained almost unaffected. Little degradation, however, was observed in the east component.

  As the lunisolar diurnal and semi-diurnal tidal constituents have periods close to 23.93 h and 11.97 h, the observed attenuation of harmonic signals may be beneficial for tidal modelling.

- The use of the ESM-corrected PCC resulted in systematic shifts in solutions. The east and the vertical component were the ones affected most, as the observed shifts reached up to several mm. Those in the north direction remained below 1 mm. However, only 5 of 18 shifts were statistically significant (at the 1-σ level). The elevated shifts in the vertical direction are most likely associated with the estimation of tropospheric delays, as they are highly correlated with PCC and the estimated station heights.

Additionally, the ESM-corrected PCC were applied on a global scale to assess their impact on the estimated satellite orbits as well as on PPP solutions. After estimating satellite orbits with type-mean and ESM-corrected PCC, station positions were recomputed with the respective orbit sets. This was done to achieve homogeneity in the processing. The orbit quality was evaluated

based on the orbit overlaps at day boundaries (DBD). Both orbit estimation and the consequent PPP processing was performed twice: with estimation of ZTDs and clock biases, and with these parameters imported and kept fixed. This was done to facilitate investigation of propagation of errors induced by deficiencies in the antenna PCC into the estimated ZTDs and clock biases.

Daily results. The following summarizes details of the ESM-corrected PCC performance for processing of a global network of stations:

- When tropospheric delays and clock biases are imported and fixed, the performed modifications to the PCC are not sensed by satellites, as judged from the power spectra of the orbit DBD time series. As each satellite is observed by multiple stations, the introduced PCC modifications are averaged out. Also, nearly no changes to the constellation-specific frequencies were identified in the consecutive PPP solutions.

- When tropospheric delays and clock biases are estimated, little improvements in computed orbits are observed. The frequency analysis of the orbit DBD time series has shown that positive changes are mainly observed at low frequencies ($\leq$10 cpy), whereas no significant changes were noted in the upper frequency range. Since the use of ESM-corrected PCC is known to have a positive effect on the ZTD estimation (e.g., Iwabuchi et al., 2004; Granström, 2006), the observed improvements are presumably due to a more accurate estimation of delays caused by neutral atmosphere.

- Additionally, little ($\sim$1%) improvement in station vertical coordinate scatter was observed in a homogeneous and consistent processing employing ESM-corrected PCC with estimation of ZTDs and clock biases. The horizontal coordinate components of stations were also slightly affected due to modifications in the PCC, however, no systematic improvement or degradation, as judged from the computed power spectra, was noted. Similar to the improvements observed in the orbits, the observed positive changes in vertical coordinate component of stations are presumably associated with a more accurate estimation of ZTDs at individual epochs.

- Another valuable discovery is associated with the number of accepted observations. The use of the ESM-corrected PCC has resulted in a lower rejection rate of observations in the least-squares adjustment in NAPEOS compared to the "type-mean" processing . The average improvement was little ($\sim$0.0028%), however, this is regarded as an indication of the ESM-corrected PCC models outperforming the type-mean PCC models.

- Analysis of the estimated ZTDs computed using type-mean and ESM-corrected PCC over 30 days showed that on average the introduced impact at majority of stations was insignificant.

At some stations, however, the use of the ESM-corrected PCC resulted in shifts in the estimated ZTDs up to 8.8 mm compared to the type-mean results. Comparison to the RS data did not show any improvements in the ZTDs, but these may remain unrevealed due to low sampling of RS data. This assumption is supported by increased variability of "ESM-corrected" ZTDs compared to the respective "type-mean" estimates.

Although the ESM-corrected PCC performed better than the type-mean PCC models, their full potential presumably remained hidden behind the high-power GPS-specific signals observed in the produced solutions. The results confirm that errors in the EOP and solar radiation modelling are predominantly responsible for these spurious signals.

Chapter 8

Conclusions

This thesis presents a thorough study of the impact of ground station antenna/radome phase centre corrections (PCC) on GNSS solutions, in particular, on computed satellite orbits and station positions. Two aspects have been investigated: the use of antenna-specific (individual) PCC models instead of the International GNSS Service (IGS) type-mean PCC models and development of empirical site models (ESMs) for mitigation of multipath and site-specific effects. As the individual PCC for antenna/radome combinations are estimated by only a few agencies worldwide, their availability on a global scale is very limited. The ESM-corrected PCC are aimed to overcome this problem, as they can be estimated for any station that has a sufficient amount of observations and, thus, global solutions can be produced.

Due to a repeating satellite-station geometry (e.g., sidereal periodicity for GPS), deficiencies in station PCC may result in harmonic signals in GNSS solutions. Because of this the current work is particularly focused on the impact of employed PCC on generation of the constellation-specific harmonic signals in solutions that may potentially correlate with other geophysical signals and deteriorate their estimation and modelling. The GPS data were used for all analysis, however, this work can be easily extended onto GLONASS or other GNSS, provided that enough observation data are available. Respecting GLONASS, which has a full set of satellites in its constellation, integer phase ambiguity resolution is not yet fully supported for it by GNSS processing software packages. In turn, this may impose limitation on the quality of results.

8.1 Summary of the results

Individual and type-mean antenna/radome PCC differences. Despite continuous efforts of the IGS to ameliorate their products, in particular, the type-mean antenna/radome PCC, these were shown to be far from being well suitable for all antennas employed by the geodetic community.

- Due to manufacturing processes and physical properties of materials, individual PCC for the IGS-standard choke ring geodetic antennas within the same model range may significantly vary from each other, showing differences up to ∼4 mm and ∼2.8 mm for the GPS L_1 and L_2 frequencies.

- The use of an averaged type-mean model for antennas within the same model range inevitably leads to inaccuracies in solutions.
- Once installed, antennas may suffer from potential unaccounted site-effects, e.g., electromagnetic coupling between antenna and monument, and multipath. This may result in further deviations of the antenna phase centre from the applied models.

The impact from using individual instead of the type-mean PCC on GNSS solutions was studied based on the data of three regional networks in Europe. The total number of antenna/radome combinations included in the study reached 76, representing typical examples of equipment widely used within national and international geodetic networks. Additionally, the IGb08 core network was used as a base network to support global solutions due to the necessity to ensure uniform and global coverage. The IGb08 core network complemented by additional stations was also used for validation of orbit determination processing sequences and estimation of products (clock biases, tropospheric delays) that were reused in consecutive analyses.

Empirical site models. In order to account for potential site-specific effects, a method based on post-fit phase residuals, which included construction of ESMs, was adopted. Additionally, it was adapted for the employed GNSS processing software package (NAPEOS).

- The GPS L_1 and L_2 phase residuals were reconstructed from the ionosphere-free phase residuals. Additionally, spherical harmonic fits to the reconstructed residuals were performed. Finally, the ESM-corrected PCC in the IGS-compliant (ANTEX) format were obtained. In turn, this ensured versatility due to compatibility of the derived PCC with various GNSS software processing packages.

Benefits from using the individual and ESM-corrected instead of type-mean PCC for GNSS solutions were assessed based on historical GPS datasets covering the period from 2004 to 2014. For this period quality of the GPS orbits computed using different sets of PCC was assessed based on their overlaps at day boundaries (day boundary differences; DBDs). Additionally, precise point positioning (PPP) coordinate time series (CTS) obtained in a consistent manner (i.e., keeping the same set of PCC for orbit estimation and consecutive PPP processing), as well as zenith tropospheric delays (ZTDs) were analysed.

Impact of individual PCC on solutions. Despite the small deviations of the individual from type-mean PCC, the use of antenna-specific models was beneficial for both orbit determination and consecutive PPP. The sub-daily PPP solutions revealed neither positive, nor negative changes after switching the PCC. However, the impact on computed orbits was more extensive, resulting in overall improvement of computed orbits and station CTS.

- The analysis of sub-daily PPP solutions revealed no significant changes from using the individual instead of the type-mean PCC. The sub-daily coordinate repeatabilities were not affected.

- The use of individual PCC resulted in biases in sub-daily PPP solutions. While for the horizontal components these did not exceed 0.76 mm, biases of up to 7.2 mm were observed in the vertical direction.

- Despite inevitably elevated uncertainties in orbits computed using a regional network of stations irrespectively of the employed set of PCC, the solutions obtained with individual PCC showed up to 44% reduced DBDs and up to 54% (for vertical component) reduced scatter of daily PPP solutions.

- No particular attenuation at the constellation-specific (draconitic) frequencies was observed in the solutions.

- The observed improvements are most likely associated with a more optimal correction of raw observations by individual PCC, leading to a reduced number of rejected measurements during the least-squares adjustment, and, consequently, a more constrained and robust solution.

- Comparison of ZTD estimates obtained using type-mean and individual PCC on average did not reveal much impact from switching the PCC. However, the observed results are associated with tight constraints imposed on station coordinates and loosening the these may show different results. The computed ZTDs showed very good agreement with the respective radiosonde-derived (RS) measurements regardless of the PCC choice.

However, it should be noted that in case of a globally distributed network the introduction of individual PCC for a limited set of stations may not lead to such a dramatic improvement in the solutions. The impact may potentially be more significant over areas with a sparse distribution of stations, e.g., in the Southern Hemisphere (the Indian and Pacific oceans, Antarctica), if individual PCC for these stations are used instead of the type-mean models.

The obtained results suggest that the use of antenna-specific (individual) instead of the IGS type-mean PCC is expected to positively affect uncertainties of solutions. This involves improvements in satellite orbits and station coordinates, and benefits for studies of geophysical processes, e.g., tectonic plate motion, tidal and non-tidal deformations, and glacial isostatic adjustment.

Impact of ESMs on solutions. The use of the ESM-corrected PCC was evaluated based on the analyses of both sub-daily and daily PPP solutions as well as of the satellite orbits. In all

PPP solution types the most significant improvements were observed in the vertical coordinate components where the scatter of solutions was reduced. At the same time, observed impact on the horizontal coordinate components was marginal. The orbital solutions computed using a global network consisting of up to 131 stations were also very little affected. However, the use of the ESM-corrected PCC marked positive trends in increasing robustness of solutions through a more accurate adjustment of raw observations and, consequently, a reduction of the multipath effect.

- The analysis of sub-daily PPP solutions obtained using ESM-corrected PCC revealed positive trends in reducing scatter of computed station heights. This effect was observed at 4 out of 6 investigated stations.

- The derived ESM-corrected PCC proved their efficiency in reducing multipath, which was shown through attenuation of harmonic signals at the constellation-specific frequencies (i.e., with periods close to 23.93 h and 11.97 h). This may have a positive impact on tide-related studies using GNSS, as the aforementioned signals have frequencies similar to K_1 and K_2, which are the lunisolar diurnal and semi-diurnal tidal constituents, respectively.

- In order to provide an indication of potential improvements from using ESMs on a global scale, the GPS orbits were computed with altered PCC (PCO only). The analysis of the DBDs demonstrated the potential of ESMs to improve the power spectra of solutions primarily at low frequencies (< 5 cpy).

- Analysis of daily solutions using the ESM-corrected PCC has shown very little impact on the power spectra of the computed orbit DBDs. The observed power at low frequencies ($\leq$10 cpy) was reduced, on average, by 2%.

- The power spectra of all solutions indicated the persisting presence of harmonic signals at the GPS-specific (draconitic) frequencies. This suggests that the contribution of deficiencies in PCC in generation of those signals is presumably low.

- The PPP CTS obtained with the ESM-corrected PCC in a consistent processing showed reduced scatter in the vertical direction, compared to the solutions obtained with the IGS type-mean PCC. It should be noted that these improvements are most likely associated with more accurate estimates of tropospheric delays. This conclusion is based on the analysis of series of solutions with different sets of PCC in which tropospheric delays were imported and kept fixed. Modifications in the PCC had nearly no impact on solutions (orbits and PPP coordinates) when tropospheric delays were not estimated. This correlates with the previous studies of Iwabuchi et al. (2004) and Granström (2006), suggesting improvements in tropospheric estimation due to the use of ESM.

- Another positive aspect in using the ESM-corrected PCC consists in a more accurate adjustment of raw observations, resulting in an increased amount of accepted data compared to processing with the IGS type-mean PCC. In turn, this finding indicates a potentially increased robustness of obtained solutions, however, the author admits that this increase was not permanent throughout the entire processing interval. This may be associated with low temporal resolution of the ESMs (new ESMs were estimated only when changes to antennas or radomes occurred) or other reasons, e.g., inaccurate a priori coordinates for stations, undocumented modifications of antennas and radomes, etc. The exact reason for this could not be identified.

- Despite the expectations, analysis of the ZTD estimates obtained using type-mean and ESM-corrected PCC for a set of 38 stations on average did not reveal any notable improvement. These findings are also supported by comparison of the ZTDs with the respective RS-derived measurements. However, noteworthy are shifts up to 8.8 mm in ZTDs averaged over 30 days at individual stations due to the PCC switch despite the tight constraints applied to station coordinates. These are expected to be amplified if the constraints are loosened.

8.2 Recommendations for future work

The persisting presence of the GPS draconitic signatures in all solutions suggested that their main contributors (EOP, solar radiation modelling errors, etc.) were masking potential benefits from using the individual and ESM-corrected PCC. Reprocessing with these models improved may reveal more benefits from using the ESM-corrected PCC.

The methodology of the ESM estimation could be improved, firstly, by modifying the ESM validity period, or setting a sliding window for the accumulation of residuals. Also, alternative algorithms may be applied for spherical harmonic representation of the data. The method employed in this study may potentially introduce artefacts in the boundary regions, i.e, around the areas with no data. Different approaches may include the use of scalar spherical harmonics with vector coefficients or spherical cap harmonics.

The little improvements observed with the ESM-corrected PCC were presumably achieved partly due to the improved estimation of tropospheric delays. However, the low sampling of RS-derived measurements was insufficient to derive any meaningful conclusion. As a recommendation for future work the ZTD estimates from other sources, e.g., microwave radiometers designed to provide continuous measurements of the atmosphere should be used. Alternatively, numerical weather prediction models that assimilate measurements from various techniques can be employed.

Instead of the Global Mapping Function (GMF) for tropospheric delays that was used in all computations in this work Vienna mapping functions (VMF) can be employed. In addition

to potential improvements of the estimated tropospheric delays, these may further increase both accuracy and precision of computed ESMs and highlight their contribution to providing corrections for antenna/radome combinations.

Modifications in the ground-based antenna/radome PCC may result in changes of the satellite-based PCC, as the latter are defined using GNSS observations through fixing the TRF scale (Schmid and Rothacher, 2003). As the use of the individual PCC may result in significant biases in coordinate solutions, this may have an impact on the satellite PCC. Although the number of stations with individual PCC is limited, their impact on the satellite PCC should not be underestimated. The same refers to the PCC modifications brought by the ESMs. This outlines one of the directions for future work.

This study was limited to GPS only primarily because of the phase integer ambiguity resolution, fully supported by NAPEOS for this GNSS. However, GLONASS is fully operational and other GNSSs emerge. Thus, the research could be extended to other GNSS provided that sufficient amount of data is available. This includes not only the observation data, but also individual PCC for the selected GNSS. It should be noted that no individual PCC are yet available for, e.g., Galileo or BeiDou, however, this may improve in the future. Also, the methodology of the ESM derivation for other GNSS is similar to the one presented in this study and may be directly applied irrespective of the type of orbit employed.

Considering draconitic periods for GLONASS and Galileo being 353.2 days and 355.6 days, respectively (Meindl, 2011), the corresponding signals from GPS, GLONASS and Galileo may amplify each other. Therefore, the multi-GNSS analysis in the context of draconitic signatures from these systems is expected to be very beneficial for future products of satellite geodesy.

References

Agnew, D. C., Larson, K. M., 2007. Finding the repeat times of the GPS constellation. GPS Solutions 11 (1), 71–76.

Ahmed, F., Václavovic, P., Teferle, F. N., Douša, J., Bingley, R., Laurichesse, D., 2016. Comparative analysis of real-time precise point positioning zenith total delay estimates. GPS Solutions 20 (2), 187–199.

Alber, C., Ware, R., Rocken, C., Braun, J., 2000. Obtaining single path phase delays from GPS double differences. Geophysical Research Letters 27 (17), 2661–2664.

Altamimi, Z., Collilieux, X., 2009. IGS contribution to the ITRF. Journal of Geodesy 83 (3-4), 375–383.

Altamimi, Z., Collilieux, X., Legrand, J., Garayt, B., Boucher, C., 2007. ITRF2005: A new release of the International Terrestrial Reference Frame based on time series of station positions and Earth Orientation Parameters. Journal of Geophysical Research 112 (B9).

Altamimi, Z., Collilieux, X., Métivier, L., 2011. ITRF2008: an improved solution of the international terrestrial reference frame. Journal of Geodesy 85 (8), 457–473.

Altamimi, Z., Métivier, L., Collilieux, X., 2012. ITRF2008 plate motion model. Journal of Geophysical Research 117 (B7).

Amiri-Simkooei, A. R., 2013. On the nature of GPS draconitic year periodic pattern in multivariate position time series. Journal of Geophysical Research: Solid Earth 118 (5), 2500–2511.

Axelrad, P., Comp, C. J., MacDoran, P. F., 1996. SNR-based multipath error correction for GPS differential phase. Transactions on Aerospace and Electronic Systems, IEEE 32 (2), 650–660.

Baire, Q., Bruyninx, C., Legrand, J., Pottiaux, E., Aerts, W., Defraigne, P., Bergeot, N., Chevalier, J. M., 2014. Influence of different GPS receiver antenna calibration models on geodetic positioning. GPS Solutions 18 (4), 529–539.

Balanis, C. A., 2005. Antenna theory: analysis and design. Wiley Interscience, Hoboken, NJ.

Beutler, G., Brockmann, E., Gurtner, W., Hugentobler, U., Mervart, L., Rothacher, M., Verdun, A., 1994. Extended orbit modeling techniques at the CODE processing center of the International GPS Service for Geodynamics (IGS): Theory and initial results. Manuscr. Geod. 19, 367–386.

Bevis, M., Businger, S., Herring, T. A., Rocken, C., Anthes, R. A., Ware, R. H., 1992. GPS meteorology: Remote sensing of atmospheric water vapor using the global positioning system. Journal of Geophysical Research: Atmospheres 97 (D14), 15787–15801.

Bilich, A., Larson, K. M., 2007. Mapping the GPS multipath environment using the signal-to-noise ratio (SNR). Radio Science 42 (6), RS6003.

Bilich, A., Larson, K. M., Axelrad, P., 2008. Modeling GPS phase multipath with SNR: Case study from the Salar de Uyuni, Boliva. Journal of Geophysical Research 113 (B4).

Bilich, A., Mader, G. L., 2010. GNSS Absolute Antenna Calibration at the National Geodetic Survey. In: Proceedings of the 23rd International Technical Meeting of The Satellite Division of the Institute of Navigation. Portland, OR, pp. 1369–1377.

Blackman, R. B., Tukey, J. W., 1958. The measurement of power spectra from the point of view of communications engineering — part I. Bell System Technical Journal 37 (1), 185–282.

Blewitt, G., Kreemer, C., Hammond, W. C., Plag, H.-P., Stein, S., Okal, E., 2006. Rapid determination of earthquake magnitude using GPS for tsunami warning systems. Geophysical Research Letters 33 (11).

Blewitt, G., Lavallee, D., 2002. Effect of annual signals on geodetic velocity. Journal of Geophysical Research 107 (B7).

Boehm, J., Heinkelmann, R., Schuh, H., 2007. Short Note: A global model of pressure and temperature for geodetic applications. Journal of Geodesy 81 (10), 679–683.

Boehm, J., Niell, A., Tregoning, P., Schuh, H., 2006. Global Mapping Function (GMF): A new empirical mapping function based on numerical weather model data. Geophysical Research Letters 33 (7).

Boehm, J., Schuh, H., 2004. Vienna mapping functions in VLBI analyses. Geophysical Research Letters 31 (1), L01603.

Bruyninx, C., 2006. EUREF Electronic Mail #3020. URGENT: collection of individual absolute antenna calibrations for EPN stations.
URL `http://www.epncb.oma.be/ftp/mail/eurefmail.3020`, accessed on 01 Feb 2015.

Bruyninx, C., Habrich, H., Söhne, W., Kenyeres, A., Stangl, G., Völksen, C., 2012. Enhancement of the EUREF Permanent Network services and products. In: Kenyon, S., Pacino, M. C., Marti, U. (Eds.), Geodesy for Planet Earth. Vol. 136. Springer Berlin Heidelberg, pp. 27–34.

Byun, S. H., Hajj, G. A., Young, L. E., 2002. Development and application of GPS signal multipath simulator: GPS signal multipath simulator. Radio Science 37 (6), 10–1–10–23.

Chen, G., Herring, T. A., 1997. Effects of atmospheric azimuthal asymmetry on the analysis of space geodetic data. Journal of Geophysical Research: Solid Earth 102 (B9), 20489–20502.

Chen, Q., van Dam, T., Sneeuw, N., Collilieux, X., Weigelt, M., Rebischung, P., 2013. Singular spectrum analysis for modeling seasonal signals from GPS time series. Journal of Geodynamics 72, 25–35.

Collilieux, X., Métivier, L., Altamimi, Z., Dam, T. v., Ray, J., 2011. Quality assessment of GPS reprocessed terrestrial reference frame. GPS Solutions 15 (3), 219–231.

Collilieux, X., van Dam, T., Ray, J., Coulot, D., Métivier, L., Altamimi, Z., 2012. Strategies to mitigate aliasing of loading signals while estimating GPS frame parameters. Journal of Geodesy 86 (1), 1–14.

Dach, R., Hugentobler, U., Fridez, P., Meindl, M. (Eds.), 2007. Bernese GPS Software Version 5.0. Astronomical Institute, University of Bern.

Dach, R., Jean, Y. (Eds.), 2014. International GNSS Service Technical Report 2013. IGS Central Bureau. Astronomica Institute, University of Bern.

Dach, R., Schmid, R., Schmitz, M., Thaller, D., Schaer, S., Lutz, S., Steigenberger, P., Wübbena, G., Beutler, G., 2011. Improved antenna phase center models for GLONASS. GPS Solut. 15 (1), 49–65.

Davis, J. L., Herring, T. A., Shapiro, I. I., Rogers, A. E. E., Elgered, G., 1985. Geodesy by radio interferometry: Effects of atmospheric modeling errors on estimates of baseline length. Radio science 20 (6), 1593–1607.

Davis, J. L., Wernicke, B. P., Tamisiea, M. E., 2012. On seasonal signals in geodetic time series. Journal of Geophysical Research: Solid Earth 117 (B1), 1403.

DeMets, C., Gordon, R. G., Argus, D. F., 2010. Geologically current plate motions. Geophysical Journal International 181 (1), 1–80.

Dietrich, R., Rülke, A., Scheinert, M., 2005. Present-day vertical crustal deformations in West Greenland from repeated GPS observations. Geophysical Journal International 163 (3), 865–874.

Dilßner, F., Seeber, G., Wübbena, G., Schmitz, M., 2008. Impact of near-field effects on the GNSS position solution. In: Proceedings of the 21st International Technical Meeting of the Satellite Division of The Institute of Navigation (ION GNSS 2008). Savannah, GA, pp. 612–624.

Dong, D., Fang, P., Bock, Y., Cheng, M. K., Miyazaki, S., 2002. Anatomy of apparent seasonal variations from GPS-derived site position time series. Journal of Geophysical Research: Solid Earth 107 (B4), ETG 9–1–ETG 9–16.

Dousa, J., Bennitt, G. V., 2013. Estimation and evaluation of hourly updated global GPS Zenith Total Delays over ten months. GPS Solutions 17 (4), 453–464.

Dow, J. M., Neilan, R. E., Rizos, C., 2009. The International GNSS Service in a changing landscape of Global Navigation Satellite Systems. Journal of Geodesy 83 (3-4), 191–198.

Elgered, G., Davis, J. L., Herring, T. A., Shapiro, I. I., 1991. Geodesy by radio interferometry: Water vapor radiometry for estimation of the wet delay. Journal of Geophysical Research: Solid Earth 96 (B4), 6541–6555.

Elósegui, P., Davis, J. L., Jaldehag, R. T. K., Johansson, J. M., Niell, A. E., Shapiro, I. I., 1995. Geodesy using the Global Positioning System: The effects of signal scattering on estimates of site position. Journal of Geophysical Research: Solid Earth 100 (B6), 9921–9934.

Estey, L. H., Meertens, C. M., 1999. TEQC: the multi-purpose toolkit for GPS/GLONASS data. GPS solutions 3 (1), 42–49.

Fritsche, M., Dietrich, R., Knöfel, C., Rülke, A., Vey, S., Rothacher, M., Steigenberger, P., 2005. Impact of higher-order ionospheric terms on GPS estimates. Geophysical Research Letters 32 (23).

Ge, M., Gendt, G., Dick, G., Zhang, F. P., Reigber, C., 2005. Impact of GPS satellite antenna offsets on scale changes in global network solutions. Geophysical Research Letters 32 (6).

Geirsson, H., Árnadóttir, T., Völksen, C., Jiang, W., Sturkell, E., Villemin, T., Einarsson, P., Sigmundsson, F., Stefánsson, R., 2006. Current plate movements across the Mid-Atlantic Ridge determined from 5 years of continuous GPS measurements in Iceland. Journal of Geophysical Research 111 (B9).

Gendt, G., 2005. [IGSMAIL-5189]: Planned changes to IGS antenna calibrations. URL `http://igscb.jpl.nasa.gov/pipermail/igsmail/2005/005260.html`, accessed on 01 Feb 2015.

Geng, J., Williams, S. D., Teferle, F. N., Dodson, A. H., 2012. Detecting storm surge loading deformations around the southern North Sea using subdaily GPS. Geophysical Journal International 191 (2), 569–578.

Granström, C., 2006. Site-dependent effects in high-accuracy applications of GNSS. Technical report L - Department of Radio and Space Science, Chalmers University of Technology, Göteborg, Sweden, no: 13L. Department of Radio and Space Science, Space Geodesy and Geodynamics, Chalmers University of Technology,.

Greaves, M., Bingley, R. M., Baker, D. F., Hansen, D. N., Appleby, G., Sherwood, R., Clarke, P. J., Ziebart, M., 2014. National Report of Great Britain 2014. Tech. rep., OSGB, NERC.

Griffiths, J., Ray, J. R., 2009. On the precision and accuracy of IGS orbits. Journal of Geodesy 83 (3-4), 277–287.

Griffiths, J., Ray, J. R., 2013. Sub-daily alias and draconitic errors in the IGS orbits. GPS Solutions 17 (3), 413–422.

Griffiths, J., Rebischung, P., Garayt, B., Ray, J., 2012. IGS preparations for the next reprocessing and ITRF. Vol. 14 of Geophysical Research Abstracts. pp. EGU2012–3181.

Görres, B., Campbell, J., Becker, M., Siemes, M., 2006. Absolute calibration of GPS antennas: laboratory results and comparison with field and robot techniques. GPS Solutions 10 (2), 136–145.

Haase, J., Ge, M., Vedel, H., Calais, E., 2003. Accuracy and variability of GPS tropospheric delay measurements of water vapor in the western Mediterranean. Journal of Applied Meteorology 42 (11), 1547–1568.

Hansen, D. N., Teferle, F. N., Bingley, R. M., Williams, S. D. P., 2012. New estimates of present-day crustal/land motions in the British Isles based on the BIGF network. In: Kenyon, S., Pacino, M. C., Marti, U. (Eds.), Geodesy for Planet Earth. Vol. 136. Springer Berlin Heidelberg, Berlin, Heidelberg, pp. 665–671.

Hatanaka, Y., Sawada, M., Horita, A., Kusaka, M., 2001a. Calibration of antenna-radome and monument-multipath effect of GEONET-Part 1: Measurement of phase characteristics. Earth Planets and Space 53 (1), 13–22.

Hatanaka, Y., Sawada, M., Horita, A., Kusaka, M., Johnson, J. M., Rocken, C., 2001b. Calibration of antenna-radome and monument-multipath effect of GEONET-Part 2: Evaluation of the phase map by GEONET data. Earth Planets and Space 53 (1), 23–30.

Hauschild, A., Montenbruck, O., Thoelert, S., Erker, S., Meurer, M., Ashjaee, J., 2012. A multi-technique approach for characterizing the SVN49 signal anomaly, part 1: receiver tracking and IQ constellation. GPS Solutions 16 (1), 19–28.

Ho, C. M., Mannucci, A. J., Lindqwister, U. J., Pi, X., Tsurutani, B. T., 1996. Global ionosphere perturbations monitored by the Worldwide GPS Network. Geophysical Research Letters 23 (22), 3219–3222.

Hoechner, A., Babeyko, A. Y., Sobolev, S. V., 2008. Enhanced GPS inversion technique applied to the 2004 Sumatra earthquake and tsunami. Geophysical Research Letters 35 (8).

Hofmann-Wellenhof, B., Lichtenegger, H., Wasle, E., 2008. GNSS–global navigation satellite systems GPS, GLONASS, Galileo, and more. SpringerWienNewYork.

Hugentobler, U., Van der Marel, H., Springer, T., 2006. Identification and mitigation of GNSS errors. In: IGS 2006 workshop proceedings. Darmstadt, Gemany.

Hurst, K., Bar-Sever, Y., 1998. In-situ GPS antenna phase center calibration. In: Proceedings of the Workshop OPS/MET. Tokyo, Japan, pp. 54–63.

Iwabuchi, T., Shoji, Y., Shimada, S., Nakamura, H., 2004. Tsukuba GPS dense net campaign observations: comparison of the stacking maps of post-fit phase residuals estimated from three software packages. Journal of the Meteorological Society of Japan. Ser. II 82 (1B), 315–330.

Johansson, J. M., Davis, J. L., Scherneck, H.-G., Milne, G. A., Vermeer, M., Mitrovica, J. X., Bennett, R. A., Jonsson, B., Elgered, G., Elósegui, P., Koivula, H., Poutanen, M., Rönnäng, B. O., Shapiro, I. I., 2002. Continuous GPS measurements of postglacial adjustment in Fennoscandia 1. Geodetic results. Journal of Geophysical Research: Solid Earth 107 (B8), ETG 3–1–ETG 3–27.

Kedar, S., 2003. The effect of the second order GPS ionospheric correction on receiver positions. Geophysical Research Letters 30 (16).

Khan, S. A., Wahr, J., Leuliette, E., van Dam, T., Larson, K. M., Francis, O., 2008. Geodetic measurements of postglacial adjustments in Greenland. Journal of Geophysical Research 113 (B2).

King, M. A., Bevis, M., Wilson, T., Johns, B., Blume, F., 2012. Monument-antenna effects on GPS coordinate time series with application to vertical rates in Antarctica. Journal of Geodesy 86 (1), 53–63.

King, M. A., Watson, C. S., 2010. Long GPS coordinate time series: Multipath and geometry effects. Journal of Geophysical Research: Solid Earth 115 (B4), B04403.

Kouba, J., 2009. A guide to using International GNSS Service (IGS) products. URL `https://igscb.jpl.nasa.gov/igscb/resource/pubs/UsingIGSProductsVer21.pdf`, accessed on 01 Feb 2015.

Larson, K. M., Bodin, P., Gomberg, J., 2003. Using 1-Hz GPS data to measure deformations caused by the Denali fault earthquake. Science 300 (5624), 1421–1424.

Larson, K. M., Freymueller, J. T., Philipsen, S., 1997. Global plate velocities from the Global Positioning System. Journal of Geophysical Research: Solid Earth 102 (B5), 9961–9981.

Larson, K. M., Small, E. E., Gutmann, E. D., Bilich, A. L., Braun, J. J., Zavorotny, V. U., 2008. Use of GPS receivers as a soil moisture network for water cycle studies. Geophysical Research Letters 35 (24).

Lau, L., Cross, P., 2007. Development and testing of a new ray-tracing approach to GNSS carrier-phase multipath modelling. Journal of Geodesy 81 (11), 713–732.

Lidberg, M., Johansson, J. M., Scherneck, H.-G., Davis, J. L., 2007. An improved and extended GPS-derived 3d velocity field of the glacial isostatic adjustment (GIA) in Fennoscandia. Journal of Geodesy 81 (3), 213–230.

Lidberg, M., Johansson, J. M., Scherneck, H.-G., Milne, G. A., 2010. Recent results based on continuous GPS observations of the GIA process in Fennoscandia from BIFROST. Journal of Geodynamics 50 (1), 8–18.

Lomb, N. R., 1976. Least-squares frequency analysis of unequally spaced data. Astrophysics and space science 39 (2), 447–462.

Löfgren, J. S., Haas, R., 2014. Sea level measurements using multi-frequency GPS and GLONASS observations. EURASIP Journal on Advances in Signal Processing 2014 (1), 1–13.

Mader, G. L., 1999. GPS antenna calibration at the National Geodetic Survey. GPS solutions 3 (1), 50–58.

Meindl, M., 2011. Combined analysis of observations from different global navigation satellite systems. Schweizerische Geodätische Komm., Zürich.

Moore, M., Watson, C., King, M., McClusky, S., Tregoning, P., 2014. Empirical modelling of site-specific errors in continuous GPS data. Journal of Geodesy 88 (9), 887–900.

Moore, T., 1994. An introduction to the global positioning system and its applications. In: Developments in the Use of Global Positioning Systems. pp. 1/1–1/6.

Nield, G. A., Barletta, V. R., Bordoni, A., King, M. A., Whitehouse, P. L., Clarke, P. J., Domack, E., Scambos, T. A., Berthier, E., 2014. Rapid bedrock uplift in the Antarctic Peninsula explained by viscoelastic response to recent ice unloading. Earth and Planetary Science Letters 397, 32–41.

Niell, A., 1997. Near-field problems for GPS antennas. In: The Global Positioning System for the Geosciences: Summary and Proceedings of a Workshop on Improving the GPS Reference Station Infrastructure for Earth, Oceanic, and Atmospheric Science Applications, 1997th Edition. National Academies Press, Boulder, CO, pp. 219–222.

Ning, T., Elgered, G., Johansson, J. M., 2009. The impact of microwave absorber and radome geometries on geodetic measurements with ground-based GNSS antennas. In: Proc. of 2nd Colloquium Scientific and Fundamental Aspects of the Galileo Programme, European Space Agency, 15-19 October, 2009, Padua, Italy. Vol. 400.

Ning, T., Elgered, G., Johansson, J. M., 2011. The impact of microwave absorber and radome geometries on GNSS measurements of station coordinates and atmospheric water vapour. Advances in Space Research 47 (2), 186–196.

Pacione, R., Fionda, E., Ferrara, R., Lanotte, R., Sciarretta, C., Vespe, F., 2002. Comparison of atmospheric parameters derived from GPS, VLBI and a ground-based microwave radiometer in Italy. Physics and Chemistry of the Earth 27 (4), 309–316.

Park, K., Elosegui, P., Davis, J. L., Corey, B. E., Niell, A. E., Jarlemark, P. O., Normandeau, J. E., Meertens, C. E., Andreatta, V. A., 2003. Development of an in situ antenna and multipath calibration system for GPS geodesy. AGU Fall Meeting 2003 , G41C–07.

Penna, N. T., King, M. A., Stewart, M. P., 2007. GPS height time series: Short-period origins of spurious long-period signals. Journal of Geophysical Research: Solid Earth 112 (B2), B02402.

Petrie, E. J., King, M. A., Moore, P., Lavallée, D. A., 2010. Higher-order ionospheric effects on the GPS reference frame and velocities. Journal of Geophysical Research 115 (B3).

Prawirodirdjo, L., 2004. Instantaneous global plate motion model from 12 years of continuous GPS observations. Journal of Geophysical Research 109 (B8).

Ray, J., 1999. [IGSMAIL-2320] Handling mixed receiver types.
URL `http://igscb.jpl.nasa.gov/mail/igsmail/1999/msg00211.html`, accessed on 01 Feb 2015.

Ray, J., 2000. [IGSMAIL-2744]: new pseudorange bias convention.
URL `http://igscb.jpl.nasa.gov/mail/igsmail/2000/msg00084.html`, accessed on 01 Feb 2015.

Ray, J., 2009. International GNSS Service Data Reprocessing Campaign.
URL `http://acc.igs.org/reprocess.html`, accessed on 01 Feb 2015.

Ray, J., Altamimi, Z., Collilieux, X., van Dam, T., 2008. Anomalous harmonics in the spectra of GPS position estimates. GPS Solutions 12 (1), 55–64.

Ray, J. R., van Dam, T. M., Altamimi, Z., Collilieux, X., 2006. Anomalous harmonics in the spectra of GPS position estimates. AGU Fall Meeting , G43A–0985.

Rebischung, P., 2011. [IGSMAIL-6354]: Upcoming switch to IGS08/igs08.atx.
URL `http://igscb.jpl.nasa.gov/pipermail/igsmail/2011/006346.html`, accessed on 01 Feb 2015.

Rebischung, P., 2012. [IGSMAIL-6663] IGb08: an update on IGS08.
URL `https://igscb.jpl.nasa.gov/pipermail/igsmail/2012/007853.html`, accessed on 01 Feb 2015.

Rebischung, P., Griffiths, J., Ray, J., Schmid, R., Collilieux, X., Garayt, B., 2012. IGS08: the IGS realization of ITRF2008. GPS Solutions 16 (4), 483–494.

Rius, A., Nogués-Correig, O., Ribó, S., Cardellach, E., Oliveras, S., Valencia, E., Park, H., Tarongí, J. M., Camps, A., van der Marel, H., van Bree, R., Altena, B., Martín-Neira, M., 2012. Altimetry with GNSS-R interferometry: first proof of concept experiment. GPS Solutions 16 (2), 231–241.

Rocken, C., Meertens, C., Stephens, B., Braun, J., VanHove, T., Perry, S., Ruud, O., McCallum, M., Richardson, J., 1995. UNAVCO Academic Research Infrastructure (ARI) receiver and antenna test report. UNAVCO Boulder Facility internal report .

Rodriguez-Solano, C., Hugentobler, U., Steigenberger, P., Allende-Alba, G., 2013. Improving the orbits of GPS block IIA satellites during eclipse seasons. Advances in Space Research 52 (8), 1511–1529.

Rodriguez-Solano, C., Hugentobler, U., Steigenberger, P., Bloßfeld, M., Fritsche, M., 2012a. Adjustable box-wing model for GNSS satellites: impact on geodetic parameters.
URL `http://www.iapg.bgu.tum.de/mediadb/3835102/3835103/IGS2012_BOXW.pdf`, accessed on 01 Feb 2015.

Rodriguez-Solano, C. J., Hugentobler, U., Steigenberger, P., 2012b. Impact of Albedo Radiation on GPS Satellites. In: Kenyon, S., Pacino, M. C., Marti, U. (Eds.), Geodesy for Planet Earth. No. 136 in International Association of Geodesy Symposia. Springer Berlin Heidelberg, pp. 113–119.

Rodriguez-Solano, C. J., Hugentobler, U., Steigenberger, P., Bloßfeld, M., Fritsche, M., 2014. Reducing the draconitic errors in GNSS geodetic products. Journal of Geodesy .

Rodriguez-Solano, C. J., Hugentobler, U., Steigenberger, P., Lutz, S., 2012c. Impact of Earth radiation pressure on GPS position estimates. Journal of Geodesy 86 (5), 309–317.

Romero, I., Rebischung, P., Ray, J., Schmid, R., Fisher, S., Griffiths, J., 2013. Position corrections due to uncalibrated GNSS antenna radomes at IGS co-located geodetic observing stations. AGU Fall Meeting , G13B–0946.

Romero, N., 2008a. [IGSMAIL-5778]: a new CC2noncc.
URL `https://igscb.jpl.nasa.gov/mail/igsmail/2008/msg00100.html`, accessed on 01 Feb 2015.

Romero, N., 2008b. [IGSMAIL-5828]: new CC2noncc (v6.1).
URL `https://igscb.jpl.nasa.gov/mail/igsmail/2008/msg00150.html`, accessed on 01 Feb 2015.

Rost, C., Wanninger, L., 2009. Carrier phase multipath mitigation based on GNSS signal quality measurements. Journal of Applied Geodesy 3 (2), 81–87.

Rost, C., Wanninger, L., 2010. Carrier phase multipath corrections based on GNSS signal quality measurements to improve CORS observations. In: Position Location and Navigation Symposium (PLANS), 2010 IEEE/ION. pp. 1162–1167.

Rothacher, M., Mader, G., 2003. Receiver and satellite antenna phase center offsets and variations. In: Tetreault, P., Neilan, R. E., Gowey, K. (Eds.), Proc. IGS 2002 Network, Data and Analysis Centre Workshop. IGS, Ottawa, Canada, pp. 141–152.

Rothacher, M., Schaer, S., Mervart, L., Beutler, G., 1995. Determination of antenna phase center variations using GPS data. In: Proceedings of the IGS Workshop "Special Topics and New Directions". pp. 205–220.

Rothacher, M., Schmid, R., 2010. ANTEX: The Antenna Exchange Format, Version 1.4.
URL `http://igscb.jpl.nasa.gov/igscb/station/general/antex14.txt`, accessed on 01 Feb 2015.

Rothacher, M., Thaller, D., 2006. IERS Message No. 103: SINEX Version 2.02.
URL `http://www.iers.org/iers/publications/messages/`, accessed on 01 Feb 2015.

Saastamoinen, J., 1972. Atmospheric correction for the troposphere and stratosphere in radio ranging satellites. In: The Use of Artificial Satellites for Geodesy. Vol. 15 of Geophys. Monogr. Ser. AGU, Washington, DC, pp. 247–251.

Scargle, J. D., 1982. Studies in astronomical time series analysis. II - Statistical aspects of spectral analysis of unevenly spaced data. The Astrophysical Journal 263, 835–853.

Schaer, S., 1999. Mapping and predicting the Earth's ionosphere using the Global Positioning System. No. 59 in Geodätisch-geophysikalische Arbeiten in der Schweiz ; 59 ; Geodätisch-geophysikalische Arbeiten in der Schweiz. Schweizer. Geodät. Komm., Zürich.

Schaer, S., 2001. [IGSMAIL-3212]: CODE DCB data archive initiated.
URL `http://igscb.jpl.nasa.gov/mail/igsmail/2001/msg00060.html`, accessed on 01 Feb 2015.

Schmid, R., 2014. [IGSMAIL-6914] igs08_1793.atx: Update including Block IIF-6 satellite SVN67/PRN06.
URL `https://igscb.jpl.nasa.gov/pipermail/igsmail/2014/008104.html`, accessed on 01 Feb 2015.

Schmid, R., Mader, G., Herring, T., 2005. From relative to absolute antenna phase center corrections. In: Meindl, M. (Ed.), Proceedings of the IGS Workshop and Symposium 2004. Astronomical Institute, University of Bern, Bern, Switzerland, position Paper der Session "Antenna Effects".

Schmid, R., Rothacher, M., 2003. Estimation of elevation-dependent satellite antenna phase center variations of GPS satellites. Journal of Geodesy 77 (7-8), 440–446.

Schmid, R., Steigenberger, P., Gendt, G., Ge, M., Rothacher, M., 2007. Generation of a consistent absolute phase center correction model for GPS receiver and satellite antennas. Journal of Geodesy 81 (12), 781–798.

Seitz, M., Angermann, D., Bloßfeld, M., Drewes, H., Gerstl, M., 2012. The 2008 DGFI realization of the ITRS: DTRF2008. Journal of Geodesy 86 (12), 1097–1123.

Sidorov, D., Teferle, F. N., 2016. Impact of Antenna Phase Centre Calibrations on Position Time Series: Preliminary Results. In: IAG 150 Years. Vol. 143 of International Association of Geodesy Symposia. Springer Berlin Heidelberg, pp. 117–123.

Spofford, P. R., Remondi, B. W., 1994. The National Geodetic Survey Standard GPS Format SP3.
URL http://igscb.jpl.nasa.gov/igscb/data/format/sp3_docu.txt, accessed on 01 Feb 2015.

Springer, T., Otten, M., Flohrer, C., Pereira, F., Gini, F., Enderle, W., 2014. GNSS satellite orbit modelling at ESOC. Pasadena, CA, USA.

Springer, T. A., 2000. Common Interests of the IGS and the IVS. In: International VLBI Service for Geodesy and Astrometry 2000 General Meeting Proceedings. Vol. -1. pp. 296–305.

Springer, T. A., 2009. NAPEOS - mathematical models and algorithms. Tech. Rep. DOPS-SYS-TN-0100-OPS-GN, issue 1.0, ESA-ESOC.

Springer, T. A., Beutler, G., Rothacher, M., 1999. A new solar radiation pressure model for GPS satellites. GPS solutions 2 (3), 50–62.

Stewart, M. P., Penna, N. T., Lichti, D. D., 2005. Investigating the propagation mechanism of unmodelled systematic errors on coordinate time series estimated using least squares. Journal of Geodesy 79 (8), 479–489.

Tabibi, S., Nievinski, F. G., van Dam, T., Monico, J. F., 2015. Assessment of modernized GPS L5 SNR for ground-based multipath reflectometry applications. Advances in Space Research 55 (4), 1104–1116.

Teferle, F., 2013. The GNSS Coordinate Time Series Analysis (CTSAna) Tools.

Teferle, F. N., Hunegnaw, A., Williams, S., Foden, P., Woodworth, P., 2014. Recent activities at the King Edward Point Geodetic Observatory, South Georgia, in support of TIGA objectives. In: IGS Workshop 2014: Celebrating 20 Years of Service 1994-2014. Pasadena, California, USA.

Teunissen, P. J. G., 1996. GPS carrier phase ambiguity fixing concepts. In: Kleusberg, A., Teunissen, P. J. G. (Eds.), GPS for Geodesy. No. 60 in Lecture Notes in Earth Sciences. Springer Berlin Heidelberg, pp. 263–335.

Teunissen, P. J. G., 2003. Theory of carrier phase ambiguity resolution. Wuhan University Journal of Natural Sciences 8 (2), 471–484.

Thoelert, S., Meurer, M., Erker, S., Montenbruck, O., Hauschild, A., Fenton, P., 2012. A multi-technique approach for characterizing the SVN49 signal anomaly, part 2: chip shape analysis. GPS Solutions 16 (1), 29–39.

Tregoning, P., Watson, C., 2009. Atmospheric effects and spurious signals in GPS analyses. Journal of Geophysical Research 114 (B9).

Tregoning, P., Watson, C., 2011. Correction to "Atmospheric effects and spurious signals in GPS analyses". Journal of Geophysical Research 116 (B2).

Tregoning, P., Watson, C., Ramillien, G., McQueen, H., Zhang, J., 2009. Detecting hydrologic deformation using GRACE and GPS. Geophysical Research Letters 36 (15), 401.

Trimble Navigation Limited, 1997. A New Level of Accuracy for Differential GPS Mapping Applications using EVEREST Multipath Rejection Technology.

van Dam, T., Wahr, J., Milly, P. C. D., Shmakin, A. B., Blewitt, G., Lavallée, D., Larson, K. M., 2001. Crustal displacements due to continental water loading. Geophysical Research Letters 28 (4), 651–654.

Vedel, H., Mogensen, K. S., Huang, X.-Y., 2001. Calculation of zenith delays from meteorological data comparison of NWP model, radiosonde and GPS delays. Physics and Chemistry of the Earth, Part A: Solid Earth and Geodesy 26 (6-8), 497–502.

Wang, J., Zhang, L., 2008. Systematic Errors in Global Radiosonde Precipitable Water Data from Comparisons with Ground-Based GPS Measurements. Journal of Climate 21 (10), 2218–2238.

Wang, J., Zhang, L., Dai, A., Van Hove, T., Van Baelen, J., 2007. A near-global, 2-hourly data set of atmospheric precipitable water from ground-based GPS measurements. Journal of Geophysical Research 112 (D11).

Warren, D. L. M., Raquet, J. F., 2003. Broadcast vs. precise GPS ephemerides: a historical perspective. GPS Solutions 7 (3), 151–156.

Wieczorek, M. A., 2014. SHTOOLS - Tools for working with spherical harmonics (v2.9.1).

Williams, S. D. P., 2003. Offsets in Global Positioning System time series. Journal of Geophysical Research 108 (B6).

Williams, S. D. P., 2008. CATS: GPS coordinate time series analysis software. GPS Solutions 12 (2), 147–153.

Wübbena, G., Menge, F., Schmitz, M., Seeber, G., Völksen, C., 1996. A new approach for field calibration of absolute antenna phase center variations. In: Proceedings of ION GPS. Vol. 9. pp. 1205–1214.

Wübbena, G., Schmitz, M., Boettcher, G., 2006a. Near-field effects on GNSS sites: analysis using absolute robot calibrations and procedures to determine corrections. In: IGS Workshop 2006. The International GNSS Service (IGS): Perspectives and Visions for 2010 and beyond. Darmstadt, Gemany.

Wübbena, G., Schmitz, M., Boettcher, G., Schumann, C., 2006b. Absolute GNSS antenna calibration with a robot: repeatability of phase variations, calibration of GLONASS and determination of carrier-to-noise pattern. In: IGS Workshop 2006. The International GNSS Service (IGS): Perspectives and Visions for 2010 and beyond. Darmstadt, Germany.

Wübbena, G., Schmitz, M., Matzke, N., 2010. On GNSS in-situ station calibration of near-field multipath. In: International Symposium on GNSS Space-based and Ground-based Augmentation Systems and Aplications. Brussels, Belgium.

Zeimetz, P., Kuhlmann, H., 2008. On the accuracy of absolute GNSS antenna calibration and the conception of a new anechoic chamber. In: Integrating Generations, FIG Working Week 2008. Stockholm, Sweden.

Zhu, S. Y., Massmann, F.-H., Yu, Y., Reigber, C., 2003. Satellite antenna phase center offsets and scale errors in GPS solutions. Journal of Geodesy 76 (11-12), 668–672.

Zumberge, J. F., Heflin, M. B., Jefferson, D. C., Watkins, M. M., Webb, F. H., 1997. Precise point positioning for the efficient and robust analysis of GPS data from large networks. Journal of Geophysical Research 102 (B3), 5005–5017.

Appendix A

Uncalibrated hardware delays

Due to the presence of uncalibrated hardware delays in both satellites and receivers, phase ambiguities of a satellite-receiver pair loose their integer properties. This is a major problem for the PPP ambiguity fixing. Uncalibrated phase delays in connection with ambiguity resolution are introduced in the following.

Following Hofmann-Wellenhof et al. (2008), GNSS observation equation for carrier phases reads

$$\Phi_r^s(t) = \frac{1}{\lambda^s}\varrho_r^s(t) + N_r^s + \frac{c}{\lambda^s}\Delta\delta_r^s(t) \tag{A.1}$$

where $\Phi_r^s(t)$ is the measured carrier phase expressed in cycles, λ^s is the wavelength, $\varrho_r^s(t)$ is the geometric distance between the observing point and the satellite. N_r^s is the time-dependent phase ambiguity, c is the speed of light and $\Delta\delta_r^s(t)$ is the combined receiver and satellite clock bias.

By making substitutions $\Delta\delta_r^s(t) = \delta_r(t) - \delta^s(t)$ and $f^s = \frac{c}{\lambda^s}$, we obtain

$$\Phi_r^s(t) + f^s\delta^s(t) = \frac{1}{\lambda^s}\varrho_r^s(t) + N_r^s + f^s\delta_r(t) \tag{A.2}$$

Equation (A.2) contains terms $f^s\delta^s(t)$ and $f^s\delta_r(t)$, which include clock errors at the satellite and receiver sides, respectively. It should be noted that these clock errors also absorb uncalibrated phase delays in the hardware at both sides. As these delays are merged with phase ambiguity N_r^s, its integer property is lost. Making differences between observations of two satellites by one receiver allows to eliminate clock errors at the receiver side, or $f^s\delta_r(t)$ term. Alternatively, differences of observations of the common satellite performed by two receivers eliminate clock errors at the satellite side, or $f^s\delta^s(t)$ term. These differences are known as single-difference observables. Going further and making differences of observations between two receivers simultaneously observing two common satellites eliminates both satellite and receiver clock errors. This is known as double-difference (DD) observables. This allows to recover the integer property of phase ambiguities and make phase ambiguity resolution trivial in double-difference processing.

As NAPEOS employs undifferenced processing, resolving phase ambiguities is problematic. However, when a network of stations is processed, `Ambfix` is able to construct DD observables and, thus, resolve integer ambiguities at the DD level. The resolved ambiguities are later treated by `Bahn` as additional constraints.

Appendix B

IGS type-mean and individual PCC differences

55 stations with individual antenna/radome PCC were selected for this study. The actual amount of processed antenna/radome PCC reached 76 due to equipment changes at stations. Thus, 22 different kinds of antenna/radome combinations were considered. The individual antenna PCC for these combinations were compared to the respective IGS type-mean models. The PCC differences for the EPN, GeoNet and UNOTT, NRCan and SPSLux stations are shown in Figures B.1, B.2, B.3 and B.4, respectively.

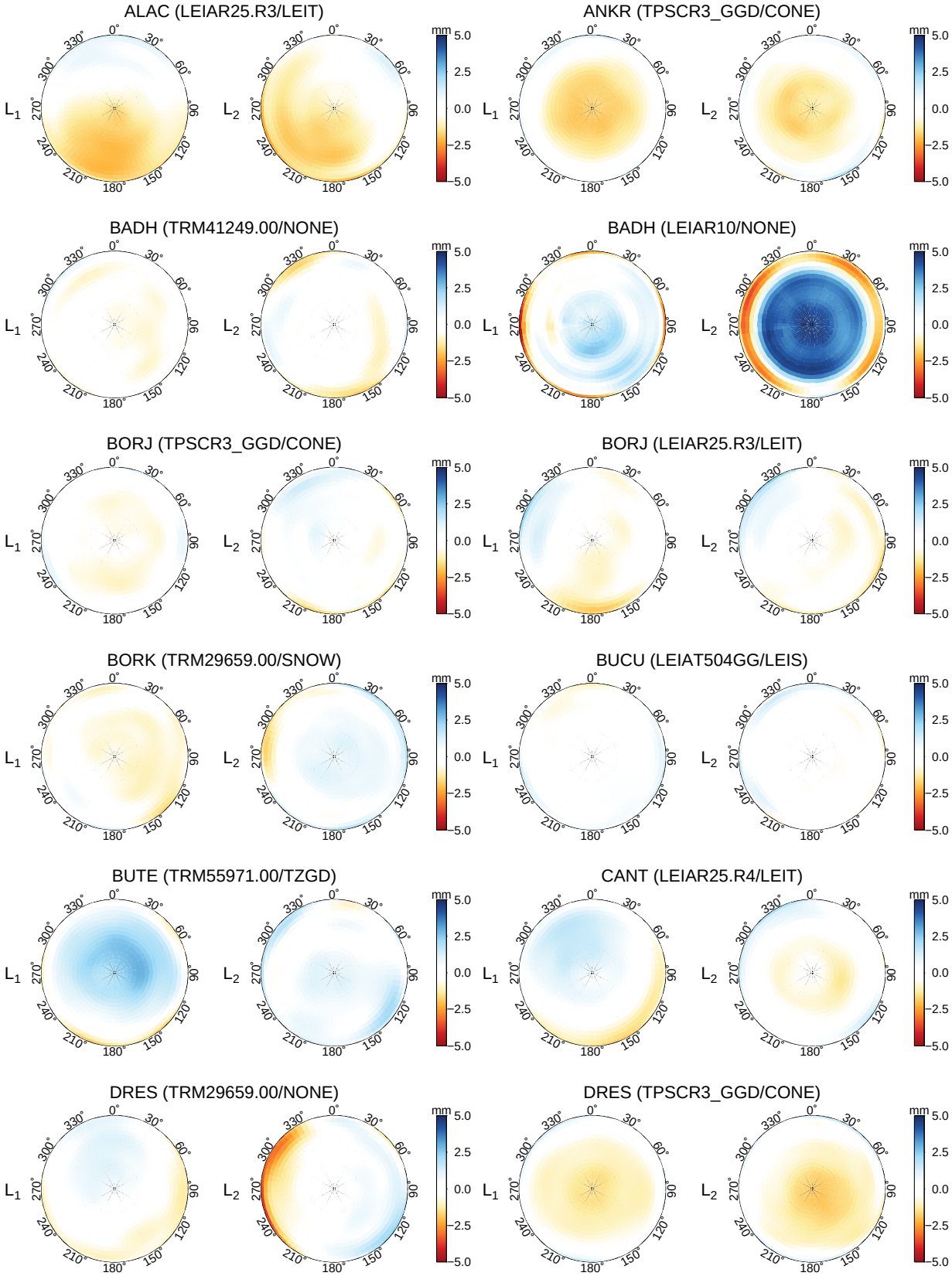

Figure B.1: Skyplots of differences between type-mean and individual PCC for EPN stations. Next to station names the respective antenna/radome combinations are denoted in brackets *(continued on next page)*.

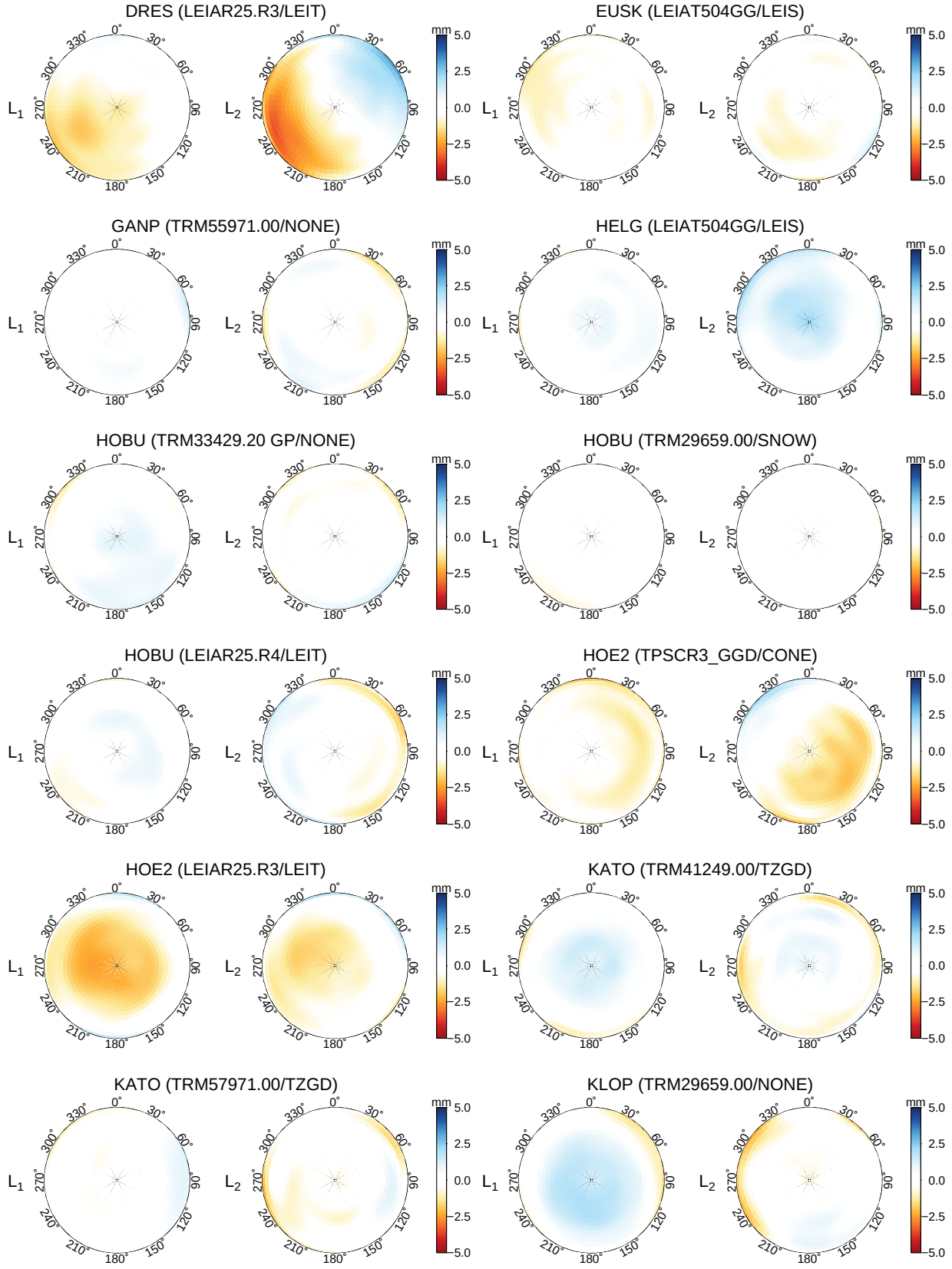

Figure B.1: Skyplots of differences between type-mean and individual PCC for EPN stations. Next to station names the respective antenna/radome combinations are denoted in brackets *(continued from previous page).*

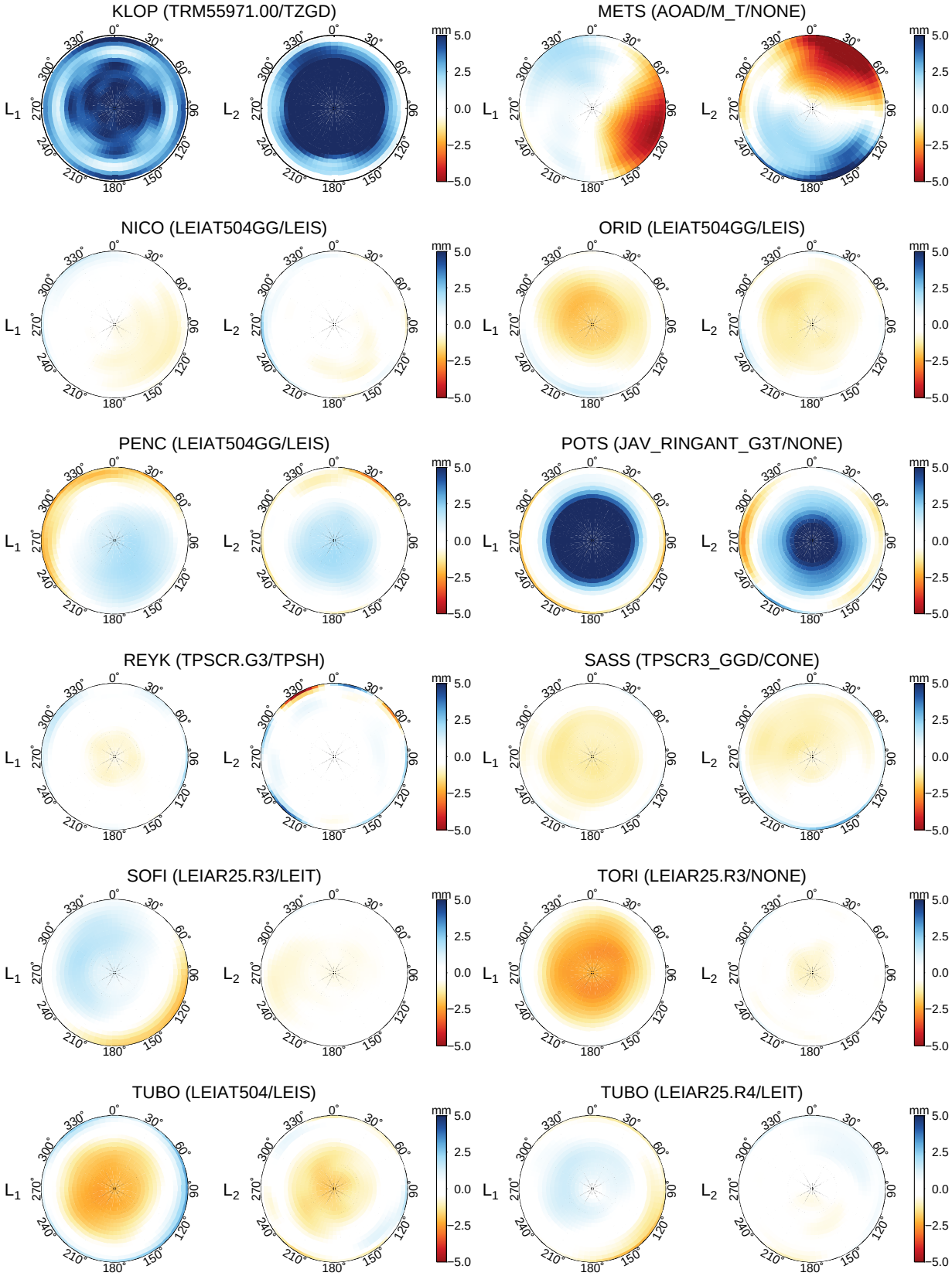

Figure B.1: Skyplots of differences between type-mean and individual PCC for EPN stations. Next to station names the respective antenna/radome combinations are denoted in brackets *(continued from previous page)*.

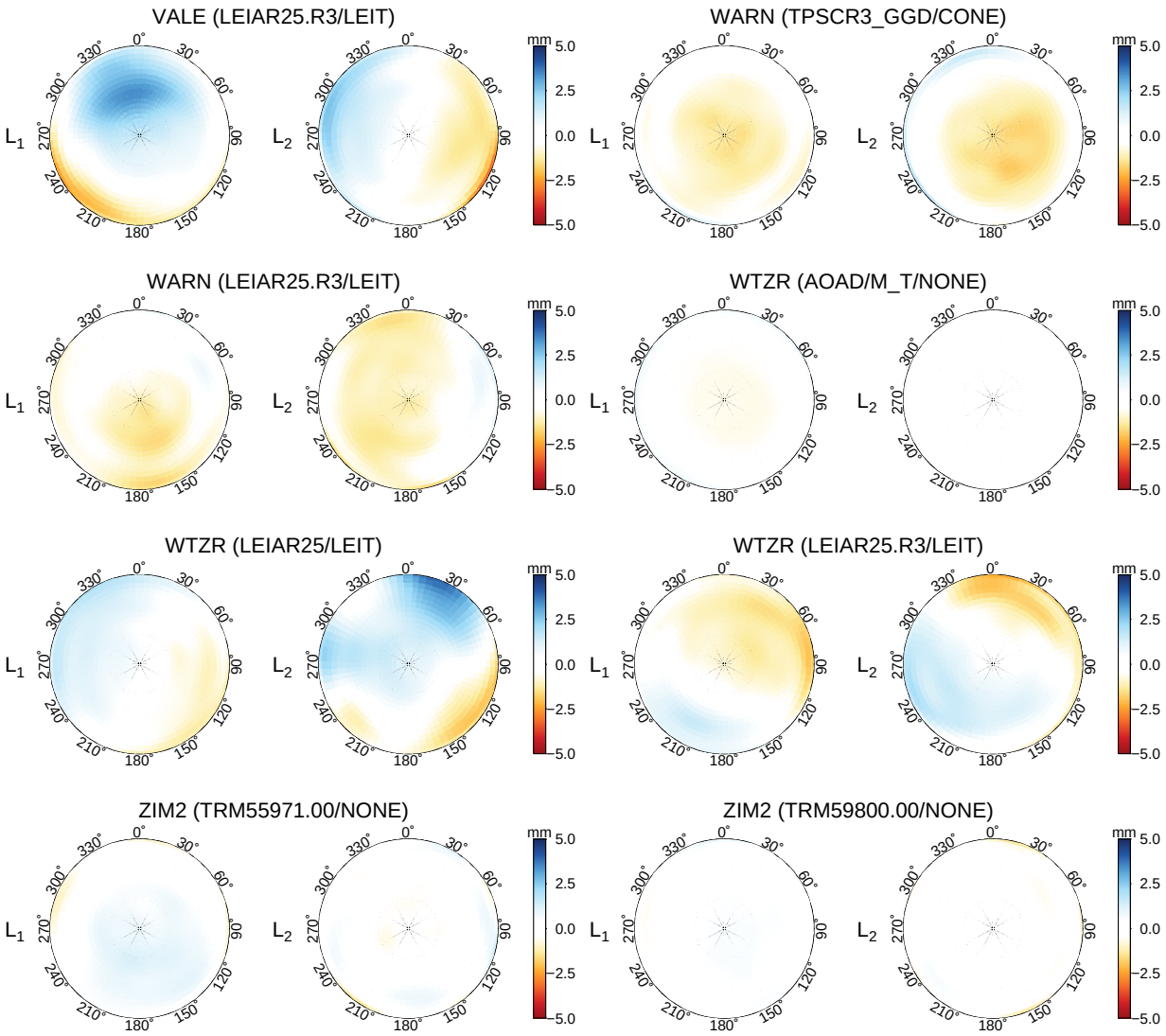

Figure B.1: Skyplots of differences between type-mean and individual PCC for EPN stations. Next to station names the respective antenna/radome combinations are denoted in brackets *(continued from previous page)*.

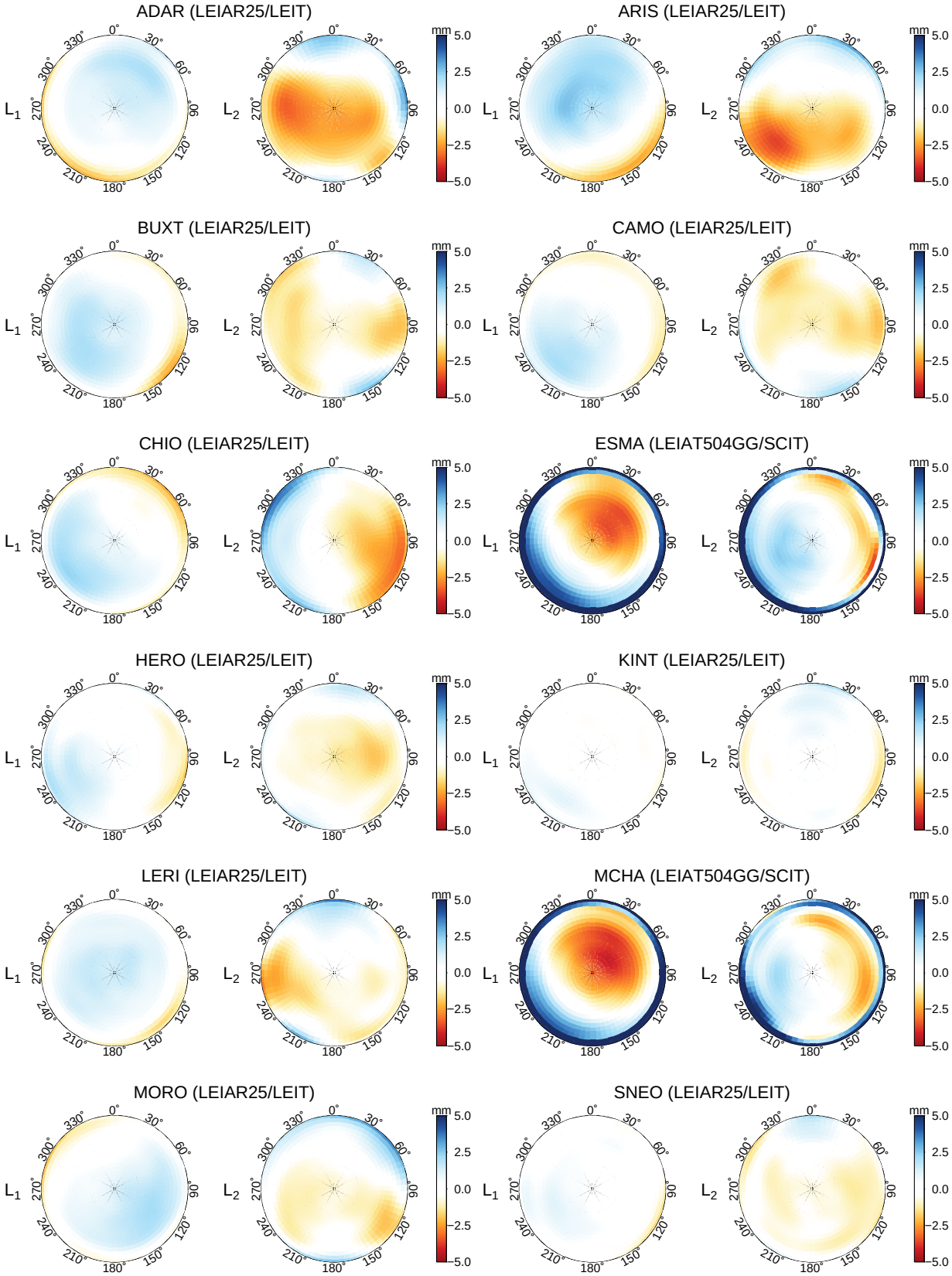

Figure B.2: Skyplots of differences between type-mean and individual PCC for GeoNet and UNOTT stations. Next to station names the respective antenna/radome combinations are denoted in brackets *(continued on next page)*.

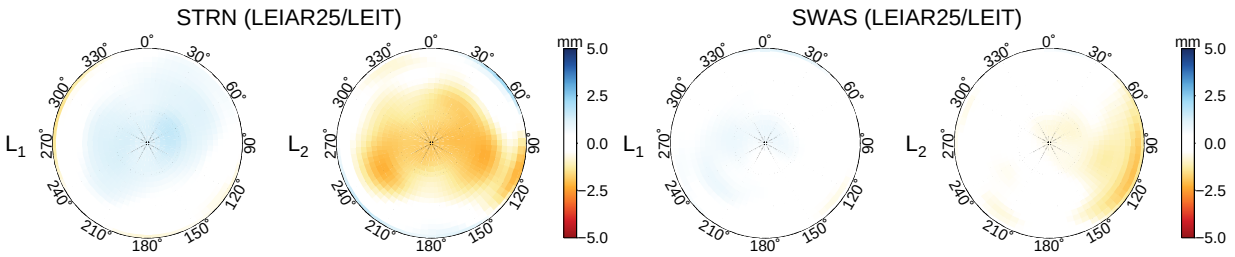

Figure B.2: Skyplots of differences between type-mean and individual PCC for GeoNet and UNOTT stations. Next to station names the respective antenna/radome combinations are denoted in brackets *(continued from previous page)*.

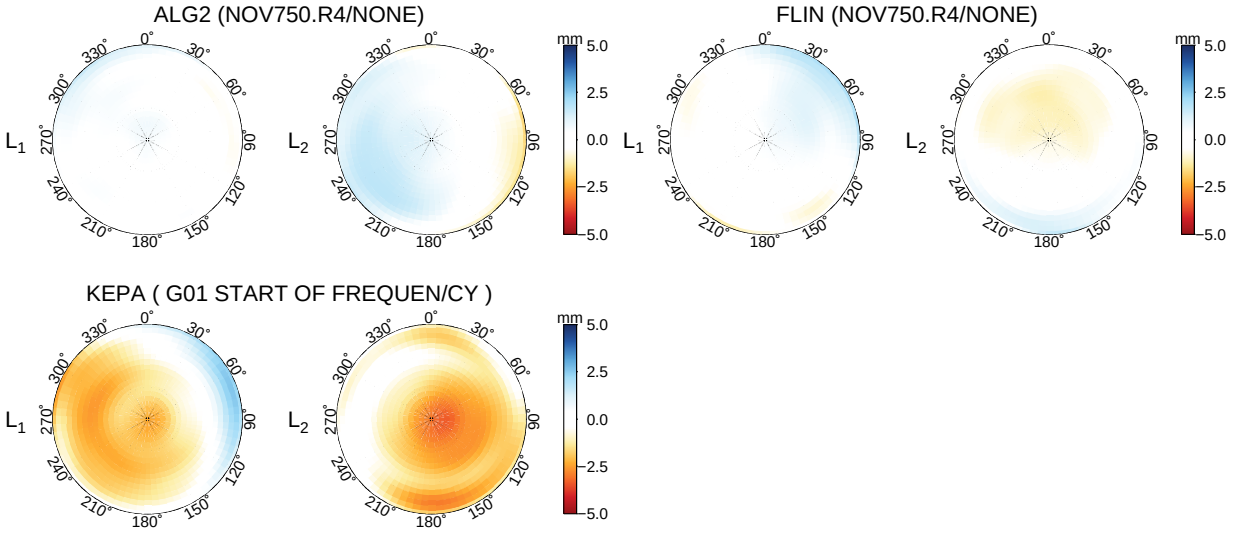

Figure B.3: Skyplots of differences between type-mean and individual PCC for NRCan stations ALG2 and FLIN, and station KEPA. Next to station names the respective antenna/radome combinations are denoted in brackets.

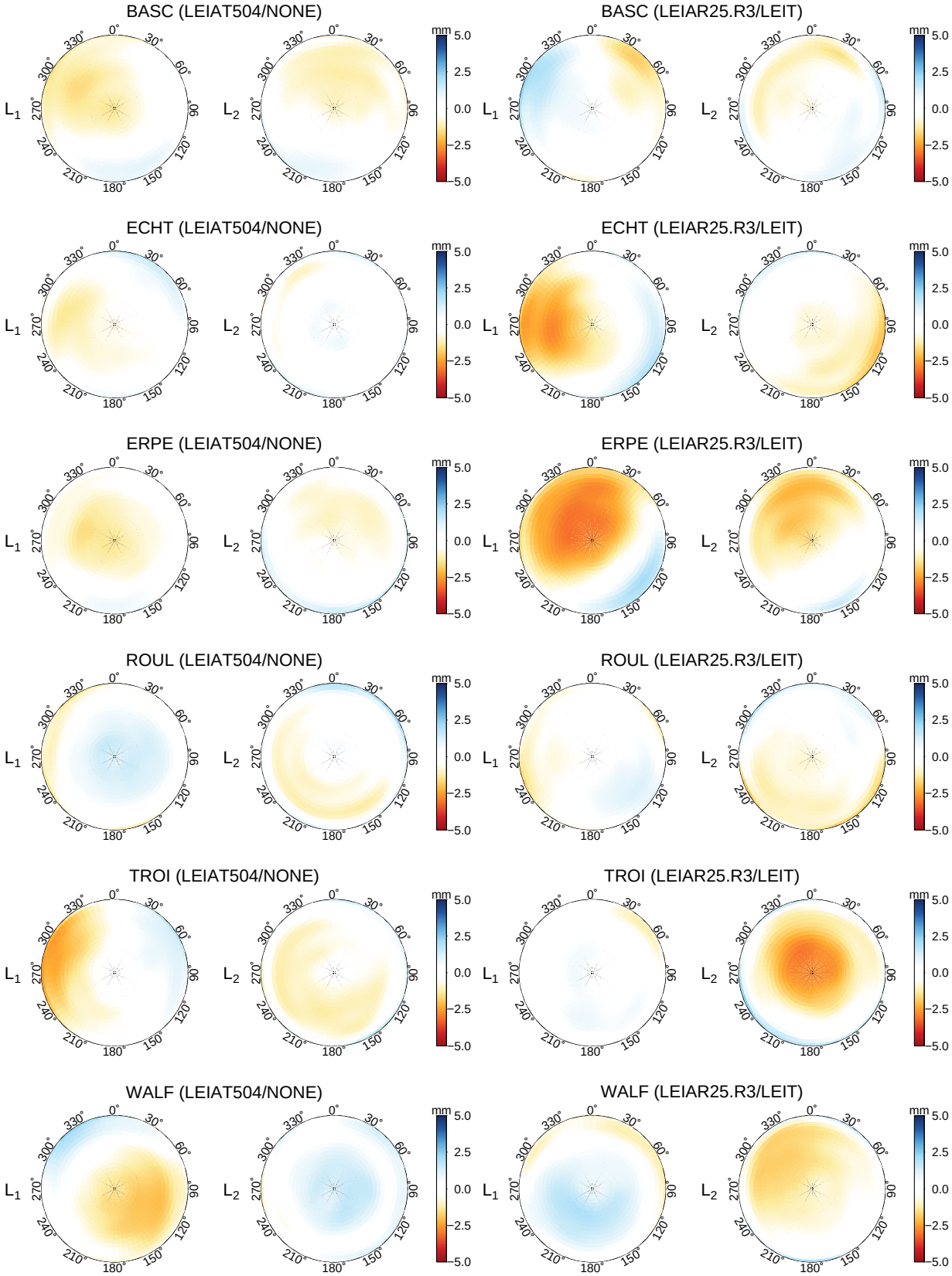

Figure B.4: Skyplots of differences between type-mean and individual PCC for SPSLux stations. Next to station names the respective antenna/radome combinations are denoted in brackets.

Appendix C

IGb08 core stations

The IGb08 core network was developed to achieve the uniformity of global coverage and stability of the reference frame. It consists of 91 primary and 101 secondary reference frame stations. The secondary stations are intended to be used if no data is available from primary stations in the vicinity. Table C.1 provides the list of the primary and secondary (substitutional) stations.

Table C.1: IGb08 core stations.

Station	DOMES	Substitution for	Longitude [°]	Latitude [°]
ALIC	50137M001		133 53 07.8	-23 40 12.4
ARTU	12362M001		58 33 37.6	56 25 47.3
ASC1	30602M001		345 35 16.5	-7 57 04.3
ASPA	50503S006		189 16 39.2	-14 19 33.9
AUCK	50209M001		174 50 03.7	-36 36 10.2
CHTI	50242M001	AUCK	183 22 58.3	-43 44 07.7
BJFS	21601M001		115 53 32.9	39 36 30.9
OSN1	23904S001	BJFS	127 01 26.5	37 04 39.2
DAEJ	23902M002	BJFS	127 22 28.1	36 23 57.9
SUWN	23903M001	BJFS	127 03 15.2	37 16 31.8
BOGT	41901M001		285 55 08.6	4 38 24.2
QUI2	42003S003	BOGT	281 30 23.0	-0 12 54.5
BRAZ	41606M001		312 07 19.6	-15 56 50.9
BRFT	41602M002		321 34 28.0	-3 52 38.8
FORT	41602M001	BRFT	321 34 27.7	-3 52 38.8
BRMU	42501S004		295 18 13.4	32 22 13.4
CAS1	66011M001		110 31 10.9	-66 17 00.0
CCJM	21732S003		142 11 04.4	27 05 44.0
CEDU	50138M001		133 48 35.3	-31 51 59.9
ADE1	50109S001	CEDU	138 38 50.4	-34 43 44.3
CHAT	50207M001		183 26 02.9	-43 57 20.8
CHUR	40128M002		265 54 40.5	58 45 32.6
BAKE	40152M001	CHUR	263 59 51.5	64 19 04.1
FLIN	40135M001	CHUR	258 01 19.0	54 43 32.1
COCO	50127M001		96 50 02.2	-12 11 18.0
CONZ	41719M002		286 58 28.2	-36 50 37.5
ANTC	41713S001	CONZ	288 28 04.6	-37 20 19.3
SANT	41705M003	CONZ	289 19 53.2	-33 09 01.0
CFAG	41517S001	CONZ	291 46 02.4	-31 36 07.8
CRO1	43201M001		295 24 56.4	17 45 24.8
DARW	50134M001		131 07 57.8	-12 50 37.3
JAB1	50136M001	DARW	132 53 38.0	-12 39 31.8
DAV1	66010M001		77 58 21.4	-68 34 38.3
MAW1	66004M001	DAV1	62 52 14.5	-67 36 17.1
DGAR	30802M001		72 22 12.8	-7 16 10.8
MALD	22901S001	DGAR	73 31 34.6	4 11 19.2
DRAO	40105M002		240 22 30.0	49 19 21.4
BREW	40473M001	DRAO	240 19 02.5	48 07 53.4
NANO	40138M001	DRAO	235 54 48.6	49 17 41.3
ALBH	40129M003	DRAO	236 30 45.1	48 23 23.2
DUM1	91501M001		140 00 06.9	-66 39 54.3

(continued on next page)

Table C.1: IGb08 core stations *(continued from previous page).*

Station	DOMES	Substitution for	Longitude [°]	Latitude [°]
GLPS	42005M002		269 41 46.7	-0 44 34.7
GALA	42005M001	GLPS	269 41 46.9	-0 44 33.7
GOLD	40405S031		243 06 38.7	35 25 30.5
JPLM	40400M007	GOLD	241 49 36.3	34 12 17.3
VNDP	40420M007	GOLD	239 23 00.7	34 33 22.7
MONP	40497M004	GOLD	243 34 39.5	32 53 30.9
GOUG	30608M001		350 07 09.4	-40 20 55.7
GUAM	50501M002		144 52 06.0	13 35 21.5
GUUG	82301M001	GUAM	144 48 09.7	13 25 59.5
GUAT	40901S001		269 28 47.3	14 35 25.4
MANA	41201S001	GUAT	273 45 03.6	12 08 56.1
SSIA	41401S001	GUAT	270 53 00.2	13 41 49.5
HOB2	50116M004		147 26 19.4	-42 48 16.9
HOFN	10204M002		344 48 07.4	64 16 02.2
SCOR	43006M002	HOFN	338 02 58.7	70 29 07.2
IISC	22306M002		77 34 13.3	13 01 16.1
BAN2	22306M003	IISC	77 30 41.8	13 02 03.5
HYDE	22307M001	IISC	78 33 03.1	17 25 02.1
IRKT	12313M001		104 18 58.4	52 13 08.4
IRKJ	12313M002	IRKT	104 18 58.2	52 13 08.4
ULAB	24201M001	IRKT	107 03 08.3	47 51 54.2
NVSK	12319M001	IRKT	83 14 07.5	54 50 26.1
ISPA	41703M007		250 39 20.1	-27 07 29.9
EISL	41703M003	ISPA	250 37 00.1	-27 08 53.5
KARR	50139M001		117 05 49.8	-20 58 53.1
KERG	91201M002		70 15 19.8	-49 21 05.2
KHAJ	12361M001		135 02 46.1	48 31 17.2
KOKB	40424M004		200 20 06.2	22 07 34.5
HNLC	49970S001	KOKB	202 08 07.6	21 18 11.8
KOUC	92727S001		164 17 14.4	-20 33 31.2
NOUM	92701M003	KOUC	166 24 36.7	-22 16 11.4
KUNM	21609M001		102 47 49.9	25 01 46.3
KWJ1	50506M001		167 43 48.8	8 43 19.9
LAE1	51002M001		146 59 35.4	-6 40 25.3
LHAZ	21613M002		91 06 14.4	29 39 26.3
LHAS	21613M001	LHAZ	91 06 14.3	29 39 26.4
LPGS	41510M001		302 04 03.7	-34 54 24.2
BUE2	41505S007	LPGS	301 28 50.5	-34 34 25.3
MAC1	50135M001		158 56 08.9	-54 29 58.3
MALI	33201M001		40 11 39.8	-2 59 45.2
MAS1	31303M002		344 22 00.2	27 45 49.4

(continued on next page)

Table C.1: IGb08 core stations *(continued from previous page).*

Station	DOMES	Substitution for	Longitude [°]	Latitude [°]
GMAS	31303S004	MAS1	344 21 56.6	27 45 53.2
MBAR	33901M001		30 44 16.3	-0 36 05.2
MCIL	21789S001		153 58 43.1	24 17 24.3
MCM4	66001M003		166 40 09.5	-77 50 18.0
MDO1	40442M012		255 59 06.0	30 40 49.8
PIE1	40456M001	MDO1	251 52 51.8	34 18 05.4
MKEA	40477M001		204 32 37.1	19 48 04.8
MAUI	40445S008	MKEA	203 44 34.7	20 42 23.9
MQZG	50214M001		172 39 16.9	-43 42 09.8
OUS2	50212M002	MQZG	170 30 39.3	-45 52 10.1
NKLG	32809M002		9 40 19.6	0 21 14.0
NLIB	40465M001		268 25 30.3	41 46 17.7
DUBO	40137M001	NLIB	264 08 01.7	50 15 31.7
NOT1	12717M004		14 59 23.2	36 52 33.0
MATE	12734M008	NOT1	16 42 16.0	40 38 56.8
MAT1	12734M009	NOT1	16 42 16.3	40 38 56.6
CAGL	12725M003	NOT1	8 58 21.9	39 08 09.2
NRIL	12364M001		88 21 35.2	69 21 42.5
OHI2	66008M005		302 05 55.2	-63 19 15.8
OHI3	66008M006	OHI2	302 05 55.0	-63 19 15.9
OHIG	66008M001	OHI2	302 05 58.7	-63 19 14.6
PALM	66005M002		295 56 55.9	-64 46 30.3
PARC	41716S001		289 07 12.4	-53 08 13.0
RIOG	41507M004	PARC	292 14 55.9	-53 47 07.6
COYQ	41715S001	PARC	288 06 28.5	-45 30 51.6
PDEL	31906M004		334 20 14.0	37 44 51.8
PETP	12355M002		158 36 25.4	53 04 00.2
PIMO	22003M001		121 04 39.8	14 38 08.5
POL2	12348M001		74 41 39.3	42 40 47.1
CHUM	25601M001	POL2	74 45 03.9	42 59 54.6
SELE	12352M001	POL2	77 01 00.8	43 10 43.4
KIT3	12334M001	POL2	66 53 07.6	39 08 05.1
POLV	12336M001		34 32 34.5	49 36 09.4
GLSV	12356M001	POLV	30 29 48.2	50 21 51.0
CRAO	12337M002	POLV	33 59 27.5	44 24 47.7
MDVO	12309M002	POLV	37 13 24.9	56 01 38.9
QAQ1	43007M001		313 57 08.0	60 42 54.9
KELY	43005M002	QAQ1	309 03 18.5	66 59 14.7
QIKI	40166M001	QAQ1	295 57 58.8	67 33 33.6
RAMO	20703S001		34 45 47.3	30 35 51.3
DRAG	20710S001	RAMO	35 23 31.4	31 35 35.5

(continued on next page)

Table C.1: IGb08 core stations *(continued from previous page).*

Station	DOMES	Substitution for	Longitude [°]	Latitude [°]
NICO	14302M001	RAMO	33 23 47.2	35 08 27.5
TEHN	20404M002	RAMO	51 20 02.7	35 41 50.2
RBAY	30315M001		32 04 42.1	-28 47 43.9
HRAO	30302M004	RBAY	27 41 13.1	-25 53 24.3
HARB	30302M009	RBAY	27 42 26.0	-25 53 13.0
PRE1	30310S001	RBAY	28 13 26.5	-25 44 46.8
REUN	97401M003		55 34 18.1	-21 12 29.6
SCH2	40133M002		293 10 02.5	54 49 55.5
NAIN	40164M001	SCH2	298 18 40.6	56 32 13.1
SCUB	40701M001		284 14 15.6	20 00 43.4
AOML	49914S001	SCUB	279 50 16.0	25 44 04.8
STJO	40101M001		307 19 20.1	47 35 42.8
HLFX	40120M001	STJO	296 23 19.3	44 41 00.7
EPRT	49928S001	STJO	293 00 28.3	44 54 31.3
BARH	49927S001	STJO	291 46 41.9	44 23 42.1
SUTH	30314M002		20 48 37.6	-32 22 48.7
SUTM	30314M004	SUTH	20 48 39.2	-32 22 53.1
SIMO	30307M001	SUTH	18 26 22.4	-34 11 16.5
SYOG	66006S002		39 35 01.4	-69 00 25.0
THTI	92201M009		210 23 36.7	-17 34 37.4
TAH1	92201S011	THTI	210 23 37.7	-17 34 37.3
THU3	43001M002		291 10 29.8	76 32 13.3
THU1	43001M001	THU3	291 12 43.1	76 32 14.4
ALRT	40162M001	THU3	297 39 34.3	82 29 39.4
TIDB	50103M108		148 58 47.9	-35 23 57.1
MOBS	50182M001	TIDB	144 58 31.2	-37 49 45.8
TIXI	12360M001		128 51 59.1	71 38 04.1
TNML	23604S001		120 59 14.4	24 47 52.6
TCMS	23604S002	TNML	120 59 14.6	24 47 52.7
TWTF	23603S002	TNML	121 09 52.2	24 57 12.8
SHAO	21605M002	TNML	121 12 01.5	31 05 58.7
TOW2	50140M001		147 03 20.4	-19 16 09.4
TRO1	10302M006		18 56 22.7	69 39 45.7
TROM	10302M003	TRO1	18 56 17.9	69 39 45.8
NYA1	10317M003	TRO1	11 51 55.1	78 55 46.3
NYAL	10317M001	TRO1	11 51 54.3	78 55 46.5
TSKB	21730S005		140 05 14.9	36 06 20.4
MTKA	21741S002	TSKB	139 33 40.9	35 40 46.2
KGNI	21704S005	TSKB	139 29 17.2	35 42 37.2
UNSA	41514M001		294 35 32.4	-24 43 38.8
USNO	40451S003		282 56 01.5	38 55 08.2

(continued on next page)

Table C.1: IGb08 core stations *(continued from previous page).*

Station	DOMES	Substitution for	Longitude [°]	Latitude [°]
GODE	40451M123	USNO	283 10 23.4	39 01 18.2
USN3	40451S007	USNO	282 56 01.4	38 55 14.0
VESL	66009M001		357 09 29.5	-71 40 25.6
WHIT	40136M001		224 46 40.3	60 45 01.8
INVK	40150M001	WHIT	226 28 22.9	68 18 22.2
FAIR	40408M001	WHIT	212 30 02.7	64 58 40.7
YELL	40127M003	WHIT	245 31 09.4	62 28 51.2
WIND	31101M001		17 05 21.9	-22 34 29.7
WSRT	13506M005		6 36 16.2	52 54 52.5
KOSG	13504M003	WSRT	5 48 34.7	52 10 42.3
BRUS	13101M004	WSRT	4 21 33.1	50 47 52.1
POTS	14106M003	WSRT	13 03 57.9	52 22 45.4
YAR1	50107M004		115 20 49.1	-29 02 47.5
YARR	50107M006	YAR1	115 20 49.1	-29 02 47.7
NNOR	50181M001	YAR1	116 11 33.7	-31 02 55.4
PERT	50133M001	YAR1	115 53 06.9	-31 48 07.0
YEBE	13420M001		356 54 40.9	40 31 29.6
VILL	13406M001	YEBE	356 02 52.8	40 26 36.9
SFER	13402M004	YEBE	353 47 39.6	36 27 51.6
RABT	35001M002	YEBE	353 08 44.5	33 59 53.1
YIBL	25001M001		56 06 44.4	22 11 11.2
BHR2	24901M002	YIBL	50 36 29.3	26 12 32.9
ZAMB	34601M001		28 18 39.6	-15 25 31.9

Appendix D

Software Implementations

In order to produce ESMs for stations, the author developed a software tool, namely, `antennaSH`. This tool was implemented in Fortran 95 and used some routines that are publicly available. In particular, the routine `DGELSY` from LAPACK package and routines `SHExpandLSQ` and `MakeGridPoint` from SHTOOLS package were employed. `antennaSH` as well as other routines are briefly introduced in the following.

LAPACK

The Linear Algebra PACKage (LAPACK) is a collection of routines for solving systems of simultaneous linear equations, least-squares solutions of linear systems of equations, eigenvalue problems, and singular value problems. LAPACK is freely available from Netlib repository at the University of Tennessee, Knoxville (UTK) and Oak Ridge National Laboratory (ORNL) through `http://www.netlib.org/lapack/`.

DGELSY. The routine `DGELSY`[1] belongs to a family of LAPACK `xGELS` routines that are designed to solve a system of underdetermined and overdetermined systems of linear equations. `DGELSY` computes the minimum-norm solution to a real linear least squares problem

$$minimise \ \|\mathbf{A}\mathbf{x} - \boldsymbol{b}\|$$

using a complete orthogonal factorisation[2] of $\mathbf{A}$. $\mathbf{A}$ is an $[M \times N]$ matrix which may be rank-deficient.

SHTOOLS

SHTOOLS is an archive of Fortran 95 and Python software designed to perform spherical harmonic transformations and reconstructions, as well as other actions on data expressed in spherical harmonics, e.g., rotations, spectral analyses, etc. SHTOOLS can be freely downloaded from a repository at the Paris Institute of Earth Physics (IPGP) through `http://shtools.ipgp.fr/`.

[1] `http://www.netlib.org/lapack/explore-html/d6/d4b/dgelsy_8f_source.html`
[2] `http://www.netlib.org/lapack/lug/node43.html`

Spherical harmonics

Any real-valued spherical function f may be expanded as a linear combination of basis functions

$$f(\overrightarrow{\omega}) = \sum_{l=0}^{\infty} \sum_{m=-l}^{l} y_l^m(\overrightarrow{\omega}) f_l^m, \tag{D.1}$$

where the coefficients f_l^m are computed by projecting f onto each basis function y_l^m

$$f_l^m = \int_{\Omega_{4\pi}} y_l^m(\overrightarrow{\omega}) f(\overrightarrow{\omega}) d\overrightarrow{\omega} \tag{D.2}$$

As the expansion goes to infinity, this requires an infinite number of coefficients. However, the number of bands can be limited to $l = n-1$, allowing to keep frequencies up to an n^{th} order. This results in an approximation $\tilde{f}$ of the original function f

$$f(\overrightarrow{\omega}) = \sum_{l=0}^{n-1} \sum_{m=-l}^{l} y_l^m(\overrightarrow{\omega}) f_l^m, \tag{D.3}$$

More information on spherical harmonics can be found in Atkinson and Han (2012)[3].

SHExpandLSQ. The routine `SHExpandLSQ` is designed to expand a set of irregularly sampled data points into spherical harmonics using a least squares inversion. Complete documentation can be found at
`http://www.ipgp.fr/~wieczor/SHTOOLS/www/man/shexpandlsq.html`
The routine was used to produce spherical harmonics from the set of L_1 and L_2 residuals.

MakeGridPoint. The routine `MakeGridPoint` expands a set of spherical harmonic coefficients at a single point. Complete documentation can be found at
`http://www.ipgp.fr/~wieczor/SHTOOLS/www/man/makegridpoint.html`
The routine was used to obtain correction values for each $5° \times 5°$ bin to be later merged with initial PCC.

antennaSH

The program `antennaSH` was developed by the author to derive L_1 and L_2 out of L_3 (ionosphere-free) phase residuals and produce spherical harmonic representations for those. These representations are then output in ANTEX format and can be easily merged with antenna PCC.

[3]Atkinson, K., Han, W., 2012. Spherical Harmonics, in: Spherical Harmonics and Approximations on the Unit Sphere: An Introduction, Lecture Notes in Mathematics. Springer Berlin Heidelberg, pp. 11â86.

`antennaSH` uses routines `DGELSY` from LAPACK, `SHExpandLSQ` and `MakeGridPoint` from SHTOOLS. Its main functional elements are shown in Figure D.1. The input data containing L_3 phase residuals are processed by `solve_LS`, which calls `DGELSY` to solve for L_1 and L_2 phase residuals for each $1^\circ \times 1^\circ$ bin. Then `SHExpandLSQ` performs spherical harmonic representation separately for L_1 and L_2 and `MakeGridPoint` is used to obtain final corrections for each $5^\circ \times 5^\circ$ bin. The output is provided in ANTEX format (without header) and can be used for further merging with antenna PCC. The source code of the program in Fortran 95 as well as an executable binary for Debian-based Linux systems are provided on the supplied CD-ROM.

Usage example:

```
$ ./antennaSH residual_file esm.atx
```

`residual_file` and `esm.atx` are input residual data and output ESM, respectively.

Input data example:

```
[SVN]     [Epoch(s)][Epoch(year)]   [Azi]    [Ele]         [Residual]

GPS27         264495 2011.0905789  140.095   14.229       5.692792910850
GPS27         264525 2011.0905798  140.177   14.021      -5.358946509660
GPS27         264555 2011.0905808  140.259   13.813      11.298707249800
GPS27         264585 2011.0905817  140.340   13.605      -0.087216903921
GPS27         264615 2011.0905827  140.422   13.398     -15.886420442300
GPS27         264645 2011.0905836  140.503   13.192     -35.765588108900
GPS27         264675 2011.0905846  140.584   12.985     -26.073019398600
...
```

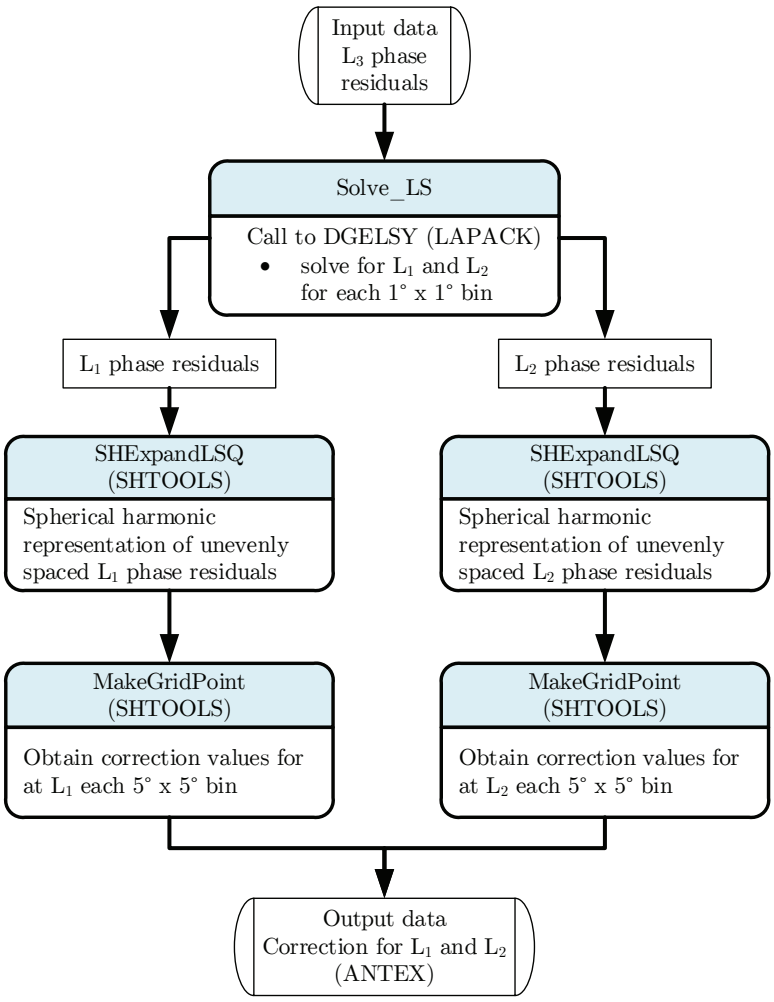

Figure D.1: Main functional elements of `antennaSH`.

Appendix E

Derived ESMs

This section presents ESMs for stations introduced in Section 4.2 of Chapter 4, as well as provides quality control information for all derived ESMs. The shown ESMs together with ESMs for all other stations derived in the frame of this study are available on the supplied CD-ROM.

ESMs for stations

Figures E.1 – E.4 demonstrate ESMs for EPN, GeoNet, UNOTT, SPSLux and NRCan stations, as well as station KEPA. Each ESM corresponds to a specific antenna/radome combination installed on a station during specific period of time. The ESM-corrected PCC for stations, which are combinations of respective type-mean PCC and the derived ESMs are not shown here but provided on the supplied CD-ROM.

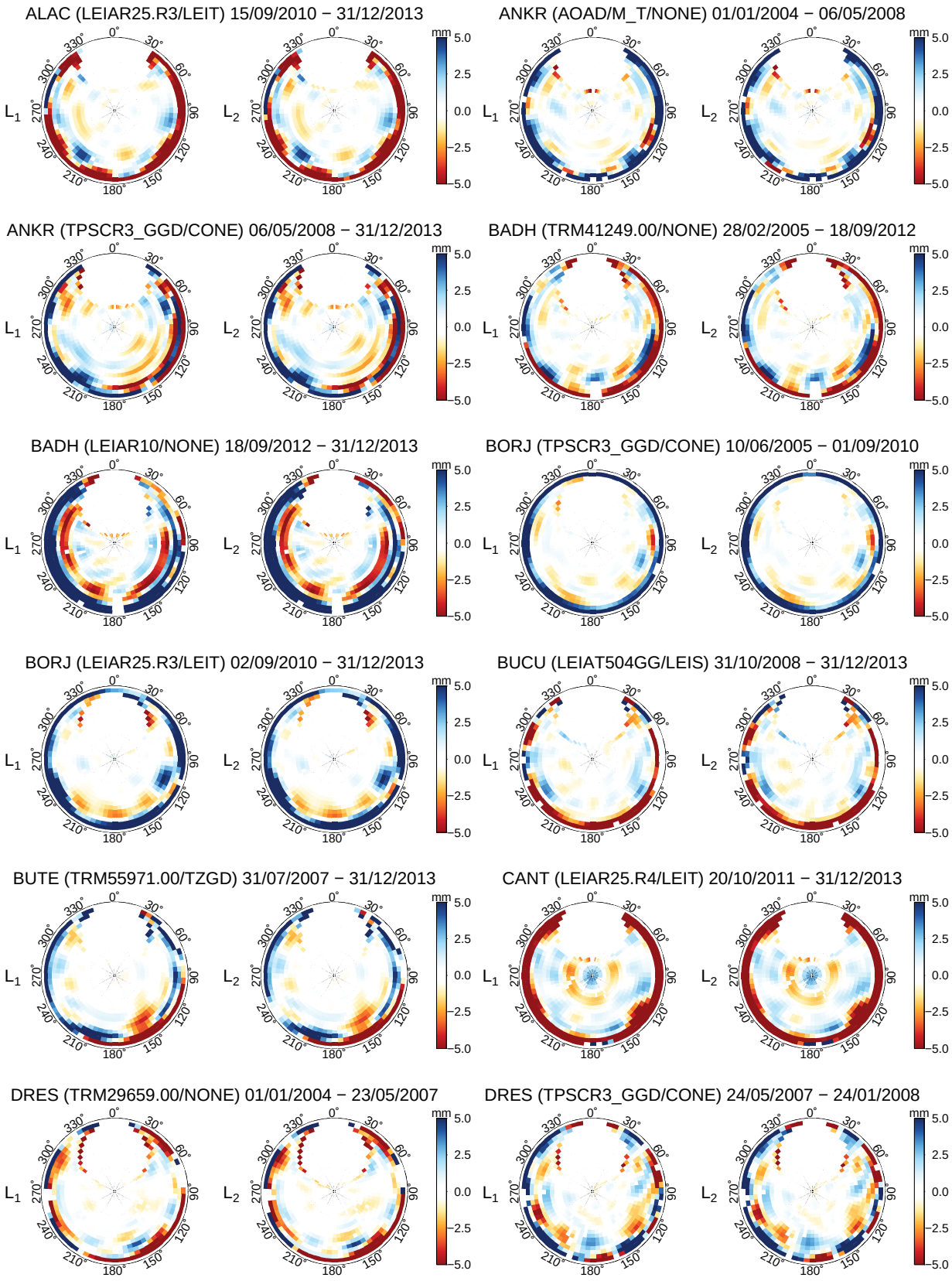

Figure E.1: Skyplots of ESMs for EPN stations *(continued on next page)*.

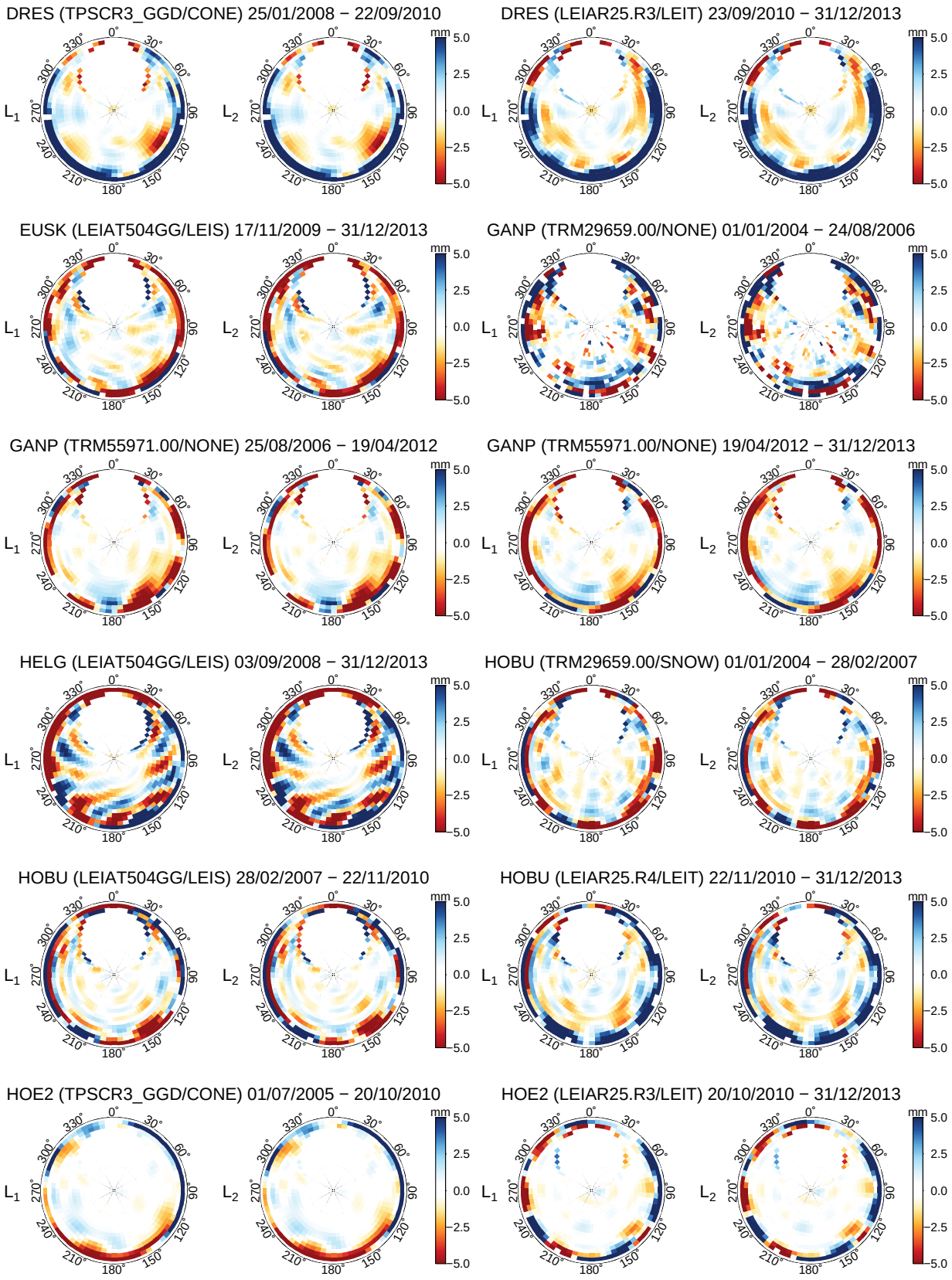

Figure E.1: Skyplots of ESMs for EPN stations *(continued from previous page)*.

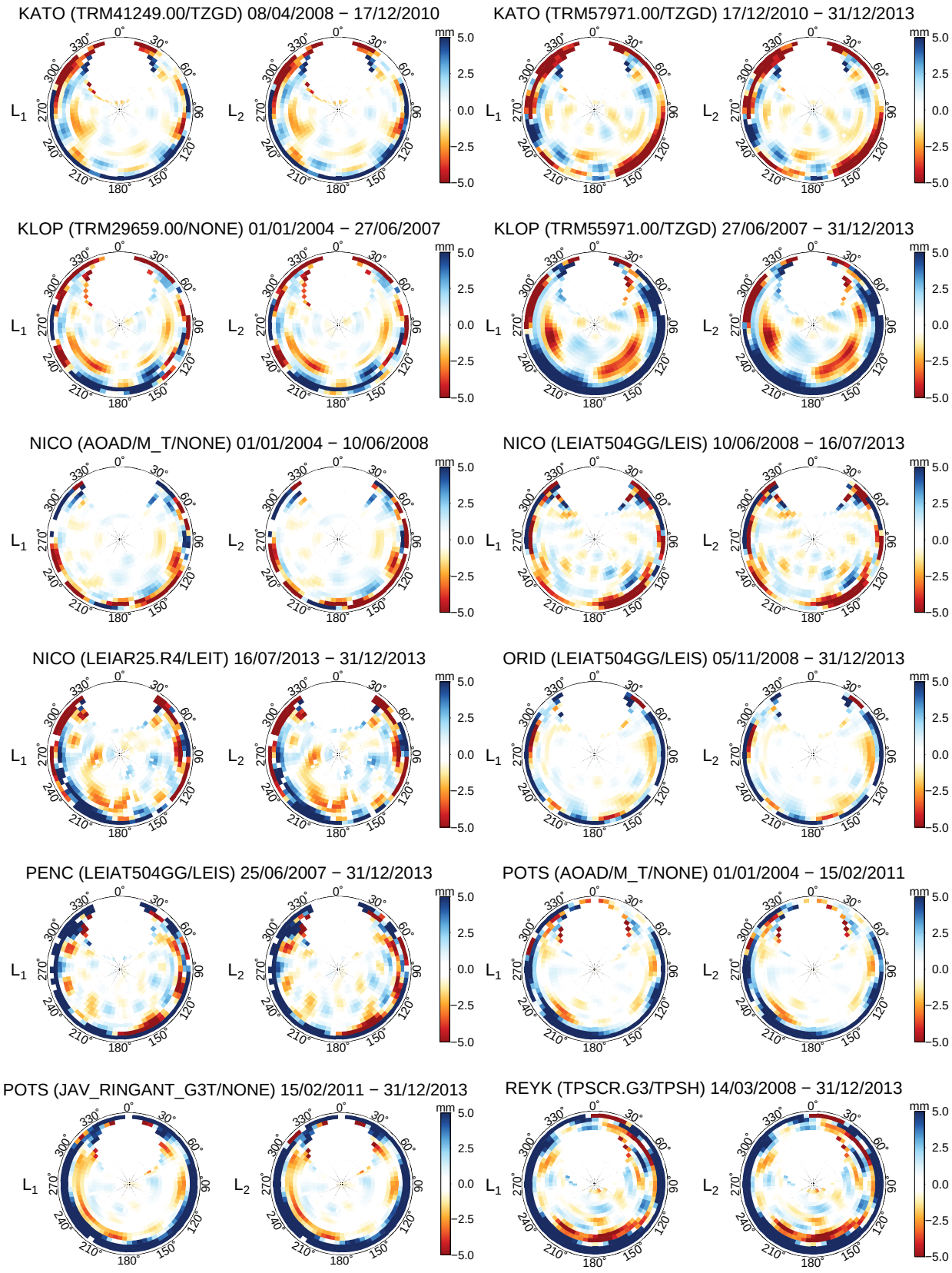

Figure E.1: Skyplots of ESMs for EPN stations *(continued from previous page)*.

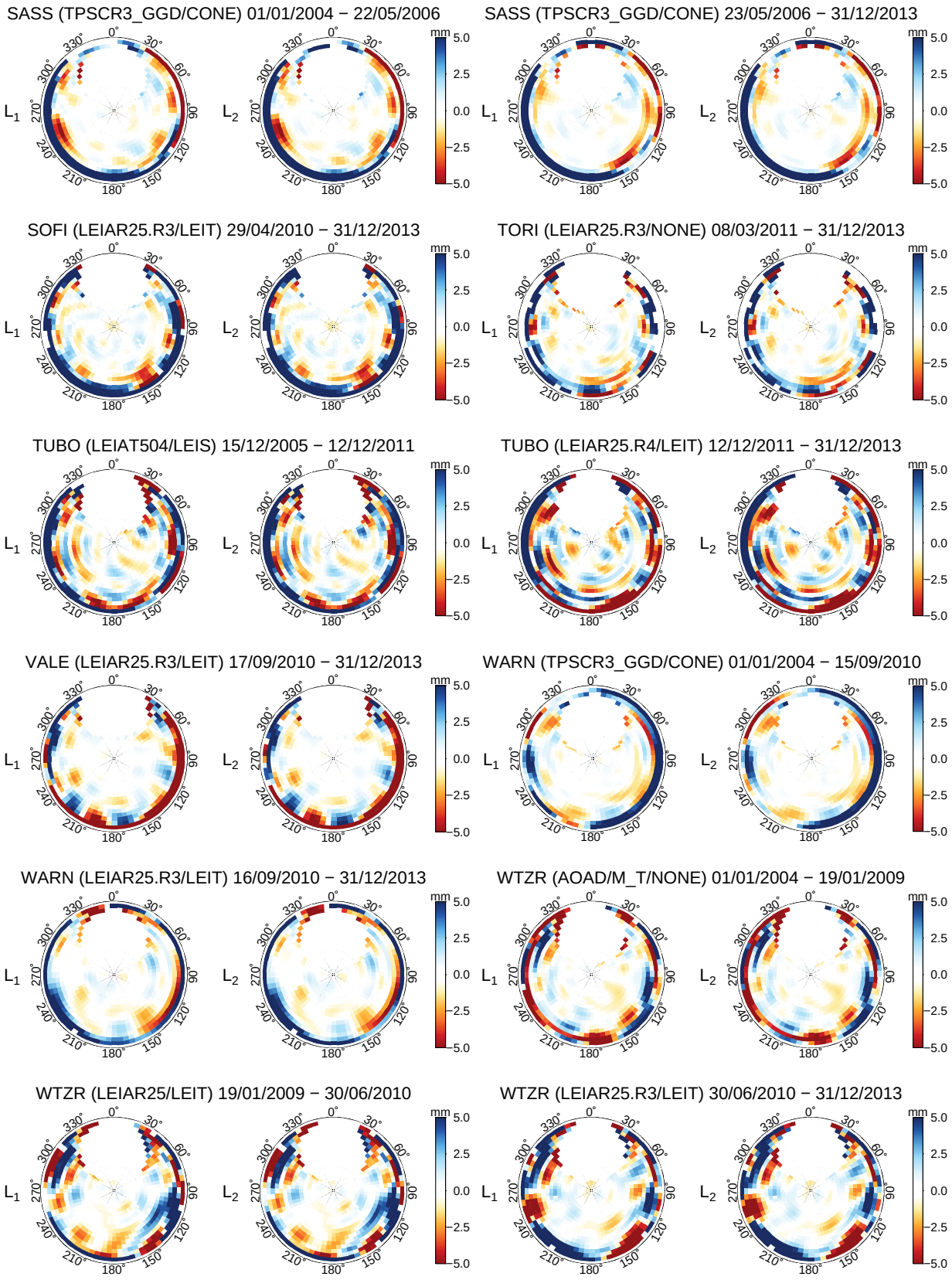

Figure E.1: Skyplots of ESMs for EPN stations *(continued from previous page)*.

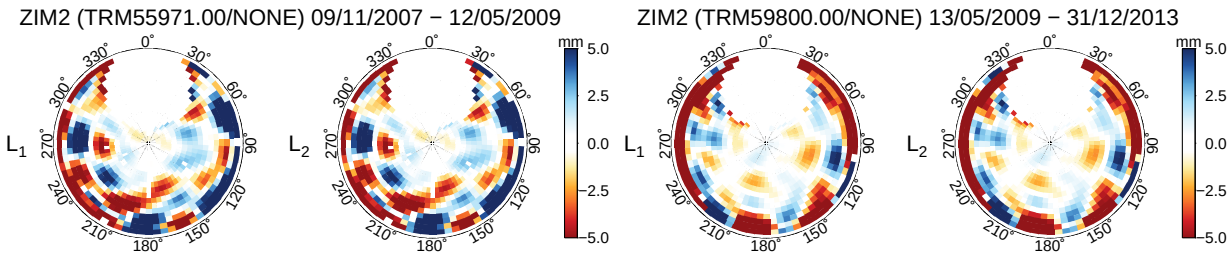

Figure E.1: Skyplots of ESMs for EPN stations *(continued from previous page)*.

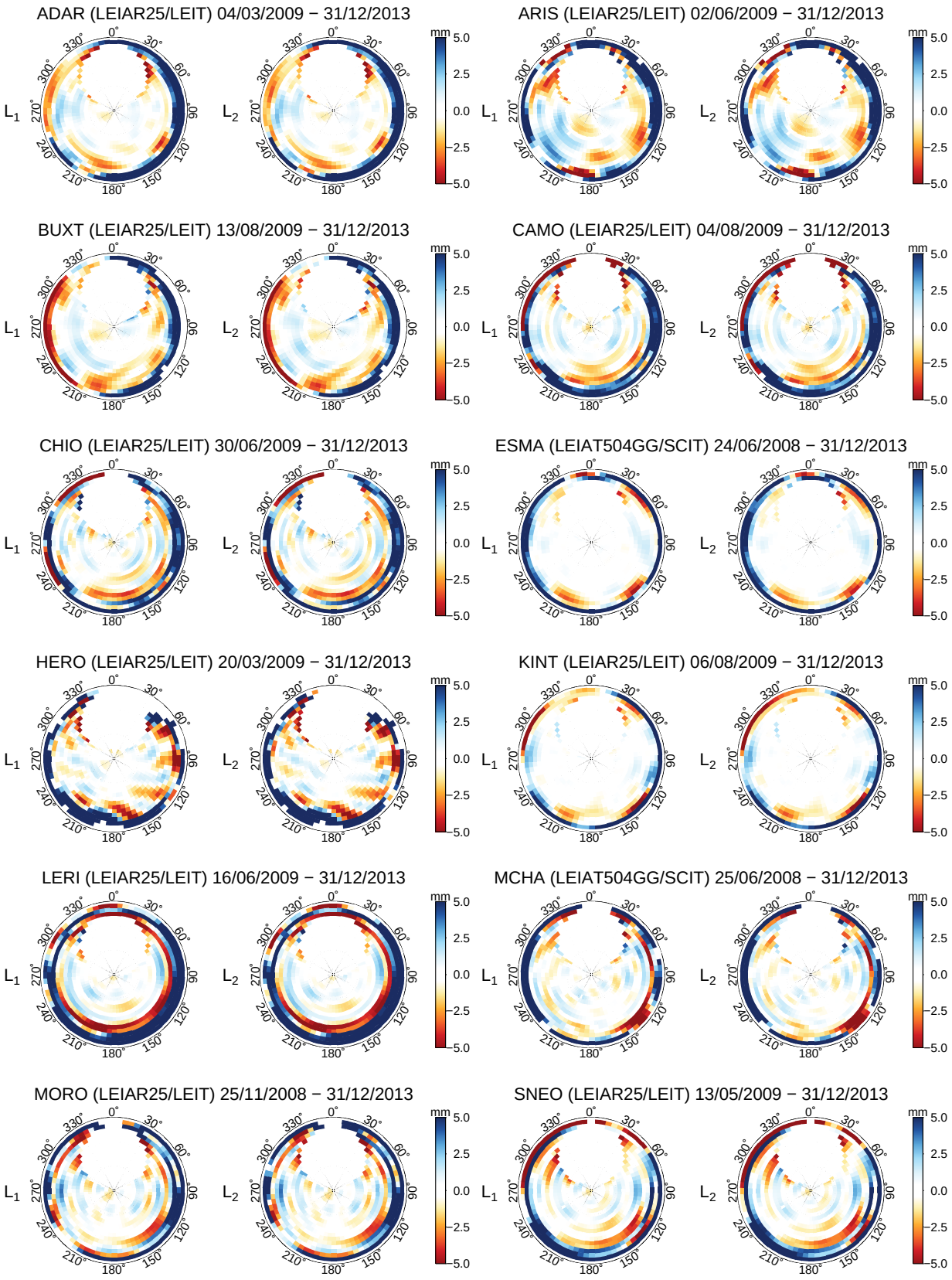

Figure E.2: Skyplots of ESMs for GeoNet and UNOTT stations *(continued on next page)*.

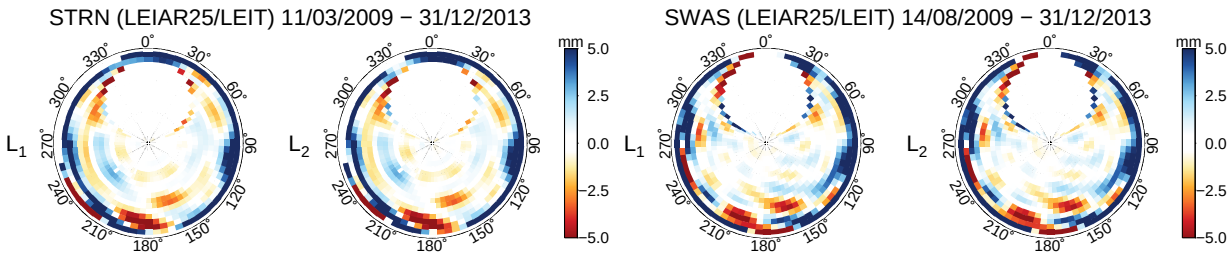

Figure E.2: Skyplots of ESMs for GeoNet and UNOTT stations *(continued from previous page)*.

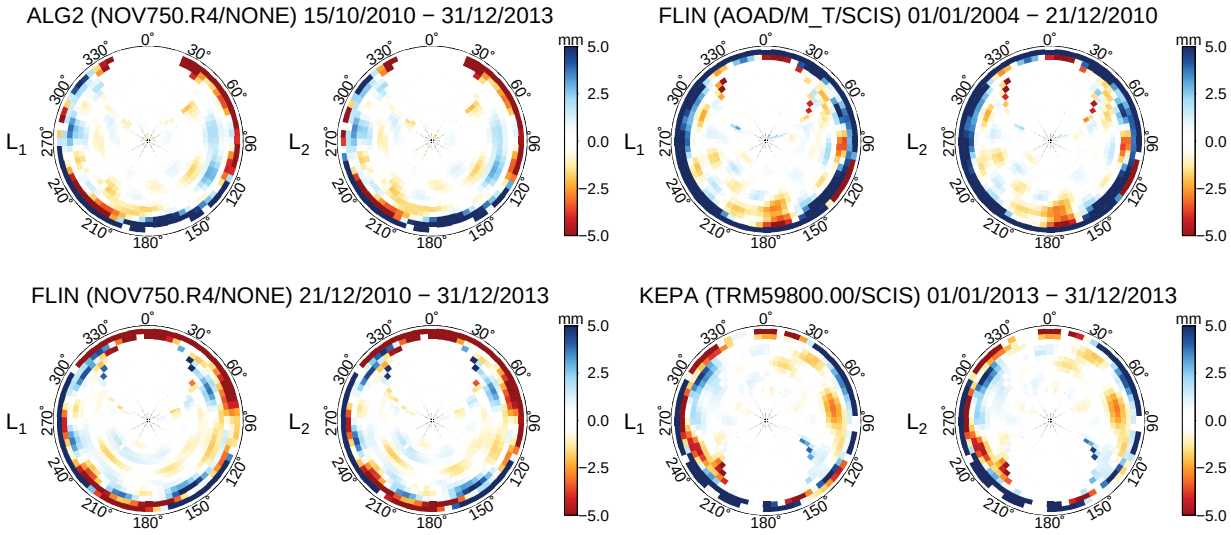

Figure E.3: Skyplots of ESMs for NRCan station ALG2 and FLIN, and station KEPA.

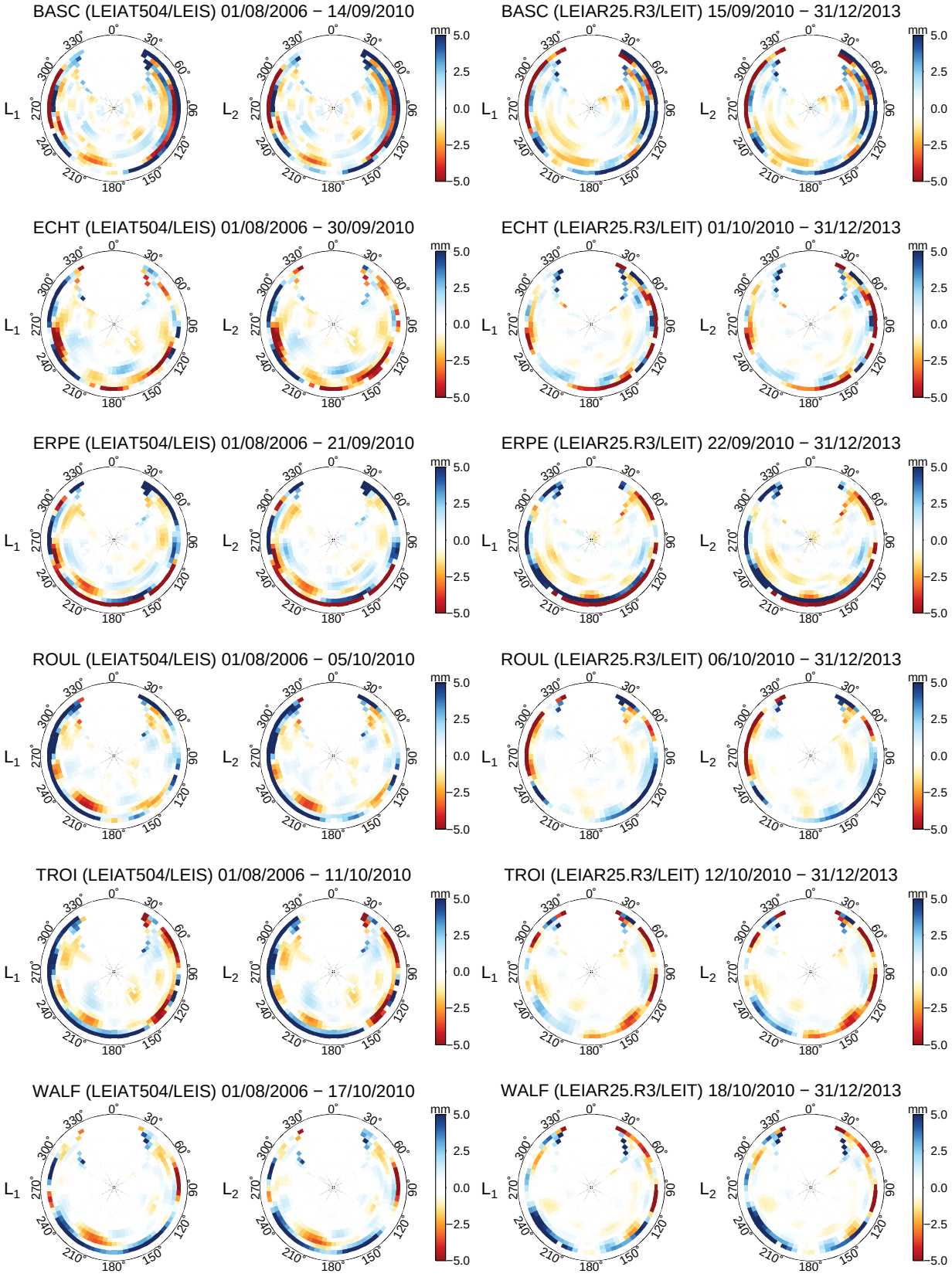

Figure E.4: Skyplots of ESMs for SPSLux stations.

ESM quality control

To compute the ESMs, the reconstructed L_1 and L_2 phase residuals were smoothed by creating their spherical harmonic representation. However, it is often problematic to develop accurate spherical harmonic fits to highly variable data. Additionally, some parts of the sphere may have no data, forcing the values to zero. In turn, this may potentially introduce artefacts.

The PCC provided in the ANTEX format typically have resolution of $5^\circ \times 5^\circ$ in azimuth and elevation. To ensure versatility and the possibility of further merging with the type-mean PCC, the same resolution was used for the derived ESMs. However, to quantify the accuracy of the performed fits to the data, the values of the spherical harmonic representation were compared to the actual data within each $1^\circ \times 1^\circ$ bin. The respective statistical data for each ESM, and, respectively, for each antenna/radome combination, are provided in Table E.1.

The first four columns in Table E.1 contain information about station name, antenna/radome combination employed and a period during which observation residuals were collected for consecutive ESM estimation. According to the methodology of ESM estimation discussed in Section 5.4 of Chapter 5, no changes to antenna/radome combination are allowed during this time interval. The last four columns provide an indication of quality of ESM fits for two GPS frequencies L_1 and L_2. Once the averaged residuals within each $1^\circ \times 1^\circ$ bin are computed and spherical harmonic representation of these data is performed, mean differences between the fitted and the actual averaged data across all bins are obtained. These mean differences together with the respective standard deviations are provided in the column "Mean". Deviation of this mean difference from 0 would imply a biased spherical harmonic fit onto the data, whereas the aforementioned standard deviation characterizes variability of mean residuals across all bins. The minimum and maximum values show extreme excursions of the fitted data from the averaged residuals.

Thus, well performing ESMs in Table E.1 are mainly characterized by small standard deviation, whereas the minimum and maximum values are secondary quality indicators. For ESMs with elevated standard deviation the increase of degree and order of spherical harmonic representation may be appropriate. It should be noted that relatively low degree and order of ESM spherical harmonic representation used in this study was governed by the need of their subsequent merge with type-mean PCC in ANTEX format.

Table E.1: ESM spherical harmonic representation evaluation.

Station	Antenna/radome		From	To	Freq.	Mean [mm]	Min [mm]	Max [mm]
ADAR	LEIAR25	LEIT	04/03/2009	31/12/2013	L_1	0.0 ± 7.0	−275.6	232.0
					L_2	0.0 ± 7.3	−323.3	258.0
ALAC	LEIAR25.R3	LEIT	15/09/2010	31/12/2013	L_1	−0.0 ± 7.0	−557.7	108.4
					L_2	−0.0 ± 7.2	−621.9	97.5
ALG2	NOV750.R4	NONE	15/10/2010	31/12/2013	L_1	−0.0 ± 6.9	−278.4	149.5
					L_2	−0.0 ± 6.8	−158.7	145.3
ALIC	AOAD/M_T	NONE	01/01/2004	19/07/2011	L_1	−0.0 ± 9.6	−314.7	242.1
					L_2	−0.0 ± 9.7	−342.4	234.5
ALIC	LEIAR25.R3	NONE	20/07/2011	31/12/2013	L_1	0.0 ± 12.2	−358.7	451.4
					L_2	0.0 ± 12.3	−455.6	402.1
ANKR	AOAD/M_T	NONE	01/01/2004	06/05/2008	L_1	0.0 ± 9.0	−413.5	156.0
					L_2	0.0 ± 9.0	−379.0	151.4
ANKR	TPSCR3_GGD	CONE	06/05/2008	31/12/2013	L_1	0.0 ± 6.4	−134.5	117.3
					L_2	0.0 ± 6.5	−142.4	113.3
ARIS	LEIAR25	LEIT	02/06/2009	31/12/2013	L_1	−0.0 ± 8.6	−276.4	266.1
					L_2	−0.0 ± 8.9	−266.8	331.8
ARTU	ASH700936D_M	DOME	01/01/2004	31/12/2013	L_1	−0.0 ± 5.6	−197.6	80.0
					L_2	−0.0 ± 5.6	−200.5	72.2
ASPA	TRM33429.20+GP	UNAV	01/01/2004	01/10/2008	L_1	0.0 ± 4.3	−50.1	85.8
					L_2	0.0 ± 4.5	−52.7	85.4
ASPA	TRM55971.00	NONE	01/10/2008	31/12/2013	L_1	0.0 ± 6.1	−140.4	123.9
					L_2	−0.0 ± 6.1	−160.5	94.0
AUCK	TRM41249.00	NONE	03/11/2005	28/02/2011	L_1	−0.0 ± 5.9	−116.6	106.8
					L_2	−0.0 ± 6.0	−110.1	84.3
AUCK	TRM55971.00	NONE	01/03/2011	31/12/2013	L_1	−0.0 ± 6.5	−105.8	121.2
					L_2	−0.0 ± 6.6	−109.9	133.4
BADH	TRM41249.00	NONE	28/02/2005	18/09/2012	L_1	0.0 ± 7.7	−185.1	145.2
					L_2	0.0 ± 8.0	−362.4	106.3
BADH	LEIAR10	NONE	18/09/2012	31/12/2013	L_1	0.0 ± 9.0	−204.5	172.4
					L_2	0.0 ± 8.9	−95.0	231.9
BAN2	AOAD/M_T	NONE	01/01/2004	31/12/2013	L_1	0.0 ± 8.1	−102.8	140.1
					L_2	0.0 ± 8.1	−85.6	141.6
BASC	LEIAT504	LEIS	01/08/2006	14/09/2010	L_1	−0.0 ± 7.4	−74.1	80.9
					L_2	−0.0 ± 7.6	−80.3	85.2
BASC	LEIAR25.R3	LEIT	15/09/2010	31/12/2013	L_1	−0.0 ± 4.9	−46.1	46.6
					L_2	−0.0 ± 4.9	−40.6	43.9
BJFS	ASH700936B_M	SNOW	01/01/2004	21/05/2010	L_1	0.0 ± 6.4	−96.1	107.8
					L_2	0.0 ± 6.4	−98.8	130.2
BJFS	TRM59800.00	SCIS	22/05/2010	31/12/2013	L_1	−0.0 ± 6.8	−77.4	125.7
					L_2	−0.0 ± 6.8	−83.6	158.1

(continued on next page)

Table E.1: ESM spherical harmonic representation evaluation *(continued from previous page).*

Station	Antenna/radome		From	To	Freq.	Mean [mm]	Min [mm]	Max [mm]
BOGT	AOAD/M_T	NONE	01/01/2004	06/07/2005	L_1	-0.0 ± 6.2	-73.60	78.20
					L_2	-0.0 ± 6.2	-68.90	101.20
BOGT	ASH701945G_M	NONE	12/07/2005	13/12/2007	L_1	0.0 ± 5.7	-62.60	90.60
					L_2	0.0 ± 5.8	-67.50	82.00
BOGT	ASH701945E_M	NONE	13/12/2007	06/06/2008	L_1	-0.0 ± 7.8	-79.10	147.20
					L_2	-0.0 ± 7.9	-107.70	146.90
BOGT	ASH701945G_M	NONE	07/06/2008	09/09/2009	L_1	0.0 ± 6.5	-112.30	125.60
					L_2	0.0 ± 6.7	-133.40	122.60
BOGT	ASH701945E_M	NONE	09/09/2009	31/12/2013	L_1	0.0 ± 4.9	-61.70	82.50
					L_2	0.0 ± 4.9	-52.20	59.40
BORJ	TPSCR3_GGD	CONE	10/06/2005	01/09/2010	L_1	-0.0 ± 5.4	-86.10	88.10
					L_2	-0.0 ± 5.5	-88.40	107.30
BORJ	LEIAR25.R3	LEIT	02/09/2010	31/12/2013	L_1	0.0 ± 5.9	-161.40	160.30
					L_2	0.0 ± 6.1	-162.00	231.40
BRAZ	AOAD/M_T	NONE	01/01/2004	12/03/2007	L_1	0.0 ± 7.1	-133.90	120.70
					L_2	0.0 ± 7.2	-129.30	123.10
BRAZ	TRM41249.00	NONE	13/03/2007	18/09/2012	L_1	-0.0 ± 6.7	-232.70	153.60
					L_2	-0.0 ± 6.7	-256.50	167.10
BRAZ	TRM59800.00	NONE	18/09/2012	27/11/2012	L_1	-0.0 ± 16.7	-73.60	93.20
					L_2	-0.0 ± 17.3	-89.40	91.70
BRAZ	TRM41249.00	NONE	27/11/2012	25/04/2013	L_1	-0.0 ± 9.5	-68.70	92.90
					L_2	0.0 ± 9.6	-70.10	103.40
BRAZ	TRM59800.00	NONE	25/04/2013	31/12/2013	L_1	-0.0 ± 8.7	-176.50	99.80
					L_2	-0.0 ± 8.8	-184.10	114.60
BRFT	LEIAT504	NONE	06/09/2005	31/12/2013	L_1	-0.0 ± 11.9	-412.10	502.30
					L_2	-0.0 ± 11.9	-472.60	581.00
BRMU	TRM29659.00	UNAV	01/01/2004	28/09/2011	L_1	0.0 ± 7.0	-366.30	184.90
					L_2	0.0 ± 7.1	-426.80	209.30
BRMU	JAVRINGANT_DM	NONE	28/09/2011	31/12/2013	L_1	0.0 ± 8.6	-266.70	330.40
					L_2	0.0 ± 8.6	-319.90	173.60
BUCU	LEIAT504GG	LEIS	31/10/2008	31/12/2013	L_1	-0.0 ± 8.7	-298.70	254.60
					L_2	-0.0 ± 8.5	-286.30	258.80
BUTE	TRM55971.00	TZGD	31/07/2007	31/12/2013	L_1	0.0 ± 7.2	-113.40	151.90
					L_2	0.0 ± 7.3	-131.50	169.60
BUXT	LEIAR25	LEIT	03/08/2009	31/12/2013	L_1	-0.0 ± 5.9	-118.40	168.00
					L_2	-0.0 ± 6.2	-199.80	163.20
CAMO	LEIAR25	LEIT	04/08/2009	31/12/2013	L_1	-0.0 ± 10.9	-195.90	721.00
					L_2	-0.0 ± 11.5	-171.50	867.30
CANT	LEIAR25.R4	LEIT	20/10/2011	31/12/2013	L_1	-0.0 ± 8.4	-117.80	91.50
					L_2	-0.0 ± 8.4	-171.90	100.70

(continued on next page)

Table E.1: ESM spherical harmonic representation evaluation *(continued from previous page).*

Station	Antenna/radome		From	To	Freq.	Mean [mm]	Min [mm]	Max [mm]
CAS1	AOAD/M_T	AUST	01/01/2004	31/12/2013	L_1	0.0 ± 16.2	−332.00	1115.90
					L_2	0.0 ± 16.3	−415.70	1049.30
CCJM	TRM29659.00	DOME	01/01/2004	31/12/2013	L_1	−0.0 ± 4.7	−87.50	108.20
					L_2	−0.0 ± 4.8	−75.90	168.80
CEDU	AOAD/M_T	AUST	01/01/2004	27/06/2006	L_1	−0.0 ± 12.2	−169.70	428.40
					L_2	−0.0 ± 13.0	−230.80	508.00
CEDU	AOAD/M_T	AUST	15/07/2006	31/12/2013	L_1	0.0 ± 5.4	−57.70	78.50
					L_2	0.0 ± 5.5	−72.70	100.30
CHAT	ASH701945C_M	NONE	01/01/2004	31/12/2013	L_1	0.0 ± 5.6	−79.60	99.20
					L_2	0.0 ± 5.6	−94.40	96.30
CHIO	LEIAR25	LEIT	30/06/2009	31/12/2013	L_1	−0.0 ± 9.1	−162.40	113.40
					L_2	−0.0 ± 9.2	−235.70	95.30
CHUR	AOAD/M_T	NONE	01/01/2004	28/03/2008	L_1	0.0 ± 8.5	−123.90	129.30
					L_2	0.0 ± 8.5	−110.20	140.70
CHUR	ASH701945E_M	NONE	28/03/2008	31/03/2009	L_1	−0.0 ± 7.4	−69.20	183.40
					L_2	0.0 ± 7.4	−79.30	153.70
CHUR	AOAD/M_T	NONE	01/04/2009	01/09/2010	L_1	0.0 ± 14.2	−315.40	424.00
					L_2	0.0 ± 14.6	−355.70	492.70
CHUR	ASH701945E_M	NONE	02/09/2010	31/12/2013	L_1	0.0 ± 8.5	−110.70	227.80
					L_2	0.0 ± 8.5	−173.80	201.70
COCO	AOAD/M_T	AUST	01/01/2004	24/06/2004	L_1	−0.0 ± 9.7	−108.80	154.60
					L_2	−0.0 ± 10.0	−145.80	152.80
COCO	AOAD/M_T	NONE	24/06/2004	31/12/2013	L_1	0.0 ± 5.7	−147.60	124.90
					L_2	0.0 ± 5.8	−167.50	124.50
CONZ	JPSREGANT_DD_E1	NONE	01/01/2004	17/05/2005	L_1	−0.0 ± 7.1	−92.40	124.70
					L_2	−0.0 ± 7.3	−141.60	126.40
CONZ	TPSCR3_GGD	CONE	17/05/2005	19/07/2011	L_1	0.0 ± 7.3	−446.50	209.40
					L_2	0.0 ± 7.4	−309.20	236.90
CRO1	AOAD/M_T	JPLA	01/01/2004	19/01/2005	L_1	0.0 ± 5.7	−75.30	63.00
					L_2	0.0 ± 5.8	−79.40	78.40
CRO1	ASH701945G_M	JPLA	04/08/2005	01/04/2011	L_1	−0.0 ± 4.4	−183.60	94.50
					L_2	−0.0 ± 4.3	−110.80	65.10
CRO1	ASH701945G_M	NONE	01/04/2011	24/06/2011	L_1	−0.0 ± 8.3	−78.80	71.10
					L_2	0.0 ± 8.3	−52.20	74.10
CRO1	ASH701945G_M	JPLA	24/06/2011	31/12/2013	L_1	0.0 ± 5.1	−79.30	55.20
					L_2	0.0 ± 5.1	−75.50	53.30
DARW	ASH700936D_M	NONE	01/01/2004	31/12/2013	L_1	−0.0 ± 9.6	−286.80	349.00
					L_2	−0.0 ± 10.3	−354.00	485.00
DAV1	AOAD/M_T	AUST	01/01/2004	01/08/2007	L_1	−0.0 ± 10.5	−105.10	124.40
					L_2	−0.0 ± 10.6	−179.10	107.20

(continued on next page)

Table E.1: ESM spherical harmonic representation evaluation *(continued from previous page).*

Station	Antenna/radome		From	To	Freq.	Mean [mm]	Min [mm]	Max [mm]
DAV1	ASH701945G_M	AUST	01/08/2007	20/02/2011	L_1	0.0 ± 11.6	−210.90	157.10
					L_2	0.0 ± 11.9	−283.90	180.60
DAV1	LEIAR25.R3	LEIT	21/02/2011	31/12/2013	L_1	−0.0 ± 10.5	−281.70	293.90
					L_2	−0.0 ± 10.3	−215.90	225.10
DGAR	ASH701945E_M	NONE	18/05/2004	31/12/2013	L_1	0.0 ± 4.6	−191.10	80.10
					L_2	0.0 ± 4.4	−165.90	68.00
DRAO	AOAD/M_T	NONE	01/01/2004	11/03/2013	L_1	0.0 ± 5.2	−183.10	204.20
					L_2	−0.0 ± 5.2	−162.90	166.30
DRAO	TRM59800.00	SCIS	11/03/2013	31/12/2013	L_1	0.0 ± 7.6	−105.60	146.40
					L_2	0.0 ± 7.6	−86.20	113.90
DRES	TRM29659.00	NONE	01/01/2004	23/05/2007	L_1	0.0 ± 8.9	−124.70	138.40
					L_2	−0.0 ± 9.1	−123.90	195.40
DRES	TPSCR3_GGD	CONE	24/05/2007	24/01/2008	L_1	0.0 ± 9.0	−88.20	123.40
					L_2	0.0 ± 9.2	−108.90	97.00
DRES	TPSCR3_GGD	CONE	25/01/2008	22/09/2010	L_1	0.0 ± 6.7	−114.10	74.20
					L_2	0.0 ± 6.8	−127.80	75.90
DRES	LEIAR25.R3	LEIT	23/09/2010	31/12/2013	L_1	−0.0 ± 6.6	−126.60	118.10
					L_2	−0.0 ± 6.6	−121.30	66.60
DUM1	ASH700936E	SNOW	01/01/2004	31/12/2013	L_1	−0.0 ± 8.2	−95.40	210.50
					L_2	−0.0 ± 8.3	−139.80	211.80
ECHT	LEIAT504	LEIS	01/08/2006	30/09/2010	L_1	−0.0 ± 6.9	−70.20	68.20
					L_2	0.0 ± 7.1	−65.20	74.10
ECHT	LEIAR25.R3	LEIT	01/10/2010	31/12/2013	L_1	0.0 ± 4.4	−69.90	140.40
					L_2	0.0 ± 4.5	−69.60	145.70
ERPE	LEIAT504	LEIS	01/08/2006	21/09/2010	L_1	0.0 ± 7.7	−84.40	82.40
					L_2	0.0 ± 7.8	−77.30	85.20
ERPE	LEIAR25.R3	LEIT	22/09/2010	31/12/2013	L_1	−0.0 ± 5.6	−97.40	55.90
					L_2	−0.0 ± 5.5	−63.80	52.90
ESMA	LEIAT504GG	SCIT	24/06/2008	31/12/2013	L_1	−0.0 ± 5.8	−118.50	187.00
					L_2	−0.0 ± 6.0	−161.80	216.00
EUSK	LEIAT504GG	LEIS	17/11/2009	31/12/2013	L_1	0.0 ± 13.3	−497.40	415.70
					L_2	0.0 ± 14.1	−647.70	395.80
GANP	TRM29659.00	NONE	01/01/2004	24/08/2006	L_1	−0.0 ± 15.4	−125.70	107.60
					L_2	−0.0 ± 15.7	−111.50	134.30
GANP	TRM55971.00	NONE	25/08/2006	19/04/2012	L_1	−0.0 ± 6.9	−152.70	294.10
					L_2	−0.0 ± 6.8	−194.90	246.50
GANP	TRM55971.00	NONE	19/04/2012	31/12/2013	L_1	0.0 ± 7.4	−112.70	185.40
					L_2	0.0 ± 7.3	−128.60	183.60
GLPS	ASH701945B_M	SCIT	01/01/2004	13/11/2012	L_1	−0.0 ± 4.3	−170.00	60.40
					L_2	−0.0 ± 4.1	−79.50	55.60

(continued on next page)

Table E.1: ESM spherical harmonic representation evaluation *(continued from previous page).*

Station	Antenna/radome		From	To	Freq.	Mean [mm]	Min [mm]	Max [mm]
GLPS	ASH701945B_M	NONE	13/11/2012	06/12/2012	L_1	0.0 ± 12.7	−79.90	66.90
					L_2	−0.0 ± 13.0	−73.90	63.30
GLPS	ASH701945B_M	SCIT	06/12/2012	31/12/2013	L_1	0.0 ± 5.3	−79.70	55.30
					L_2	0.0 ± 5.4	−61.70	53.50
GOLD	AOAD/M_T	NONE	01/01/2004	31/12/2013	L_1	−0.0 ± 4.6	−195.10	136.60
					L_2	−0.0 ± 4.6	−161.20	159.60
GOUG	TRM29659.00	TCWD	01/01/2004	31/12/2013	L_1	0.0 ± 3.7	−39.90	44.20
					L_2	0.0 ± 3.7	−39.00	47.10
GUAM	AOAD/M_T	JPLA	01/01/2004	17/05/2006	L_1	−0.0 ± 7.2	−139.70	124.20
					L_2	0.0 ± 7.3	−133.80	141.20
GUAM	ASH701945B_M	JPLA	18/05/2006	31/12/2013	L_1	0.0 ± 5.3	−218.10	128.40
					L_2	−0.0 ± 5.4	−233.40	138.40
GUAT	TRM29659.00	UNAV	01/01/2004	28/11/2011	L_1	0.0 ± 11.1	−469.40	479.80
					L_2	0.0 ± 11.1	−553.50	399.80
GUAT	LEIAR25.R3	LEIT	28/11/2011	31/12/2013	L_1	−0.0 ± 8.6	−142.30	169.40
					L_2	−0.0 ± 8.7	−174.40	193.70
HELG	LEIAT504GG	LEIS	03/09/2008	31/12/2013	L_1	0.0 ± 7.5	−196.60	124.10
					L_2	0.0 ± 7.7	−162.90	207.00
HERO	LEIAR25	LEIT	20/03/2009	31/12/2013	L_1	0.0 ± 9.3	−288.30	181.20
					L_2	0.0 ± 9.8	−441.20	188.40
HOB2	AOAD/M_T	NONE	01/01/2004	31/12/2013	L_1	−0.0 ± 8.7	−244.00	259.50
					L_2	−0.0 ± 8.6	−200.70	225.80
HOBU	TRM29659.00	SNOW	01/01/2004	28/02/2007	L_1	0.0 ± 8.8	−124.80	484.30
					L_2	0.0 ± 8.6	−165.40	444.50
HOBU	LEIAT504GG	LEIS	28/02/2007	22/11/2010	L_1	−0.0 ± 11.6	−371.70	266.60
					L_2	0.0 ± 11.9	−380.00	354.30
HOBU	LEIAR25.R4	LEIT	22/11/2010	31/12/2013	L_1	−0.0 ± 8.3	−277.00	161.40
					L_2	−0.0 ± 8.5	−321.20	209.90
HOE2	TPSCR3_GGD	CONE	01/07/2005	20/10/2010	L_1	−0.0 ± 5.6	−116.50	103.40
					L_2	0.0 ± 5.7	−152.50	108.20
HOE2	LEIAR25.R3	LEIT	20/10/2010	31/12/2013	L_1	0.0 ± 6.4	−190.40	93.70
					L_2	0.0 ± 6.4	−119.10	96.60
HOFN	TRM29659.00	NONE	01/01/2004	22/09/2007	L_1	0.0 ± 8.6	−87.20	127.20
					L_2	0.0 ± 8.6	−75.00	138.70
HOFN	TPSCR3_GGD	CONE	23/09/2007	05/05/2013	L_1	−0.0 ± 7.2	−186.10	221.10
					L_2	0.0 ± 7.4	−240.10	263.30
HOFN	LEIAR25.R4	LEIT	05/05/2013	31/12/2013	L_1	−0.0 ± 10.5	−154.60	124.80
					L_2	−0.0 ± 10.6	−163.80	124.40
IISC	AOAD/M_T	NONE	01/01/2004	08/01/2008	L_1	0.0 ± 5.8	−74.20	111.80
					L_2	0.0 ± 5.8	−76.10	92.40

(continued on next page)

Table E.1: ESM spherical harmonic representation evaluation *(continued from previous page).*

Station	Antenna/radome		From	To	Freq.	Mean [mm]	Min [mm]	Max [mm]
IISC	ASH701945E_M	NONE	09/01/2008	31/12/2013	L_1	−0.0 ± 5.1	−83.80	65.90
					L_2	−0.0 ± 5.2	−78.60	53.10
IRKT	AOAD/M_T	NONE	01/01/2004	31/12/2013	L_1	−0.0 ± 11.2	−375.40	319.90
					L_2	−0.0 ± 11.3	−395.20	361.10
ISPA	ASH701945E_M	SCIT	13/02/2004	31/12/2013	L_1	0.0 ± 12.5	−554.20	368.30
					L_2	0.0 ± 13.9	−890.90	404.60
KARR	AOAD/M_T	AUST	01/01/2004	18/05/2010	L_1	0.0 ± 6.7	−97.90	75.50
					L_2	0.0 ± 6.7	−77.50	109.10
KARR	TRM59800.00	NONE	19/05/2010	31/12/2013	L_1	0.0 ± 6.9	−93.50	147.30
					L_2	0.0 ± 7.0	−110.70	116.80
KATO	TRM41249.00	TZGD	08/04/2008	17/12/2010	L_1	−0.0 ± 6.2	−79.70	78.70
					L_2	−0.0 ± 6.3	−99.70	66.00
KATO	TRM57971.00	TZGD	17/12/2010	31/12/2013	L_1	0.0 ± 6.1	−76.90	108.20
					L_2	0.0 ± 6.1	−86.70	69.10
KEPA	TRM59800.00	SCIS	01/01/2013	31/12/2013	L_1	0.0 ± 7.7	−93.80	96.10
					L_2	0.0 ± 7.6	−109.30	98.10
KERG	TRM29659.00	NONE	01/01/2004	05/09/2008	L_1	−0.0 ± 6.8	−67.10	120.70
					L_2	−0.0 ± 6.9	−76.90	115.50
KERG	ASH701945E_M	SNOW	05/09/2008	31/12/2013	L_1	0.0 ± 7.6	−118.60	95.10
					L_2	0.0 ± 7.6	−109.10	123.00
KHAJ	JPSREGANT_SD_E1	NONE	01/01/2004	31/12/2013	L_1	0.0 ± 8.0	−185.90	151.00
					L_2	0.0 ± 8.2	−210.00	175.10
KINT	LEIAR25	LEIT	06/08/2009	31/12/2013	L_1	−0.0 ± 5.6	−193.70	129.50
					L_2	−0.0 ± 5.5	−88.20	114.30
KIRO	AOAD/M_T	OSOD	01/01/2004	31/12/2013	L_1	−0.0 ± 7.4	−105.60	101.90
					L_2	−0.0 ± 7.5	−123.10	81.80
KLOP	TRM29659.00	NONE	01/01/2004	27/06/2007	L_1	0.0 ± 8.7	−162.60	126.30
					L_2	0.0 ± 8.7	−178.50	114.60
KLOP	TRM55971.00	TZGD	27/06/2007	31/12/2013	L_1	−0.0 ± 8.6	−167.20	265.50
					L_2	−0.0 ± 8.9	−212.00	292.30
KOKB	ASH701945C_M	NONE	01/01/2004	18/05/2004	L_1	−0.0 ± 11.7	−140.20	143.00
					L_2	−0.0 ± 11.7	−140.40	135.70
KOKB	ASH701945G_M	NONE	18/05/2004	31/12/2013	L_1	0.0 ± 5.6	−237.20	280.90
					L_2	−0.0 ± 5.7	−131.90	322.60
KOUC	ASH700936D_M	SNOW	01/01/2004	16/05/2006	L_1	0.0 ± 13.6	−64.90	61.90
					L_2	−0.0 ± 14.3	−67.10	65.10
KOUC	TRM41249.00	TZGD	16/05/2006	16/11/2009	L_1	−0.0 ± 6.9	−117.10	136.80
					L_2	−0.0 ± 7.1	−123.80	156.60
KOUC	TRM57971.00	TZGD	16/11/2009	31/12/2013	L_1	0.0 ± 7.0	−171.50	201.40
					L_2	0.0 ± 7.2	−190.80	187.70

(continued on next page)

Table E.1: ESM spherical harmonic representation evaluation *(continued from previous page).*

Station	Antenna/radome		From	To	Freq.	Mean [mm]	Min [mm]	Max [mm]
KUNM	AOAD/M_T	NONE	01/01/2004	31/12/2013	L_1	0.0 ± 9.4	−189.30	304.50
					L_2	0.0 ± 9.7	−247.40	374.60
LAE1	ASH700936A_M	NONE	01/01/2004	31/12/2013	L_1	0.0 ± 6.6	−97.30	59.60
					L_2	0.0 ± 6.6	−89.10	65.20
LERI	LEIAR25	LEIT	16/06/2009	31/12/2013	L_1	0.0 ± 5.6	−116.60	81.80
					L_2	0.0 ± 5.8	−215.20	96.90
LHAZ	ASH701941.B	SNOW	01/01/2004	12/09/2013	L_1	−0.0 ± 5.6	−188.10	75.90
					L_2	−0.0 ± 5.5	−154.90	129.30
LHAZ	ASH701941.B	NONE	12/09/2013	31/12/2013	L_1	−0.0 ± 9.1	−73.60	75.60
					L_2	−0.0 ± 9.1	−63.90	68.80
LPGS	AOAD/M_T	NONE	01/01/2004	15/03/2012	L_1	0.0 ± 4.3	−56.90	60.00
					L_2	−0.0 ± 4.3	−74.20	56.70
LPGS	TPSCR.G3	NONE	15/03/2012	03/10/2012	L_1	−0.0 ± 8.6	−66.90	65.20
					L_2	−0.0 ± 8.7	−72.80	64.00
LPGS	JAV_RINGANT_G3T	NONE	04/10/2012	31/12/2013	L_1	−0.0 ± 6.9	−79.50	94.60
					L_2	−0.0 ± 6.8	−78.10	78.80
MAC1	AOAD/M_T	AUST	01/01/2004	31/12/2013	L_1	0.0 ± 5.2	−216.80	191.30
					L_2	0.0 ± 5.8	−277.50	186.70
MAR6	AOAD/M_T	OSOD	01/01/2004	31/12/2013	L_1	0.0 ± 9.4	−216.80	210.50
					L_2	0.0 ± 9.7	−212.00	257.00
MAS1	AOAD/M_T	NONE	01/01/2004	07/07/2008	L_1	0.0 ± 7.3	−126.50	99.90
					L_2	0.0 ± 7.3	−82.90	120.00
MAS1	ASH701945E_M	NONE	07/07/2008	18/06/2012	L_1	0.0 ± 8.4	−314.40	258.20
					L_2	0.0 ± 8.3	−267.20	242.80
MAS1	LEIAR25.R4	NONE	18/06/2012	31/12/2013	L_1	−0.0 ± 11.7	−327.70	350.80
					L_2	−0.0 ± 11.1	−282.40	370.60
MAW1	AOAD/M_T	AUST	01/01/2004	31/12/2013	L_1	−0.0 ± 20.9	−743.50	474.50
					L_2	−0.0 ± 21.1	−681.70	310.20
MBAR	ASH701945B_M	SCIS	01/01/2004	31/12/2013	L_1	−0.0 ± 6.7	−447.70	257.70
					L_2	−0.0 ± 7.3	−539.40	421.50
MCHA	LEIAT504GG	SCIT	25/06/2008	31/12/2013	L_1	−0.0 ± 13.6	−484.40	380.70
					L_2	−0.0 ± 13.3	−418.30	396.00
MCIL	TRM29659.00	DOME	01/01/2004	17/01/2013	L_1	0.0 ± 5.5	−289.30	239.50
					L_2	0.0 ± 5.4	−338.40	129.50
MCIL	TRM59800.80	DOME	17/01/2013	31/12/2013	L_1	−0.0 ± 9.0	−141.80	213.30
					L_2	−0.0 ± 9.1	−164.80	185.40
MCM4	AOAD/M_T	JPLA	01/01/2004	31/12/2013	L_1	−0.0 ± 10.6	−292.90	328.80
					L_2	−0.0 ± 10.9	−325.00	336.40
MDO1	AOAD/M_T	JPLA	01/01/2004	22/02/2013	L_1	−0.0 ± 7.5	−206.50	133.00
					L_2	−0.0 ± 7.5	−214.30	216.40

(continued on next page)

Table E.1: ESM spherical harmonic representation evaluation *(continued from previous page).*

Station	Antenna/radome		From	To	Freq.	Mean [mm]	Min [mm]	Max [mm]
MDO1	AOAD/M_T	NONE	22/02/2013	09/08/2013	L_1	-0.0 ± 9.9	-90.70	93.90
					L_2	-0.0 ± 10.0	-88.70	95.90
MDO1	AOAD/M_T	JPLA	09/08/2013	31/12/2013	L_1	-0.0 ± 13.0	-96.90	157.60
					L_2	0.0 ± 13.1	-94.30	166.70
MKEA	AOAD/M_T	NONE	01/01/2004	31/12/2013	L_1	0.0 ± 9.2	-412.60	226.20
					L_2	0.0 ± 9.4	-282.30	272.40
MORO	LEIAR25	LEIT	25/11/2008	31/12/2013	L_1	-0.0 ± 11.7	-694.30	291.80
					L_2	-0.0 ± 11.5	-600.30	320.40
MQZG	ASH701945C_M	SCIS	01/01/2004	28/02/2005	L_1	0.0 ± 7.4	-94.10	73.40
					L_2	0.0 ± 7.5	-96.20	79.70
MQZG	TRM41249.00	NONE	28/02/2005	09/02/2011	L_1	0.0 ± 4.8	-85.80	105.20
					L_2	0.0 ± 4.8	-81.40	77.20
MQZG	TRM55971.00	NONE	09/02/2011	31/12/2013	L_1	-0.0 ± 4.9	-72.20	69.10
					L_2	-0.0 ± 5.0	-72.00	85.90
NICO	AOAD/M_T	NONE	01/01/2004	10/06/2008	L_1	-0.0 ± 7.6	-146.80	156.30
					L_2	-0.0 ± 7.6	-108.50	134.90
NICO	LEIAT504GG	LEIS	10/06/2008	16/07/2013	L_1	0.0 ± 8.9	-264.50	158.60
					L_2	0.0 ± 9.1	-263.50	154.20
NICO	LEIAR25.R4	LEIT	16/07/2013	31/12/2013	L_1	0.0 ± 11.1	-108.50	115.20
					L_2	0.0 ± 11.3	-105.00	186.80
NKLG	TRM29659.00	NONE	01/01/2004	04/05/2010	L_1	-0.0 ± 4.9	-60.60	60.80
					L_2	-0.0 ± 5.0	-55.10	67.90
NKLG	TRM59800.00	SCIS	05/05/2010	31/12/2013	L_1	-0.0 ± 7.5	-199.80	122.90
					L_2	-0.0 ± 7.5	-205.00	145.30
NLIB	AOAD/M_T	JPLA	01/01/2004	31/12/2013	L_1	0.0 ± 8.7	-175.70	216.50
					L_2	-0.0 ± 8.8	-180.30	203.40
NOT1	TRM29659.00	NONE	01/01/2004	31/12/2013	L_1	-0.0 ± 4.8	-88.00	107.10
					L_2	-0.0 ± 4.9	-87.50	109.80
NRIL	ASH701945B_M	SCIT	01/01/2004	31/12/2013	L_1	0.0 ± 8.3	-242.80	268.00
					L_2	0.0 ± 9.0	-297.30	288.90
OHI2	AOAD/M_T	DOME	01/01/2004	30/01/2009	L_1	0.0 ± 9.7	-113.00	332.60
					L_2	0.0 ± 9.9	-142.00	397.90
OHI2	TPSCR.G3	TPSH	30/01/2009	31/12/2013	L_1	0.0 ± 10.1	-173.20	426.70
					L_2	0.0 ± 10.4	-249.30	443.70
ORID	LEIAT504GG	LEIS	05/11/2008	31/12/2013	L_1	-0.0 ± 6.3	-492.00	126.80
					L_2	-0.0 ± 5.7	-307.10	138.40
PALM	ASH700936D_M	SCIS	08/03/2008	31/12/2013	L_1	-0.0 ± 8.1	-297.00	184.90
					L_2	-0.0 ± 7.4	-175.30	148.60
PARC	ASH700936D_M	SNOW	01/01/2004	01/11/2009	L_1	-0.0 ± 7.8	-126.20	267.60
					L_2	-0.0 ± 7.7	-163.10	237.70

(continued on next page)

Table E.1: ESM spherical harmonic representation evaluation *(continued from previous page).*

Station	Antenna/radome		From	To	Freq.	Mean [mm]	Min [mm]	Max [mm]
PARC	TRM57971.00	NONE	01/11/2009	31/12/2013	L_1	-0.0 ± 7.5	−97.50	170.70
					L_2	-0.0 ± 7.5	−130.90	99.60
PDEL	LEIAT504	NONE	01/01/2004	05/04/2008	L_1	-0.0 ± 6.9	−143.20	118.00
					L_2	-0.0 ± 7.1	−155.80	148.70
PDEL	LEIAT504GG	NONE	05/04/2008	31/12/2013	L_1	0.0 ± 7.1	−369.40	294.70
					L_2	0.0 ± 7.2	−336.10	243.30
PENC	LEIAT504GG	LEIS	25/06/2007	31/12/2013	L_1	0.0 ± 10.9	−263.40	243.10
					L_2	0.0 ± 11.9	−507.70	265.20
PETP	AOAD/M_T	DOME	01/01/2004	31/12/2013	L_1	-0.0 ± 7.3	−117.70	100.10
					L_2	-0.0 ± 7.4	−147.60	93.50
PIMO	ASH701945C_M	NONE	01/01/2004	31/12/2013	L_1	-0.0 ± 4.9	−145.90	94.90
					L_2	0.0 ± 5.2	−202.80	110.40
POL2	ASH701945C_M	NONE	01/01/2004	22/10/2009	L_1	-0.0 ± 4.6	−67.60	69.90
					L_2	-0.0 ± 4.6	−86.40	72.40
POL2	TPSCR.G3	NONE	23/10/2009	31/12/2013	L_1	-0.0 ± 4.8	−94.10	80.00
					L_2	0.0 ± 4.9	−151.30	83.20
POLV	TRM29659.00	NONE	01/01/2004	13/02/2013	L_1	0.0 ± 5.0	−81.00	98.00
					L_2	0.0 ± 5.1	−70.70	97.20
POLV	LEIAR10	NONE	13/02/2013	31/12/2013	L_1	-0.0 ± 10.4	−312.30	149.50
					L_2	-0.0 ± 10.4	−246.60	106.70
POTS	AOAD/M_T	NONE	01/01/2004	15/02/2011	L_1	-0.0 ± 6.5	−188.40	182.30
					L_2	-0.0 ± 6.7	−186.90	151.60
POTS	JAV_RINGANT_G3T	NONE	15/02/2011	31/12/2013	L_1	0.0 ± 7.2	−124.20	145.10
					L_2	0.0 ± 7.2	−101.60	130.00
QAQ1	ASH701945E_M	SCIS	01/01/2004	31/12/2013	L_1	0.0 ± 4.4	−88.00	79.00
					L_2	0.0 ± 4.5	−118.70	84.00
RAMO	ASH701945B_M	SNOW	01/01/2004	31/12/2013	L_1	-0.0 ± 5.3	−171.80	188.80
					L_2	-0.0 ± 5.5	−196.30	320.70
RBAY	AOAD/M_T	NONE	01/01/2004	31/12/2013	L_1	-0.0 ± 8.8	−259.40	308.20
					L_2	-0.0 ± 8.7	−269.60	289.40
REUN	ASH701073.3	NONE	01/01/2004	03/12/2008	L_1	0.0 ± 6.1	−99.00	95.20
					L_2	0.0 ± 6.1	−88.90	96.00
REUN	TRM55971.00	NONE	03/12/2008	31/12/2013	L_1	0.0 ± 7.6	−148.40	218.00
					L_2	0.0 ± 7.5	−166.90	165.60
REYK	TPSCR.G3	TPSH	14/03/2008	31/12/2013	L_1	-0.0 ± 10.7	−171.40	262.10
					L_2	-0.0 ± 10.6	−176.00	207.80
ROUL	LEIAT504	LEIS	01/08/2006	05/10/2010	L_1	0.0 ± 6.6	−66.50	72.30
					L_2	0.0 ± 6.7	−60.20	64.00
ROUL	LEIAR25.R3	LEIT	06/10/2010	31/12/2013	L_1	0.0 ± 3.8	−40.80	53.50
					L_2	0.0 ± 3.9	−41.50	70.60

(continued on next page)

Table E.1: ESM spherical harmonic representation evaluation *(continued from previous page).*

Station	Antenna/radome		From	To	Freq.	Mean [mm]	Min [mm]	Max [mm]
SASS	TPSCR3_GGD	CONE	01/01/2004	22/05/2006	L_1	-0.0 ± 7.8	-159.60	109.70
					L_2	-0.0 ± 8.1	-206.40	130.60
SASS	TPSCR3_GGD	CONE	23/05/2006	31/12/2013	L_1	0.0 ± 4.5	-104.90	68.90
					L_2	0.0 ± 4.6	-131.90	60.60
SCH2	AOAD/M_T	NONE	01/01/2004	06/10/2008	L_1	-0.0 ± 4.1	-67.60	58.30
					L_2	-0.0 ± 4.1	-57.00	67.40
SCH2	ASH701945E_M	NONE	06/10/2008	31/12/2013	L_1	0.0 ± 7.4	-128.90	176.90
					L_2	-0.0 ± 7.2	-136.10	176.00
SCUB	ASH700936C_M	SNOW	01/01/2004	31/12/2013	L_1	0.0 ± 5.3	-85.90	138.60
					L_2	0.0 ± 5.3	-102.30	103.70
SNEO	LEIAR25	LEIT	13/05/2009	31/12/2013	L_1	-0.0 ± 9.2	-129.20	164.70
					L_2	-0.0 ± 9.2	-172.60	129.50
SPT0	AOAD/M_T	OSOD	01/01/2004	06/05/2008	L_1	-0.0 ± 6.3	-82.10	104.20
					L_2	-0.0 ± 6.4	-96.40	94.70
SPT0	AOAD/M_T	OSOD	07/05/2008	31/12/2013	L_1	0.0 ± 8.8	-241.60	354.70
					L_2	0.0 ± 9.1	-333.00	336.20
STJO	AOAD/M_T	NONE	01/01/2004	18/03/2010	L_1	-0.0 ± 4.6	-97.90	89.10
					L_2	-0.0 ± 4.7	-104.50	78.50
STJO	AOAD/M_T	NONE	18/03/2010	31/12/2013	L_1	0.0 ± 5.7	-149.00	111.90
					L_2	0.0 ± 5.7	-174.60	104.50
STRN	LEIAR25	LEIT	11/03/2009	31/12/2013	L_1	0.0 ± 6.7	-160.70	269.60
					L_2	0.0 ± 6.9	-320.10	316.60
SUTH	ASH701945C_M	NONE	01/01/2004	01/06/2004	L_1	0.0 ± 11.7	-124.10	93.50
					L_2	0.0 ± 11.9	-98.40	100.60
SUTH	ASH701945G_M	NONE	01/06/2004	31/12/2013	L_1	0.0 ± 8.3	-209.60	273.20
					L_2	0.0 ± 8.1	-214.40	303.80
SWAS	LEIAR25	LEIT	14/08/2009	31/12/2013	L_1	-0.0 ± 7.9	-320.20	173.70
					L_2	-0.0 ± 7.9	-261.80	210.90
SYOG	AOAD/M_T	DOME	01/01/2004	31/12/2013	L_1	-0.0 ± 3.9	-65.10	42.00
					L_2	-0.0 ± 3.9	-66.90	46.20
THTI	TRM29659.00	NONE	01/01/2004	12/01/2004	L_1	-0.0 ± 0.0	0.00	0.00
					L_2	-0.0 ± 0.0	0.00	0.00
THTI	ASH701945E_M	NONE	13/01/2004	31/12/2013	L_1	0.0 ± 4.5	-100.10	140.30
					L_2	0.0 ± 4.4	-90.90	112.90
THU3	ASH701073.1	SCIS	01/01/2004	31/12/2013	L_1	-0.0 ± 7.4	-312.80	242.50
					L_2	-0.0 ± 6.9	-206.40	204.70
TIDB	AOAD/M_T	JPLA	01/01/2004	31/12/2013	L_1	-0.0 ± 6.8	-183.20	298.90
					L_2	-0.0 ± 6.8	-173.10	252.80
TIXI	ASH700936D_M	SCIS	01/01/2004	20/10/2010	L_1	0.0 ± 8.6	-115.30	250.20
					L_2	0.0 ± 8.7	-109.00	227.40

(continued on next page)

Table E.1: ESM spherical harmonic representation evaluation *(continued from previous page).*

Station	Antenna/radome		From	To	Freq.	Mean [mm]	Min [mm]	Max [mm]
TIXI	TPSCR3_GGD	NONE	20/10/2010	31/12/2013	L_1	0.0 ± 14.1	−189.50	354.90
					L_2	0.0 ± 14.1	−254.10	400.50
TNML	AOAD/M_T	NONE	01/01/2004	31/12/2013	L_1	−0.0 ± 4.5	−73.10	89.20
					L_2	−0.0 ± 4.6	−82.70	69.40
TORI	LEIAR25.R3	NONE	08/03/2011	31/12/2013	L_1	−0.0 ± 7.9	−264.80	109.70
					L_2	−0.0 ± 7.9	−215.70	109.00
TOW2	AOAD/M_T	AUST	01/01/2004	23/09/2011	L_1	0.0 ± 4.7	−123.70	199.10
					L_2	0.0 ± 4.9	−164.20	228.00
TOW2	LEIAR25.R3	NONE	23/09/2011	31/12/2013	L_1	−0.0 ± 5.6	−127.30	116.80
					L_2	−0.0 ± 5.8	−84.70	188.90
TRO1	ASH701073.1	SCIS	01/01/2004	13/07/2004	L_1	−0.0 ± 13.9	−210.80	239.90
					L_2	−0.0 ± 13.9	−208.90	230.80
TRO1	AOAD/M_T	NONE	13/07/2004	23/08/2007	L_1	0.0 ± 7.5	−160.30	113.60
					L_2	0.0 ± 7.6	−131.80	99.10
TRO1	TRM55971.00	NONE	23/08/2007	26/07/2010	L_1	−0.0 ± 8.2	−155.40	101.50
					L_2	−0.0 ± 8.4	−200.10	123.90
TRO1	TRM59800.00	SCIS	26/07/2010	31/12/2013	L_1	−0.0 ± 7.1	−82.10	211.20
					L_2	−0.0 ± 7.2	−110.50	200.20
TROI	LEIAT504	LEIS	01/08/2006	11/10/2010	L_1	−0.0 ± 6.4	−73.10	75.70
					L_2	−0.0 ± 6.5	−68.50	107.70
TROI	LEIAR25.R3	LEIT	12/10/2010	31/12/2013	L_1	0.0 ± 3.8	−72.70	63.90
					L_2	0.0 ± 3.9	−79.60	90.20
TSKB	AOAD/M_T	DOME	01/01/2004	01/07/2011	L_1	−0.0 ± 6.9	−168.00	267.40
					L_2	−0.0 ± 7.2	−160.60	376.20
TUBO	LEIAT504	LEIS	15/12/2005	12/12/2011	L_1	−0.0 ± 10.4	−290.70	335.40
					L_2	−0.0 ± 11.1	−498.30	364.90
TUBO	LEIAR25.R4	LEIT	12/12/2011	31/12/2013	L_1	0.0 ± 8.2	−256.00	166.60
					L_2	0.0 ± 8.0	−163.20	151.70
UNSA	AOAD/M_T	NONE	01/01/2004	23/07/2008	L_1	0.0 ± 8.4	−128.70	137.10
					L_2	0.0 ± 8.5	−134.80	143.00
UNSA	TPSCR3_GGD	NONE	24/07/2008	31/12/2013	L_1	−0.0 ± 6.6	−90.00	85.60
					L_2	−0.0 ± 6.6	−84.10	82.20
USNO	AOAD/M_T	NONE	01/01/2004	31/12/2013	L_1	0.0 ± 6.1	−105.40	135.20
					L_2	0.0 ± 6.2	−114.60	127.20
VALE	LEIAR25.R3	LEIT	17/09/2010	31/12/2013	L_1	0.0 ± 6.5	−100.10	166.10
					L_2	0.0 ± 6.4	−93.60	127.50
VESL	TRM29659.00	TCWD	01/01/2004	31/12/2013	L_1	−0.0 ± 13.5	−330.10	564.60
					L_2	−0.0 ± 14.2	−276.10	717.70
VIS0	AOAD/M_T	OSOD	01/01/2004	31/12/2013	L_1	0.0 ± 7.6	−145.70	152.70
					L_2	0.0 ± 7.6	−162.50	126.10

(continued on next page)

Table E.1: ESM spherical harmonic representation evaluation *(continued from previous page).*

Station	Antenna/radome		From	To	Freq.	Mean [mm]	Min [mm]	Max [mm]
WALF	LEIAT504	LEIS	01/08/2006	17/10/2010	L_1	0.0 ± 6.1	−57.40	57.60
					L_2	0.0 ± 6.2	−56.80	58.00
WALF	LEIAR25.R3	LEIT	18/10/2010	31/12/2013	L_1	−0.0 ± 4.1	−49.30	55.00
					L_2	−0.0 ± 4.1	−51.90	53.10
WARN	TPSCR3_GGD	CONE	01/01/2004	15/09/2010	L_1	−0.0 ± 6.8	−182.40	127.60
					L_2	−0.0 ± 6.8	−114.30	159.10
WARN	LEIAR25.R3	LEIT	16/09/2010	31/12/2013	L_1	0.0 ± 6.7	−128.90	190.90
					L_2	−0.0 ± 6.7	−111.00	243.40
WHIT	AOAD/M_T	NONE	01/01/2004	31/12/2013	L_1	0.0 ± 5.5	−167.30	105.30
					L_2	0.0 ± 5.5	−155.20	86.90
WIND	ASH700936C_M	SNOW	01/01/2004	28/02/2011	L_1	−0.0 ± 6.3	−83.50	93.90
					L_2	−0.0 ± 6.4	−80.50	98.70
WIND	JAV_RINGANT_G3T	NONE	28/02/2011	31/12/2013	L_1	0.0 ± 6.8	−163.80	100.80
					L_2	0.0 ± 6.9	−175.10	112.60
WSRT	AOAD/M_T	DUTD	01/01/2004	31/12/2013	L_1	−0.0 ± 3.5	−137.50	57.20
					L_2	−0.0 ± 3.6	−148.70	56.40
YEBE	TRM29659.00	NONE	01/01/2004	31/12/2013	L_1	0.0 ± 7.7	−163.60	400.70
					L_2	0.0 ± 7.7	−161.50	294.20
YIBL	ASH701945C_M	NONE	01/01/2004	31/12/2013	L_1	0.0 ± 7.2	−114.10	84.10
					L_2	0.0 ± 7.2	−112.50	96.40
ZAMB	AOAD/M_T	NONE	01/01/2004	31/12/2013	L_1	0.0 ± 8.5	−281.30	276.50
					L_2	0.0 ± 8.5	−332.30	177.30
ZIM2	TRM55971.00	NONE	09/11/2007	12/05/2009	L_1	0.0 ± 7.3	−79.60	141.30
					L_2	0.0 ± 7.4	−103.70	131.90
ZIM2	TRM59800.00	NONE	13/05/2009	31/12/2013	L_1	−0.0 ± 8.1	−426.50	263.00
					L_2	−0.0 ± 8.5	−571.30	253.00
ZYWI	TRM55971.00	TZGD	26/11/2007	31/12/2013	L_1	−0.0 ± 7.4	−110.20	202.20
					L_2	−0.0 ± 7.4	−104.80	178.30